



MID-AMERICA TRANSPORTATION CENTER

Report # MATC-UNL: 004-33

Final Report
WBS: 25-1121-0005-004-33

UNIVERSITY OF
Nebraska
Lincoln

THE UNIVERSITY
OF IOWA

THE UNIVERSITY OF
KU KANSAS

MISSOURI
S&T

LINCOLN
UNIVERSITY
MISSOURI



UNIVERSITY OF
Nebraska
Omaha

University of Nebraska
Medical Center

KU MEDICAL
CENTER
The University of Kansas

Protecting Critical Civil Infrastructure Against Impact from Commercial Vehicles - Phase II

Daniel G. Linzell, PhD PE

Associate Dean for Graduate and International Programs
Department of Civil and Environmental Engineering
University of Nebraska-Lincoln

Chen Fang, PhD

Post-Doctoral Research Associate
Midwest Roadside Safety Facility

Qusai Abdulkarim Alomari

Research Graduate Associate
Department of Civil and Environmental
Engineering

UNIVERSITY OF
Nebraska
Lincoln

2021

A Cooperative Research Project sponsored by
U.S. Department of Transportation- Office of the Assistant
Secretary for Research and Technology

The contents of this report reflect the views of the authors, who are responsible for the facts and the accuracy of the information presented herein. This document is disseminated in the interest of information exchange. The report is funded, partially or entirely, by a grant from the U.S. Department of Transportation's University Transportation Centers Program. However, the U.S. Government assumes no liability for the contents or use thereof.

MATC

Protecting Critical Civil Infrastructure Against Impact from Commercial Vehicles

Phase II Final Report

Daniel G. Linzell, Ph.D., P.E., F.ASCE, F.SEI
Associate Dean for Graduate and International Programs
College of Engineering
Leslie D. Martin Professor
Department of Civil and Environmental Engineering
University of Nebraska-Lincoln

Chen Fang, Ph.D., A.M.ASCE
Post-Doctoral Research Associate
Midwest Roadside Safety Facility
College of Engineering
University of Nebraska-Lincoln

Qusai Abdulkarim Alomari,
Graduate Research Assistant
Department of Civil and Environmental Engineering
University of Nebraska-Lincoln

A Report on Research Sponsored by

Mid-America Transportation Center

University of Nebraska–Lincoln

March 2019 (month and year report was received/published by NTC/MATC)

Technical Report Documentation Page

1. Report No. 25-1121-0005-004-33	2. Government Accession No.	3. Recipient's Catalog No.	
4. Title and Subtitle Protecting Critical Civil Infrastructure Against Impact from Commercial Vehicles - Phase II		5. Report Date September 2021	
		6. Performing Organization Code	
7. Author(s) Daniel G. Linzell https://orcid.org/0000-0002-7158-1776 , Chen Fang https://orcid.org/0000-0002-2883-6497 , Qusai Abdulkarim Alomari		8. Performing Organization Report No. 22-1121-0005-004-33	
9. Performing Organization Name and Address Mid-America Transportation Center Prem S. Paul Research Center at Whittier School 2200 Vine St. Lincoln, NE 68583-0851		10. Work Unit No. (TRAIS)	
		11. Contract or Grant No. 69A3551747107	
12. Sponsoring Agency Name and Address Office of the Assistant Secretary for Research and Technology 1200 New Jersey Ave., SE Washington, D.C. 20590		13. Type of Report and Period Covered July 2019 – September 2021	
		14. Sponsoring Agency Code MATC TRB RiP No. 91994-61	
15. Supplementary Notes Conducted in cooperation with the U.S. Department of Transportation, Federal Highway Administration.			
16. Abstract Pier columns could be under-designed for commercial vehicle impacts and additional events that could occur, such as blast. This research study focused on improving resiliency and robustness of bridge piers and pier columns when subjected to combined vehicle collision and air blast. To achieve this goal, a multi-column highway bridge pier and its supporting foundation was used as the prototypical supporting unit for the analytically focused study. Three-dimensional LS-DYNA numerical models were developed of single circular reinforced concrete (RC) columns and piers along with their supporting spread footings and piles. Collision loads were supplied from a modeled Ford F800 Single-Unit truck. Air blasts of varying magnitude were represented using an LS-DYNA Arbitrary Lagrangian-Eulerian approach. The model was validated against published RC structural element impact and blast tests. Developed models were used to investigate bridge column and pier response to vehicle collision and air blast. Parametric studies were conducted to analyze the effects of specific design parameters on performance and serviceability. Using these results, damage indices were developed by comparing residual axial load capacities of a damaged column to the column's undamaged ultimate axial capacity. Analysis techniques were also studied and a simple performance-based design procedure proposed. Numerical models that examined the effectiveness with which different retrofit schemes, namely use of an FRP wrap or polyurea coating around the periphery of the columns, improved resistance to air blast and vehicle impact.			
17. Key Words Bridge; Reinforced Concrete; Column; Collision; Blast; Vehicle		18. Distribution Statement Data and reports will be limited to members of the program until publications and presentations are submitted.	
19. Security Classif. (of this report) Unclassified	20. Security Classif. (of this page) Unclassified	21. No. of Pages 206	22. Price

Table of Contents

Acknowledgments.....	xi
Disclaimer	xii
Abstract	xiii
Chapter 1 Introduction and Background.....	1
1.1 Background.....	1
1.2 Problem Statement	3
1.3 Objective	3
1.4 Scope.....	4
Chapter 2 Numerical Model Development and Validation	5
2.1 Introduction.....	5
2.2 Vehicle collision and air blast modeling.....	5
2.2.1 Vehicle collision modeling	5
2.2.2 Air blast modeling.....	6
2.3 Material models and element formulations.....	8
2.3.1 Concrete	8
2.3.2 Steel.....	9
2.3.3 Soil	10
2.3.4 Explosive and air.....	10
2.4 Model coupling and boundary conditions.....	12
2.5 Validation studies.....	14
2.6 Studied Pier Column	14
2.7 Conclusions.....	16
Chapter 3 Numerical Simulation of an Isolated Column Subjected to Vehicle Collision and Air Blast	17
3.1 Introduction.....	17
3.2 Load Sequence Study.....	17
3.2.1 Load sequence.....	17
3.2.2 Analytical procedure.....	18
3.2.3 Column response.....	19
3.3 Response of Bridge Column to Vehicle Collision and Air Blast.....	24
3.4 Bridge column damage	35
3.4.1 Concrete surface cracking (M1).....	36
3.4.2 Concrete cover spalling (M2)	37
3.4.3 Formation of plastic hinge (M3)	38
3.4.4 Direct shear failure (M4)	39
3.4.5 Reinforcement failure (M5)	40
3.4.6 Concrete breach (M6)	41
3.5 Conclusions.....	47
Chapter 4 Isolated Bridge Columns Performance under Combined Vehicle Collision and Air Blast	49
4.1 Introduction.....	49
4.2 Parameter matrix	49
4.2.1 Fixed parameters	49

4.2.2 Study matrix.....	50
4.3 Parametric study results	50
4.3.1 Concrete spalling severity and reinforcement buckling.....	51
4.3.1.1 Column diameter.....	51
4.3.1.2 Column height.....	55
4.3.1.3 Longitudinal reinforcement ratio	58
4.3.1.4 Shear reinforcement (hoop) spacing	63
4.3.1.5 Axial load ratio	68
4.3.2 Shear resistance.....	73
4.3.2.1 Column diameter.....	75
4.3.2.2 Column height.....	75
4.3.2.3 Longitudinal reinforcement ratio	76
4.3.2.4 Shear reinforcement (hoop) spacing	77
4.3.2.5 Axial load ratio	78
4.3.3 Residual axial capacity	79
4.3.3.1 Column diameter.....	81
4.3.3.2 Column height.....	82
4.3.3.3 Longitudinal reinforcement ratio	82
4.3.3.4 Shear reinforcement (hoop) spacing	83
4.3.3.5 Axial load ratio	84
4.3.3.6 Empirical formula for determination of column residual axial load capacity	85
4.4 Conclusions	89
Chapter 5 Performance-based Design and Analysis Framework	91
5.1 Introduction.....	91
5.2 Principles of performance-based design	91
5.3 Performance-based design framework.....	93
5.3.1 Demand-to-capacity calculation	93
5.3.2 Performance objectives.....	94
5.3.3 Quantification of performance level	96
5.3.4 Design procedure	98
5.4 Validation of design framework	101
5.5 Conclusions	105
Chapter 6 Investigation of In-Situ Retrofit Schemes.....	107
6.1 Introduction.....	107
6.2 Numerical modeling of strengthened bridge column.....	107
6.2.1 FRP	107
6.2.2 Polyurea	109
6.2.3 Model development	110
6.2.4 Model validation	111
6.2.4.1 FRP wrapped column under impact load.....	111
6.2.4.2 FRP-wrapped slab under blast	115
6.3 Numerical studies.....	117
6.3.1 Studied column	117
6.3.2 Simulations of CFRP-wrapped bridge column.....	119

6.3.2.1 Collision velocity	119
6.3.2.2 Scaled distance	122
6.3.3 Simulations of polyurea-coated bridge column	126
6.3.3.1 Collision velocity	126
6.3.3.2 Scaled distance	129
6.4 Parametric studies	134
6.4.1 CFRP strength	134
6.4.2 CFRP thickness	137
6.4.3 Polyurea thickness	140
6.5 Comparison of CFRP and polyurea retrofit effectiveness	143
6.6 Conclusions	148
Chapter 7 Multi-column Bridge Piers to Vehicle Collision and Air Blast	151
7.1 Introduction	151
7.2 Finite element modeling	151
7.2.1 Pier geometries and design details	151
7.2.2 Material models	154
7.2.3 Boundary conditions	154
7.3 Response of Multi-Column Pier to Vehicle Collision and Air Blast	155
7.3.1 Combined collision-blast loading and pier response	155
7.3.2 Pier damage	167
7.4 Parametric studies and discussions	171
7.4.1 Collision angle	172
7.4.2 Collision location	175
7.4.3 Axial load ratio	178
7.4.4 Shear reinforcement (hoop) spacing	180
7.4.5 Longitudinal reinforcement ratio	182
7.5 Multi-column pier retrofit	184
7.6 Conclusions	188
Chapter 8 Conclusions and On-going Research	190
8.1 Introduction	190
8.2 Findings	190
8.2.1 Isolated column	191
8.2.1.1 Isolated column response:	191
8.2.1.2 Isolated column performance:	193
8.2.2 Multi-column pier	197
8.2.2.1 Multi-column pier response:	197
8.2.2.2 Multi-column pier performance:	198
8.3 On-going Research	199
References	201

List of Figures

Figure 1.1 I-65 vehicle collision and explosion [1].....	1
Figure 1.2 Pier column damage, protective barrier in place.....	2
Figure 2.1 Ford F800 single-unit truck (SUT) model.....	6
Figure 2.2 Blast damage threshold [14].....	8
Figure 2.3 FE model of isolated RC column under vehicle collision and air blast	13
Figure 2.4 Prototype pier and column (unit: mm) [32].....	15
Figure 2.5 Finite element model of column and foundation.....	15
Figure 2.6 Column cross-sections (unit: mm).	16
Figure 3.1 Studied load sequences.....	18
Figure 3.2 Column damage for three load sequences with $v_0 = 120$ km/h; $Z = 0.25$ m/kg ^{1/3}	20
Figure 3.3 Damage states of 1050 mm diameter column for three load sequences	22
Figure 3.4 Reinforcement damage: (a) I1-B2; (b) I1-B1; (c) B1-I2.....	23
Figure 3.5 750 mm diameter column: (a) times of interest; (b) damage propagation; (c) reinforcement behavior; (d) column deformation ($v_0 = 120$ km/h, $Z = 0.25$ m/kg ^{1/3}).....	29
Figure 3.6 1050 mm diameter column: (a) times of interest; (b) damage propagation; (c) reinforcement behavior; (d) column deformation ($v_0 = 120$ km/h, $Z = 0.25$ m/kg ^{1/3}).....	30
Figure 3.7 1350 mm diameter column: (a) times of interest; (b) damage propagation; (c) reinforcement behavior; (d) column deformation ($v_0 = 120$ km/h, $Z = 0.25$ m/kg ^{1/3}).....	31
Figure 3.8 Lateral displacement time-history	32
Figure 3.9 Concrete surface cracking	37
Figure 3.10 Concrete cover spalling	38
Figure 3.11 Formation of plastic hinge.....	39
Figure 3.12 Shear failure	40
Figure 3.13 Reinforcement failure.....	41
Figure 3.14 Concrete breach.....	42
Figure 3.15 750 mm diameter column final damage states for representative loading cases.....	44
Figure 3.16 1050 mm diameter column final damage states for representative loading cases.....	45
Figure 3.17 1350 mm diameter column final damage states for representative loading cases.....	46
Figure 4.1 Column diameter effect on damage categories.	54
Figure 4.2 Diameter effect on average longitudinal reinforcement axial strains: (a) $v_0 = 65$ km/h; $Z = 0.30$ m/kg ^{1/3} ; (b) $v_0 = 95$ km/h; $Z = 0.25$ m/kg ^{1/3} ; (c) $v_0 = 120$ km/h; $Z = 0.25$ m/kg ^{1/3}	54
Figure 4.3 Diameter effects on maximum deflection.	55
Figure 4.4 Column height effect on damage categories	57
Figure 4.5 Column height effect on average longitudinal reinforcement axial strains.....	57
Figure 4.6 Column height effect on maximum deflection.....	58
Figure 4.7 Longitudinal reinforcement ratio effect on damage categories.....	61
Figure 4.8 Longitudinal reinforcement ratio effects on average longitudinal reinforcement axial strains: (a) $v_0 = 95$ km/h; $Z = 0.25$ m/kg ^{1/3} ; (b) $v_0 = 120$ km/h; $Z = 0.25$ m/kg ^{1/3}	62
Figure 4.9 Longitudinal reinforcement ratio effect on maximum deflection	63
Figure 4.10 Shear reinforcement effect on damage categories.....	66
Figure 4.11 Shear reinforcement effect on average longitudinal reinforcement axial strain: (a) $v_0 = 95$ km/h; $Z = 0.30$ m/kg ^{1/3} ; (b) $v_0 = 120$ km/h; $Z = 0.25$ m/kg ^{1/3}	67
Figure 4.12 Shear reinforcements on maximum deflection.....	68

Figure 4.13 Axial load ratio effect on damage categories	71
Figure 4.14 Axial load ratio effect on average longitudinal reinforcement axial strains: (a) $v_0 = 95$ km/h; $Z = 0.30 \text{ m/kg}^{1/3}$; (b) $v_0 = 120$ km/h; $Z = 0.25 \text{ m/kg}^{1/3}$	72
Figure 4.15 Axial load ratio effects on maximum column deflection	73
Figure 4.16 Representative shear diagrams for columns in various cases: (a) $v_0 = 65$ km/h; $Z = 0.25 \text{ m/kg}^{1/3}$; (b) $v_0 = 95$ km/h; $Z = 0.30 \text{ m/kg}^{1/3}$; (c) $v_0 = 120$ km/h; $Z = 0.25 \text{ m/kg}^{1/3}$	74
Figure 4.17 Diameter effect on normalized base shear: (a) $v_0 = 65$ km/h; $Z = 0.30 \text{ m/kg}^{1/3}$; (b) $v_0 = 95$ km/h; $Z = 0.25 \text{ m/kg}^{1/3}$; (c) $v_0 = 120$ km/h; $Z = 0.25 \text{ m/kg}^{1/3}$	75
Figure 4.18 Height effect on normalized base shear: (a) $v_0 = 65$ km/h; $Z = 0.30 \text{ m/kg}^{1/3}$; (b) $v_0 = 95$ km/h; $Z = 0.25 \text{ m/kg}^{1/3}$; (c) $v_0 = 120$ km/h; $Z = 0.25 \text{ m/kg}^{1/3}$	76
Figure 4.19 Longitudinal reinforcement ratio effect on normalized base shear: (a) $v_0 = 65$ km/h; $Z = 0.30 \text{ m/kg}^{1/3}$; (b) $v_0 = 95$ km/h; $Z = 0.25 \text{ m/kg}^{1/3}$; (c) $v_0 = 120$ km/h; $Z = 0.25 \text{ m/kg}^{1/3}$	77
Figure 4.20 Hoop spacing effects on normalized base shear forces: (a) $v_0 = 65$ km/h; $Z = 0.30 \text{ m/kg}^{1/3}$; (b) $v_0 = 95$ km/h; $Z = 0.25 \text{ m/kg}^{1/3}$; (c) $v_0 = 120$ km/h; $Z = 0.25 \text{ m/kg}^{1/3}$	78
Figure 4.21 Axial load ratio effect on normalized base shear: (a) $v_0 = 65$ km/h; $Z = 0.30 \text{ m/kg}^{1/3}$; (b) $v_0 = 95$ km/h; $Z = 0.25 \text{ m/kg}^{1/3}$; (c) $v_0 = 120$ km/h; $Z = 0.25 \text{ m/kg}^{1/3}$	79
Figure 4.22 Representative axial load-mid-height displacement curve, 1050 mm diameter column ($v_0 = 95$ km/h; $Z = 0.30 \text{ m/kg}^{1/3}$)	80
Figure 4.23 λ_{res} vs. E_t for different column diameters.....	81
Figure 4.24 λ_{res} vs. E_t for different column heights ($D = 1050$ mm).....	82
Figure 4.25 λ_{res} vs. E_t for different longitudinal reinforcement ratios ($D = 1050$ mm)	83
Figure 4.26 λ_{res} vs. E_t for different hoop spacings ($D = 1050$ mm)	84
Figure 4.27 λ_{res} vs. E_t for different axial load ratios ($D = 1050$ mm).....	85
Figure 4.28 Comparison of empirical equation and numerical results	88
Figure 5.1 Damage state for each performance level: (a) minor damage; (b) moderate damage; (c) severe damage	95
Figure 5.2 Damage index versus D/C ratio for bridge columns under combined collision and blast	97
Figure 5.3. Blast damage threshold	99
Figure 5.4 Performance-based design procedure for bridge column subjected to combined vehicle collision and air blast.....	101
Figure 5.5 Observed column damage for validation cases	105
Figure 6.1 Stress-strain curves for polyurea at different strain rates	110
Figure 6.2 Pendulum impact test setup and numerical model (mm) [57].....	112
Figure 6.3 FRP-coated pier experimental [57] and modeled failure mode	113
Figure 6.4 Numerical and experimental impact force time histories curves [57].....	114
Figure 6.5 Numerical and experimental strain time histories curves [57].....	115
Figure 6.6 Blast test and numerical model (mm) [66]	116
Figure 6.7 Pressure time histories [66]	117
Figure 6.8 Displacement time histories [66].....	117
Figure 6.9 Geometries and reinforcement details in bridge column with a coating	118
Figure 6.10 Comparison of final damage states, bare and CFRP-wrapped columns	120
Figure 6.11 Comparison of column displacement, bare and CFRP-wrapped columns.....	121
Figure 6.12 Comparison of residual axial capacity and damage indices, bare and CFRP-wrapped columns	122

Figure 6.13 Comparison of final damage states, bare and CFRP-wrapped columns	123
Figure 6.14 Comparison of column deflection and kinetic energy, bare and CFRP-wrapped columns	124
Figure 6.15 Comparison of residual axial capacity and damage index, bare and CFRP-wrapped columns	125
Figure 6.16 Comparison of final damage states, bare and polyurea-coated columns	127
Figure 6.17 Comparison of column deflection and kinetic energy, bare and polyurea-coated columns	128
Figure 6.18 Comparison of residual axial capacity and damage index, bare and polyurea-coated columns	129
Figure 6.19 Comparison of damage mode, bare and polyurea-coated columns	131
Figure 6.20 Comparison of column displacement and kinetic energy, bare and polyurea-coated columns	132
Figure 6.21 Comparison of residual axial capacity and damage index, bare and polyurea-coated columns	133
Figure 6.22 Effect of f_{FRP} on final damage states	135
Figure 6.23 Effect of f_{FRP} on column displacement	135
Figure 6.24 Effect of f_{FRP} on residual axial capacity and damage index	136
Figure 6.25 Effect of f_{FRP} on column kinetic energy	136
Figure 6.26 Effect of t_{FRP} on final damage state	138
Figure 6.27 Effect of t_{FRP} on column displacement	139
Figure 6.28 Effect of t_{FRP} on residual axial capacity and damage index	140
Figure 6.29 Effect of t_{FRP} on CFRP dissipated energies	140
Figure 6.30 Effect of t_{Pol} on column damage	141
Figure 6.31 Effect of t_{Pol} on column deflection	142
Figure 6.32 Effect of t_{Pol} on residual axial capacity and damage index	143
Figure 6.33 Effect of t_{Pol} on polyurea dissipated energies for polyurea-coated columns	143
Figure 6.34 Final damage states for different in-situ retrofit schemes	146
Figure 6.35 Comparison of displacements and dissipated energies	147
Figure 6.36 Comparison of residual axial capacity and damage index for different in-situ retrofit schemes	148
Figure 7.1 Finite element model of four-column pier [32]	152
Figure 7.2 Two and three column pier finite element models	153
Figure 7.3 Numerical models representing multi-column pier	154
Figure 7.4 Two column pier: (a) times of interest; (b) damage propagation; (c) reinforcement behavior ($v_0 = 95$ km/h, $Z = 0.25$ m/kg ^{1/3})	160
Figure 7.5 Three column pier: (a) times of interest; (b) damage propagation; (c) reinforcement behavior ($v_0 = 95$ km/h, $Z = 0.25$ m/kg ^{1/3})	163
Figure 7.6 Four column pier: (a) times of interest; (b) damage propagation; (c) reinforcement behavior ($v_0 = 95$ km/h, $Z = 0.25$ m/kg ^{1/3})	166
Figure 7.7 Damage and reinforcement deformation for two-column pier	169
Figure 7.8 Damage and reinforcement deformation for three-column pier	170
Figure 7.9 Damage and reinforcement deformation for four-column pier	171
Figure 7.10 Vehicle-pier collision angle	172
Figure 7.11 Effect of θ_i on pier damage	174

Figure 7.12 Effect of θ_i on maximum displacement of impacted column	174
Figure 7.13 Vehicle-pier collision location	175
Figure 7.14 Pier damage for three collision locations	177
Figure 7.15 Maximum displacement of impacted column with three collision locations	177
Figure 7.16 Effect of α_{ALE} on pier damage	179
Figure 7.17 Effect of α_{ALE} on maximum displacement of impacted column	179
Figure 7.18 Effect of s_v on pier damage	181
Figure 7.19 Effect of s_v on maximum displacement of impacted column	181
Figure 7.20 Effect of ρ_L on pier damage	183
Figure 7.21 Effect of ρ_L on maximum displacement of impacted column	183
Figure 7.22 Comparison of pier damage for CFRP and polyurea retrofit schemes	186
Figure 7.23 Comparison of displacement for CFRP and polyurea retrofit schemes	187
Figure 7.24 Comparison of column kinetic energy for CFRP and polyurea retrofit schemes ...	187

List of Tables

Table 2.1 Material properties of concrete and steel reinforcement	9
Table 2.2 Soil material parameters	10
Table 2.3 TNT explosive material and EOS parameters	11
Table 2.4 Air material and EOS parameters	12
Table 3.1 Response of 750 mm, 1050 mm, and 1350 mm diameter columns, I1-B2.	33
Table 4.1 Examined parameters.....	50
Table 4.2 Diameter effect on damage	53
Table 4.3 Height effects on damage.	56
Table 4.4 Longitudinal reinforcement ratio effect on damage	60
Table 4.5 Shear reinforcement effect on damage	65
Table 4.6. Axial load ratio effect on damage.....	70
Table 5.1 Performance-based design criteria under combined collision-blast cases.....	98
Table 5.2 Evaluation of damage index and performance level for representative cases	98
Table 5.3 Validation studies for proposed performance-based criteria	102
Table 6.1 Material properties of CFRP composite	108
Table 6.2 Polyurea material properties	110
Table 6.3 Effect of FRP strength on column response	134
Table 6.4 Effect of CFRP thickness on column response.....	137
Table 6.5 Effect of polyurea thickness on column response	141
Table 6.6 Comparison of in-situ retrofit schemes.....	144
Table 7.1 Effect of collision angle on pier response.....	172
Table 7.2 Effect of collision location on pier response	175
Table 7.3 Effect of axial load ratio on pier response	178
Table 7.4 Effect of hoop spacing on pier response	180
Table 7.5 Effect of longitudinal reinforcement ratio on pier response	182
Table 8.1 Identified damage state	191
Table 8.2 Effects of specified design parameters	192
Table 8.3 Performance-based design criteria for combined collision and blast	193
Table 8.4 Effects of controlling parameters for retrofit schemes	194
Table 8.5 Comparison of CFRP wrap and polyurea coating	195
Table 8.6 Comparison of controlling design parameter and retrofit schemes	196

Acknowledgments

This research is funded, in part, by the Mid-America Transportation Center via a grant from the U.S. Department of Transportation's University Transportation Centers Program, and this support is gratefully acknowledged. This work was completed utilizing the Holland Computing Center of the University of Nebraska, which receives support from the Nebraska Research Initiative. The authors would like to gratefully acknowledge computational support provided by the University of Nebraska's Holland Computing Center.

Disclaimer

The contents of this report reflect the views of the authors, who are responsible for the facts and the accuracy of the information presented herein. This document is disseminated in the interest of information exchange. The report is funded, partially or entirely, by a grant from the U.S. Department of Transportation's University Transportation Centers Program. However, the U.S. Government assumes no liability for the contents or use thereof.

Abstract

Pier columns could be under-designed for commercial vehicle impacts and additional events that could occur, such as blast. This research study focused on improving resiliency and robustness of bridge piers and pier columns when subjected to combined vehicle collision and air blast. To achieve this goal, a multi-column highway bridge pier and its supporting foundation was used as the prototypical supporting unit for the analytically focused study. Three-dimensional LS-DYNA numerical models were developed of single circular reinforced concrete (RC) columns and piers along with their supporting spread footings and piles. Collision loads were supplied from a modeled Ford F800 Single-Unit truck. Air blasts of varying magnitude were represented using an LS-DYNA Arbitrary Lagrangian-Eulerian approach. The model was validated against published RC structural element impact and blast tests.

Developed models were used to investigate bridge column and pier response to vehicle collision and air blast. Parametric studies were conducted to analyze the effects of specific design parameters on performance and serviceability. Using these results, damage indices were developed by comparing residual axial load capacities of a damaged column to the column's undamaged ultimate axial capacity. Analysis techniques were also studied and a simple performance-based design procedure proposed. Numerical models that examined the effectiveness with which different retrofit schemes, namely use of an FRP wrap or polyurea coating around the periphery of the columns, improved resistance to air blast and vehicle impact.

Chapter 1 Introduction and Background

1.1 Background

Bridge piers consisting of reinforced concrete (RC) columns are common substructure units. When piers are located close to travel lanes, they can be highly vulnerable to impact loads due to an accidental or purposeful vehicle collision and significant damage or complete failure could result. When the impact is coupled with an air blast, further deterioration could occur, possibly resulting in the collapse of the pier over multiple spans or the entire bridge. Current American Association of State Highway and Transportation Officials (AASHTO's) bridge design codes do not explicitly account for vehicle collision coupled with an air blast.

Numerous examples of collisions coupled with air blast exist. In Nashville, Tennessee, 2014, a reinforced concrete bridge over I-65 was impacted by a tanker truck and a subsequent explosion occurred [1]. As shown in Figure 1.1, the bridge pier and girders it supported suffered significant damage, resulting in an unsafe condition.



Figure 1.1 I-65 vehicle collision and explosion [1]

To protect bridges from vehicle collision and coupled air blasts, be they intentional or unintentional, protective devices, including crash barriers, fencing, and bollards, are often utilized to prevent direct impact and increase explosion physical standoff distance. Bridge piers are often located in a fashion where it is neither possible nor economically feasible to place the protective devices around them. As shown in Figure 1.2, if protective devices are not feasibly positioned their effectiveness can be severely compromised by vehicles. Additional steps could be taken to strengthen the supporting pier columns and caps in-situ via enhanced structural detailing and hardening techniques.

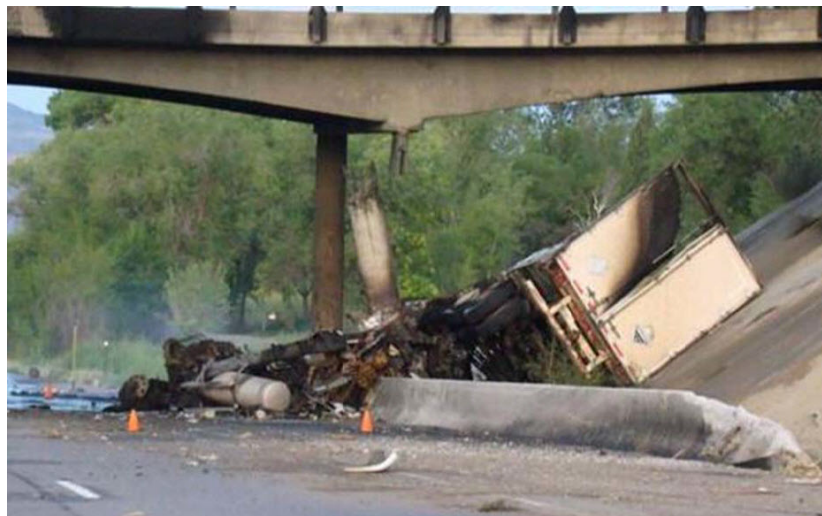


Figure 1.2 Pier column damage, protective barrier in place

AASHTO's Load and Resistance Factor Design (LRFD) Specifications and accompanying state Department of Transportation (DOT) bridge design guides and specifications are the primary design codes for highway bridge design in the U.S. [2]. The 8th edition of the LRFD mandates representing vehicle collision design loads with an equivalent static force (ESF) of 600 kips (2670 kN) at a distance of 5 ft. (1.5 m) above the ground for piers located within 20 ft. (9.1 m) from the roadway edge. Recent research indicates that the

AASHTO-LRFD impact design load may be non-conservative for heavy trucks at high velocities [3-6]. In addition, multi-hazards involving a vehicle impact and an additional event, such as a blast or fire, are not explicitly considered in the LRFD code. Hence, determining appropriate impact bridge pier columns design loads for various hazardous events and improving pier resistance to these extreme events would be beneficial.

1.2 Problem Statement

This research will address the following problems:

- (1) Limited studies have been published examining bridge pier column under collision and blast loads in an attempt to parametrize structural response and damage;
- (2) Insufficient bridge column resistance to collisions from vehicles traveling at high speeds coupled with air blast;
- (3) Lack of useful information on column response and serviceability during a coupled collision and blast event for retrofitting existing columns and constructing new columns;
- (4) Inaccurate representation of demands placed on bridge columns subjected to vehicle collision and air blast.

1.3 Objective

The overall purpose of the research study is to improve the resiliency and robustness of bridge pier columns in the event of intentional or accidental vehicle collision coupled with a possible explosion. Research studies completed to date have investigated the behavior of bridges and bridge components under either vehicle collision or blast, including experimental tests and numerical simulations on bridges and bridge components, but have not examined bridge columns under combined collision and blast loads. This research study is accomplished to help understand

the response of bridge columns subjected to vehicle collision and explosions and provide recommendations related to acceptable column design and retrofit damage mitigation schemes.

1.4 Scope

These objectives will be addressed by:

- (1) Performing a detailed literature review of: studies that investigated the response of reinforced concrete bridge column subjected to the vehicle impact and blast; current U.S. design specification as it relates to these demands; relevant, general RC structural element U.S. specification criteria; and potential retrofit techniques for improving bridge column and substructure unit performance under impact and blast;
- (2) Developing finite element models of single and multiple RC bridge columns that are validated using the experimental results from the literatures;
- (3) Completing numerical simulations of validated column models subjected to simulated truck impacts and air blasts;
- (4) Performing parametric studies that investigate the effects of significant design and demand parameters on pier column response;
- (5) Assessing column residual capacity after damage and developing a predictive equation; and
- (6) Evaluating the effectiveness of various retrofitting techniques to improve the resistance of bridge columns to impact and blast.

Chapter 2 Numerical Model Development and Validation

2.1 Introduction

The research study was conducted based on finite element modeling using LS-DYNA. In the Phase I final report, numerical model development and validation were provided in detail [7]. This chapter reviewed prototype piers for the research study and techniques utilized to create the numerical models of a highway bridge column, its foundation system, and surrounding soil and air volumes.

2.2 Vehicle collision and air blast modeling

2.2.1 Vehicle collision modeling

A realistic vehicle model is essential to determining impact performance of structural elements and systems so accurate energy is delivered to the element or system. The vehicle model utilized in this study was a Ford F800 Single-Unit Truck (SUT) model developed by the Federal Highway Administration (FHWA) at the National Crash Analysis Center (NCAC) [8], as shown in Figure 2.1. SUTs are the most commonly used truck for carrying materials and goods in various areas [9]. In addition, a large majority of harmful crashes that caused severe damage or injuries were associated with the SUT. The Fatality Analysis Reporting System (FARS) and General Estimates System (GES) [9] reported that in 2011, crashes involving a SUT truck constituted 3% of fatal accidents, 1.7% of accidents involving injuries, and 2% of accidents producing damage. The SUT model was validated against experimental tests conducted by many researchers [8], who then improved the model to better simulate material strain-rate sensitivity, the suspension system, and potential failure mechanisms. The modifications of the Ford F800 SUT model and the evaluations of the updated SUT model were performed by Battelle Memorial Institute (BMI), Oak Ridge National Laboratory (ORNL), and the University of Tennessee [10].

Highway speed limits can typically range between 24 km/h in urban areas to 120 km/h in rural locations, with a minimum speed commonly set at 65 km/h. Therefore, SUT impact speeds of 65 km/h, 95 km/h, and 120 km/h were arbitrarily selected for the current studies.

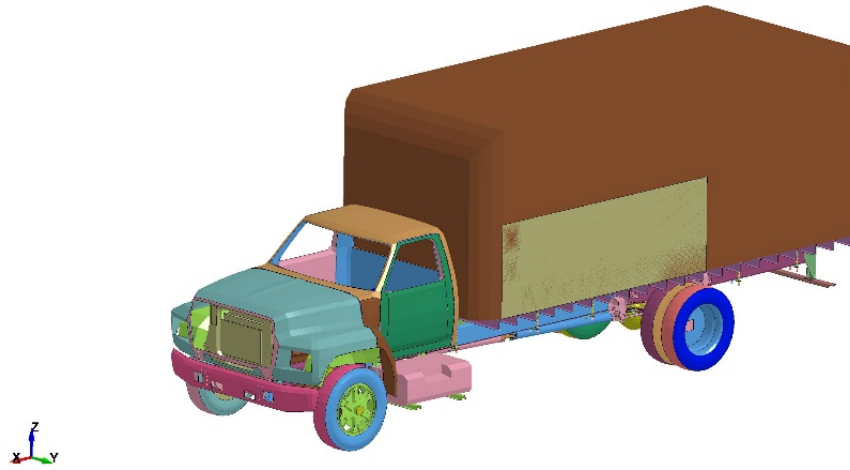


Figure 2.1 Ford F800 single-unit truck (SUT) model

2.2.2 Air blast modeling

The *Multi-Material Arbitrary Lagrangian Eulerian* (MM-ALE) formulation and Fluid Structure Interaction (FSI) algorithm in LS-DYNA [11] were employed to simulate an explosive adjacent to the column in association with the impact event. The MM-ALE formulation avoids severe mesh distortion and subsequent computational instabilities by decoupling mesh and fluid deformations over time and has been used by many researchers to effectively model air blast effects on structural components and systems. For the current study, the air blast involved three stages: (i) detonation; (ii) wave propagation in air; and (iii) interaction between the blast wave, bridge column, and modeled soil volume. Lagrangian meshes were utilized to model the bridge column and pile foundation system. ALE meshes were used for the air, soil volume, and for the explosive and each was defined as the ALE material groupings for interface reconstruction using

the *ALE Multi-Material Group* command. Lagrangian and ALE meshes were coupled together using penalty-based coupling algorithms, with contact between the blast wave and the bridge column simulated using the *Constrained Lagrange In Solid* command [11].

Blast load intensity is primarily dependent on explosive weight and standoff distance between the explosive and structure. A well-known quantity, the scaled distance (Z), is used to reflect blast intensity based on these two variables [12] and is presented in Eq. (1):

$$Z = \frac{R}{\sqrt[3]{w_{TNT}}} \quad (1.1)$$

where R represents the standoff distance and w_{TNT} is the TNT equivalent charge weight.

NCHRP Report 645 [13] recommends bridge column blast performance should be investigated for the design threat at $Z \leq 0.6 \text{ m/kg}^{1/3}$ ($1.5 \text{ ft/lbs}^{1/3}$). The current research examined RC bridge column response to a blast occurring 2500 mm (8.2 ft.) from the column face to mimic potential explosion locations associated with a coupled impact-blast event. Equivalent TNT weight was determined from the Federal Emergency Management Agency (FEMA) estimated weights for structures subjected to terrorist attack, as shown in Figure 2.2 [14]. Resulting scaled distances examined were $0.20 \text{ m/kg}^{1/3}$ ($0.5 \text{ ft/lbs}^{1/3}$), $0.25 \text{ m/kg}^{1/3}$ ($0.6 \text{ ft/lbs}^{1/3}$), and $0.30 \text{ m/kg}^{1/3}$ ($0.8 \text{ ft/lbs}^{1/3}$).

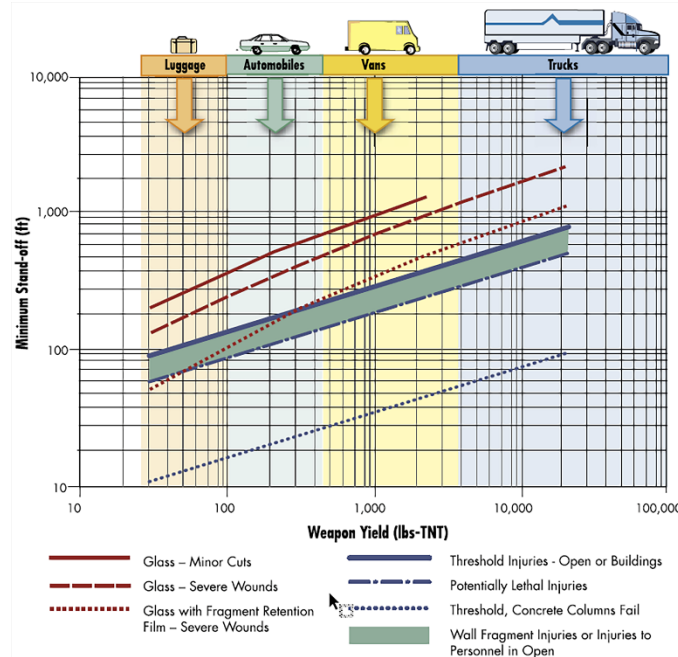


Figure 2.2 Blast damage threshold [14]

2.3 Material models and element formulations

2.3.1 Concrete

The nonlinear *Mat CSCM Concrete* material model in LS-DYNA was selected for the concrete in the column, pile cap, and piles. The CSCM concrete model (*Mat_159*) was developed by the FHWA to predict concrete response for roadside safety applications [15]. Many researchers have used the model to examine RC structural component response to impact or blast load due to its ability to accurately account for strain rate effects and subsequent damage [4, 16-18]. Detailed constitutive properties for a wide variety of concrete can be developed using a parameter initialization function based on the material's compressive strength and maximum aggregate size. The compressive strength of the concrete used was 28 MPa (4 ksi), and the maximum aggregate size was 19 mm (0.75 in.) [19]. Table 2.1 lists the concrete properties.

The CSCM concrete model uses a maximum principal strain-based erosion algorithm to delete highly distorted elements from the computation to prevent computational instabilities due

to mesh tangling. In this study, the value of the erosion coefficient was conservatively selected as 1.10 based on previous research [17, 19] and several simulation trials. This implies that element deletion will occur when the maximum principal strain reaches 10%.

A constant-stress, hexahedral solid element with hourglass control was used to model the concrete in the column, spread footing, and piles. A stiffness-based, Flanagan-Belytschko hourglass control with an hourglass coefficient (QM) of 0.1 was used to minimize nonphysical (hourglass) modes of deformation.

Table 2.1 Material properties of concrete and steel reinforcement

Material	Parameters	Value
Concrete	Mass density, ρ_c (kg/m ³)	2380
	Unconfined compressive strength, f'_c (MPa)	28
	Maximum aggregate size, d_{agg} (mm)	19
Steel	Mass density, ρ_s (kg/m ³)	7850
	Young's modulus, E_s (MPa)	2×10^5
	Poisson's ratio, ν	0.3
	Yield strength, f_y (MPa)	475
	Ultimate strain, ϵ_{fail}	0.12

2.3.2 Steel

The *Mat Piecewise Linear Plasticity model* (*Mat_24*) in LS-DYNA simulated stress-strain relationships for the steel reinforcements by accounting for the strain rate effects on the steel strength using the Cowper and Symonds model. For the current study, the Cowper-Symonds coefficients, which consider the yield stress, increase for reinforcing bars under impact and blast loading, were set as $C_s = 40$ and $p_s = 5$ [17, 19]. Steel material properties are listed in Table 2.1. The ultimate strain for the reinforcements at which the elements would be removed from the model was specified as 12% based on previous research [20]. To ensure effective

compatibility with the solid elements, a two-node, Hughes-Liu tubular beam element with cross-section integration quadrature point was used to model longitudinal and hoop reinforcement.

2.3.3 Soil

The soil volume was represented using the *Mat FHWA Soil* material (*MAT_147* in LS-DYNA) developed by the FHWA for roadside safety applications [21]. This soil model can address the effects of strain rate, kinematic hardening, and strain softening behavior, as well as the confinement influence on soil behavior. The FHWA soil model is a second order model with a smooth hyperbolic yield surface based on a first order Mohr-Coulomb yield surface. Selected material parameters were taken from recommended values in the literature [22-24] and are tabulated in Table 2.2. The soil was modeled using a solid element that incorporated the MM-ALE formulations (ELFORM=11 in LS-DYNA).

Table 2.2 Soil material parameters

Parameter	Value
Density, ρ_s (kg/m ³)	1600
Specific gravity, SPG	2.65
Bulk modulus, K (MPa)	146
Shear modulus, G (MPa)	56
Friction angle, ϕ_{max} (Degrees)	35
Cohesion, COH (MPa)	5×10^{-3}

2.3.4 Explosive and air

The air blast was simulated using LS-DYNA's *Mat High Explosive Burn* and the Jones-Wilkins-Lee (JWL) equation of state (EOS) [11]. The JWL EOS defines denotation pressure as a function of relative volume of the denotation product and an initial explosive internal energy. Table 2.3 lists material and EOS parameters for the explosive, which was

represented as TNT, in which p_{eos} is the pressure of the denotation product; V is the relative specific volume of the denotation product; A , B , R_1 , R_2 , and ω are specified constants unique to the type of explosive utilized; and $E_{0,e}$ is the denotation energy per unit volume of explosive.

A sphere-shaped explosive was selected and contained in the air mesh by defining an initial fraction of the air occupied using the *Initial Volume Fraction Geometry* command [11]. Air was the background mesh with the explosive overlaid onto that mesh using required geometric parameters that included its shape, volume, and position.

Table 2.3 TNT explosive material and EOS parameters

Parameter	Value
Mass density, ρ_{TNT} (kg/mm ³)	1.63×10^{-6}
Denotation velocity, v_D (m/s)	6930
Chapman-Jouget pressure, p_{CJ} (GPa)	21
A (GPa)	371.2
B (GPa)	3.23
R_1	4.15
R_2	0.95
ω	0.3
$E_{0,e}$ (GPa)	7.0

Air was modeled as an ideal gas using the null material model (*MAT_NULL*) with a polynomial EOS [11]. The air EOS represents a relationship between the internal energy and the pressure (p_{air}). Table 2.4 lists material and EOS parameters for the air volume [13, 23], where C_0 , C_1 , C_2 , C_3 , C_4 , C_5 , and C_6 are the constants for the polynomial equation coefficients, $E_{0,\text{air}}$ is the internal energy per unit reference volume of air, and ρ_{air} is the reference (nominal) density. The air was modeled using the solid element with the MM-ALE formulation (ELFORM=11). The standard viscous hourglass control with a reduced hourglass coefficient of 1×10^{-6} was selected for the air.

Table 2.4 Air material and EOS parameters

Parameter	Value
ρ_{air} (kg/mm ³)	1.293×10^{-9}
C_0	0
C_1	0
C_2	0
C_3	0
C_4	0.4
C_5	0.4
C_6	0
$E_{0,air}$ (MPa)	0.25

2.4 Model coupling and boundary conditions

For the RC components, a constraint-based coupling was used to couple interaction between steel reinforcement and surrounding concrete using the *Constrained Lagrange In Solid* in LS-DYNA [11, 17]. The contact between bridge column and vehicle was modeled by a segment-based contact using *Contact Automatic Surface to Surface*. A static and dynamic coefficient of friction of 0.3 was utilized for vehicle and bridge column contact [3, 25, 26].

The air and the soil were modeled using the ALE mesh, while the bridge components, including the column, spread footing, and piles, were simulated with the Lagrangian meshes. A penalty-based coupling algorithm was defined between the air domain and the column mesh using the *Constrained Lagrange In Solid* command. The contacts between the soil volume and the pile cap and piles were also simulated using the *Constrained Lagrange In Solid* command. A friction coefficient of 0.315 ($0.5\phi_{max}$) was defined between the spread footing and piles and their surrounding soil based on the static friction angle between the soil and concrete foundation system [23, 27].

To simulate infinitive volumes, a non-reflecting boundary condition (BNR) was implemented along the sides and top surface of the air domain as well as the sides and bottom

surface of the soil volume. The soil volume modeled volume that was modeled was 10000 mm deep, 10000 mm long and 10000 mm wide, as shown in Figure 2.3. This soil volume was shown to accurately represent the soil-structure interaction during impact and blast events, and avoid the effects of reflected waves at the soil sides [23, 27]. The soil volume was reasonably selected for efficient computation in this study. The bridge column was conservatively simulated as a propped-cantilever since the largest shear demand was produced at the base of the column as a result of this propped-cantilever assumption [13, 28, 29], with superstructure dead load constituting an initial uniaxial load on the column. The axial load was set to 6% of the nominal axial capacity of the bridge column. A representation of all components of the FE model is shown in Figure 2.3.

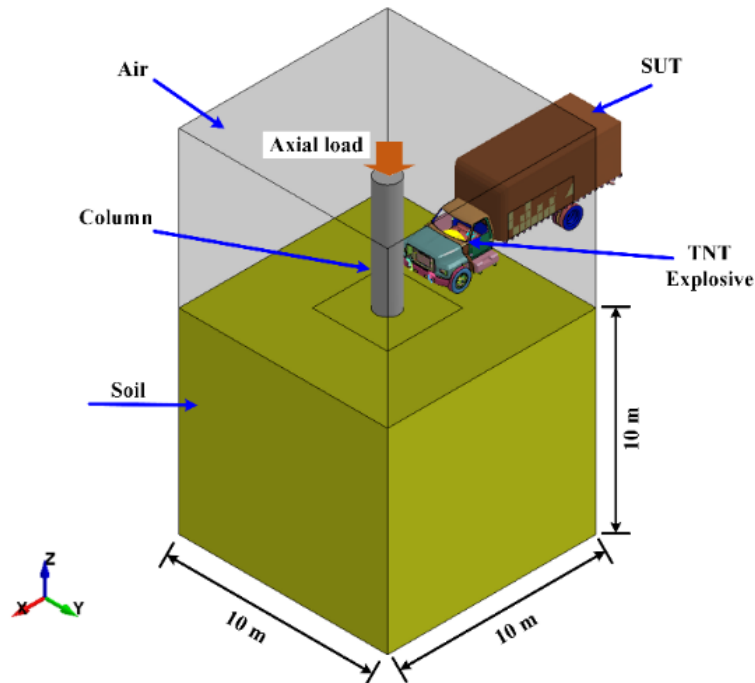


Figure 2.3 FE model of isolated RC column under vehicle collision and air blast

2.5 Validation studies

Accuracy of the FE modeling approach was examined by comparing numerical simulation results against published impact and blast tests. The authors could not locate an experimental study in the open literature examining the behavior of RC bridge columns subjected to combined impact and blast. As a result, two experimental programs reported in the literature were utilized to validate the modeling approach: one being from impact tests on RC beams [30] and the second being a reduced scale blast test of a RC column in a building frame [31]. The validation studies were completed and provided in the Phase I final report. Validation studies indicated select modeling approaches were successfully validated against test results and supported using modeling approaches to predict the response of RC members subjected to impact and blast loading.

2.6 Studied Pier Column

For the research study, a single column from a multi-column highway bridge pier, its supporting foundation, and a surrounding soil volume was modeled, as shown in Figure 2.4. The pier and column were obtained from a FHWA design example [32] where the bridge is designed in accordance with *AASHTO-LRFD Bridge Design Specification*. Figure 2.5 details a representative column finite element model. The column is a circular section having a height of 5400 mm (18 ft.) above the foundation and is supported by a pile cap that is 3600 mm (12 ft.) wide, 3600 mm (12 ft.) long, and 900 mm (3 ft.) thick. The cap is, in turn, supported by RC piles 450 mm by 450 mm (1.5 ft.) and 6000 mm (20 ft.) long.

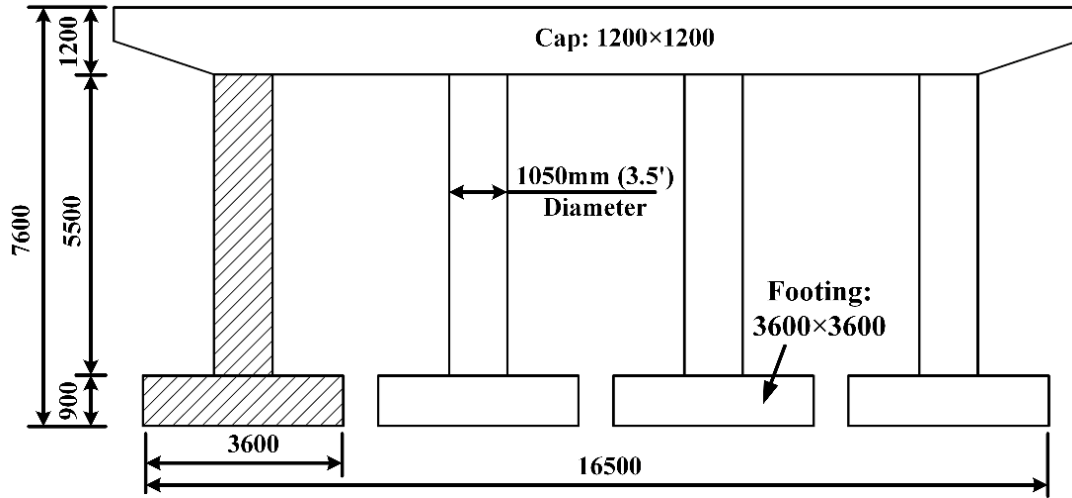


Figure 2.4 Prototype pier and column (unit: mm) [32]

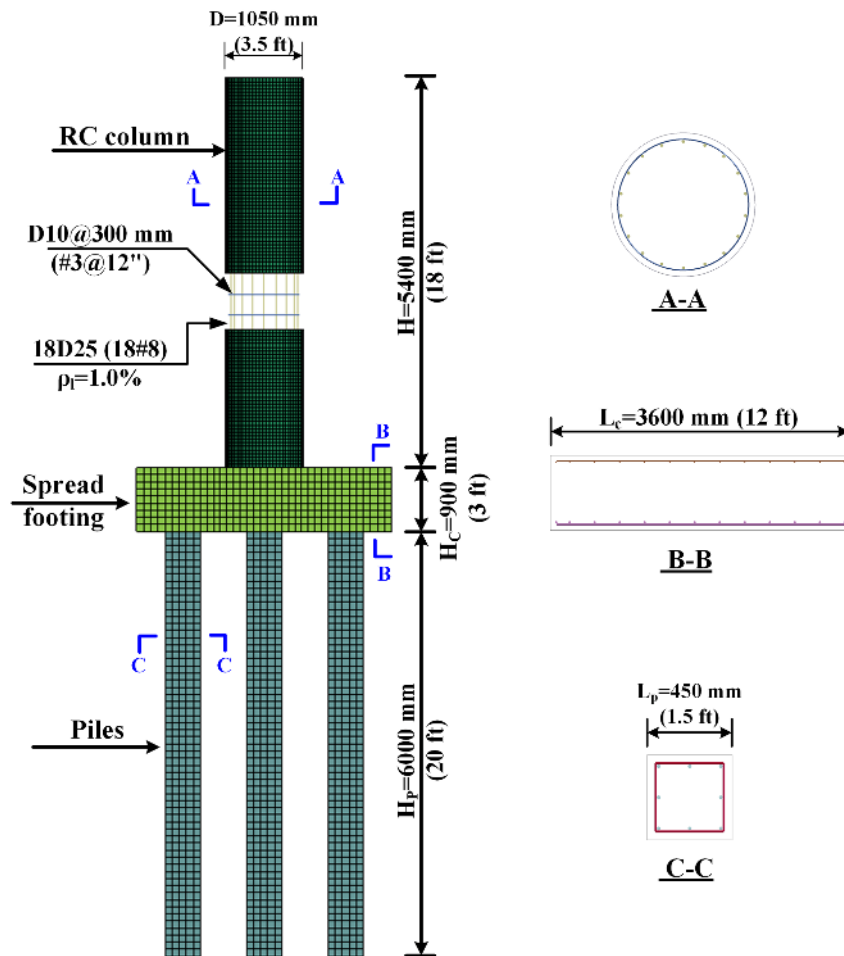


Figure 2.5 Finite element model of column and foundation.

Three column diameters, 750 mm (2.5 ft), 1050 mm (3.5 ft), and 1350 mm (4.5 ft), were selected based on the prototype bridge design and a state DOT design survey focused on current bridge column design standards. All columns were designed following AASHTO LRFD using a 1% longitudinal reinforcement ratio and shear reinforcement (hoops) spaced 300 mm (12 in.) apart. Figure 2.6 shows column cross-sections.

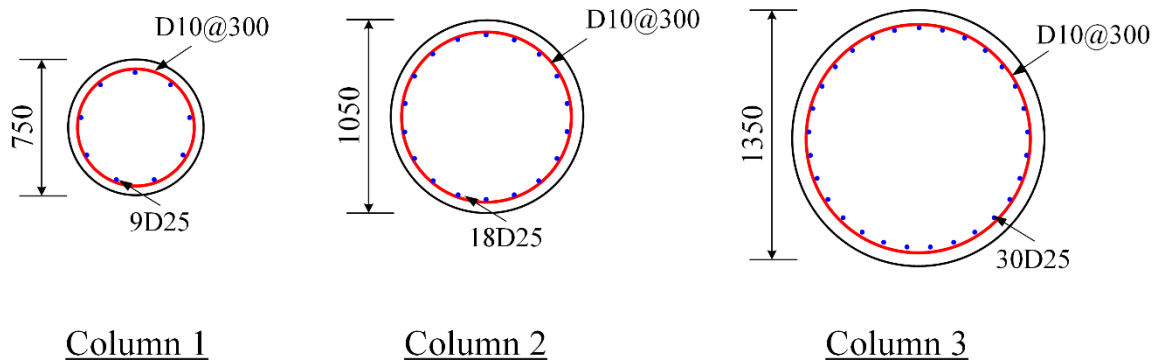


Figure 2.6 Column cross-sections (unit: mm).

2.7 Conclusions

This chapter reviewed the circular column prototype selected for the current study and provided information on physical and material models used to represent the column, its surrounding soil and air volumes and the impacting vehicle in LS-DYNA. A 3D finite element model of a single RC bridge column and its supporting footing and piles was created with the soil volume restraining its base and the air domain being used to apply load from an air blast. The impacting vehicle was a Ford F800 SUT available in LS-DYNA. The air blast was represented using LS-DYNA's MM-ALE approach. Details of numerical model development and validation were provided in the final report for Phase I [7].

Chapter 3 Numerical Simulation of an Isolated Column Subjected to Vehicle Collision and Air Blast

3.1 Introduction

Pier response to vehicle collision and air blast was first examined using numerical simulations of an SUT colliding into an isolated column coupled with an air blast. This initial study established a sequence for collision and air blast that produced maximum demand on the column. Parametric studies then investigated the performance and survivability of isolated bridge columns subjected to the critical sequence.

3.2 Load Sequence Study

The model shown in Figure 3.5 was used to identify the sequence of collision and blast loads that would most severely affect column performance. The study examined the following sequences: (i) collision followed by blast; (ii) simultaneous collision and blast; and (iii) blast followed by collision.

3.2.1 Load sequence

In all simulations, an axial load was first applied at the top of bridge column. Then, two additional events were imposed on the column. The initial load sequence was referred to as vehicle collision or collision first, blast second (I1-B2). Blast first, collision second included B1-I2 with simultaneous collision and blast termed I1-B1. Figure 3.1 details the three examined sequences.

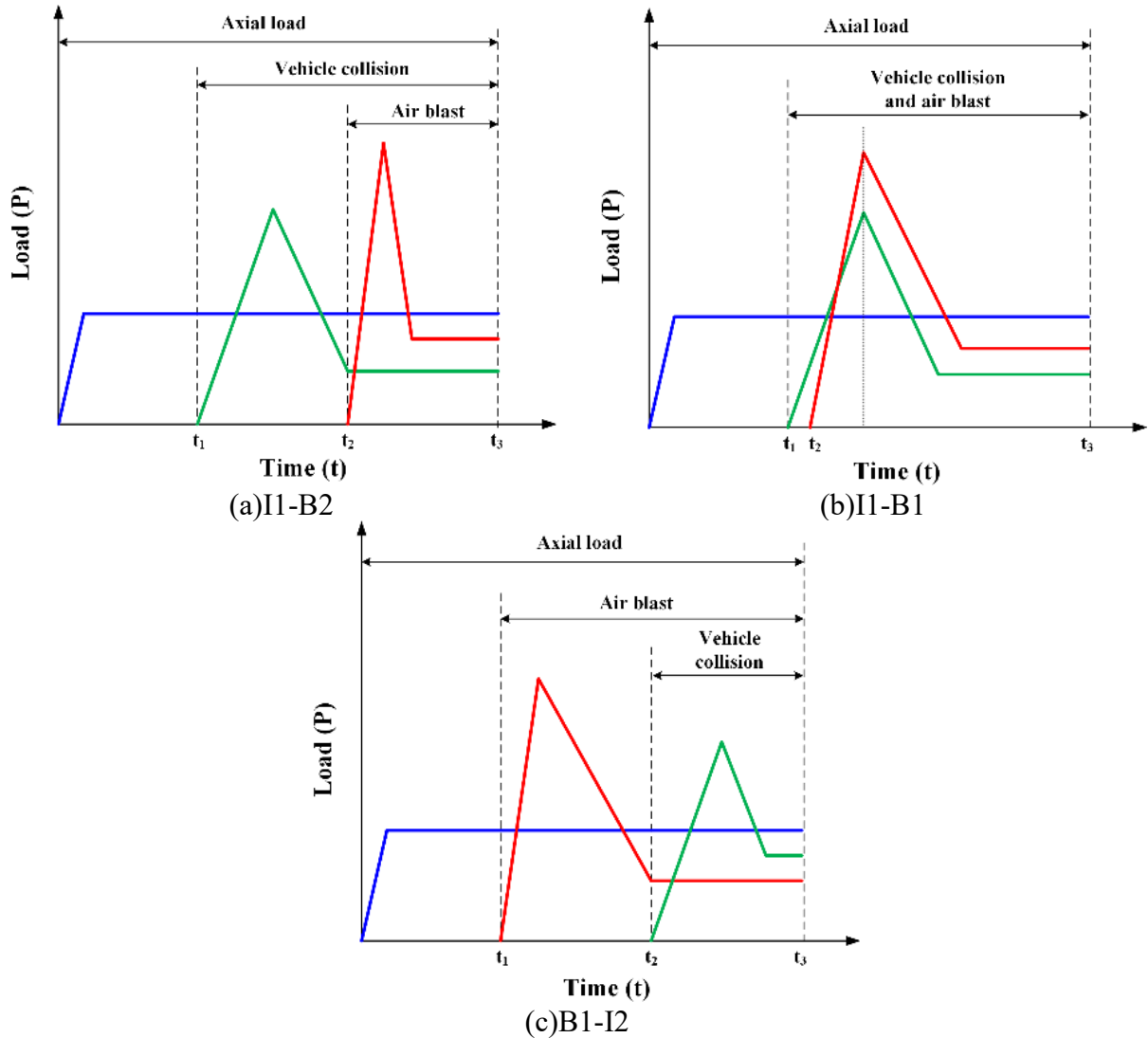


Figure 3.1 Studied load sequences.

3.2.2 Analytical procedure

Loads were applied sequentially using the following procedure:

Step I: Gravity load was applied to represent column self-weight and superimposed dead load. The load was addressed by including the gravitational constant with *Load Body Z* command and linearly increasing axial load at the column top over a 0.03 s period with *Load Node Set* command to accurately represent superstructure dead load.

Step II: The duration of subsequent events differed depending on modeled sequence. I1-B1 and B1-I2 event durations were selected so acceptable and conservative column response and degradation occurred prior to initiating Step III. The critical duration for Step II was determined using separate collision simulations at different velocities and air blast simulations at different scaled distances. Results from these studies indicated that, for I1-B2, collision event durations needed to be 0.06 s, 0.04 s, and 0.03 s at the collision velocities of 65 km/h, 95 km/h, and 120 km/h, respectively. For B1-I2, blast event duration was 0.02 s.

Step III: The second blast or collision event was included in the numerical simulation as transient response as the first event dissipated. The second event's duration terminated when column transient response dissipated.

3.2.3 Column response

Once appropriate durations were determined for each sequence, their effects on column response were examined for an extreme threat case at a vehicle collision velocity of 120 km/h and a scaled distance of $0.25 \text{ m/kg}^{1/3}$. Figure 3.2 depicts cumulative damage snapshots for a representative 750 mm and 1050 mm diameter columns subjected to examined load sequences, where the damage index is obtained from the effective plastic strain to represent concrete damage in the CSCM concrete model. As stated in Chapter 2, whether concrete damage in the form of cracking occurs is based on the damage parameter that ranges from 0 (blue) to 1 (red). As the parameter value approaches one the likelihood of cracking is higher. [15]. Concrete spalling is achieved by an erosion algorithm in the CSCM concrete model based on the concept that the highly strained elements of the deformed mesh have failed completely and may not contribute to the structural response. Steel reinforcement yields when the longitudinal stress

exceeds its yield strength. Steel reinforcement is fractured with the ultimate strain set to 12%. The 750 mm and 1050 mm diameter columns were selected because the representative damage for three load sequences was observed in the baseline column obtained from the FHWA design example. The collisions and explosions generated shock waves that softened the soil and affected performance of the column, and the footing its supporting pile.

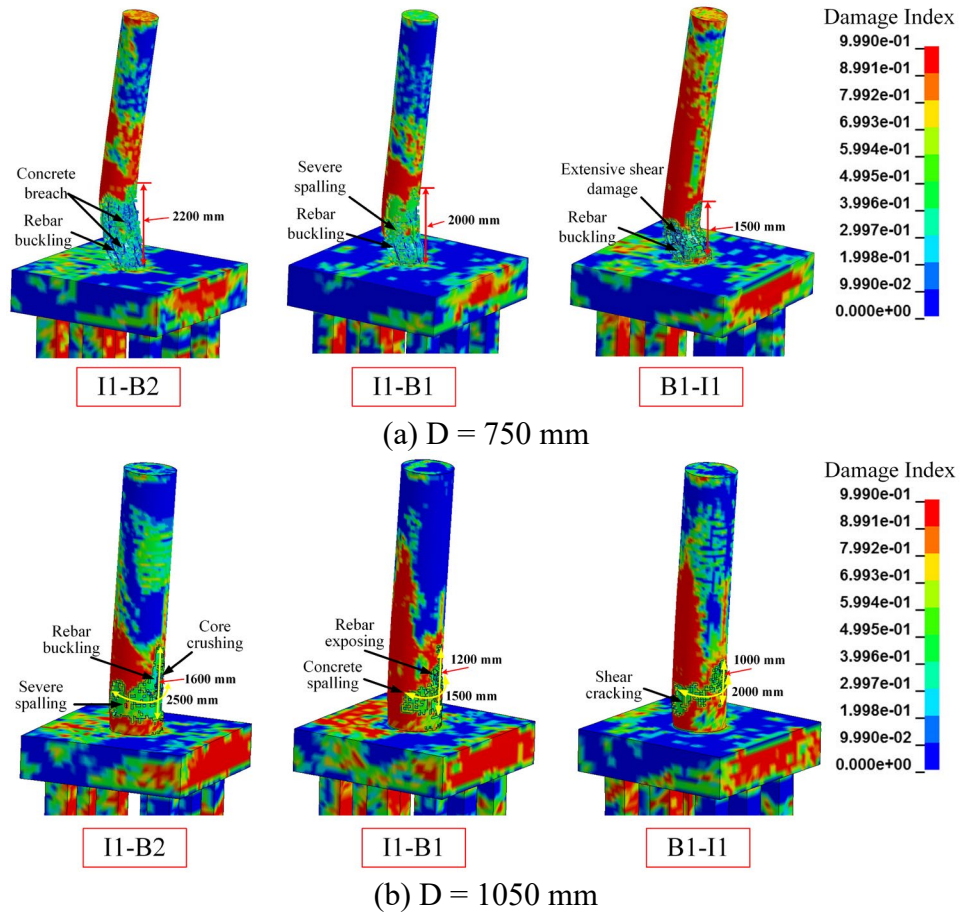
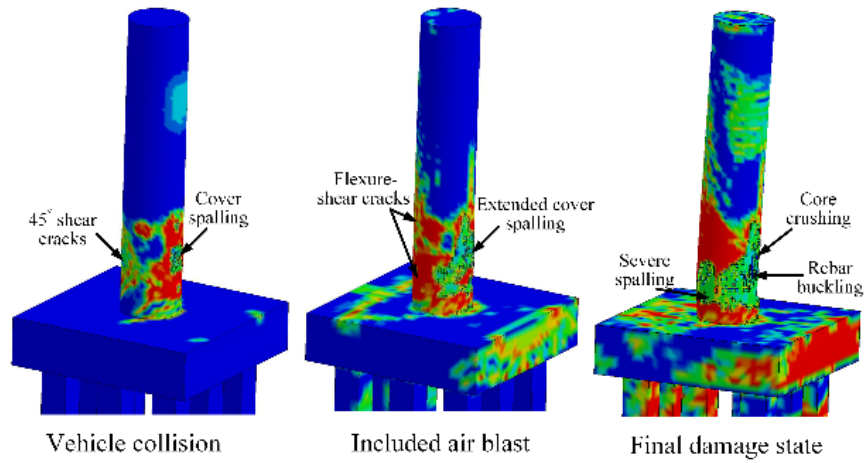


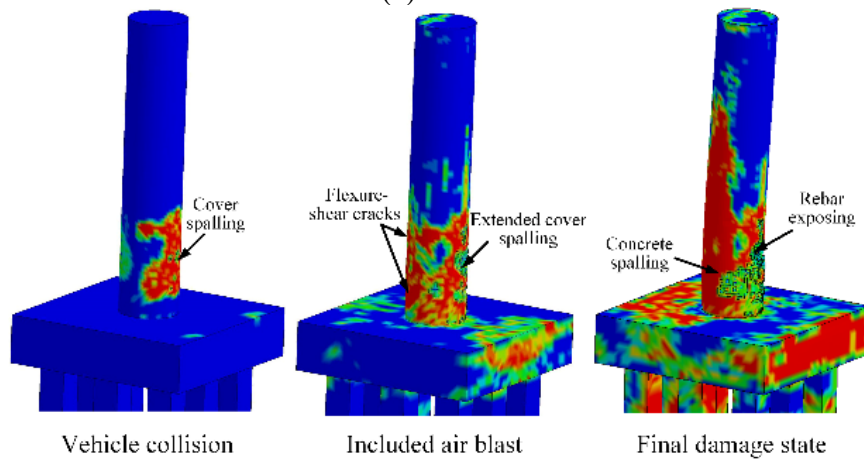
Figure 3.2 Column damage for three load sequences with $v_0 = 120$ km/h; $Z = 0.25$ m/kg^{1/3}

Numerical results showed that column damage varied under three load sequences. Each case produced significant damage in the collision region, with I1-B2 generating the most severe damage as determined using the volume of eroded concrete and deformation of reinforcements.

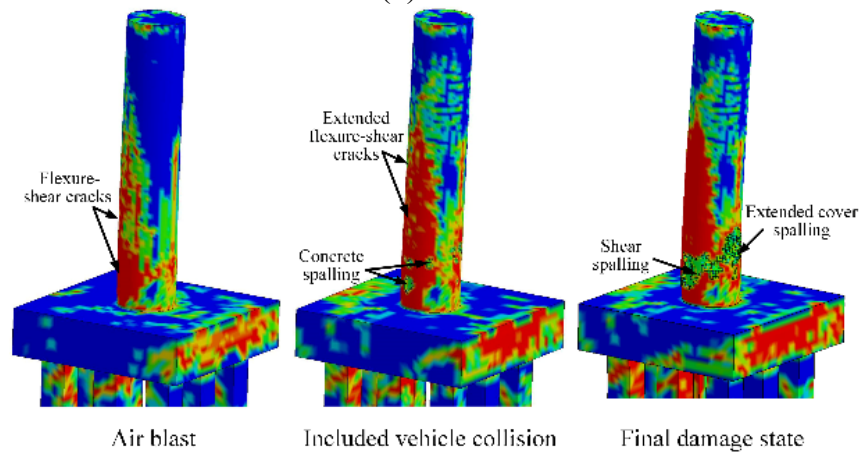
Both 750 mm and 1050 mm diameter columns experienced more amounts of spalled concrete and buckled longitudinal reinforcements in the collision region for the I1-B2 case and more core crushing on the impacted side compared to I1-B1 and B1-I2. As shown in Figure 3.3 (a), the vehicle collision (in which engine collision produced a maximum collision load) in a concentrated region resulted in localized damage at the collision location with concrete cover spalling. The subsequent air blast (applied to the column at $t = 0.06$ s) deteriorated the localized concrete cracking and generated the combined flexure-shear cracks in the collision region. Additionally, a concrete crushing crater was observed at the collision point due to the large compressive and tensile transient stresses from air blast. For the I1-B1 case, the column damage was dominated by the moderate concrete spalling and reinforcement exposing in the collision region. Compared to the I1-B2 case, less concrete spallation in the column was produced by vehicle collision before air blast was applied at $t = 0.05$ s, as shown in Figure 3.3 (b). For B1-I2, concrete cracking initiated at the rear face of the column and propagated to its core as shown in Figure 3.3 (c). The column experienced concrete cracking that encompassed shear cracks at the base and flexure cracks at mid-height before the vehicle impacted with the column. The column suffered significant concrete spalling and diagonal shear damage at the collision location. Figure 3.4 provides reinforcement damage. Each case produced significant damage in the vicinity of the collision zone, with I1-B2 generating the most severe damage as determined in terms of eroded concrete and deformation of reinforcement.



(a) I1-B2



(b) I1-B1



(c) B1-I2

Figure 3.3 Damage states of 1050 mm diameter column for three load sequences
($v_0 = 120 \text{ km/h}$; $Z = 0.25 \text{ m/kg}^{1/3}$)

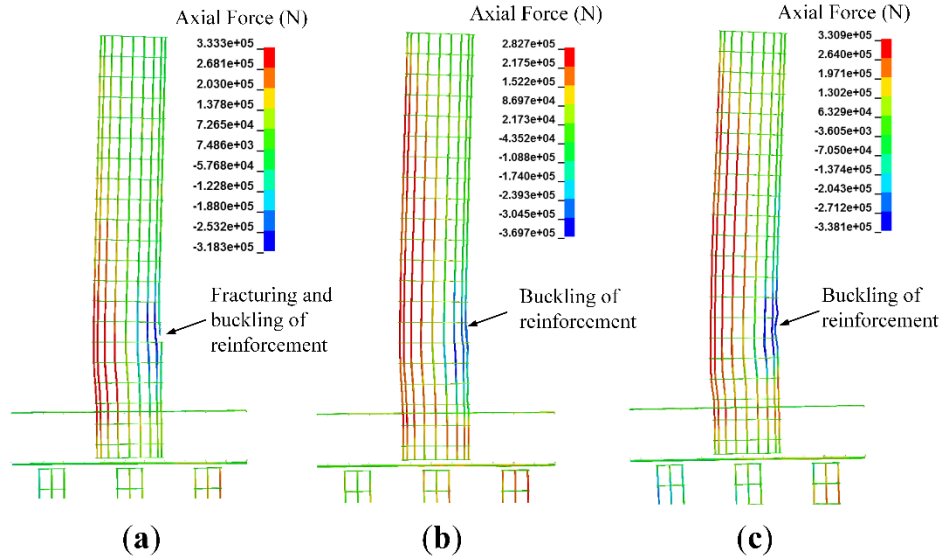


Figure 3.4 Reinforcement damage: (a) I1-B2; (b) I1-B1; (c) B1-I2.

In addition to qualitatively examining damage caused by each load sequence and measuring damage quantities, an additional evaluation helped determine the critical load sequence, as shown in Figure 3.4. At the completion of column transient response, residual axial capacities were determined by increasing axial load at the top of the column until it was unable to handle additional load. A ratio between residual axial capacity of the damaged column (i.e., additional axial load applied to achieve collapse – P_{res}) and the undamaged column's nominal axial capacity (P_n) was defined to facilitate comparison. The I1-B2 load sequence resulted in 23% of nominal capacity in the 1050 mm diameter column while I1-B1 and B1-I2 gave 33% and 36% of nominal capacity, respectively. For the 750 mm diameter column, I1-B2 also produced the lowest residual axial capacity (14% of P_n). The residual axial capacity of the damaged columns under I1-B2 was less than those for I1-B1 and B1-I2 cases. Given these results, the I1-B2 sequence was considered to be the most severe sequence and was used for all subsequent studies.

3.3 Response of Bridge Column to Vehicle Collision and Air Blast

To establish how each isolated column performed when subjected to demands from an I1-B2 load sequence, its entire response time-history was examined incrementally so the order, combination, and duration of damage and failure mechanisms could be explicitly identified. Representative results for studied column diameters subject to I1-B2 are provided below.

Figure 3.5 through Figure 3.7 show loading increments and corresponding column and reinforcement damage propagation for the 750 mm, 1050 mm, and 1350 mm diameter columns in response to I1-B2 with $v_0 = 120$ km/h and $Z = 0.25$ m/kg^{1/3}. As a reminder, damage indices are determined by LS-DYNA using effective plastic strain representing concrete damage in the CSCM concrete material model [15, 17]. As shown in the figures, column response to combined collision-blast load was analyzed at set points in time. Damage levels and propagation were quantified using the column rotation at the collision region and the ratio of buckled longitudinal reinforcement (γ_{br}) to total longitudinal reinforcement. Figure 3.8 illustrates lateral displacement development along the column height on the non-collision side face for these bridge columns at set load increments, which helps to show column deformation and damage development during a I1-B2 case. As shown in Figure 3.8, maximum column displacements were observed approximately 1000 mm above the footing in the vicinity of vehicle collision. It should be noted that displacements were produced at the column base due to interaction between the footing, piles, and surrounding soil volume.

(a) *Initial collision at $t = 0.03$ s.*

(i) For all column diameters, concrete cracking initiated at the collision point.

(b) *Truck frame collision at $t = 0.04$ s.*

- (i) For all column diameters, cracking propagated from the collision location through the column.
 - (ii) For all column diameters, a 45° shear crack formed and radiated from the collision location.
- (c) *Engine collision at $t = 0.05$ s.*
- (i) For all column diameters, maximum collision load occurred.
 - (ii) For all column diameters, concrete began spalling at the collision point.
 - (iii) For all column diameters, cracks started developing on the non-collision face and at column base.
 - (iv) For the 750 mm diameter column, engine collision produced a column rotation angle of approximately 3.1° (0.06 rad) at its bottom portion 1000 mm above the footing and 11% of longitudinal reinforcement buckled. For the 1050 mm and 1350 mm diameter columns, column deformation was small with no buckled reinforcements.
- (d) *Blast detonation at $t = 0.06$ s.*
- (i) For the 750 mm diameter column, a plastic hinge began developing at its base. Flexural cracking was evident at mid-height. A rotation angle of approximately 11.6° (0.2 rad) at the collision region and 56% of longitudinal reinforcement buckled were produced.
 - (ii) For the 1050 mm and 1350 mm diameter columns, shear cracks propagated to their bases and flexural cracking occurred at mid-height. Reinforcements also yielded at their bases. For the 1050 mm diameter column, a rotation angle of approximately 1° (0.017 rad) at its bottom

portion 1000 mm above the footing was formed. For the 1350 mm diameter column, a small rotation of approximately 0.55° (0.001 rad) at the collision location was produced.

(e) Blast engulfment at $t = 0.07$ s.

- (i) For the 750 mm diameter column, shear failure initiated at its base due to hoop fracture, excessive concrete spalling, and longitudinal reinforcement buckling. The combined collision-blast load resulted in a rotation angle of approximately 26.3° (0.46 rad) at its base and 89% of longitudinal reinforcement buckled.
- (ii) For the 1050 mm diameter column, concrete spalling propagated from the collision location and longitudinal reinforcement buckled along the collision face. A rotation angle of 5° (0.087 rad) was produced with 6% of longitudinal reinforcement buckling.
- (iii) For the 1350 mm diameter column, diagonal shear cracking propagated towards the base and flexural cracking occurred at mid-height. Concrete spalling occurred at the collision point. The combined collision-blast load produced a rotation angle of 2.4° (0.0424 rad) at its base and 6% of longitudinal reinforcements buckled in the collision region.
- (iv) For all column diameters, concrete began cracking at the footing and in the support piles due to blast wave effects.

(f) Blast wave propagation at $t = 0.08$ s.

- (i) For the 750 mm diameter column, a combination of three fractured hoops and the loss of approximately 50% of the concrete core in the collision

region resulted in a permanent displacement of 359 mm at 1000 mm above the ground and column failure. This column sustained a rotation angle of 36.9° (0.65 rad) and 89% of longitudinal reinforcements buckled in the collision region.

(ii) For the 1050 mm diameter column, concrete cover spalling propagated to the non-collision face. In the vicinity of the collision location, the concrete core began spalling, 17% of the longitudinal bars buckled, and a plastic hinge formed. The column experienced a permanent displacement of 105.5 mm at 1000 mm above the base with a rotation angle of 5.5° (0.095 rad) produced.

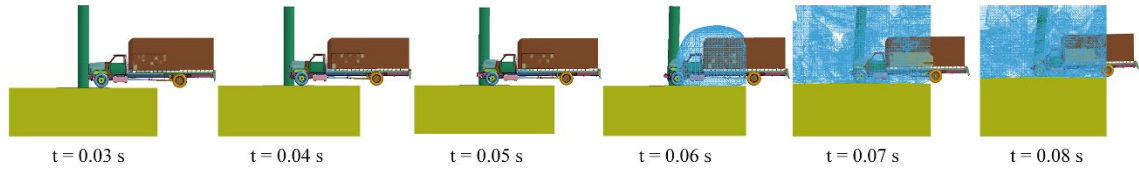
(iii) For the 1350 mm diameter column, widespread cracking and some spalling was observed at the collision location with 10% of the longitudinal bars buckled. The column sustained a maximum displacement of 65.5 mm with a rotation angle of 1.7° (0.028 rad) formed. Concrete cover spalling was also noted in the footing due to shear and bending moment transferred from the column.

(iv) For all column diameters, concrete cracking was observed throughout the height of the support piles.

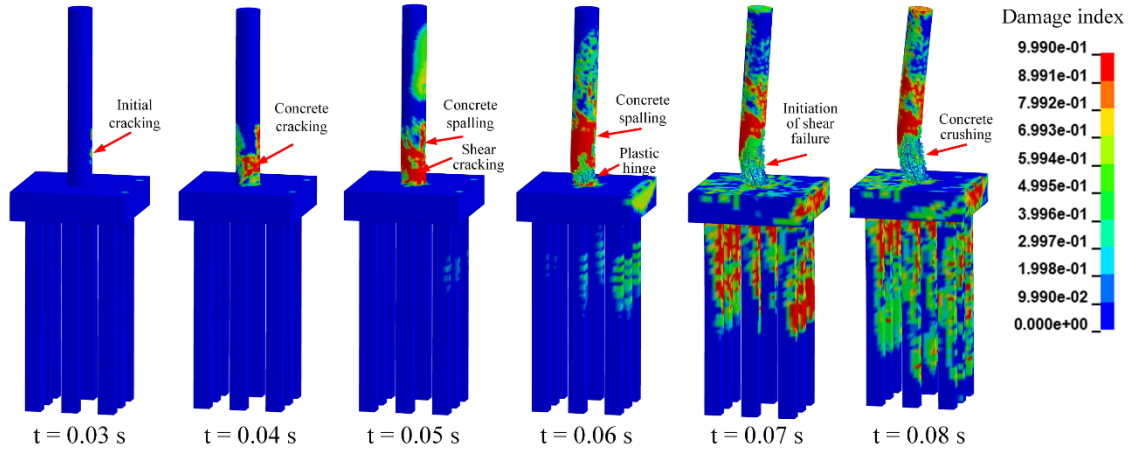
To summarize, numerical results (see Table 3.1) indicated that:

(a) The combined collision-blast load resulted in shear failure at the base of 750 mm diameter column due to extensive buckling of reinforcing bars and loss of approximately 50% of the core concrete.

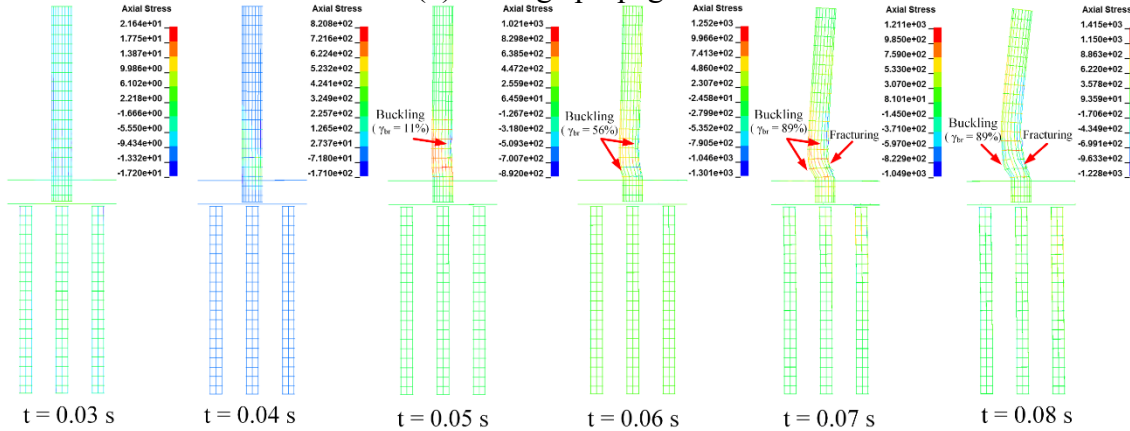
- (b) The 1050 mm diameter column formed a plastic hinge in the collision region with extensive concrete spalling.
- (c) The 1350 mm diameter column sustained distributed cracking and concrete spalling at the collision location, potentially reparable damage.



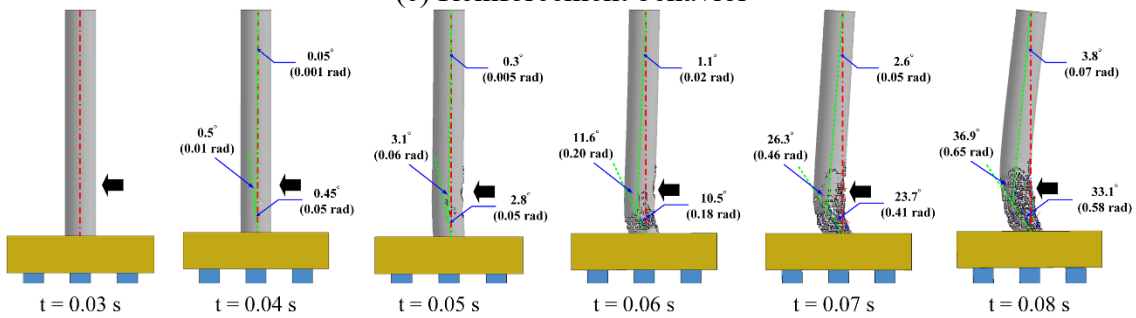
(a) Times of interest



(b) Damage propagation

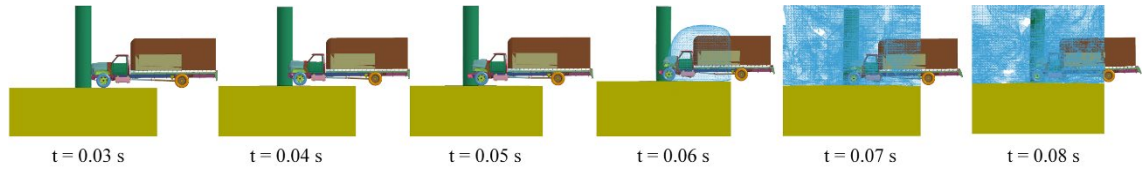


(c) Reinforcement behavior

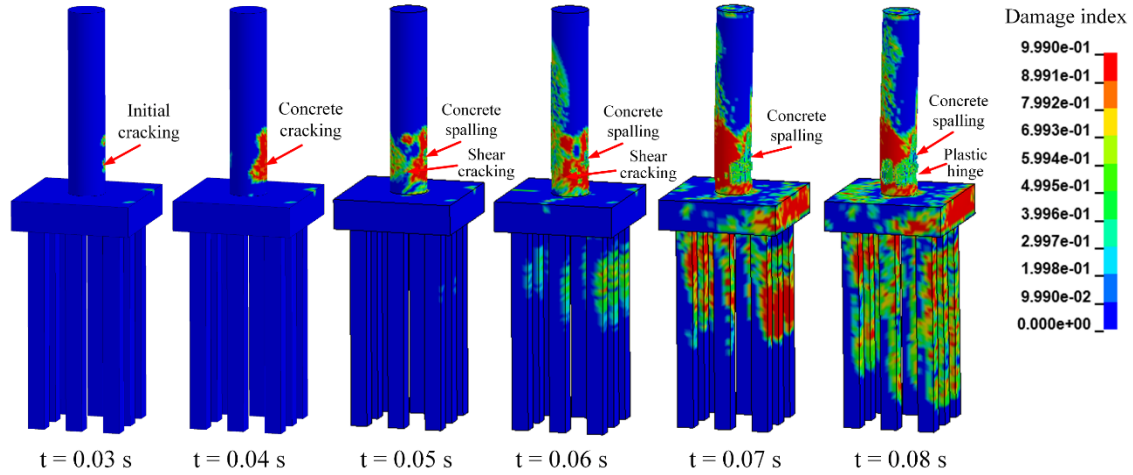


(d) Column deformation

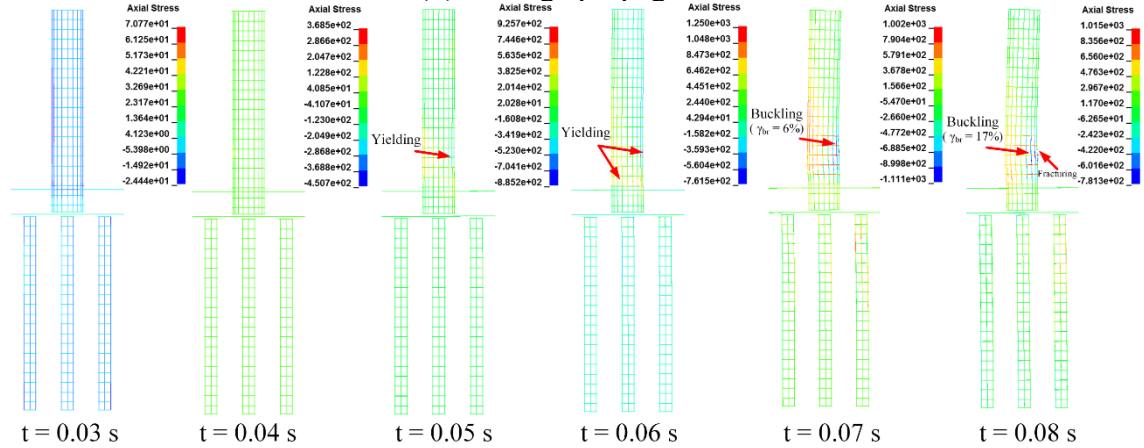
Figure 3.5 750 mm diameter column: (a) times of interest; (b) damage propagation; (c) reinforcement behavior; (d) column deformation ($v_0 = 120$ km/h, $Z = 0.25$ m/kg^{1/3})



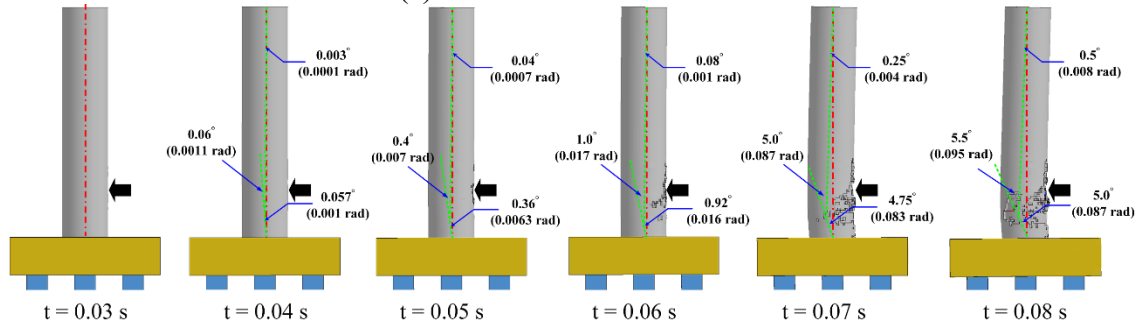
(a) Times of interest



(b) Damage propagation

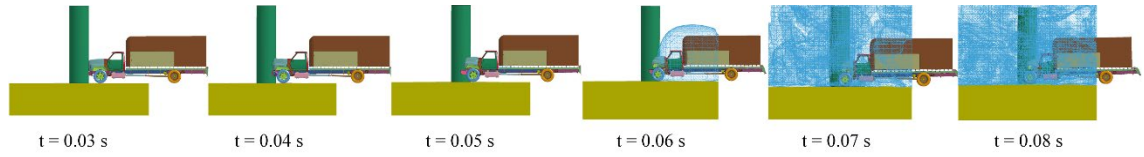


(c) Reinforcement behavior

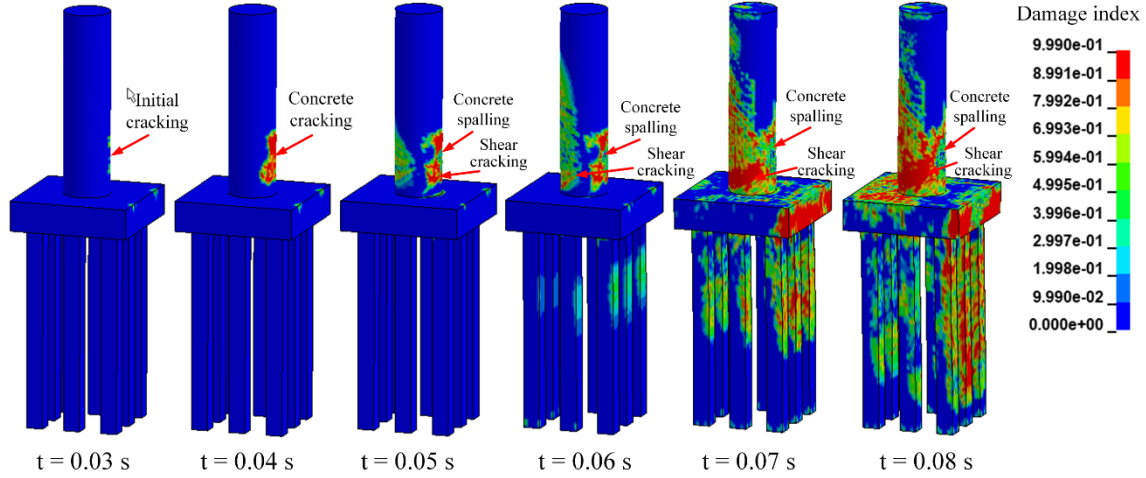


(d) Column deformation

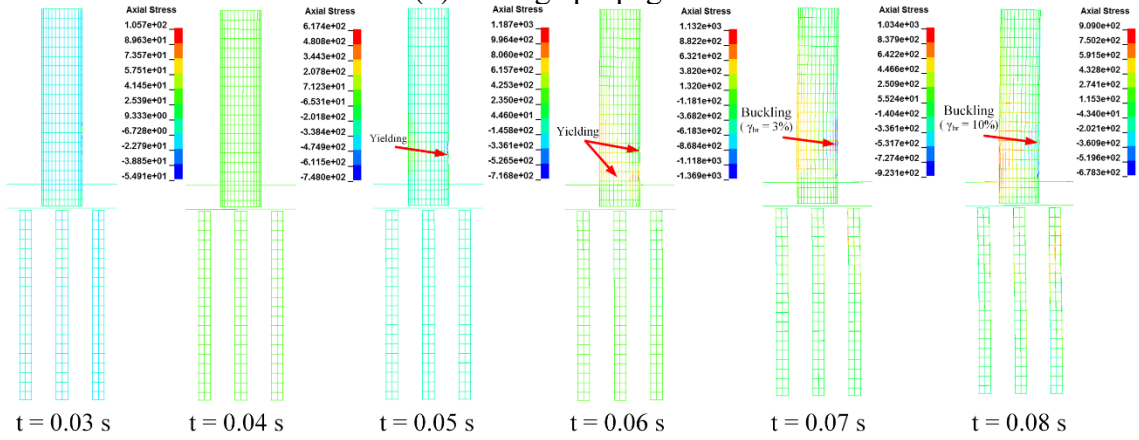
Figure 3.6 1050 mm diameter column: (a) times of interest; (b) damage propagation; (c) reinforcement behavior; (d) column deformation ($v_0 = 120 \text{ km/h}$, $Z = 0.25 \text{ m/kg}^{1/3}$)



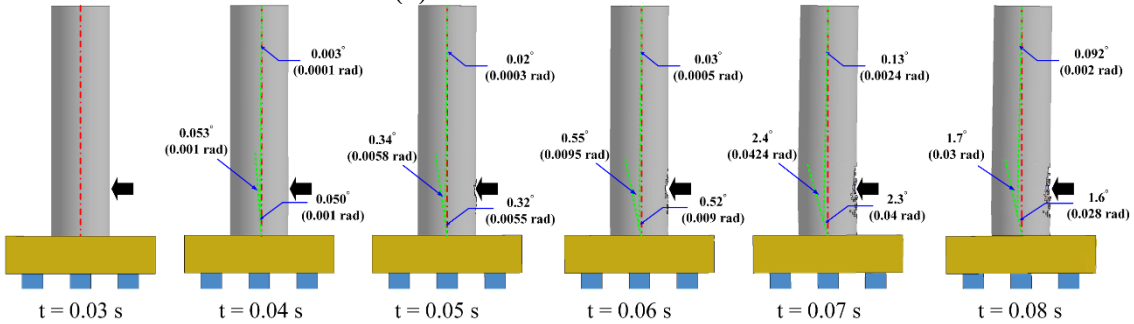
(a) Times of interest



(b) Damage propagation

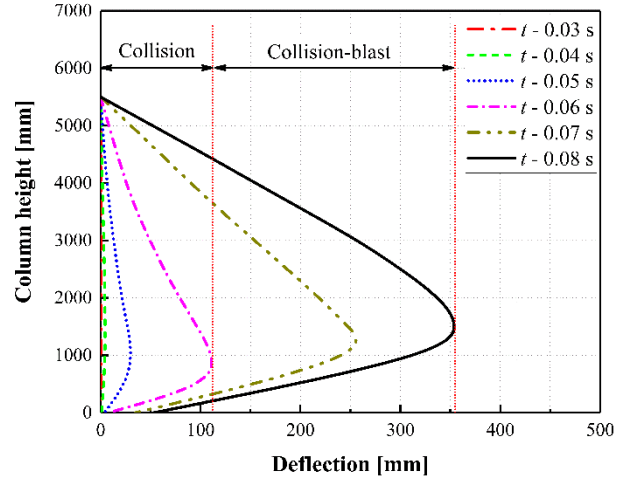


(c) Reinforcement behavior

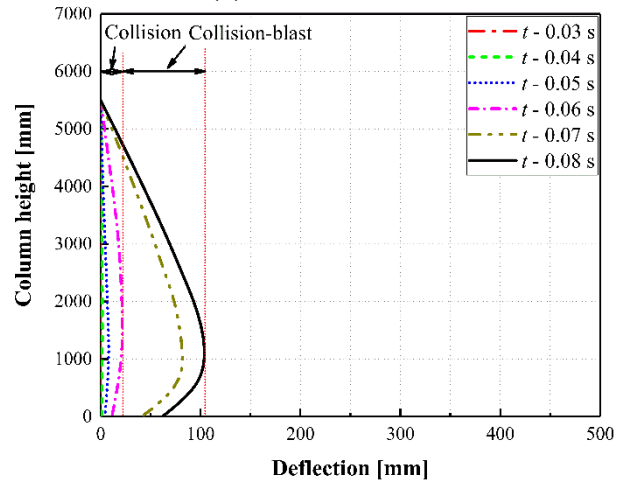


(d) Column deformation

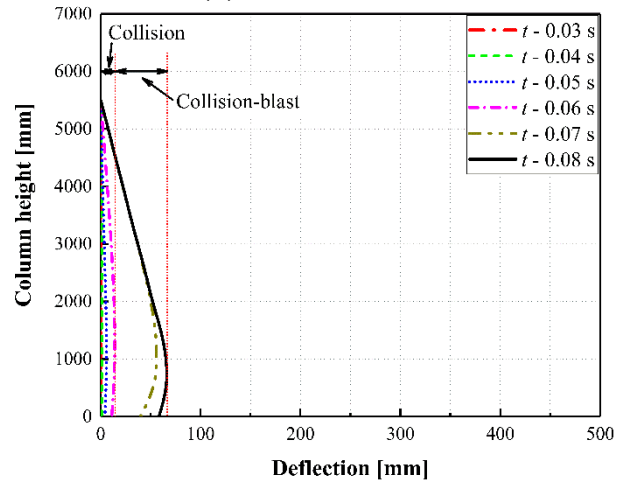
Figure 3.7 1350 mm diameter column: (a) times of interest; (b) damage propagation; (c) reinforcement behavior; (d) column deformation ($v_0 = 120 \text{ km/h}$, $Z = 0.25 \text{ m/kg}^{1/3}$)



(a) $D = 750$ mm



(b) $D = 1050$ mm



(c) $D = 1350$ mm

Figure 3.8 Lateral displacement time-history
($v_0=120$ km/h, $Z = 0.25$ m/kg^{1/3})

Table 3.1 Response of 750 mm, 1050 mm, and 1350 mm diameter columns, I1-B2.

Time step		t – 0.03s	t – 0.04s	t – 0.05s	t – 0.06s	t – 0.07s	t – 0.08s
Loading increments		Initial collision	Truck frame collision	Engine collision	Blast detonated	Blast wave engulfment	Blast wave propagation
D (mm)	Response						
750	Damage	Column - initial cracking	Column – cracking propagated with a 45° shear crack formed	Column – concrete spalling and shear cracking	Column – plastic hinge formed at the base Pile – initial cracking	Column – initiation of shear failure Footing – cracking Piles – cracking developed	Column – failed with concrete breach; Footing – cracking; Piles – cracking along the pile height
	Steel bars	Normal	Normal	Buckling ($\gamma_{br} = 11\%$)	Buckling ($\gamma_{br} = 56\%$)	Buckling ($\gamma_{br} = 89\%$)	Fracturing and buckling
	Displacement (mm)	0	4.5	30	104	263	359
1050	Damage	Column –initial cracking	Column – concrete cracking	Column – concrete spalling and shear cracking	Column – concrete spalling and shear cracking Pile – initial cracking	Column – plastic hinge formed at the base Footing – cracking Piles - cracking developed	Column – plastic hinge formed at the base; Footing – cracking; Piles – propagated cracking
	Steel bars	Normal	Normal	Yielding	Yielding at base	Buckling ($\gamma_{br} = 6\%$)	Fracturing and buckling ($\gamma_{br} = 17\%$)
	Displacement (mm)	0	1.5	8	21	85.5	106

Time step		t – 0.03s	t – 0.04s	t – 0.05s	t – 0.06s	t – 0.07s	t – 0.08s
Time step		t – 0.03s	t – 0.04s	t – 0.05s	t – 0.06s	t – 0.07s	t – 0.08s
1350	Damage	Column - initial cracking	Column – concrete cracking	Column – concrete spalling and shear cracking	Column – concrete spalling and shear cracking at base; Pile – initial cracking	Column – concrete spalling at collision and shear cracking at base; Footing – cracking Piles – cracking developed	Column – concrete spalling and combined flexure and shear cracking; Footing – concrete spalling; Piles – propagated cracking
	Steel bars	Normal	Normal	Yielding	Yielding at base	Buckling ($\gamma_{br} = 3\%$)	Buckling ($\gamma_{br} = 10\%$)
	Displacement (mm)	0	1.5	5	14.5	56.5	65.5

3.4 Bridge column damage

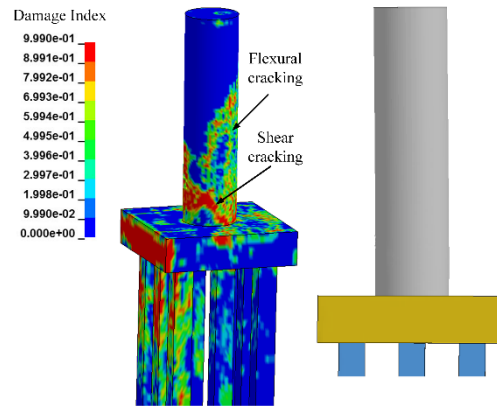
Published works of experimental and numerical studies have examined bridge column damage subjected to either vehicle collision or air blast. Do et al. [33] conducted a numerical study that reproduced bridge column damage from simulated vehicle collisions and classified the damage as follows, (i) minor local damage; (ii) flexural cracks; (iii) shear cracks at the column top, (iv) shear cracks at the column ends; and (v) punching shear failure at column base. Liu et al. [34] identified bridge column failure modes under vehicle collisions using LS-DYNA, which included: (i) concrete surface spalling; (ii) breakage of pier; (iii) rebar severance; and (iv) plastic hinge formation. Sharma et al. [18] evaluated RC bridge column performance under vehicle collision using LS-DYNA and classified column damage as: (i) minor spalling of concrete; (ii) significant cracking of concrete with buckling of bars; and (iii) loss of column capacity with fractured longitudinal bars. Williamson et al. [28, 29, 35] completed a series of blast tests on the bridge columns and identified four types of blast-related damage, including: (i) surface cracking; (ii) spalling of concrete cover; (iii) direct shear failure at the column base; and (iv) breaching of the column. Yi et al. [36, 37] used LS-DYNA to investigate the performance of a three-span, RC highway bridge subjected to blast load and identified six types of column damage: (i) eroding of concrete and pier base; (ii) shearing of a pier; (iii) rebar severance; (iv) breakage of pier; (v) spalling of concrete surface; and (vi) plastic hinge formation. Research results showed local damage to bridge components could lead to complete collapse.

Bridge columns in the current study experienced different levels of damage as a function of structural properties, support and load conditions, and energy induced by a combined collision and blast event. So that identified damage would effectively represent column performance under the combined collision-blast loads, it was of interest to classify column damage and

associate them with performance levels linked to design objective. A number of simulations were completed to develop damage classifications. Simulations analyzed the behavior of three columns from Figure 2.6 subjected to various combinations of collision and blast and used information supplied from the previously cited studies to develop the classifications criteria. In general, simulations indicated that column diameter, collision velocity and scaled distance were primary parameters influencing column response. Classifications are discussed in the sections as followed.

3.4.1 Concrete surface cracking (M1)

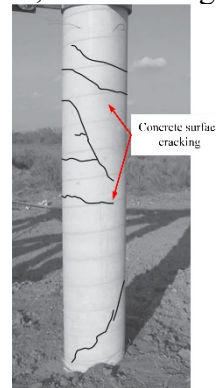
Concrete surface cracking (M1) encompasses combined, superficial flexural and shear cracking. Flexural cracking largely occurred at mid-height, and diagonal shear cracking was produced near the point of vehicle collision, as shown in Figure 3.9.



(a) Simulated damage ($D = 1350 \text{ mm}$; $v_0 = 65 \text{ km/h}$; $Z = 0.3 \text{ m/kg}^{1/3}$)



(b) Truck accident, Navarro, Texas [5]



(c) Blast test [29]

Figure 3.9 Concrete surface cracking

3.4.2 Concrete cover spalling (M2)

M2 addresses concrete cover spalling in the collision region, as shown in Figure 3.10.

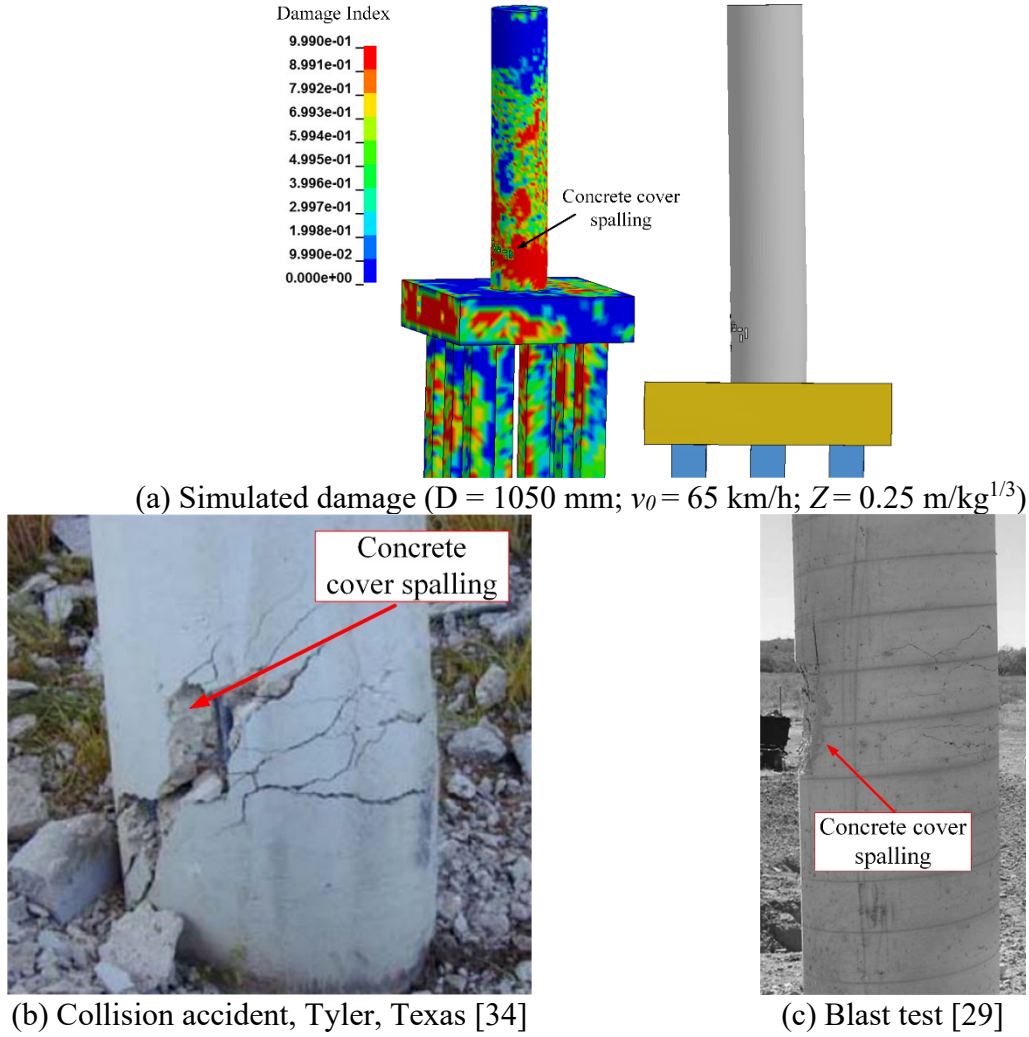
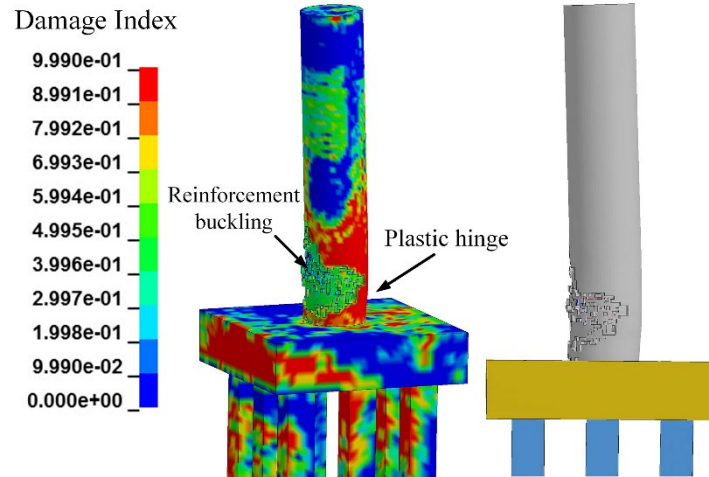


Figure 3.10 Concrete cover spalling

3.4.3 Formation of plastic hinge (M3)

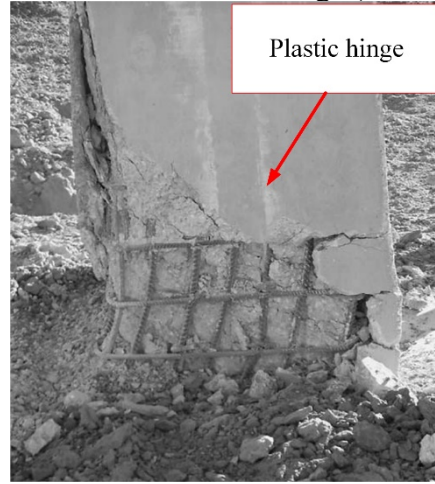
M3 represents plastic hinge formations in the vicinity of the collision with concrete core cracking and reinforcement buckling, as shown in Figure 3.11.



(a) Simulated damage ($D = 1050 \text{ mm}$; $v_0 = 120 \text{ km/h}$; $Z = 0.25 \text{ m/kg}^{1/3}$)



(b) Collision accident, Minnesota [25]

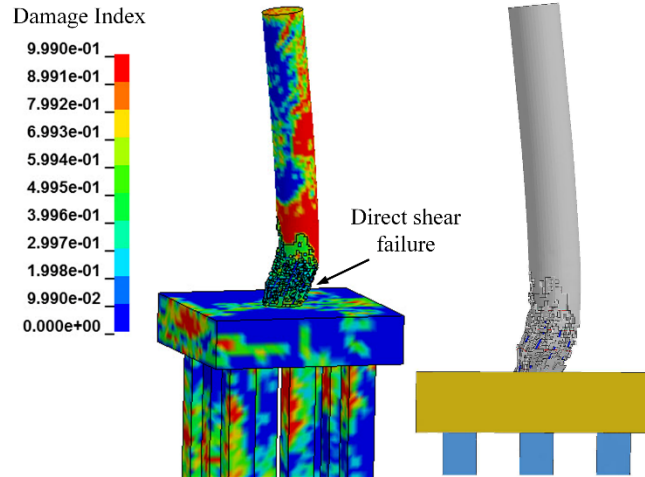


(c) Blast test [29]

Figure 3.11 Formation of plastic hinge

3.4.4 Direct shear failure (M4)

M4 represents shear failure at the column base as shown in Figure 3.12. The shear failure was caused by significant spalling and loss of concrete cover during the vehicle collision, fracturing of discrete hoops, anchorage failure, buckled longitudinal reinforcement, and subsequent loss of core concrete. These effects significantly reduced column integrity.



(a) Simulated damage ($D = 750 \text{ mm}$; $v_0 = 95 \text{ km/h}$; $Z = 0.20 \text{ m/kg}^{1/3}$)



(b) Collision accident, Texas [5]

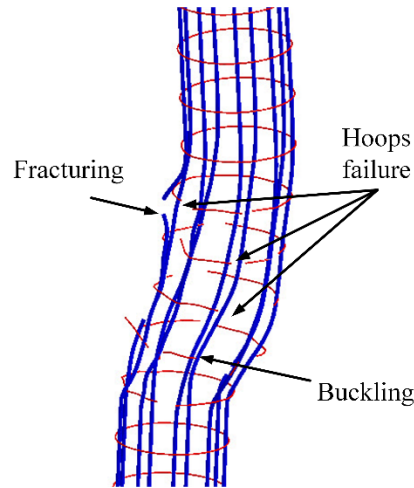


(c) Blast test [38]

Figure 3.12 Shear failure

3.4.5 Reinforcement failure (M5)

M5 encompasses shear reinforcement fracturing and longitudinal reinforcement buckling near the collision point, as shown in Figure 3.13. This failure occurred after concrete cover spalled.



(a) Simulated damage ($D = 750 \text{ mm}$; $v_0 = 120 \text{ km/h}$; $Z = 0.25 \text{ m/kg}^{1/3}$)



Reinforcement failure

(b) Collision accident, Texas [5]



Reinforcement failure

(c) Blast test [29]

Figure 3.13 Reinforcement failure

3.4.6 Concrete breach (M6)

M6 addresses column failure tied to breaching in the collision region as shown in Figure 3.14. The column experienced loss of approximately 50% of concrete core in the vicinity of the collision, with severed shear reinforcements and buckled longitudinal reinforcement. Column failure was imminent.

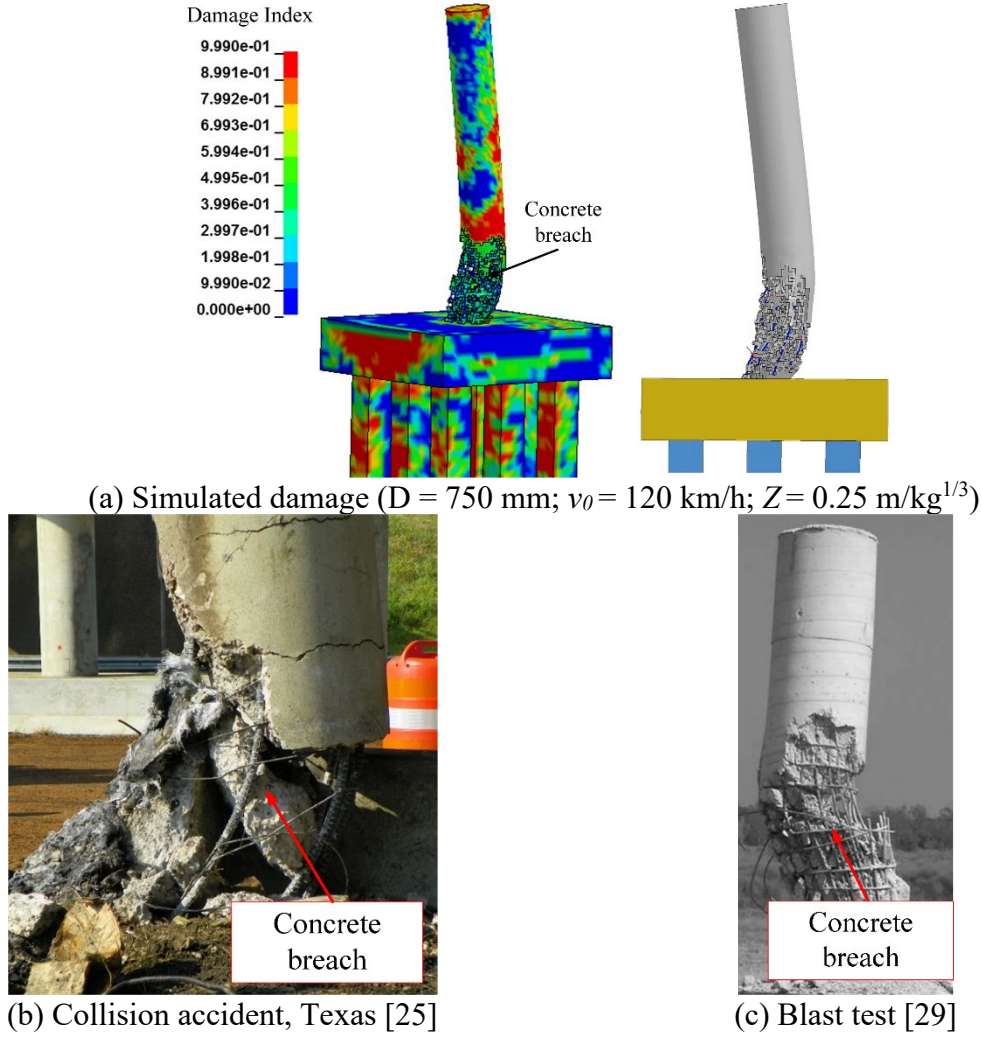


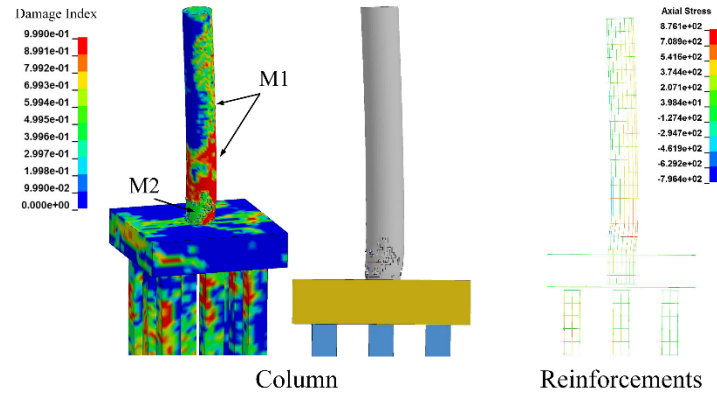
Figure 3.14 Concrete breach

Three columns with 750 mm, 1050 mm, and 1350 mm diameters were subjected to combinations of vehicle collision at three selected collision velocities and air blast at three selected scaled distances. Utilizing the defined categorizations, representative final damage states for the three modeled column diameters due to various collision and blast demands are presented in Figure 3.15 through Figure 3.17.

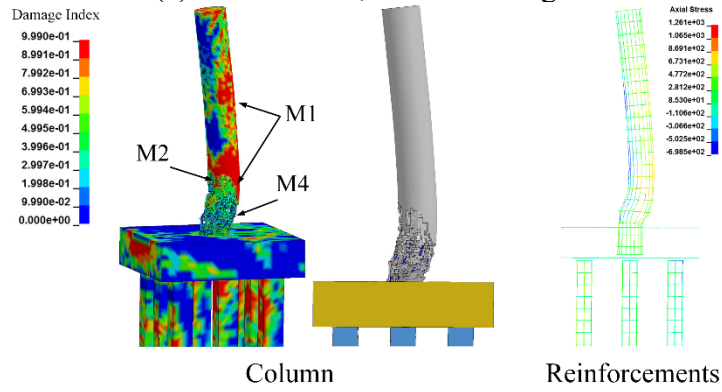
Numerical results indicated that:

- i. For $v_0 = 65$ km/h, $Z = 0.30$ m/kg^{1/3} –

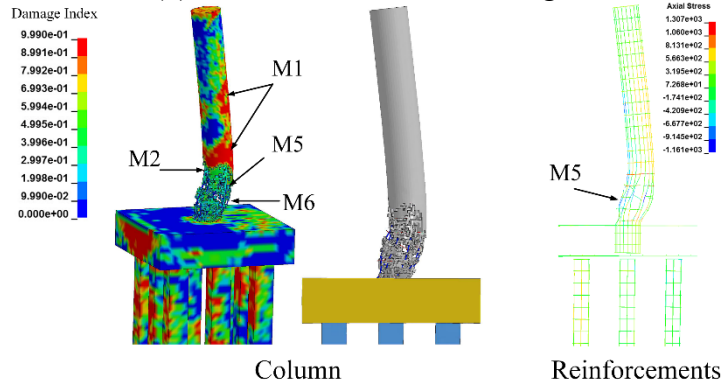
- (a) M2 was observed at the base and M1 along the column height for the 750 mm diameter column. The concrete core was intact. Overall, the column sustained minor damage, including wide-spread cracking and some spalling. The localized damages were deemed repairable for the column.
 - (b) M1 and M2 were observed for the 1050 mm and 1350 mm diameter columns. It is believed that damage could be addressed without taking the bridge out of service.
- ii. For $v_0 = 95 \text{ km/h}$, $Z = 0.25 \text{ m/kg}^{1/3}$ –
 - (a) M1, M2, and M4 were observed for the 750 mm diameter column. Shear failure occurred at the base.
 - (b) M1 and M2 were observed for the 1050 mm diameter column. It is believed that the column could remain in operation.
 - (c) The 1350 mm diameter column experienced minor damage (M1 and M2).
- iii. For $v_0 = 120 \text{ km/h}$, $Z = 0.20 \text{ m/kg}^{1/3}$ –
 - (a) M1, M2, M5, and M6 were observed for the 750 mm diameter column. This column is assumed to have failed.
 - (b) M1, M2, and M4 were observed for the 1050 mm diameter column. Shear failure occurred at the column base.
 - (c) M1 and M2 was observed for the 1350 mm diameter column. This column was deemed able to carry applied loads.



(a) $v_0 = 65 \text{ km/h}$, $Z = 0.30 \text{ m/kg}^{1/3}$

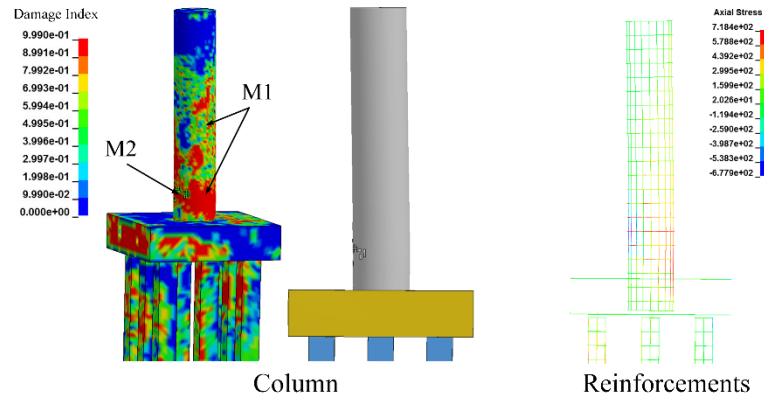


(b) $v_0 = 95 \text{ km/h}$, $Z = 0.25 \text{ m/kg}^{1/3}$

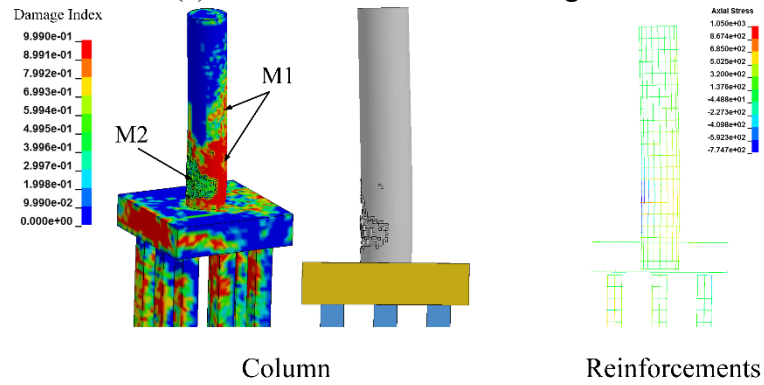


(c) $v_0 = 120 \text{ km/h}$, $Z = 0.20 \text{ m/kg}^{1/3}$

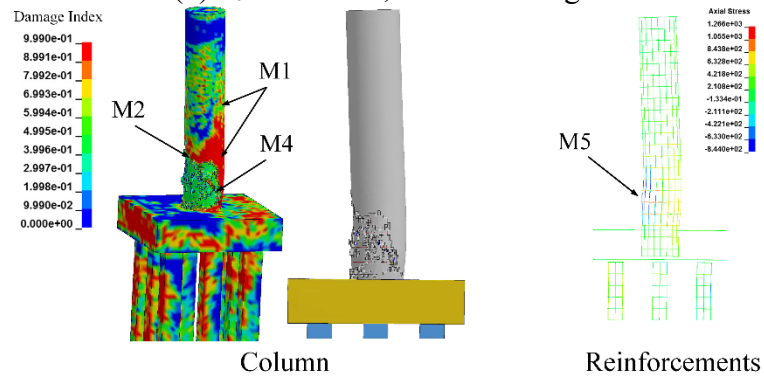
Figure 3.15 750 mm diameter column final damage states for representative loading cases



(a) $v_0 = 65 \text{ km/h}$, $Z = 0.30 \text{ m/kg}^{1/3}$

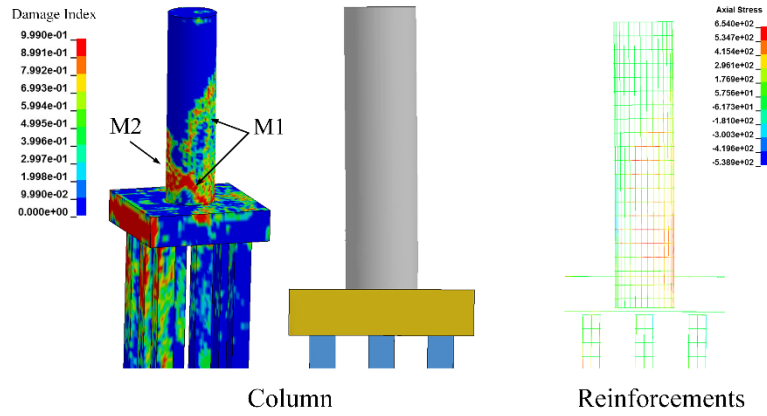


(b) $v_0 = 95 \text{ km/h}$, $Z = 0.25 \text{ m/kg}^{1/3}$

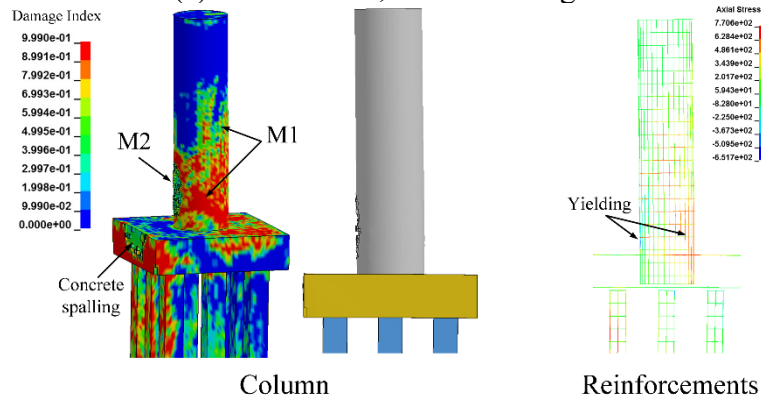


(c) $v_0 = 120 \text{ km/h}$, $Z = 0.20 \text{ m/kg}^{1/3}$

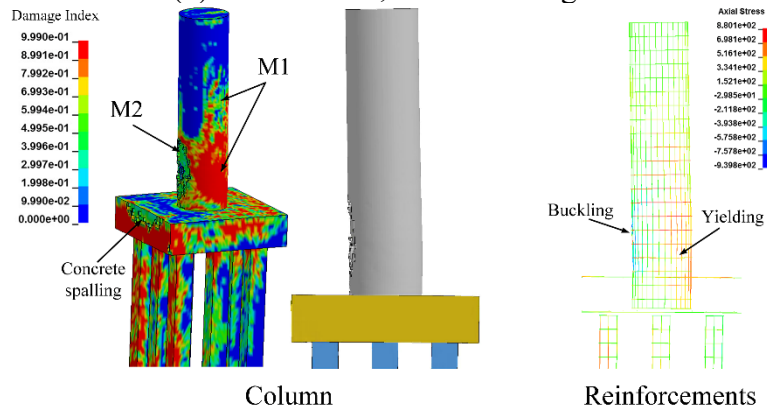
Figure 3.16 1050 mm diameter column final damage states for representative loading cases



(a) $v_0 = 65 \text{ km/h}$, $Z = 0.30 \text{ m/kg}^{1/3}$



(b) $v_0 = 95 \text{ km/h}$, $Z = 0.25 \text{ m/kg}^{1/3}$



(c) $v_0 = 120 \text{ km/h}$, $Z = 0.20 \text{ m/kg}^{1/3}$

Figure 3.17 1350 mm diameter column final damage states for representative loading cases

Numerical results indicated that the 750 mm diameter column was vulnerable to the collision and blast combination. As the collision velocity exceeded 95 km/h, examined load combinations resulted in shear failure at its base with significant concrete spalling and reinforcement buckling. Except for the highest combination of collision and blast, the 1050 mm diameter columns were largely able to continue carrying loads in their final, damaged states. At the highest combined level, direct shear failure was observed at the base. The 1350 mm diameter column largely experienced concrete cracking and spalling in the collision region with reinforcement yielding and was deemed able to carry loads for all examined collision-blast combinations.

3.5 Conclusions

This chapter summarized numerical simulations of isolated bridge columns subjected to combined vehicle collision and air blast. The simulations were used to examine column response to identify a critical load sequence and categorize representative column damage. Results from the studies indicated that:

- (1) Vehicle collision followed by air blast was the critical sequence for demand ranges and combinations that were examined.
- (2) During a collision-blast combination event, identified column damage states included:
 - (a) plastic deformation with concrete cover spalling; (b) plastic hinge formation in the collision region; (c) the onset of column shear failure; and (d) shear failure with coupled concrete crushing. Different levels of damage in bridge columns were identified for various demands from collision and blast combination and classified as,
 - (i) concrete surface cracking; (ii) concrete cover spalling; (iii) plastic hinge

- formation; (iv) direct shear failure; (v) reinforcement failure; and (vi) concrete breach.
- (3) For the six categories that were identified, concrete breach and direct shear failure were determined to be the top results in column failure. Concrete breaching damage typically representing concrete spalling and crushing in the collision region and direct shear failure were the primary failure modes to govern the performance of RC bridge column when subjected to the combined vehicle collision and air blast.
- (4) For the column diameters examined, the 750 mm diameter column was vulnerable to the collision and blast combination. Except for the highest combination of collision and blast, the 1050 mm diameter columns were largely able to continue carry loads in their final, damaged states. The 1350 mm diameter column performed operationally to carry loads for all examined collision-blast combinations.
- (5) Findings from this chapter aided the following work by performing parametric studies that investigate the effects of critical parameters on the performance of isolated bridge columns and developing a performance-based design framework.

Chapter 4 Isolated Bridge Columns Performance under Combined Vehicle Collision and Air Blast

4.1 Introduction

This chapter summarizes studies used to assess effects of specific design parameters on performance of bridge columns subjected to combined vehicle collision and air blast. An isolated column was examined. Selected design parameters included column diameter, column height, longitudinal reinforcement ratio, transverse reinforcement spacing, and applied axial load. A single-variate approach was used to examine the effect of each parameter on column response. Performance was assessed by examining parameter influences on the occurrence of column damage that was evaluated by estimating the amount of concrete spalling, column shear resistance capacity, and residual axial capacity.

4.2 Parameter matrix

4.2.1 Fixed parameters

The prototype column used for the study is shown in Figure 2.5 and was obtained from a multi-column frame pier from a highway bridge design example developed by the FHWA. Models were developed based on numerical simulations discussed in Chapters 2 and 3.

Parameters were selected based on input provided from a state DOT design survey completed in conjunction with NCHRP Report 645 [13], “*Blast-Resistant Highway Bridges: Design and Detailing Guidelines*”. The survey indicated that several design parameters were largely consistent across the country and, as a result, remained constant for the current study. These included having a:

- Circular column section;
- Concrete compressive strength of 28 MPa (4 ksi);

- Concrete cover of 50 mm (2 in.);
- A615 Grade 60 steel reinforcing bars; and
- Discrete transverse reinforcing hoops.

4.2.2 Study matrix

The study used a single-variable method to assign the parameters for the investigated columns so the effect of each parameter on column performance could be clearly assessed. Parameter values and ranges were chosen based on the AASHTO design limitations and resulting values are shown in Table 4.1, where: D is column diameter, H is column height, ρ_L is the longitudinal reinforcement ratio, s_v is the hoop spacing, α_{ALR} is service axial load to nominal axial capacity ratio, v_0 is SUT impact velocity, and Z is scaled distance.

Table 4.1 Examined parameters

D (mm)	H (mm)	ρ_L	Shear reinforcement (hoop)	s (mm)	α_{ALR}	v_0 (km/h)	Z (m/kg ^{1/3})
750	4000	1%	No.10	100	0%	65	0.20
	5400	2%		200	6%	95	0.25
	9000	3%		300	12%	120	0.30
1050	4000	1%	No.10	100	0%	65	0.20
	5400	2%		200	6%	95	0.25
	9000	3%		300	12%	120	0.30
1350	4000	1%	No.10	100	0%	65	0.20
	5400	2%		200	6%	95	0.25
	9000	3%		300	12%	120	0.30

4.3 Parametric study results

Representative results from each of the parameter examinations are summarized in the following sections. Column performance was assessed by examining: (i) volume of spalled concrete for the entire column, which reflected column damage severity, and the amount of

buckled reinforcement; (ii) shear resistance using a normalized base shear ratio determined by maximum shear force at the base divided by shear capacity; and (iii) residual axial capacity based on the peak axial load of the column during the post collision-blast event.

4.3.1 Concrete spalling severity and reinforcement buckling

Spalling severity was based on the concrete erosion ratio (γ_{bc}), which is the ratio of eroded to original concrete volume, and a similarly calculated buckled reinforcement ratio (γ_{br}). Each parameter's influence on concrete spalling intensity was discussed in the following sections.

4.3.1.1 Column diameter

As stated earlier, column diameters of 750 mm, 1050 mm, and 1350 mm were considered. Figure 4.1 depicts representative damage for each diameter while Table 4.2 summarizes diameter effects on damage. Figure 4.2 illustrates diameter effects on axial strains, which was determined by averaging the strain in each bar at the selected cross sections for the final state. Cross sections were located at 500 mm intervals along the height of the column. As expected, increasing diameter reduced damage intensity. As Figure 4.1 shows, the amount of eroded concrete and the number of bucked longitudinal reinforcement in the cross-section decreased as diameter increased. An increase in column diameter correlated with a decrease in average longitudinal reinforcement axial strains as shown in Figure 4.2.

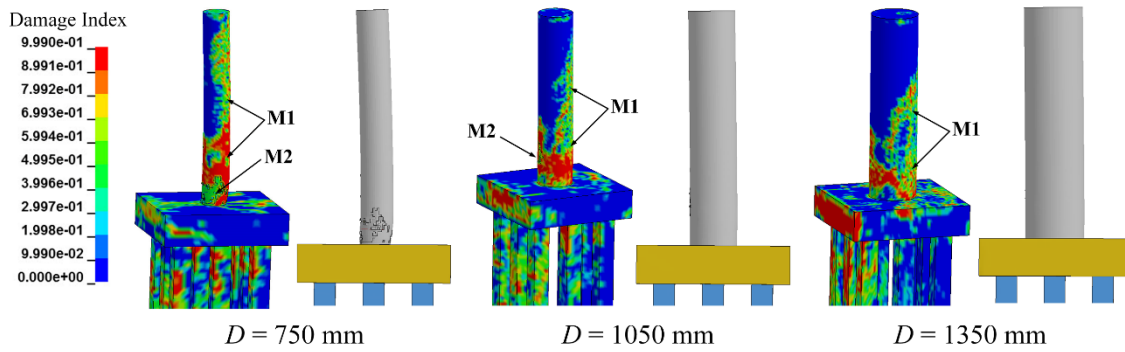
As summarized from numerical results for the collision and blast combinations selected in this study, column damage states were assigned based on damage prorogation described in Chapter 3 to demonstrate how the concrete spalling of a column relates to the damage intensity, with slender columns sustaining the most damage. All columns exhibited plastic deformation, with M1 observed along the height and M2 at the base. Columns having 750 mm and 1050 mm

diameters also exhibited plastic hinge, M3, at the base. For this damage, these columns were observed to experience approximately 15% of concrete spalled and 22% of longitudinal reinforcement buckled. A combination of M4 and M5, the onset of shear failure at the base, were observed in 750 mm and 1050 mm diameter columns with M1 and M2 in the collision region. For this damage state, about 35% of concrete spalled off for these columns and 50% of longitudinal reinforcement buckled. Combined M5 and M6, breaching of the concrete and subsequent failure, were observed in the collision region for the 750 mm diameter column, with approximately 50% of concrete spalled and more than 50% of the longitudinal reinforcement buckled.

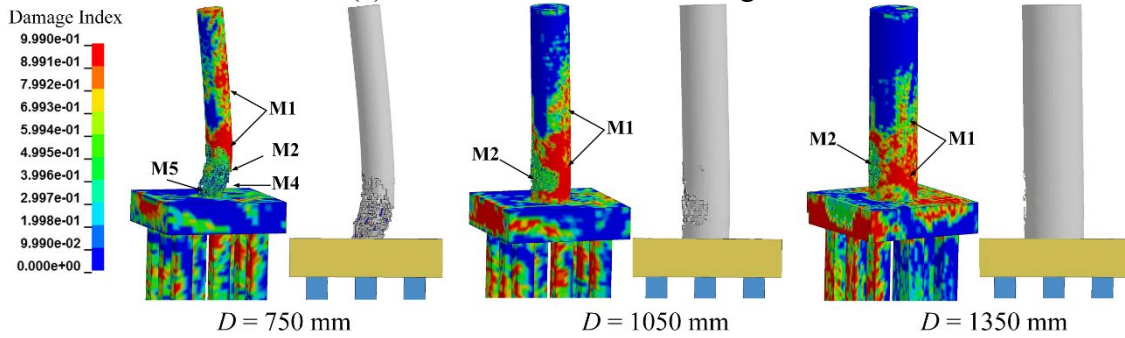
Figure 4.3 plots diameter effects on maximum deflections for various collision and blast combinations. Larger diameter columns experienced lower deflections. Differences were more pronounced between the 750 mm and 1050 mm diameter columns than the 1050 mm and 1350 mm diameter columns. The biggest differences between 750 mm and 1050 mm diameter columns were attributed to significant increase in the stiffness of the column against lateral deformation and significant improvement in the shear resistance with the increased cross-sectional modulus.

Table 4.2 Diameter effect on damage

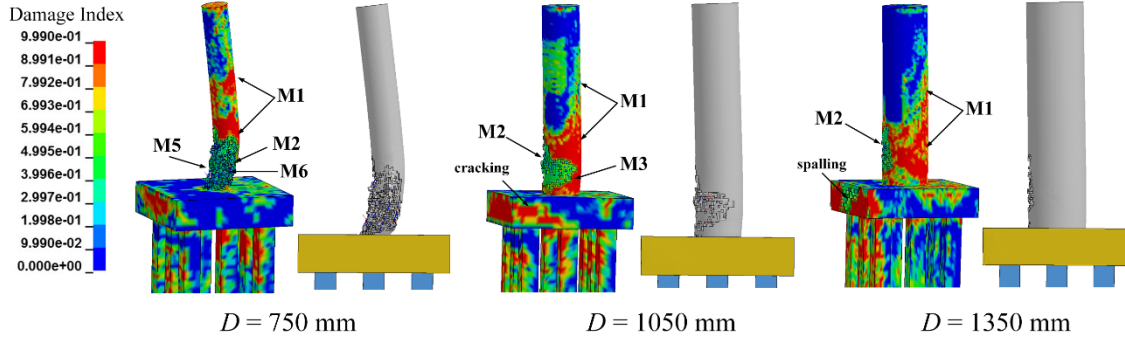
D (mm)	Load		γ_{bc}	γ_{br}	Damage categories
	v_0 (km/h)	Z (m/kg ^{1/3})			
750	65	0.3	6.4%	11.1%	M1, M2
	95	0.25	36.0%	66.7%	M1, M2, M4, M5
	120	0.25	53.1%	88.9%	M1, M2, M5, M6
1050	65	0.3	0.2%	0.0%	M1, M2
	95	0.25	6.8%	11.1%	M1, M2
	120	0.25	15%	22.2%	M1, M2, M3
1350	65	0.3	0	0	M1
	95	0.25	0.8%	6.7%	M1, M2
	120	0.25	3.5%	10.0%	M1, M2



(a) $v_0 = 65$ km/h; $Z = 0.30$ m/kg^{1/3}



(b) $v_0 = 95$ km/h; $Z = 0.25$ m/kg^{1/3}



(c) $v_0 = 120 \text{ km/h}$; $Z = 0.25 \text{ m/kg}^{1/3}$
Figure 4.1 Column diameter effect on damage categories.

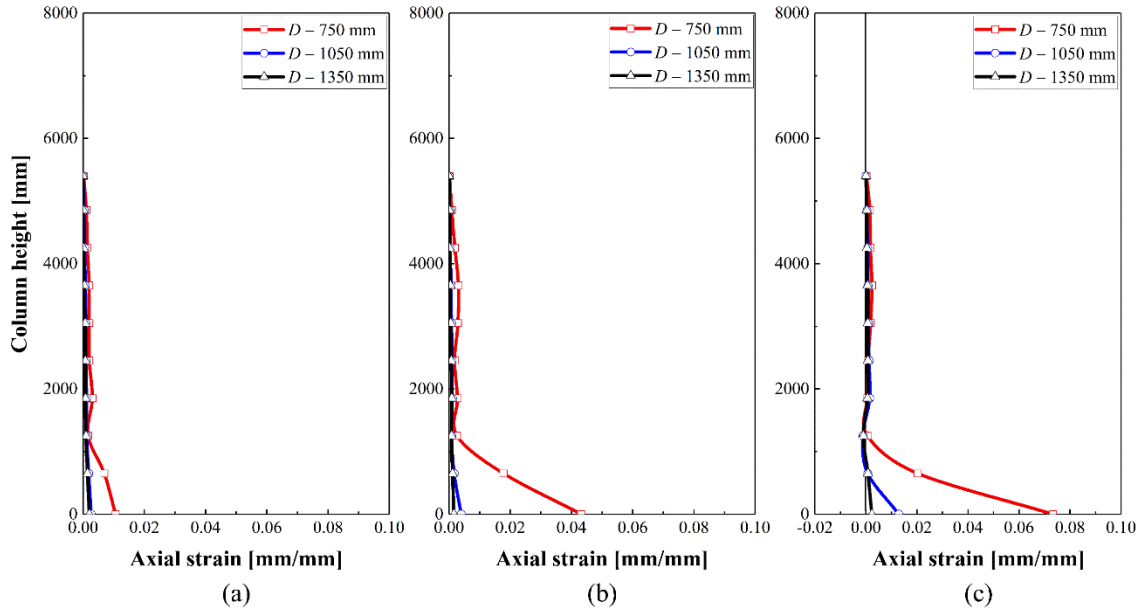
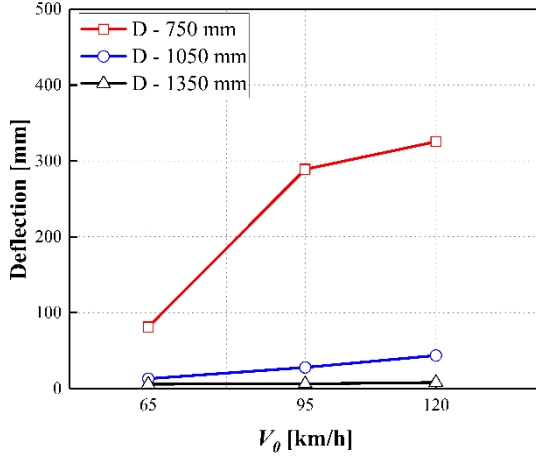
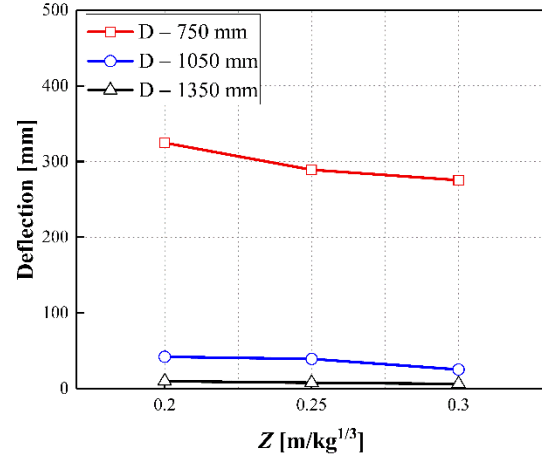


Figure 4.2 Diameter effect on average longitudinal reinforcement axial strains: (a) $v_0 = 65 \text{ km/h}$; $Z = 0.30 \text{ m/kg}^{1/3}$; (b) $v_0 = 95 \text{ km/h}$; $Z = 0.25 \text{ m/kg}^{1/3}$; (c) $v_0 = 120 \text{ km/h}$; $Z = 0.25 \text{ m/kg}^{1/3}$.



(a) with $Z = 0.25 \text{ m/kg}^{1/3}$



(b) with $v_0 = 95 \text{ km/h}$

Figure 4.3 Diameter effects on maximum deflection.

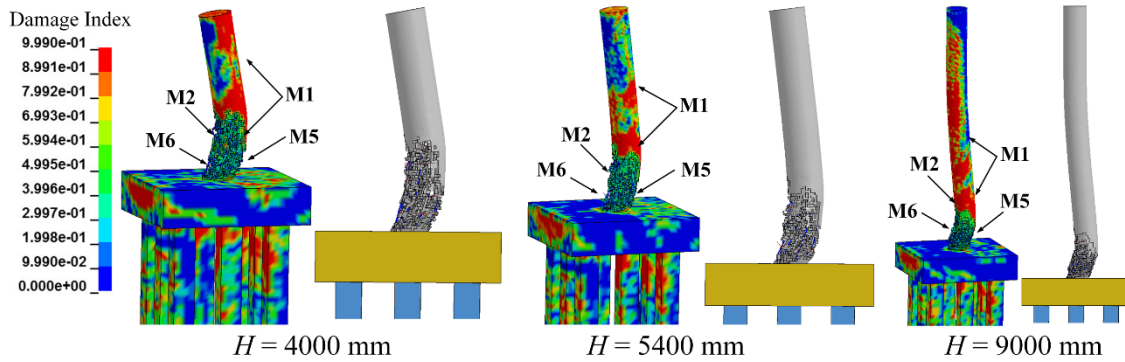
4.3.1.2 Column height

Simulations were conducted for column heights of 4000 mm, 5400 mm, and 9000 mm.

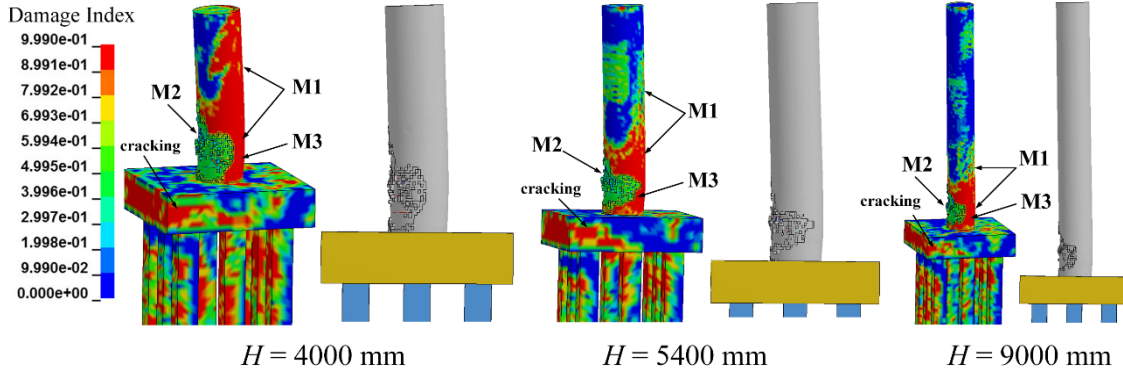
Table 4.3 summarizes height effects on column damage. Figure 4.4 presents the representative final damage state for the different heights while Figure 4.5 looks at axial strains and Figure 4.6 maximum column deflections. The table and figures indicate that, for the studied columns, variations in height had minimal effect on final damage states. In this study, the collision point was close to the column base (member end) so that column damage was shown to be localized erosion dominated by shear force in the critical column cross section.

Table 4.3 Height effects on damage.

D (mm)	H (m)	Load		γ_{bc}	γ_{br}	Damage categories
		v_0 (km/h)	Z (m/kg ^{1/3})			
750	4	65	0.3	6.6%	11.1%	M1, M2
		95	0.25	36.7%	66.7%	M1, M2, M4, M5
		120	0.25	54.2%	88.9%	M1, M2, M5, M6
	5.4	65	0.3	6.4%	11.1%	M1, M2
		95	0.25	36.0%	66.7%	M1, M2, M4, M5
		120	0.25	53.1%	88.9%	M1, M2, M5, M6
	9	65	0.3	6.4%	11.1%	M1, M2
		95	0.25	33.6%	66.7%	M1, M2, M4, M5
		120	0.25	52.2%	77.8%	M1, M2, M5, M6
1050	4	65	0.3	0.4%	0.0%	M1, M2
		95	0.25	7.0%	11.1%	M1, M2
		120	0.25	16.2%	22.2%	M1, M2, M3
	5.4	65	0.3	0.2%	0.0%	M1, M2
		95	0.25	6.8%	11.1%	M1, M2
		120	0.25	15%	22.2%	M1, M2, M3
	9	65	0.3	0.1%	0.0%	M1, M2
		95	0.25	6.3%	11.1%	M1, M2
		120	0.25	13.3%	22.2%	M1, M2, M3

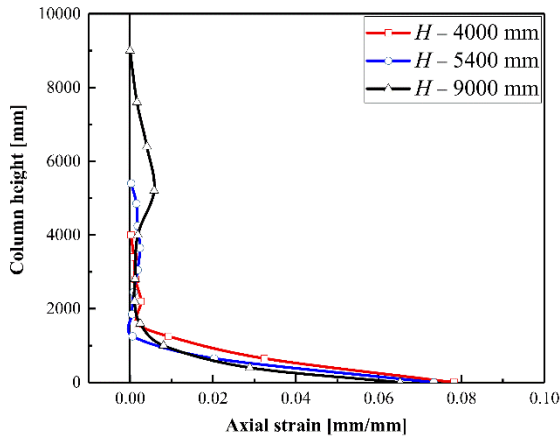


(a) $D = 750$ mm

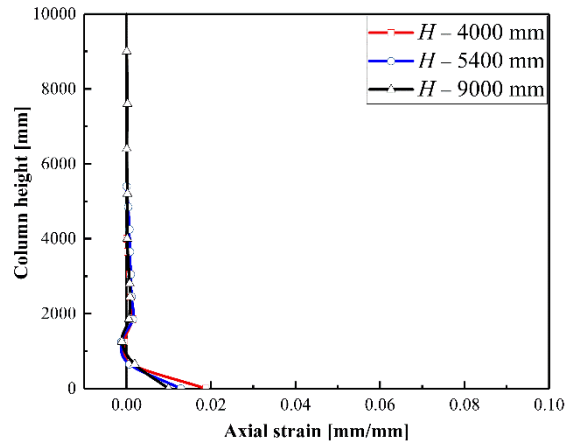


(b) $D = 1050 \text{ mm}$

Figure 4.4 Column height effect on damage categories
($v_0 = 120 \text{ km/h}$; $Z = 0.25 \text{ m/kg}^{1/3}$)



(a) $D = 750 \text{ mm}$



(b) $D = 1050 \text{ mm}$

Figure 4.5 Column height effect on average longitudinal reinforcement axial strains
($v_0 = 120 \text{ km/h}$; $Z = 0.25 \text{ m/kg}^{1/3}$).

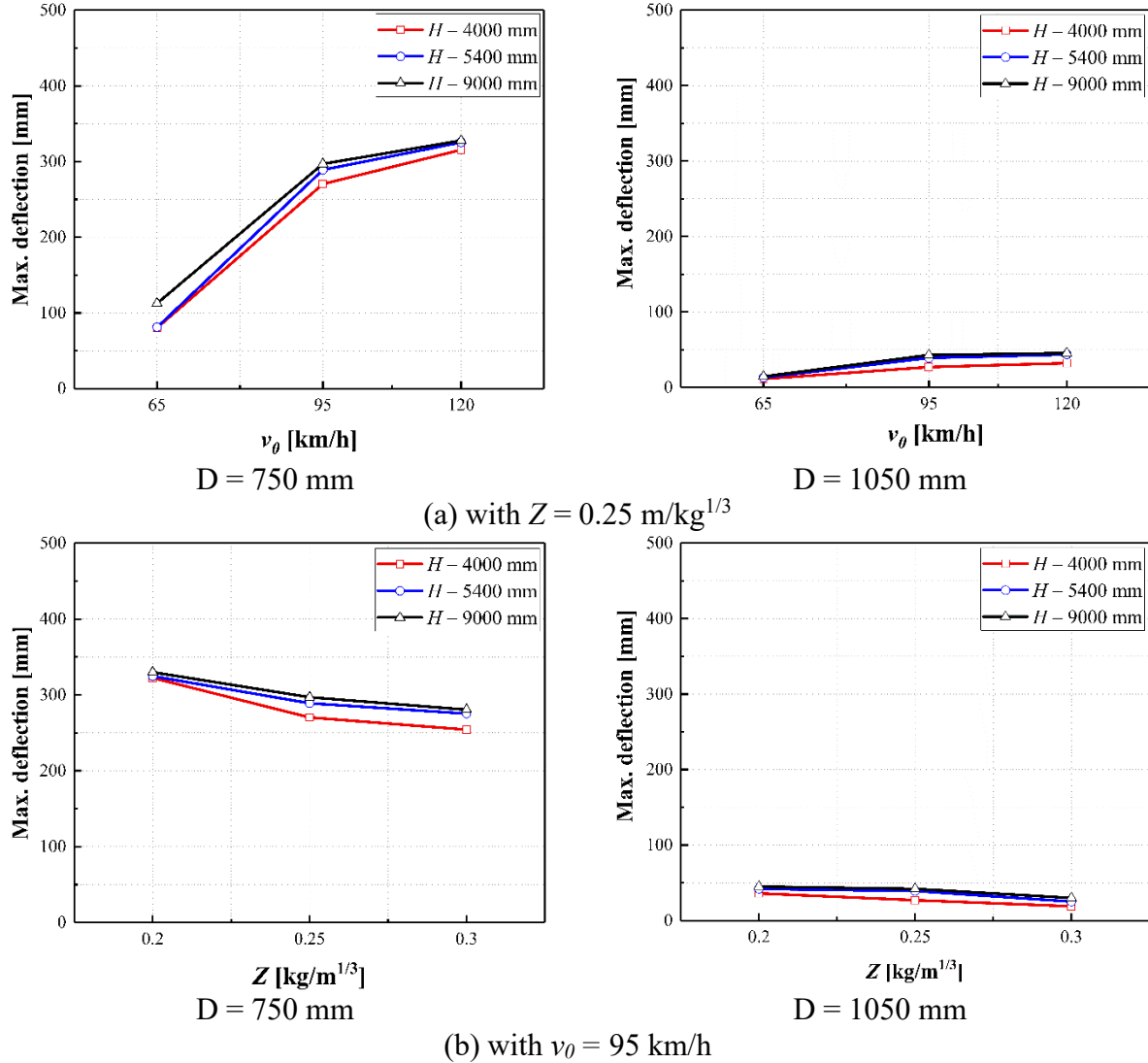


Figure 4.6 Column height effect on maximum deflection.

4.3.1.3 Longitudinal reinforcement ratio

Simulations were conducted for longitudinal reinforcement ratios of 1%, 2%, and 3%. Table 4.4 summarizes longitudinal reinforcement ratio effects on column damage. Figure 4.7 presents the representative final damage state for the different longitudinal reinforcement ratios while Figure 4.8 looks at axial strains and Figure 4.9 maximum column deflections. The table and figures indicate that an increased longitudinal reinforcement ratio reduced column damage. The amount of spalled concrete, the number of buckled longitudinal reinforcement in the cross-

section, and the average axial strains in longitudinal reinforcement decreased as the longitudinal reinforcement ratio increased. Columns with larger longitudinal reinforcement ratios experienced lower deflections as shown in Figure 4.9. Increasing the longitudinal reinforcement ratio is beneficial to the column stiffness and strength, improving column performance in the combined collision-blast events.

An increase in the longitudinal reinforcement may not ensure serviceability for the columns that were studied. As shown in Figure 4.7 (b), the combined collision-blast load resulted in a breach for the 750 mm diameter column at 1% longitudinal reinforcement ratio. At a 3% ratio the column failed due to shear at its base as the limit state shifted from being flexure dominated to shear dominated.

Table 4.4 Longitudinal reinforcement ratio effect on damage

D (mm)	ρ_L	Load		γ_{bc}	γ_{br}	Damage categories
		v_0 (km/h)	Z (m/kg ^{1/3})			
750	1%	65	0.3	6.4%	11.1%	M1, M2
		95	0.25	36.0%	66.7%	M1, M2, M4, M5
		120	0.25	53.1%	88.9%	M1, M2, M5, M6
	2%	65	0.3	5.0%	11.1%	M1, M2
		95	0.25	28.4%	77.8%	M1, M2, M4, M5
		120	0.25	36.3%	88.9%	M1, M2, M4, M5
	3%	65	0.3	4.4%	11.1%	M1, M2
		95	0.25	20.8%	44.4%	M1, M2, M3
		120	0.25	34.2%	77.8%	M1, M2, M4, M5
1050	1%	65	0.3	0.2%	0.0%	M1, M2
		95	0.25	6.8%	11.1%	M1, M2
		120	0.25	15%	22.2%	M1, M2, M3
	2%	65	0.3	0.5%	0.0%	M1, M2
		95	0.25	2.5%	5.6%	M1, M2
		120	0.25	6.2%	11.1%	M1, M2, M3
	3%	65	0.3	0.2%	0.0%	M1
		95	0.25	0.3%	0.0%	M1, M2
		120	0.25	2.8%	5.6%	M1, M2, M3

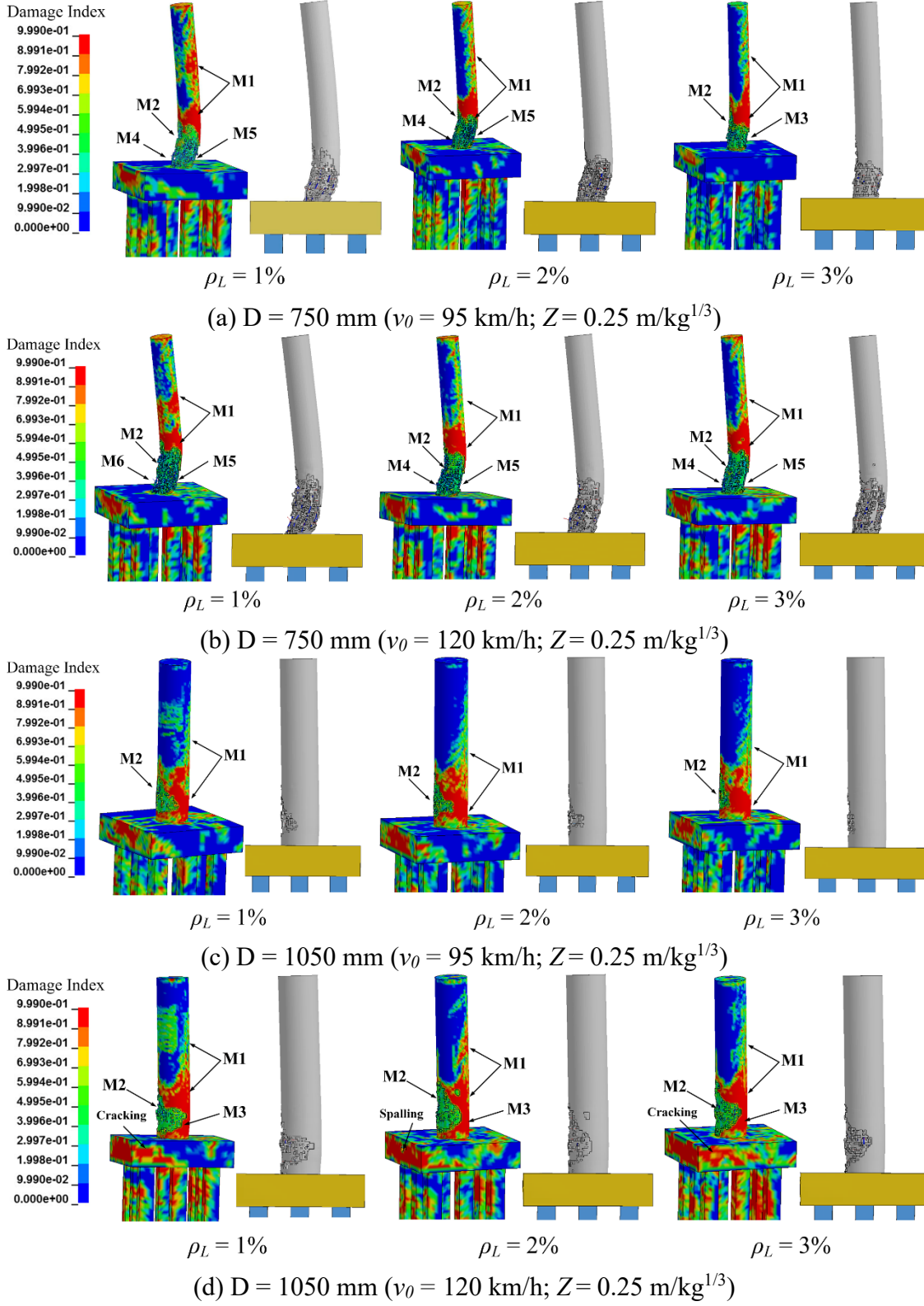
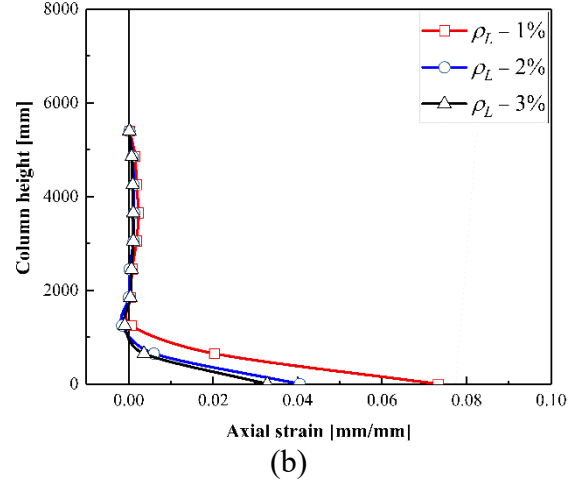
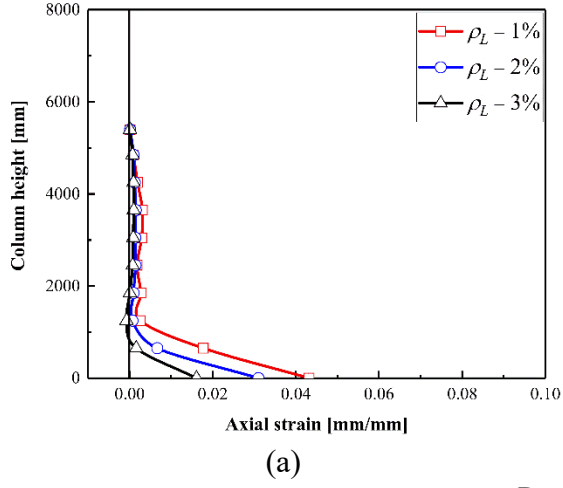
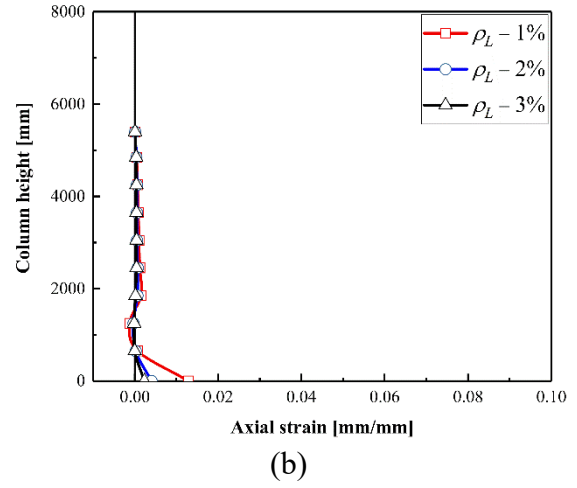
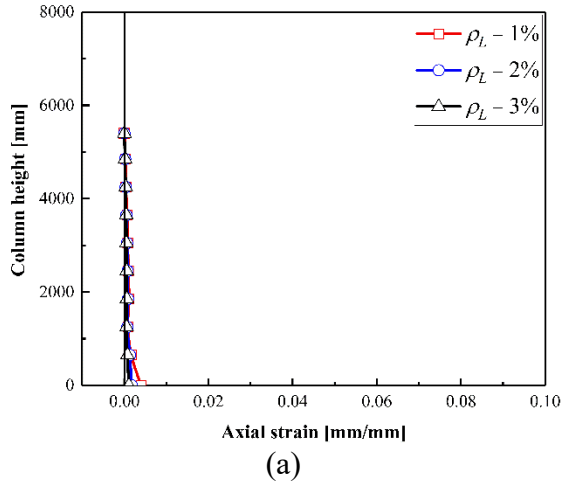


Figure 4.7 Longitudinal reinforcement ratio effect on damage categories



$D = 750 \text{ mm}$



$D = 1050 \text{ mm}$

Figure 4.8 Longitudinal reinforcement ratio effects on average longitudinal reinforcement axial strains: (a) $v_0 = 95 \text{ km/h}$; $Z = 0.25 \text{ m/kg}^{1/3}$; (b) $v_0 = 120 \text{ km/h}$; $Z = 0.25 \text{ m/kg}^{1/3}$

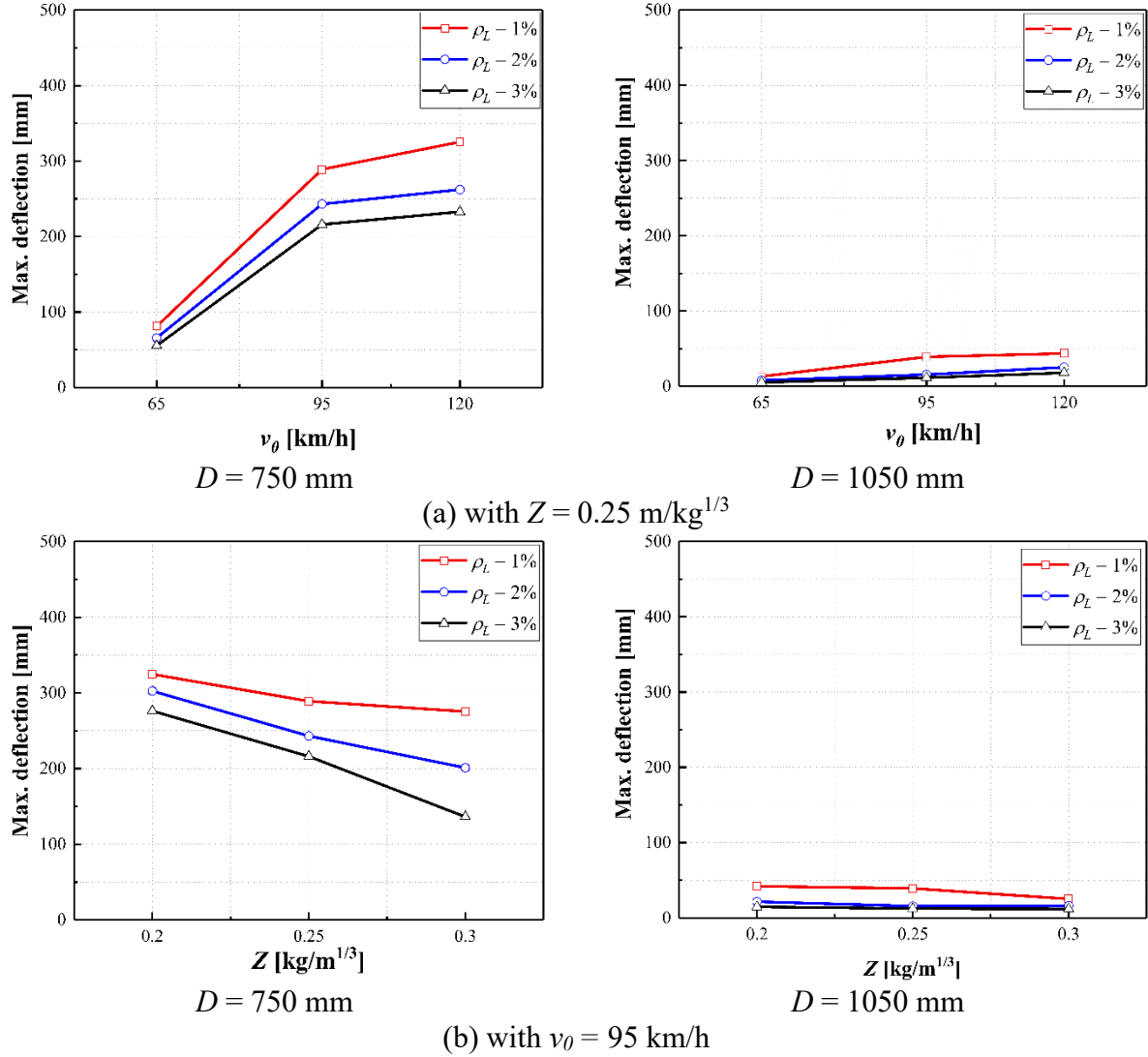


Figure 4.9 Longitudinal reinforcement ratio effect on maximum deflection

4.3.1.4 Shear reinforcement (hoop) spacing

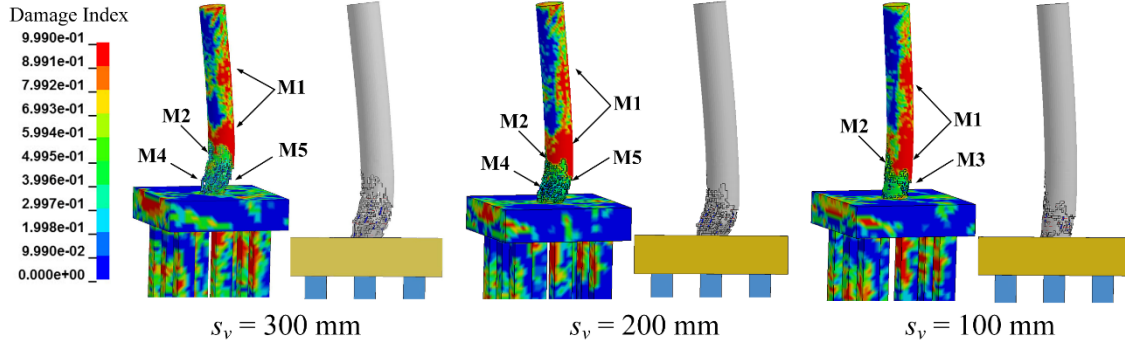
Shear reinforcement (hoop) spacings of 100 mm, 200 mm, and 300 mm were examined, with results summarized in Table 4.5. Figure 4.10 presents representative final damage states, Figure 4.11 examines axial strains, and Figure 4.12 shows maximum deflections. The table and figures indicate that increased shear reinforcement (i.e. smaller hoop spacings) reduced column damage. The amount of spalled concrete and the number of buckled longitudinal reinforcement decreased with the decreased hoop spacing. The column with the smaller hoop spacing sustained

a lower average axial strain in the longitudinal reinforcement at the column base as shown in Figure 4.11.

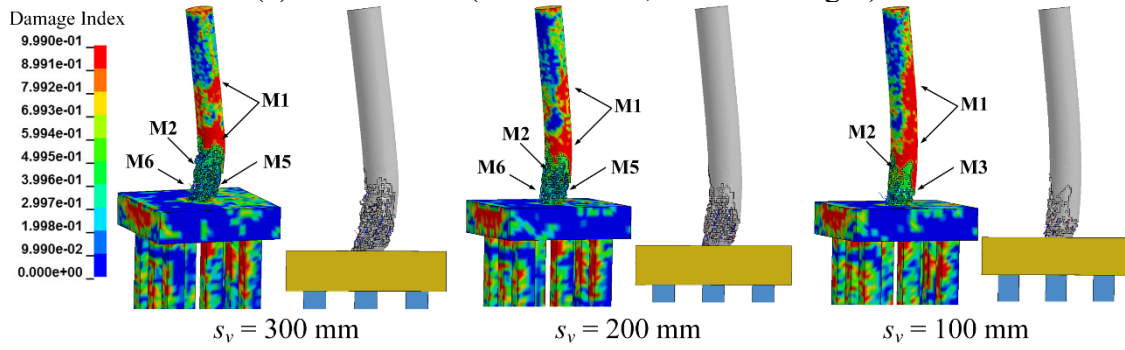
Beneficial influence of increased shear reinforcement was more pronounced when hoop spacing was reduced from 200 mm to 100 mm than from 300 mm to 200 mm. This was attributed to effective increase in the shear capacity and ductility of the column by increasing the shear reinforcement, which results in shift from shear dominated damage to flexure dominated. The desired flexural behavior would be developed as column shear capacity exceeds its flexure capacity. Furthermore, the shear reinforcement provides confinement on the core concrete and restraint against longitudinal reinforcement buckling. An increase in shear reinforcement would produce increased additional confinement and restraint effects to improve the column flexure capacity.

Table 4.5 Shear reinforcement effect on damage

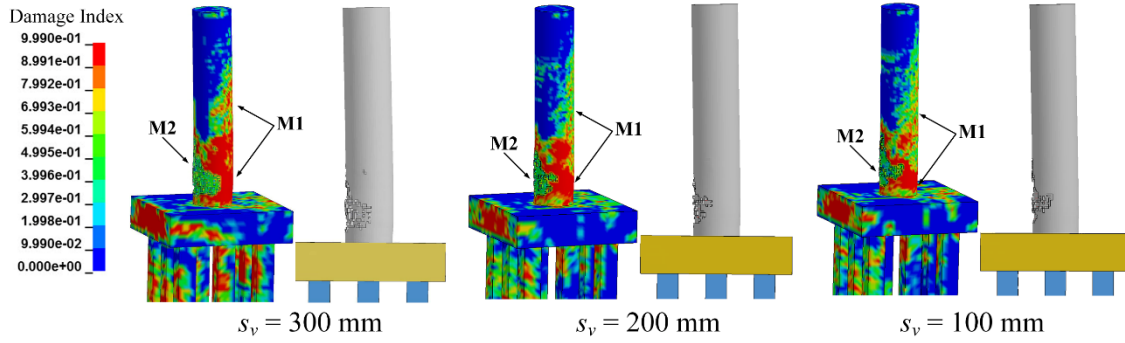
D (mm)	s_v (mm)	Load		γ_{bc}	γ_{br}	Damage categories
		v_0 (km/h)	Z (m/kg ^{1/3})			
750	100	65	0.3	4.5%	0	M1, M2
		95	0.25	16.6%	22.2%	M1, M2, M3
		120	0.25	20.3%	33.3%	M1, M2, M3
	200	65	0.3	6.6%	11.1%	M1, M2
		95	0.25	32.8%	55.6%	M1, M2, M4, M5
		120	0.25	40.5%	66.7%	M1, M2, M5, M6
	300	65	0.3	6.4%	11.1%	M1, M2
		95	0.25	36.0%	66.7%	M1, M2, M4, M5
		120	0.25	53.1%	88.9%	M1, M2, M5, M6
1050	100	65	0.3	0.2%	0	M1
		95	0.25	2.0%	0	M1, M2
		120	0.25	3.9%	5.6%	M1, M2
	200	65	0.3	0.3%	0	M1, M2
		95	0.25	5.6%	5.6%	M1, M2
		120	0.25	7.2%	11.1%	M1, M2
	300	65	0.3	0.2%	0	M1, M2
		95	0.25	6.8%	11.1%	M1, M2
		120	0.25	15%	22.2%	M1, M2, M3



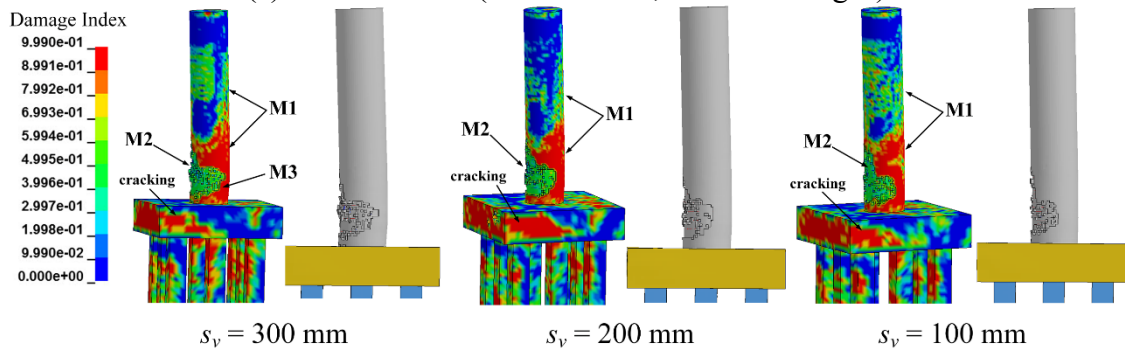
(a) $D = 750 \text{ mm}$ ($v_0 = 95 \text{ km/h}$; $Z = 0.25 \text{ m/kg}^{1/3}$)



(b) $D = 750 \text{ mm}$ ($v_0 = 120 \text{ km/h}$; $Z = 0.25 \text{ m/kg}^{1/3}$)

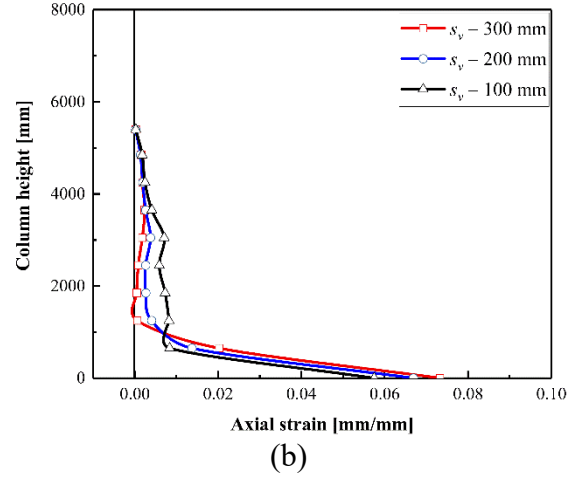
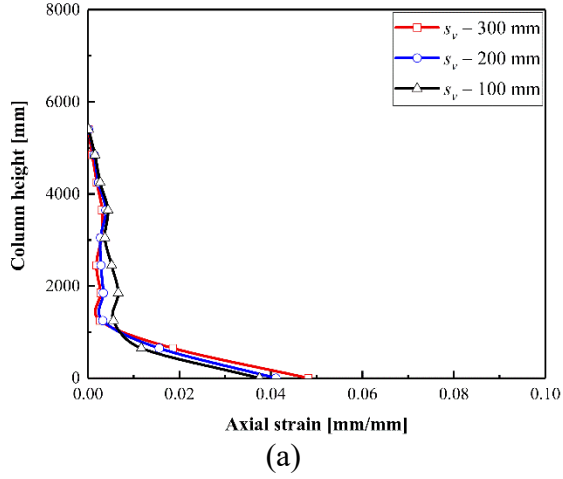


(c) $D = 1050 \text{ mm}$ ($v_0 = 95 \text{ km/h}$; $Z = 0.25 \text{ m/kg}^{1/3}$)

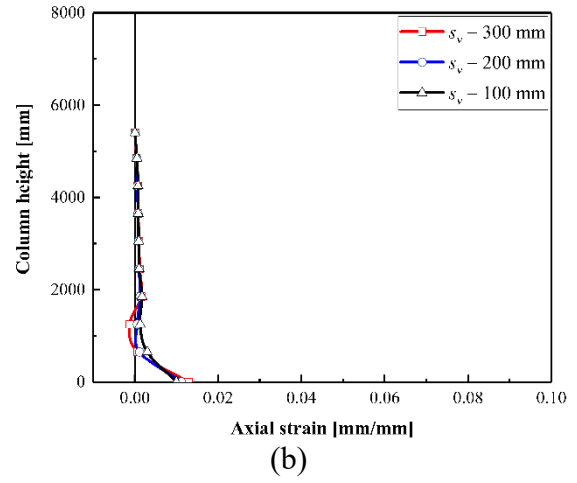
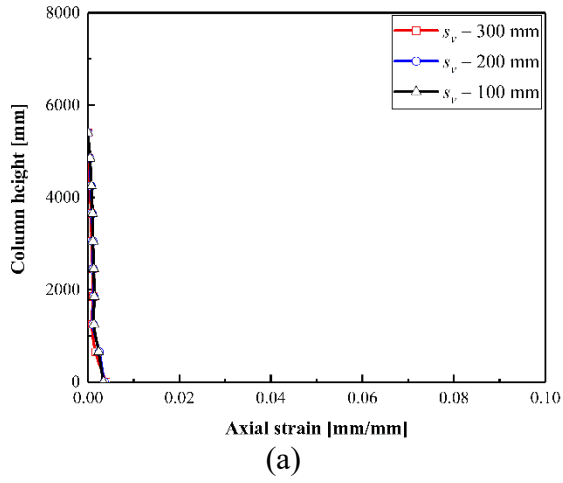


(d) $D = 1050 \text{ mm}$ ($v_0 = 120 \text{ km/h}$; $Z = 0.25 \text{ m/kg}^{1/3}$)

Figure 4.10 Shear reinforcement effect on damage categories



$D = 750 \text{ mm}$



$D = 1050 \text{ mm}$

Figure 4.11 Shear reinforcement effect on average longitudinal reinforcement axial strain: (a) $v_0 = 95 \text{ km/h}$; $Z = 0.30 \text{ m/kg}^{1/3}$; (b) $v_0 = 120 \text{ km/h}$; $Z = 0.25 \text{ m/kg}^{1/3}$

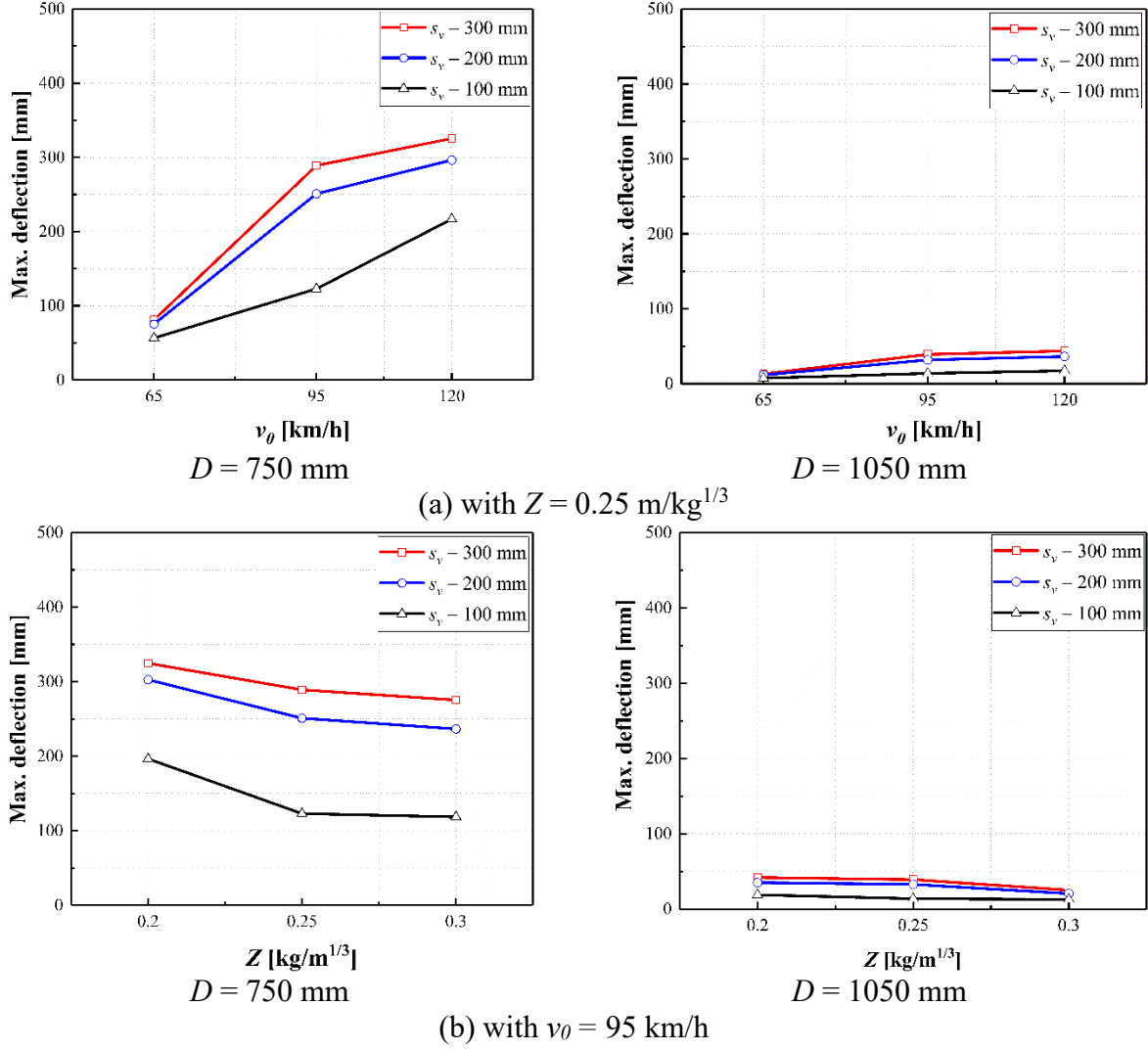


Figure 4.12 Shear reinforcements on maximum deflection

4.3.1.5 Axial load ratio

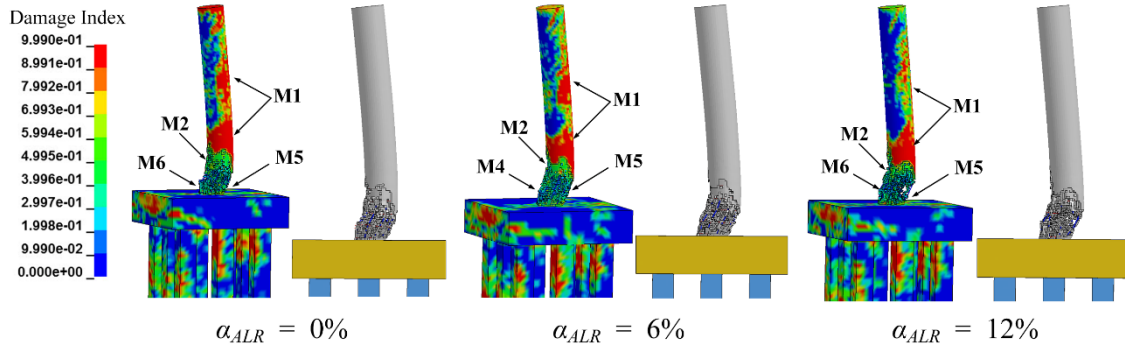
Axial service loads equal to 0%, 6%, and 12% of the nominal axial capacity were applied to the top of the column, with results summarized in Table 4.6. Figure 4.13 presents the representative final damage state for the different axial load ratios, Figure 4.14 is at the axial strains, and Figure 4.15 is maximum column deflections. The table and figures indicate that, for the studied columns, increasing axial load generally reduced column damage. As Figure 4.13 shows, the increased axial load magnitude at the top of the column produced a decrease in the

amount of spalled concrete and the number of buckled longitudinal reinforcement. An increase in axial load pre-compressed the column and resulted in an increase in its bending capacity and shear strength.

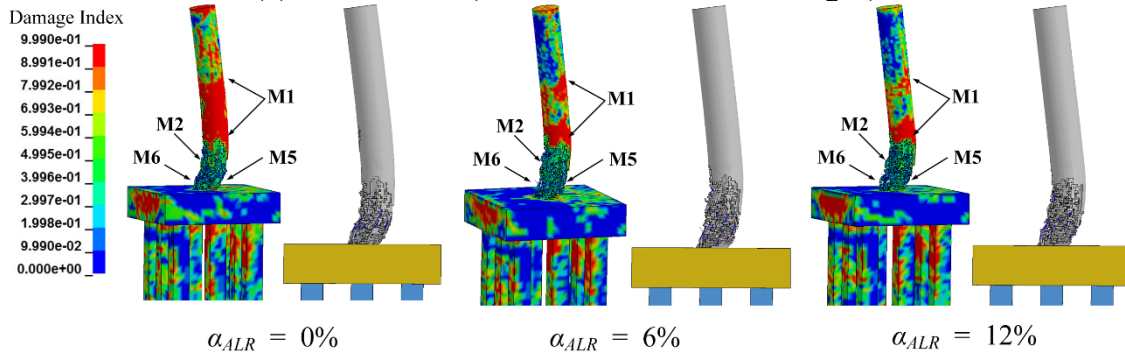
The increased axial load also slightly decreased average longitudinal reinforcement axial strains as shown in Figure 4.14. The increased axial load magnitude generally produced a slight reduction in column deflection as shown in Figure 4.15. Under the high combination of collision and blast, the columns with various axial load ratios sustained similar deflections. When the column sustained large deflection and plastic hinges at the base, a large axial load would amplify the deflection and deteriorate the column damage. As shown in Figure 6.14, at a 12% axial load ratio the column failed due to shear in the collision region as the limit state shifted from the plastic hinge to a direct shear failure, negatively influencing the column performance.

Table 4.6. Axial load ratio effect on damage

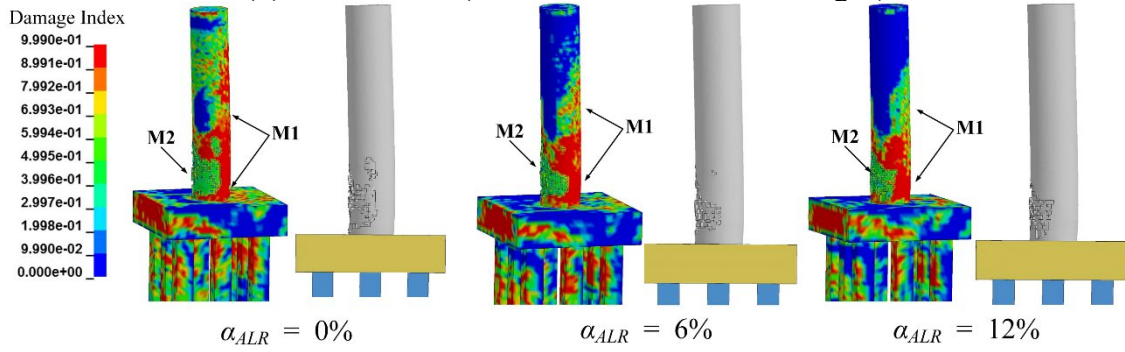
D (mm)	α_{ALR}	Load		γ_{bc}	γ_{br}	Damage categories
		v_0 (km/h)	Z (m/kg ^{1/3})			
750	0%	65	0.3	13.0%	33.3%	M1, M2, M3
		95	0.25	52.5%	77.8%	M1, M2, M5, M6
		120	0.25	58.9%	88.9%	M1, M2, M5, M6
	6%	65	0.3	8.4%	22.2%	M1, M2
		95	0.25	43.0%	66.7%	M1, M2, M4, M5
		120	0.25	53.1%	88.9%	M1, M2, M5, M6
	12%	65	0.3	5.3%	22.2%	M1, M2
		95	0.25	49.6%	66.7%	M1, M2, M5, M6
		120	0.25	62.8%	100.0%	M1, M2, M5, M6
1050	0%	65	0.3	2.7%	5.6%	M1, M2
		95	0.25	8.8%	11.1%	M1, M2
		120	0.25	18.3%	22.2%	M1, M2, M3
	6%	65	0.3	0.2%	0.0%	M1, M2
		95	0.25	6.8%	11.1%	M1, M2
		120	0.25	15.3%	16.7%	M1, M2, M3
	12%	65	0.3	0.3%	0.0%	M1
		95	0.25	2.2%	11.1%	M1, M2
		120	0.25	17.0%	27.8%	M1, M2, M3



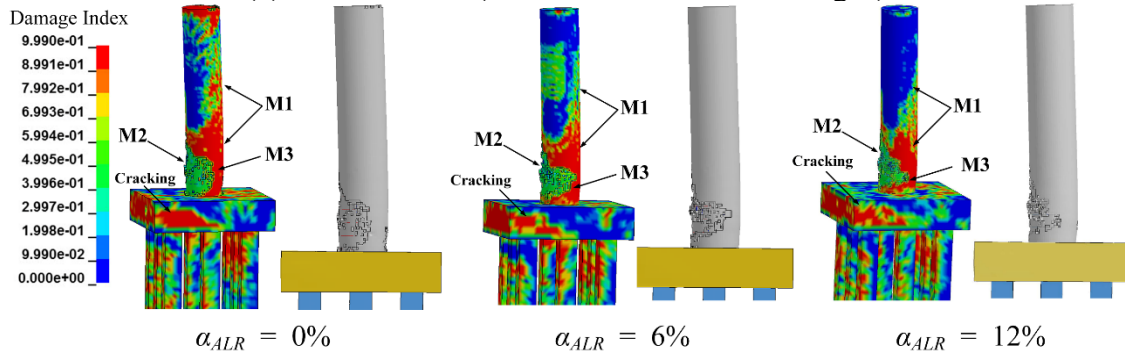
(a) $D = 750$ mm ($v_0 = 95$ km/h; $Z = 0.25$ m/kg^{1/3})



(b) $D = 750$ mm ($v_0 = 120$ km/h; $Z = 0.25$ m/kg^{1/3})

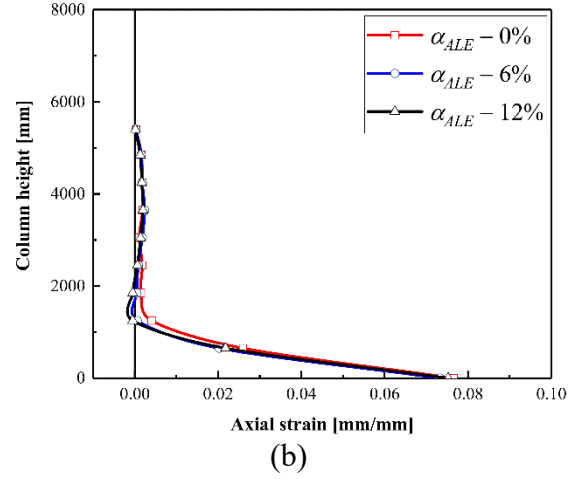
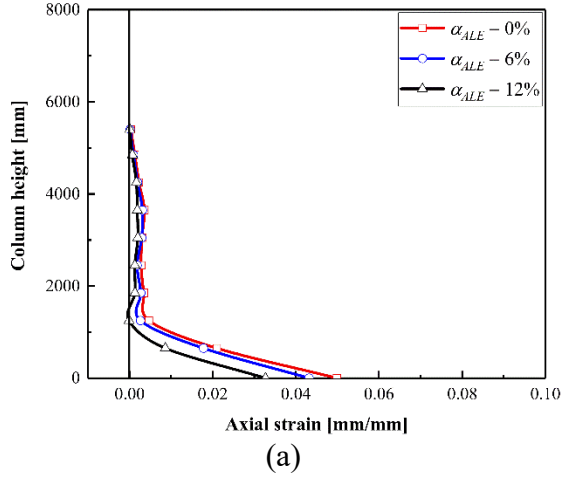


(c) $D = 1050$ mm ($v_0 = 95$ km/h; $Z = 0.25$ m/kg^{1/3})

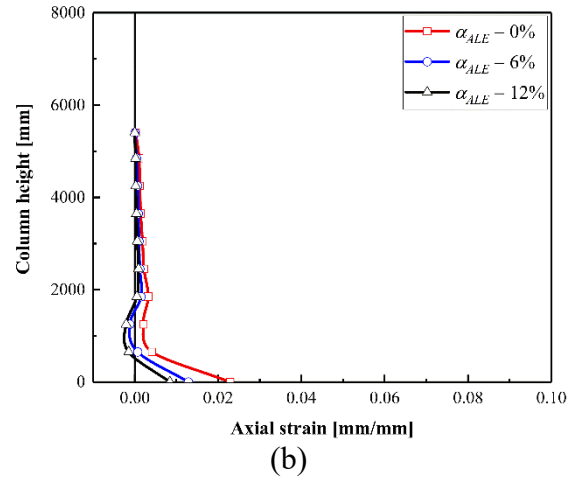
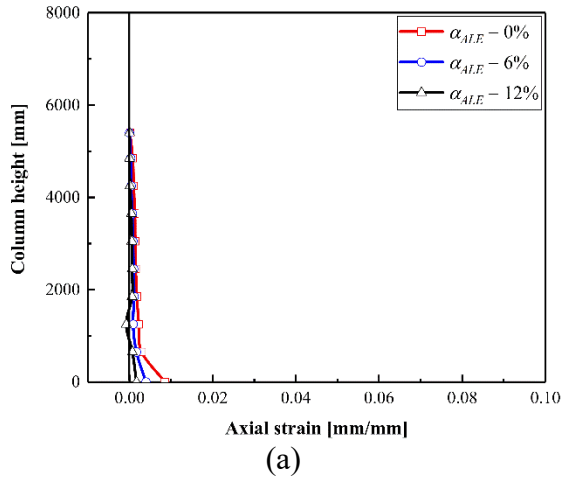


(d) $D = 1050$ mm ($v_0 = 120$ km/h; $Z = 0.25$ m/kg^{1/3})

Figure 4.13 Axial load ratio effect on damage categories



$D = 750$ mm



$D = 1050$ mm

Figure 4.14 Axial load ratio effect on average longitudinal reinforcement axial strains: (a) $v_0 = 95$ km/h; $Z = 0.30$ m/kg^{1/3}; (b) $v_0 = 120$ km/h; $Z = 0.25$ m/kg^{1/3}

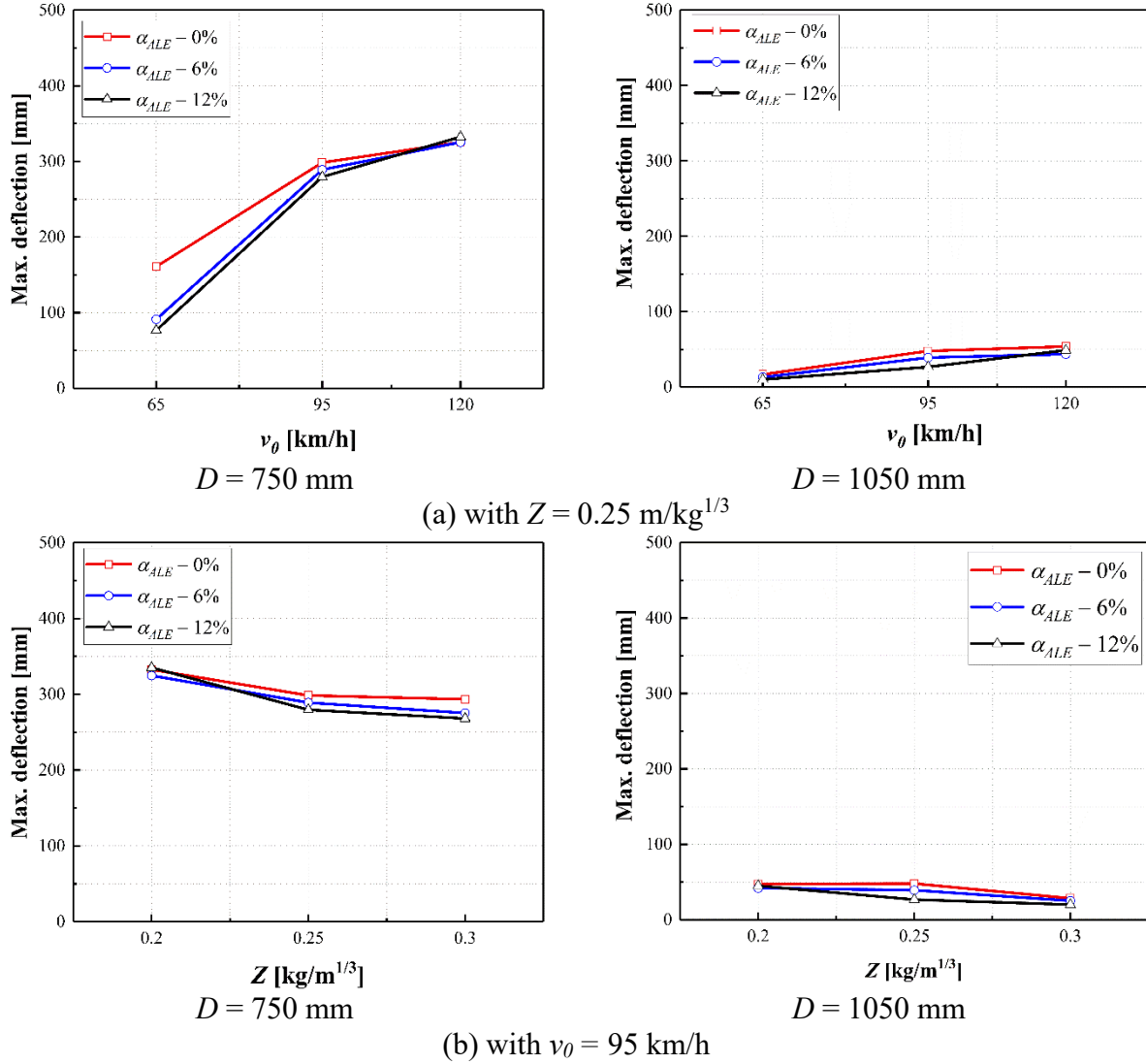


Figure 4.15 Axial load ratio effects on maximum column deflection

4.3.2 Shear resistance

As described in Section 3.3, concrete spalling failure in the collision region was observed to govern the column performance subjected to combined collision and blast. Shear failure at the base is also a type of critical damage for bridge columns that significantly influenced the column performance. In conjunction with examining concrete spalling severity in the collision region, column shear resistance was assessed using LS-DYNA's *Database Cross Section Plane* command to study the effects of each parameter. Shear resistance was computed based on the

cross-sectional force opposing the combined collision and blast event at a section of interest, with the resultant force opposing the vehicle's direction of travel. Cross sections were located at 500 mm intervals along the height of the column. Figure 4.16 contains representative shear diagrams for the 750 mm, 1050 mm, and 1350 mm diameter columns. This figure shows that the maximum shear occurred at the base. Thus, the cross-section near the base was the location where shear resistance was assessed for all modeled columns (V_{base}). Column performance was evaluated by nondimensionalizing the resisting force with respect to ultimate capacity at the base. Ultimate capacity (V_{ult}) was also determined from LS-DYNA simulations using a linearly increasing lateral load applied at the base. Normalized base shear force (V_{base}/V_{ult}) values below 1.0 meant the column survived the collision and blast, with lower ratios indicative of the column having excess reserve capacity, while columns having values above 1.0 were assumed to have failed.

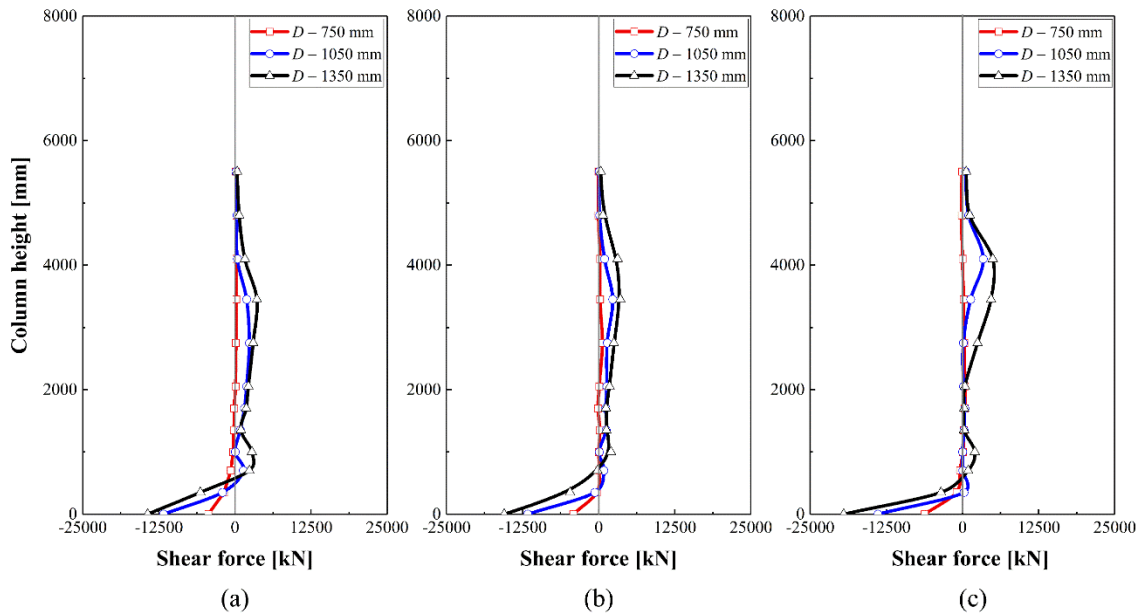


Figure 4.16 Representative shear diagrams for columns in various cases: (a) $v_0 = 65$ km/h; $Z = 0.25$ m/kg^{1/3}; (b) $v_0 = 95$ km/h; $Z = 0.30$ m/kg^{1/3}; (c) $v_0 = 120$ km/h; $Z = 0.25$ m/kg^{1/3}

4.3.2.1 Column diameter

Figure 4.17 illustrates representative normalized base shear forces for the three column diameters under different collision and blast demands. As expected, increased diameter reduced the normalized base shear (V_{base}/V_{ult}), indicating increased shear resistance. These results matched with column damage discussed in Section 6.3.1.1.

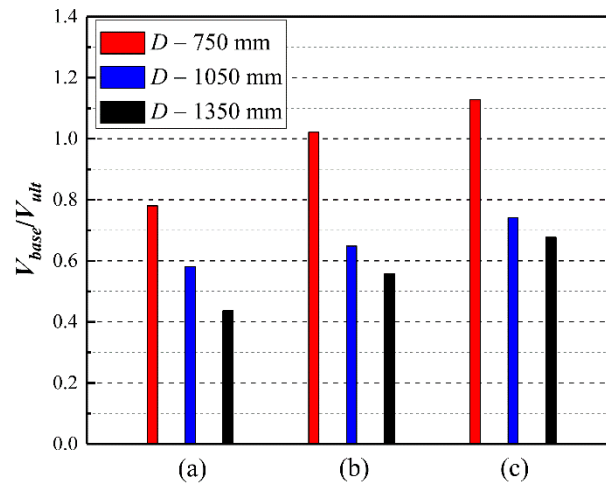


Figure 4.17 Diameter effect on normalized base shear: (a) $v_0 = 65$ km/h; $Z = 0.30$ m/kg^{1/3}; (b) $v_0 = 95$ km/h; $Z = 0.25$ m/kg^{1/3}; (c) $v_0 = 120$ km/h; $Z = 0.25$ m/kg^{1/3}

4.3.2.2 Column height

Figure 4.18 illustrates representative normalized base shear forces for the three column heights under different collision and blast demands. As shown in Figure 4.18, increased height slightly reduced the normalized base shear (V_{base}/V_{ult}), indicating increased shear resistance. The increased height improved the flexure capacity at the column base, which shifted to flexural resistance at this location and reduced shear forces. Hence, column shear resistance at the base slightly increased with the increase in the height.

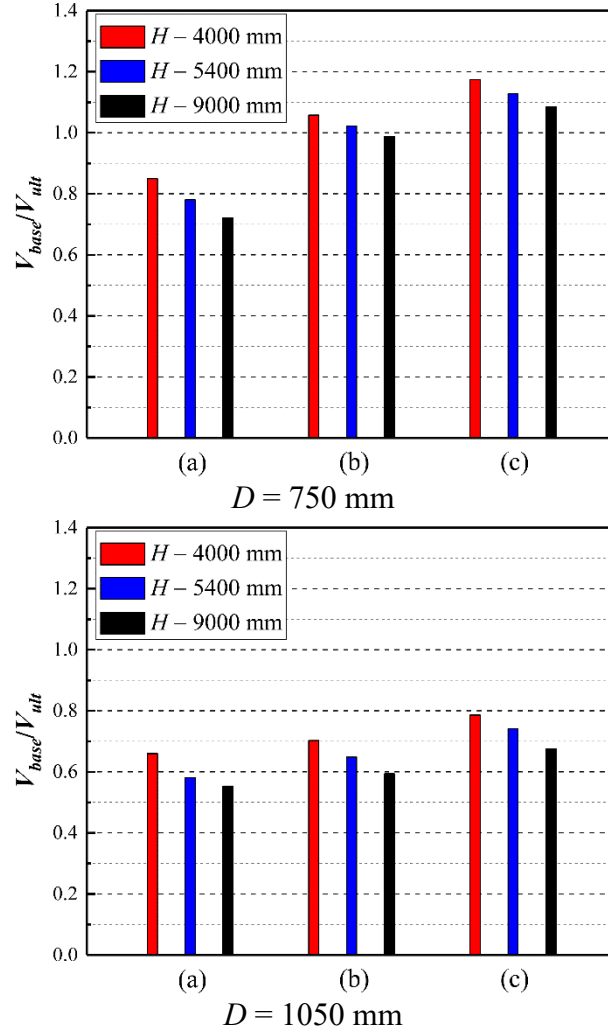


Figure 4.18 Height effect on normalized base shear: (a) $v_0 = 65$ km/h; $Z = 0.30$ m/kg^{1/3}; (b) $v_0 = 95$ km/h; $Z = 0.25$ m/kg^{1/3}; (c) $v_0 = 120$ km/h; $Z = 0.25$ m/kg^{1/3}

4.3.2.3 Longitudinal reinforcement ratio

Figure 4.19 plots representative normalized base shear for the three longitudinal reinforcement ratios. Increased longitudinal reinforcement ratio reduced the normalized base shear (V_{base}/V_{ult}), indicating increased shear resistance. An increase in the longitudinal reinforcement ratio equated to the improved column stiffness and flexural capacity. The advantages of increasing longitudinal reinforcement ratio on the increase in flexural resistance at the base, which resulted in the shift of resistance to flexure and reduced shear force at the base.

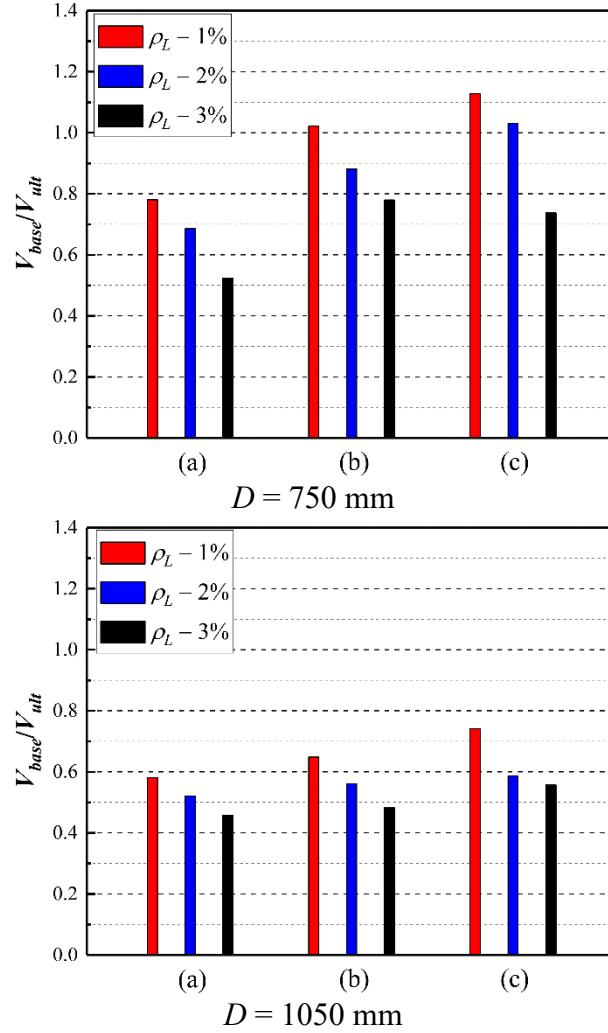


Figure 4.19 Longitudinal reinforcement ratio effect on normalized base shear: (a) $v_0 = 65 \text{ km/h}$; $Z = 0.30 \text{ m/kg}^{1/3}$; (b) $v_0 = 95 \text{ km/h}$; $Z = 0.25 \text{ m/kg}^{1/3}$; (c) $v_0 = 120 \text{ km/h}$; $Z = 0.25 \text{ m/kg}^{1/3}$

4.3.2.4 Shear reinforcement (hoop) spacing

Figure 4.20 compares normalized base shear forces for the three hoop spacings. As expected, decreased hoop spacing reduced the normalized base shear (V_{base}/V_{ult}), indicating increased shear resistance. This plot agreed with the observations from column damage in Section 3.2.1.4 which discussed the advantages of reducing hoop spacing. The increase in the hoop produced an increase in flexure and shear capacity which improved the column resistance at the column base against the demands from the combined collision and blast events.

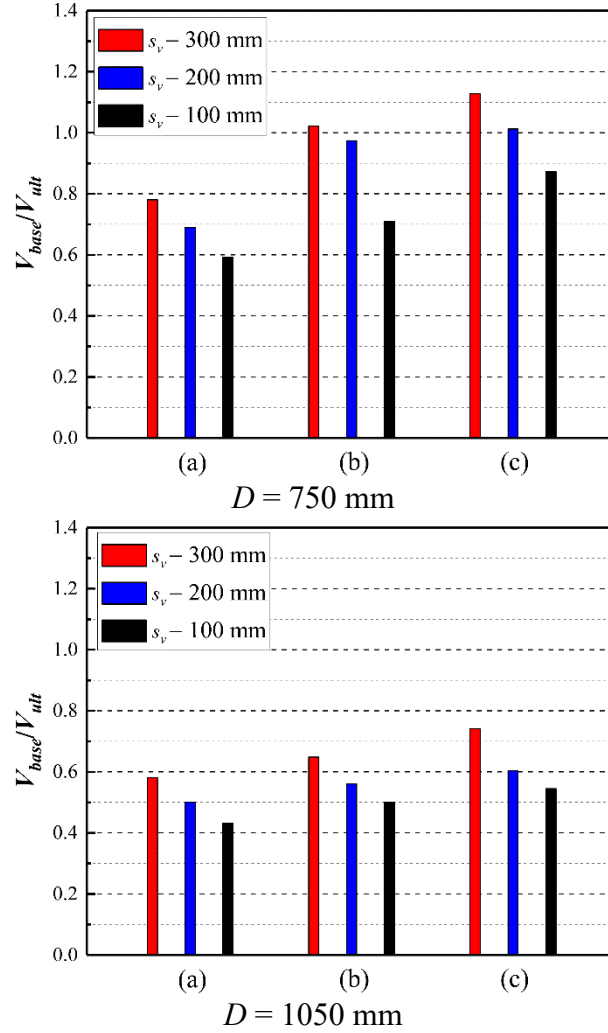


Figure 4.20 Hoop spacing effects on normalized base shear forces: (a) $v_0 = 65$ km/h; $Z = 0.30$ m/kg^{1/3}; (b) $v_0 = 95$ km/h; $Z = 0.25$ m/kg^{1/3}; (c) $v_0 = 120$ km/h; $Z = 0.25$ m/kg^{1/3}

4.3.2.5 Axial load ratio

Figure 4.21 illustrates normalized base shear for the three axial load ratios at the top of the column. Increased axial load ratio slightly reduced the normalized base shear (V_{base}/V_{ult}), indicating a slightly increased shear resistance. The increase in axial load at the top of the column produced an increased column bending capacity. The shift in resistance to flexure reduces shear forces at the column base and improved column shear resistance.

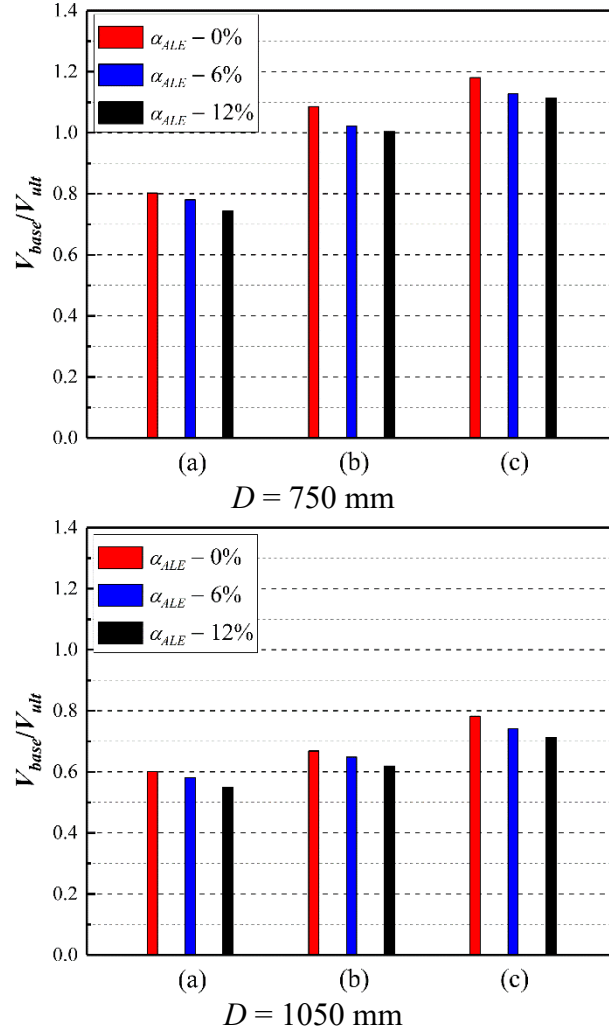


Figure 4.21 Axial load ratio effect on normalized base shear: (a) $v_0 = 65$ km/h; $Z = 0.30$ m/kg^{1/3}; (b) $v_0 = 95$ km/h; $Z = 0.25$ m/kg^{1/3}; (c) $v_0 = 120$ km/h; $Z = 0.25$ m/kg^{1/3}

4.3.3 Residual axial capacity

Columns are the primary load-carrying components in the bridge, and column failure could initiate the collapse of the entire bridge. The residual capacity in a bridge column would assist in predicting the overall performance of the bridge, determining its resistance against the collapse, and assessing the risk of collapse. To precisely determine residual axial capacity, after applying collision and blast loading, axial loads were gradually increased in the simulations by defining an axial load time history curve. Residual axial capacity was equated to the peak axial

load observed from resulting load-mid-height displacement curves [39, 40]. Representative results for a 1050 mm diameter column are shown in Figure 4.22. As the figure indicates, inertial effects produced by the collision and blast resulted in the fluctuation of axial load.

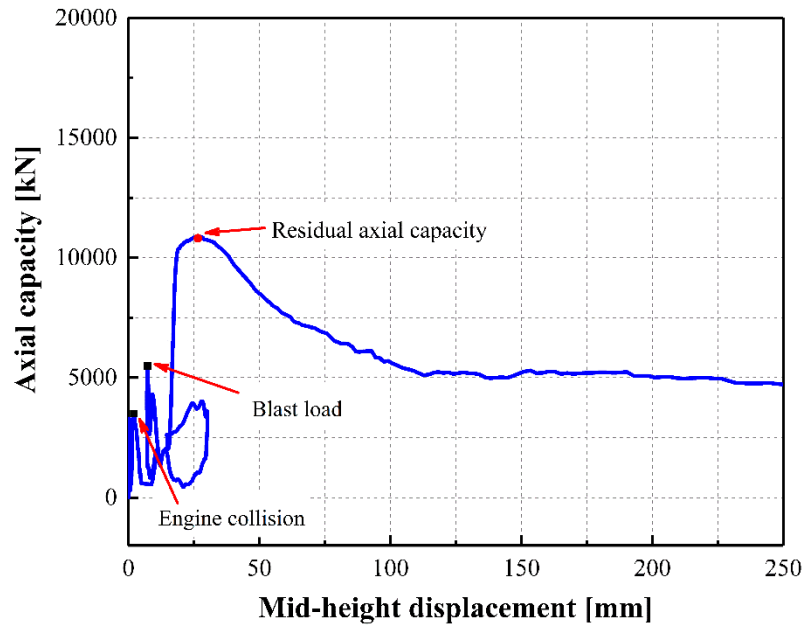


Figure 4.22 Representative axial load-mid-height displacement curve, 1050 mm diameter column ($v_0 = 95$ km/h; $Z = 0.30$ m/kg^{1/3})

An axial capacity ratio (λ_{res}) was defined that compared residual axial load capacity (P_{res}) from the damaged column to its nominal capacity (P_n) as shown in Equation 4.1. Nominal capacity was determined from the AASHTO-LRFD design equation. The following sections examined residual capacity as a function of the total imparted energy (E_t), determined by superimposing vehicle kinetic energy and internal explosion energy from the blast.

$$\lambda_{res} = \frac{P_{res}}{P_n} \quad (4.1)$$

4.3.3.1 Column diameter

Figure 4.23 plots residual axial capacity ratios at different imparted energies for various column diameters with corresponding curve fits shown. Residual axial capacity improved with increasing column diameter under various loading demands. This agrees with observed column damages as discussed in Section 6.3.1.1. The residual axial capacity was controlled by the residual cross-sectional properties of the column after the combined collision and blast event. The residual axial capacity increased with the decreased amount of spalled concrete and the reduced number of buckled longitudinal reinforcement.

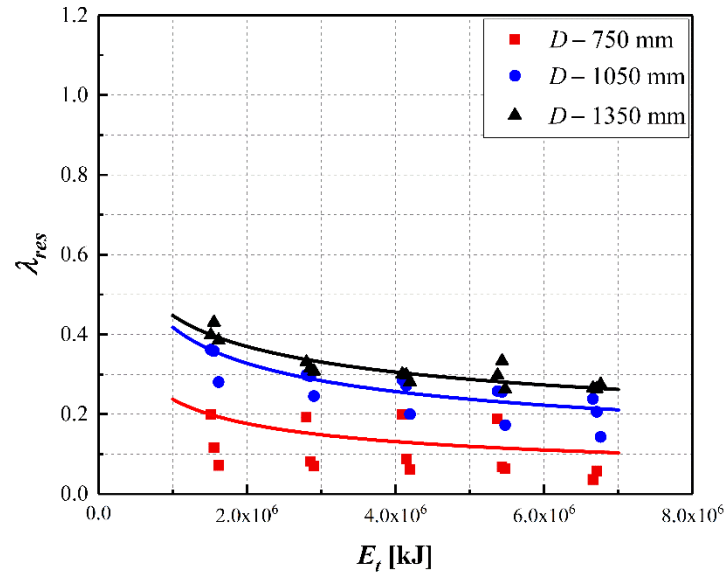


Figure 4.23 λ_{res} vs. E_t for different column diameters

4.3.3.2 Column height

Figure 4.24 plots 1050 mm diameter column residual axial capacity ratios as a function of column height. The figure indicates that a variation in column height produced little effect on residual axial capacity. This agrees with observed column damage as discussed in Section 4.3.1.2.

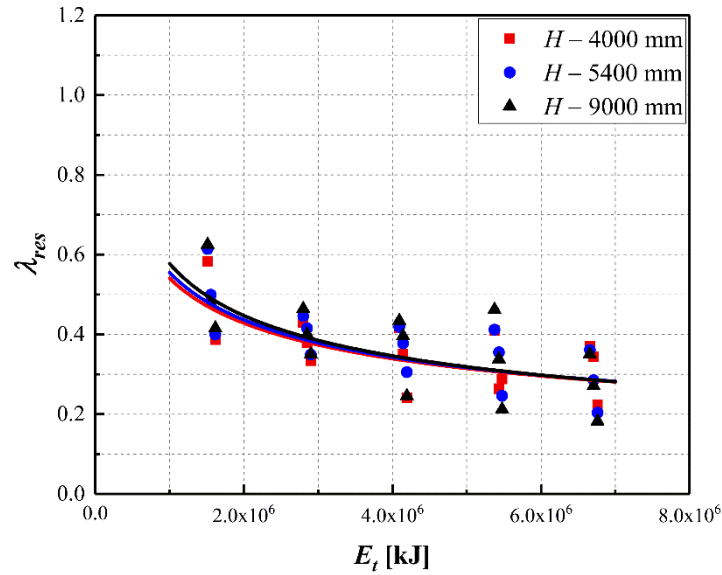


Figure 4.24 λ_{res} vs. E_t for different column heights ($D = 1050$ mm)

4.3.3.3 Longitudinal reinforcement ratio

Figure 4.25 plots residual axial capacity ratios as a function of the longitudinal reinforcement ratio. This figure indicates that residual axial capacity increased with an increasing longitudinal reinforcement ratio. Increases in residual capacity was more pronounced between columns with 1% and 2% ratios than those with 2% and 3% ratios due to more residual concrete volumes remaining at the cross section of the collision region. This agrees with observed column damages as discussed in Section 4.3.1.3.

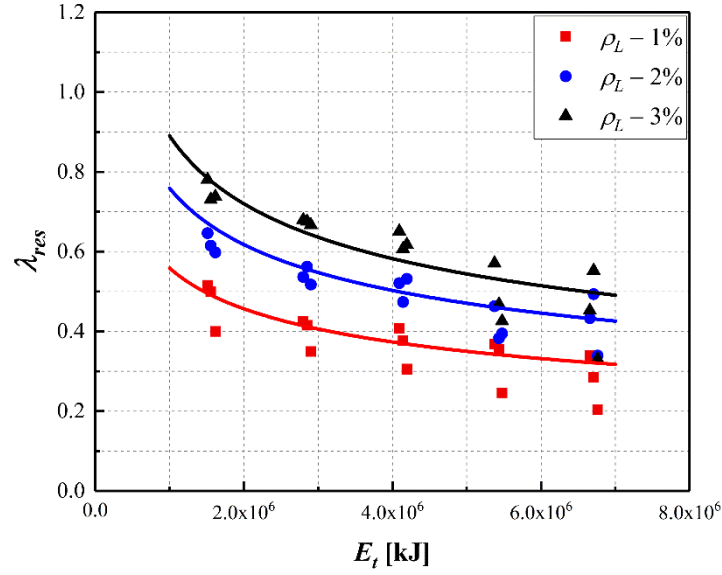


Figure 4.25 λ_{res} vs. E_t for different longitudinal reinforcement ratios ($D = 1050$ mm)

4.3.3.4 Shear reinforcement (hoop) spacing

Figure 4.26 plots residual axial capacity ratios as a function of hoop spacing and indicates that residual axial capacity increased with decreasing hoop spacing. These findings also mapped to the observed column damage categories reported in Section 4.3.1.4, with more pronounced changes in residual capacity being observed when spacing dropped from 200 mm to 100 mm.

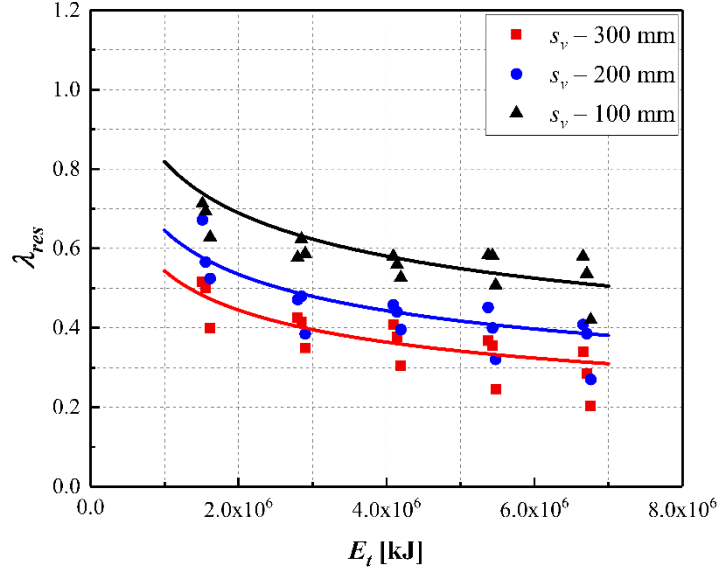


Figure 4.26 λ_{res} vs. E_t for different hoop spacings ($D = 1050$ mm)

4.3.3.5 Axial load ratio

Figure 4.27 plots residual axial capacity ratios as a function of the axial load ratio. This figure indicates that residual axial capacity slightly increased with an increasing axial service load magnitude at the top of the column, which matches discussions in Section 4.3.1.5. It was noted that the axial capacity ratios for the column with three axial load ratios were less than 0.3 in the high-level loading events, identifying the appearance of a severely damaged column. As stated in the column damage, a large axial load would deteriorate the column damage when the column sustained large deflection and plastic hinges at the base.

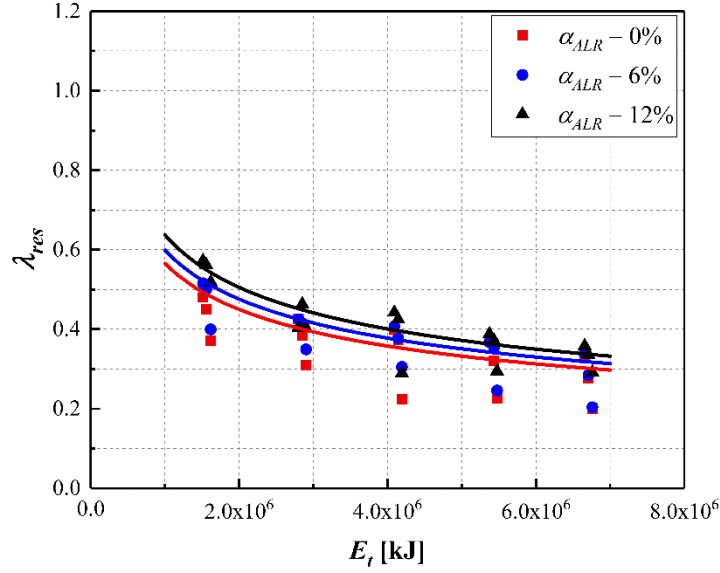


Figure 4.27 λ_{res} vs. E_t for different axial load ratios ($D = 1050$ mm)

4.3.3.6 Empirical formula for determination of column residual axial load capacity

An empirical formula was developed to determine residual axial capacity and estimate column damage under the combined collision-blast loads. The residual axial capacity represented the remaining ability of the damaged column to support the superstructures and could be used as a quantitative assessment to identify and classify the column performance levels for demands from combined collision and blast. The empirical formula considering critical design parameters is used to determine the damage index and enable straightforward designs of bridge columns for desired performance objectives in the performance-based design methodology. Multivariate regression was used to provide an estimate of residual axial capacity based on studied parameters. The empirical equation was determined as a function of total imparted energy as expressed in Equation 4.2. Imparted energy from a collision was estimated using kinetic energy calculated from impact velocity and SUT truck mass. Imparted blast energy was estimated using TNT-equivalency and published data equating 1 gram of TNT to release approximately 4000 J of energy [41]. This process produced an empirical equation shown below, which was used to assist

with the development of an effective performance-based design and evaluation presented in Chapter 5.

$$\lambda_{res} = (106.3 - 91D_g + 29\alpha_{ALLR} + 1802\rho_L + 34s_v) E_t^{(-0.54+0.28D_g+0.062\alpha_{ALLR}-0.163\rho_L-0.2s_v)} \quad (4.2)$$

Given the complexity of Equation 4.2, an investigation on testing the significance of variables on equation terms was completed to determine which variables contribute most to the components by comparing a coefficient (F) as shown in Equation 4.3 [42].

$$F = \frac{(R^2 - R_r^2)}{(1 - R^2)m} \quad (4.3)$$

where, R^2 is the correlation coefficient for the full model; R_r^2 is the correlation coefficient for the reduced model without the selected variables; and m is the number of independent variables being tested for elimination. The multivariate regression began with all independent variables and removed one tested variable at a time until a significant loss in accuracy occurred. Using this method, the simplified equation was obtained in Equation 4.4 to allow for easier implementation into analysis and design processes.

$$\lambda_{res} = (124 - 71.5D + 1031\rho_L - 88s_v) E_t^{(-0.578+0.27D)} \quad (4.4)$$

Figure 4.28 shows some examples comparing numerical results and calculated results. Calculated results matched numerical results well in most cases, and the empirical equations provided a reasonable estimation with numerical results.

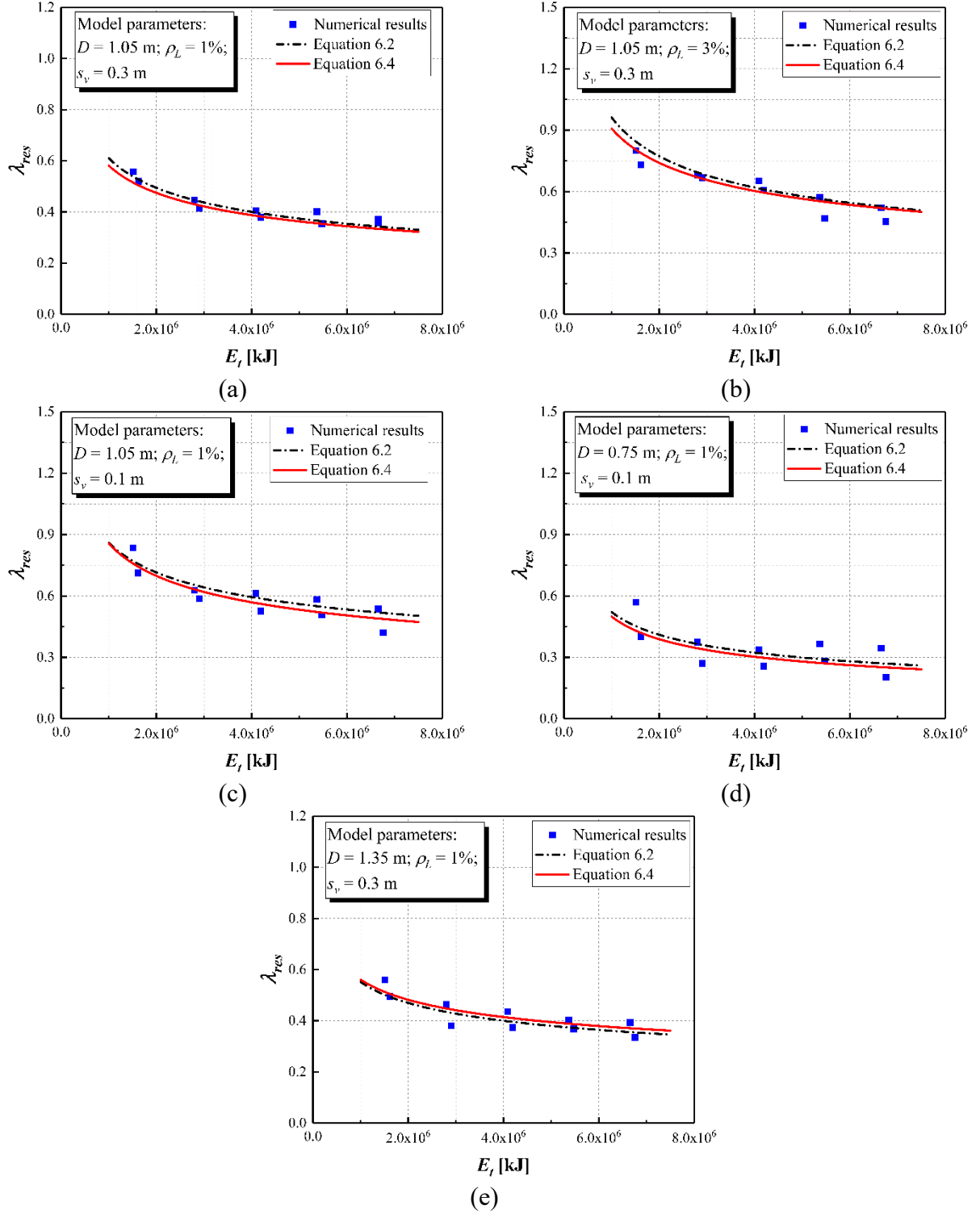


Figure 4.28 Comparison of empirical equation and numerical results

4.4 Conclusions

This chapter summarized parametric studies on isolated bridge columns subjected to combined vehicle collision and air blast. Results from this study helped determine the effects of specific design parameters on column performance and provide useful information on what parameters would provide the most benefit during design. The studies also helped assess the influence of some parameters that are, in many instances, fixed (e.g. column height). Results from the studies were also used to develop an empirical equation for determining the column residual axial capacity under the combined collision and blast. The analyses indicated that, for the isolated columns that were modeled and collision and blast loads that were imposed:

- (1) Increase in the column diameter, longitudinal reinforcement ratio, and shear reinforcement improved column resistance to collision and blast loads, irrespective of demand;
- (2) The influence of column height on column performance was largely insignificant when the collision and blast combination was applied near the column base studied in this research;
- (3) Increase in axial load imposed at the column top increased column bending capacity and shear strength and improved column resistance to collision and blast loads. A higher axial load would amplify column damage with the occurrence of plastic hinge in the collision region;
- (4) The final empirical equation, which was simplified from a more complex equation, was able to estimate column residual axial capacity for the combined collision and blast events. This equation will be used to predict the column damage intensity and

assist with development of effective performance-based design and evaluation presented in Chapter 5.

Chapter 5 Performance-based Design and Analysis Framework

5.1 Introduction

This chapter introduces a performance-based design and analysis framework for RC highway bridge columns subjected to combined vehicle collision and air blast. The framework was based on damage indices developed using residual axial load capacity of a damaged column relative to that column's undamaged ultimate axial capacity. Developed indices incorporated critical design parameters of a highway bridge column under the combined collision and blast. The indices were then utilized to estimate the column damage and corresponding performance. The developed performance-based framework allows new bridge columns to achieve the anticipated performance considering the importance of the highway bridge and project costs and helps assess the existing bridge columns performance under the combined collision and blast.

5.2 Principles of performance-based design

To address a vehicle collision with a bridge column, AASHTO-LFRD bridge design specification requires use of an equivalent static force (ESF) of 2670 kN to represent vehicle impact design load [2]. The current specification also states that the impact load should be placed 1.5 m above the ground in a direction from 0° to 15° with the edge of the pavement. This specification is based on prescriptive criteria that provides minimum standards for bridge safety. The design intent and the real performance of bridge column are not considered in the design process of the current specification. As a result, the performance of the bridge column using this criterion could exceed the minimum code requirements but may fail for some cases. Performance-based design provides a systematic approach for evaluating the performance capability of a structural component during extreme events. The objectives of performance-based design are to explicitly assess how the structural component is likely to perform under a potential

loading event, achieve desired standard of performance at a reduced cost, and determine the target performance based upon the specific needs of a project. This design methodology is developed by linking the performance level to the expected level of damage in the structural component for a given loading event. Each discretely defined performance level is related to the occurrence of specific levels of damage and the resulting losses at a specific level of loading in the form of causality, economic costs, and time out of service.

Performance-based design is well-established for the design of new or the improvement of existing buildings subjected to seismic hazards [43]. However, limited studies have been completed to investigate and evaluate performance-based design for highway bridges and very few for bridges subjected to vehicle collision or blast. Sharma et al. [18, 44] developed a framework for performance-based design and analysis of bridge columns subjected to vehicle impact. Performance levels were defined for a representative bridge column: fully operational with no damage, operational with damage, and total collapse of structure. These levels were calibrated against impact demand and resistance factors to obtain desired levels of performance when completing a design. Cao et al. [45] numerically investigated a performance-based design framework for bridge piers subjected to truck collisions using LS-DYNA. This study evaluated and categorized pier performance at three different levels as a function of shear distortion and plastic rotation along the pier: immediate use, damage control, and near collapse. Auyeung et al. [46] investigated structural response of bridge piers subjected to vehicle collisions and proposed a performance-based design methodology for bridge piers using a novel damage ratio index. Pier performance classifications included immediate serviceability, life safety, and collapse prevention and corresponded to minor, moderate, and severe damage states based on the proposed damage ratio index. Abdelkarim et al. parametrically evaluated reinforced concrete

bridge pier performance under vehicle collision and identified three performance levels based on a damage index. Shi et al. [47] numerically examined the performance of RC bridge columns subjected to blast loads and defined four damage states: low, medium, high, and collapse.

Given the lack of performance-based research considering combined vehicle collision and air blast, a study that developed a framework for bridge columns would be valuable to identify the acceptable level of performance at efficient costs based on intended utilization. Three fundamental elements are required to be considered, namely demand (D), capacity (C), and performance objectives for considered hazards. The approach could result in economical designs of new columns within needing to use detailed finite element models or create experimental data. For the current research, a key part of the process was development of a damage index based on residual and nominal axial capacities to quantitatively assess performance levels associated with different damage states.

5.3 Performance-based design framework

5.3.1 Demand-to-capacity calculation

Column demand was represented using total imparted energies from the combined collision and blast loads, while collision energy was determined from the vehicle kinetic energy and blast energy estimated using TNT-equivalency. Column capacity was represented using axial capacity to support bridge superstructure loads and calculated from AASHTO design specification equations. A demand-to-capacity (D/C) ratio was used to quantitatively estimate effects of the combined collision and blast on performance integrity [2, 45]. A higher demand-to-capacity ratio signifies a more severe situation.

5.3.2 *Performance objectives*

In the performance-based design methodology, the design starts from determining one or more performance objectives for the column in response to a specified collision and blast combination. For a combined collision and blast event, bridge column damage varied as a function of cross-sectional dimensions, reinforcement details, collision velocity, and blast intensity as presented in Chapter 3 and Chapter 4. Three different performance objectives (levels) were identified in accordance with three damage states: minor; moderate; and severe. Minor damage included minor concrete cover spalling or cracking and limited yielding of longitudinal reinforcements. As investigated in Chapter 3 and Chapter 4, the column was shown to experience less than 5% of concrete spalled and no longitudinal reinforcement buckled for this damage state. Moderate damage was defined as significant concrete spalling, minor concrete core cracking, and reinforcements exposing and buckling in the collision region. With moderate damage, the column sustained less than approximately 20% of concrete spalled and less than 30% of longitudinal reinforcement buckled. Severe damage constituted significant deterioration of concrete core and loss of the column axial load capacity. This damage state was assigned when at least 20% of concrete spalled and 30% of longitudinal reinforcement buckled. Figure 5.1 shows examples of damage state corresponding to each performance level under the combined collision and blast loads.

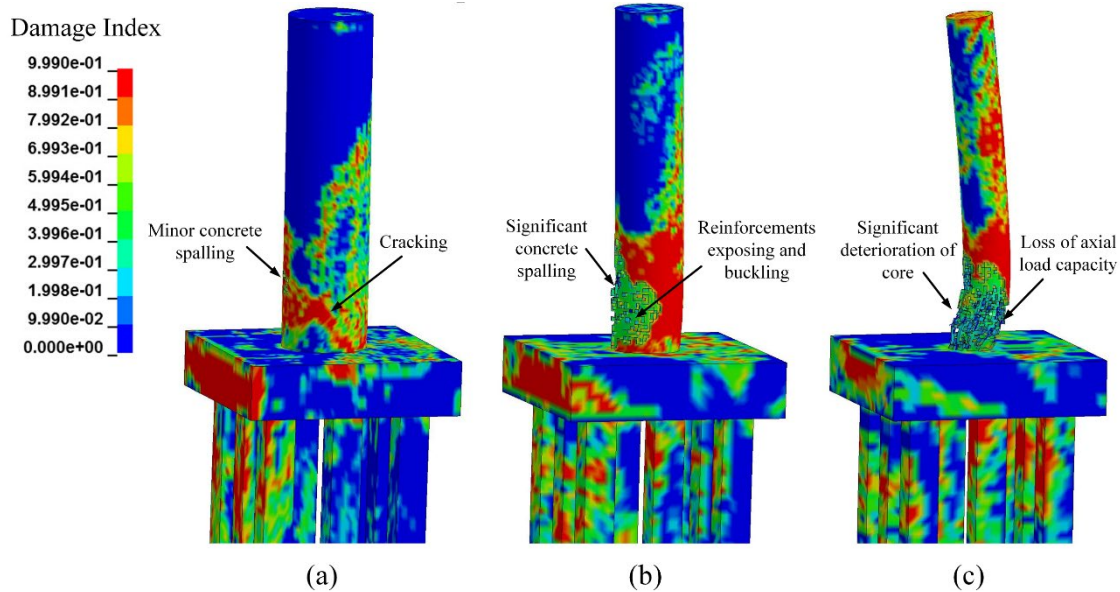


Figure 5.1 Damage state for each performance level: (a) minor damage; (b) moderate damage; (c) severe damage

Performance level associated with minor column damage was classified as immediate use and referenced as P1. The bridge column continued to perform acceptably with a minor reduction in capacity and less than 30% of column axial capacity compromised. The column could be repaired in situ to restore its capacity with no need to close the bridge. The performance level that corresponded to moderate damage state was classified as life prevention and referenced as P2. At this level of performance, the column still had limited residual axial capacity. It was assumed that collapse of the entire bridge would not occur but that bridge closure would be recommended for repair and partial replacement of structural components. In some cases, economical repairs may not restore necessary strength. The final performance level was near collapse (P3). The column was deemed unsafe with no residual axial capacity. The bridge was at high risk of collapse and should be immediately closed and partial or full replacement of primary components is needed. In some cases, the bridge may need to be replaced. Performance objectives and corresponding column damage states are listed in Table 5.1

5.3.3 Quantification of performance level

As stated earlier, a damage index was developed based on column nominal axial capacity and residual axial capacity after damage occurred from a combined vehicle collision and air blast as shown in Equation 5.1:

$$\xi_{DI} = 1 - \frac{P_{res}}{P_n} \quad (5.1)$$

where ξ_{DI} is the damage index, P_n is the nominal axial load capacity of bridge column, and P_{res} is the residual axial capacity after the combined collision-blast loads as determined from the equation:

$$\lambda_{res} = (124 - 71.5D + 1031\rho_L - 88s_v) E_t^{(-0.578+0.27D)} \quad (5.2)$$

This damage index provides a quantitative method for considering damage and assessing performance for bridge column subjected to combined collision and blast.

Figure 5.2 plots the damage index versus demand-to-capacity (D/C) ratio for bridge columns studied in Chapter 3 and Chapter 4. The appropriate range of the damage index for each performance objective could be determined by correlating observed column damage states with D/C ratios and calculated damage indices as shown in Figure 5.2. Table 5.1 lists performance levels associated with corresponding column damage states and indices for bridge columns using results from Chapter 5 and 6. Bridge columns that continued to perform at an operational condition with minor concrete spalling and longitudinal reinforcement yielding in the collision

region had damage indices between 0 and 0.3. Columns that require extensive repair to mitigate collapse from moderate damage caused by significant concrete spalling, minor core cracking, and reinforcement buckling had damage indices between 0.3 and 0.8. Columns whose damage requires immediate bridge closure for major repair due to significant concrete core crushing and loss of axial load capacity was assigned damage indices between 0.8 and 1.0. Table 5.2 lists a comparison between the calculated damage index and the observed damage state with the corresponding performance levels for several representative columns.

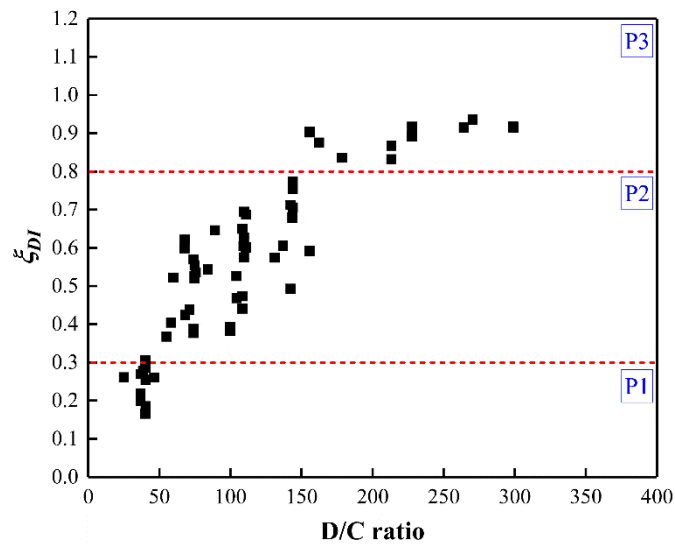


Figure 5.2 Damage index versus D/C ratio for bridge columns under combined collision and blast

Table 5.1 Performance-based design criteria under combined collision-blast cases

Performance level		Damage state	Damage description	ξ_{DI}
P1	Immediate use	Minor damage	Minor concrete cover spalling or cracking, minor yielding of longitudinal reinforcement	0~0.3
P2	Life prevention	Moderate damage	Significant concrete spalling, minor concrete core cracking, reinforcement buckling	0.3~0.8
P3	Near collapse	Severe damage	Significant deterioration of core concrete, loss of axial load capacity	0.8~1.0

Table 5.2 Evaluation of damage index and performance level for representative cases

D (mm)	ρ_L	s_v (mm)	ρ_{ALR}	v_0 (km/h)	Z (m/kg ^{1/3})	ξ_{DI}	Observed damage	Performance level
750	1%	300	6%	95	0.30	0.90	severe	P3
				120	0.25	0.92	severe	P3
1050				95	0.30	0.58	moderate	P2
				120	0.25	0.69	moderate	P2
1350				95	0.30	0.35	minor	Marginal
				120	0.25	0.62	moderate	P2
1050	2%	300	6%	95	0.30	0.44	moderate	P2
				120	0.25	0.48	moderate	P2
	3%			95	0.30	0.27	minor	P1
				120	0.25	0.38	moderate	P2
1050	1%	100	6%	95	0.30	0.29	minor	P1
				120	0.25	0.47	moderate	P2
		200		95	0.30	0.52	moderate	P2
				120	0.25	0.60	moderate	P2
1050	1%	300	0%	95	0.30	0.62	moderate	P2
				120	0.25	0.67	moderate	P2
			12%	95	0.30	0.78	moderate	P2
				120	0.25	0.71	moderate	P2

5.3.4 Design procedure

Criteria in Table 5.1 can be used to develop a performance-based design framework for bridge columns subjected to combined vehicle collision and air blast. The proposed design and

analysis procedure that follows was established to achieve a balance between an acceptable performance and economic design:

- (1) Select desired performance objectives for bridge column. Desired performance level is selected by the owners and designers based on the bridge functions, significance, and economical budget.
- (2) Define critical loading cases, including a vehicle collision at a specified velocity and an air blast with a TNT-equivalent mass. The vehicle velocity can be determined from highway speed limits for the states. The equivalent TNT weight was determined from FHMA estimated weights for structures subjected to terrorist attack as shown in Figure 5.3. The critical combined load cases are utilized to estimate the total imparted energy from the sum of the vehicle kinetic energy and blast energy.
- (3)

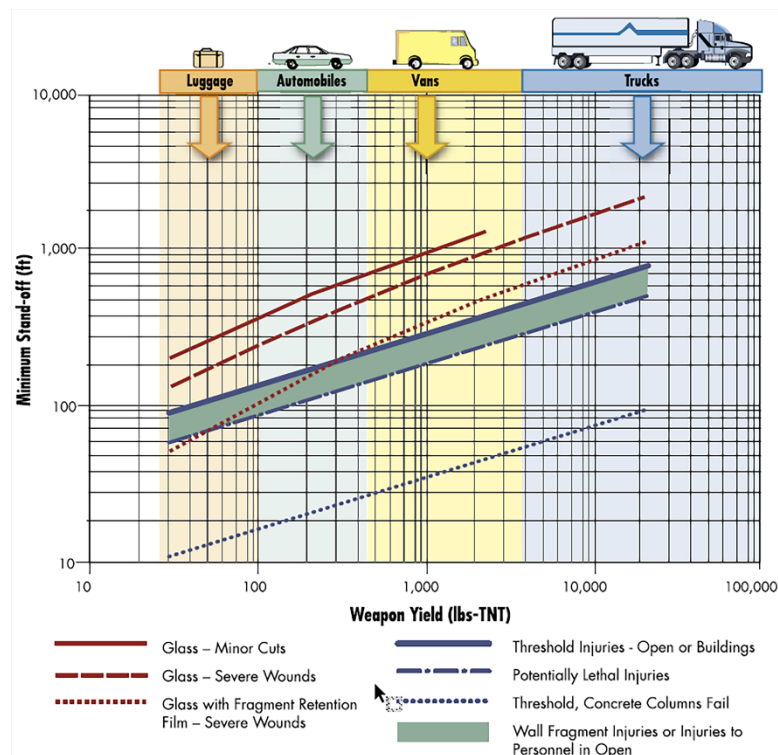


Figure 5.3. Blast damage threshold

- (4) Conduct a preliminary design following current codes and specifications when designing a new column. For analysis on an existing column, collect the column original design details.
- (5) Utilize the design nominal axial capacity determined from AASHTO design specification equations. Estimate the residual axial capacity with the preliminary design details for the new column or the original design details for the existing column and the total imparted energy using Equation 4.2. Calculate the damage index (ζ_{DI}) from these values using Equation 5.1.
- (6) Check if the estimated damage index corresponds to the desired damage state and associated performance level from Table 5.1. If not, go back to step (3) and re-design the column or update desired performance level when designing a new column. For analysis on the existing column, go to step (6) and take retrofitting strategies.
- (7) Develop improvement strategies. If the bridge column performance is identified to be beyond the target level, appropriate strategies should be taken to improve the column capacity under the combined impact and blast events.

Figure 5.4 graphically shows the process of a performance-based design and analysis for a bridge column subjected to combined collision and blast.

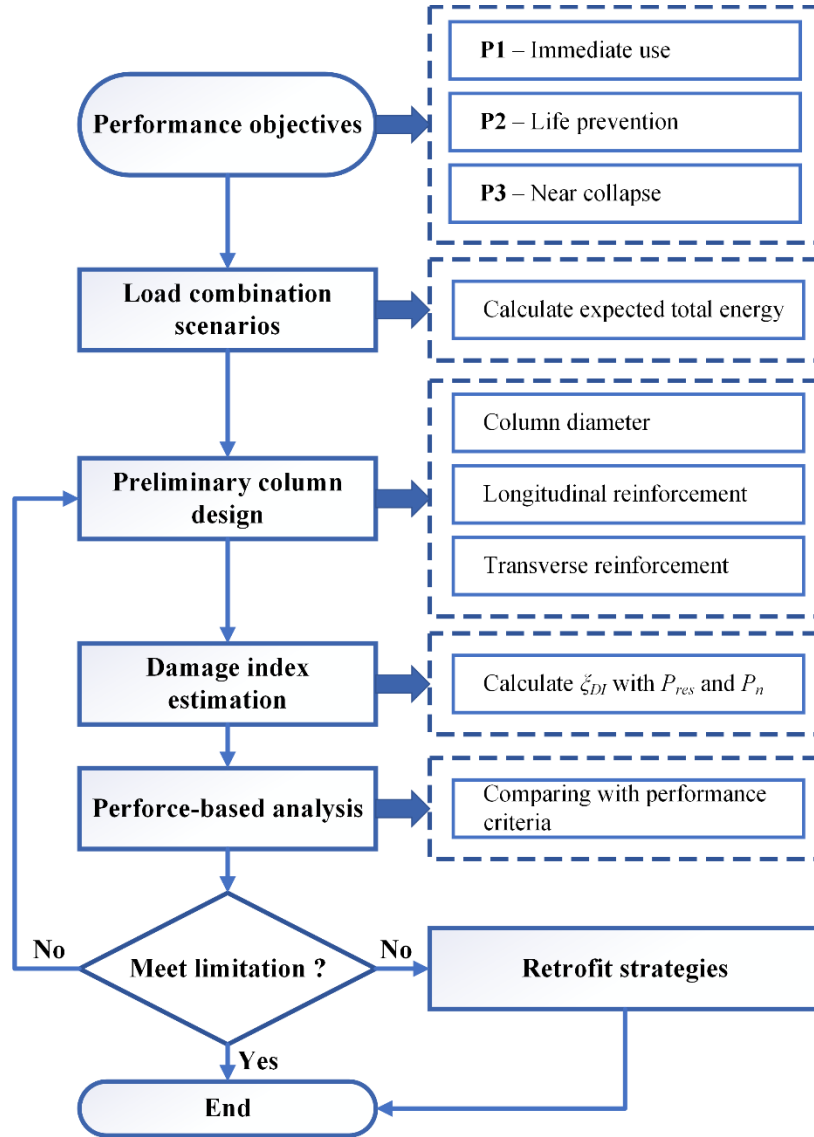


Figure 5.4 Performance-based design procedure for bridge column subjected to combined vehicle collision and air blast

5.4 Validation of design framework

The proposed performance-based design framework was evaluated by examining columns with different geometric properties from those used in Chapters 3 and 4. Table 5.3 lists examined properties, calculated damage index, and performance levels for studied cases.

According to the design process, the damage index for these validation cases was calculated to:

(1) $\zeta_{DI-VS-1} = 0.83$; (2) $\zeta_{DI-VS-2} = 0.61$; (3) $\zeta_{DI-VS-3} = 0.13$; (4) $\zeta_{DI-VS-4} = 0.53$; and (5) $\zeta_{DI-VS-5} = 0.2$,

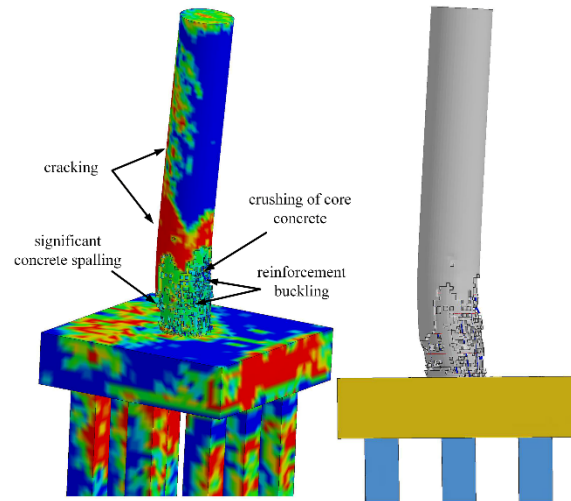
respectively. Based on the calculated damage index, column damage states in these validation cases were estimated to: (1) severe damage; (2) moderate damage; (3) minor damage; (4) moderate damage; and (5) minor damage, respectively.

Table 5.3 Validation studies for proposed performance-based criteria

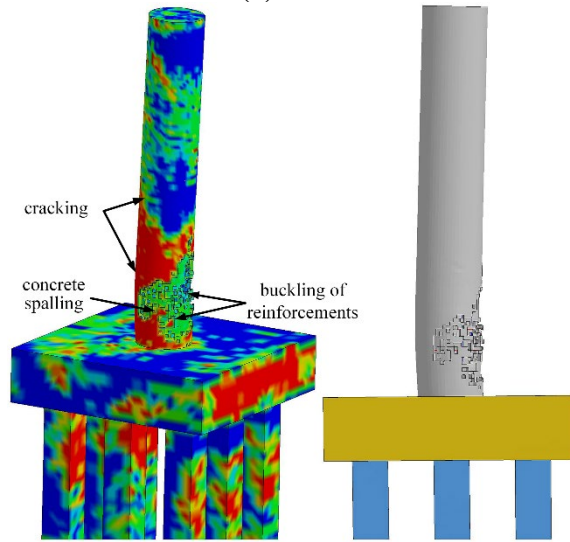
Case	D (mm)	ρ_L	s_v (mm)	v_0 (km/h)	Z (m/kg ^{1/3})	ξ_{DI}	Predicted damage	Performance level	γ_{bc}	γ_{br}	Observed damage
VS-1	900	1%	300	120	0.25	0.83	severe	P3	26%	54%	severe
VS-2	900	2%	300	95	0.25	0.61	moderate	P2	5.5%	15%	moderate
VS-3	900	3%	100	65	0.30	0.13	minor	P1	0	0	minor
VS-4	1200	1%	300	95	0.20	0.53	moderate	P2	4.2%	8%	moderate
VS-4	1200	1%	300	95	0.30	0.20	minor	P1	1.3%	0	minor

After damage indices and performance levels were determined using Equation 5.1 and Table 5.1, each column's response to the specified collision and blast demands was modeled using LS-DYNA. Results from the analyses were used to calibrate the predicted damage using the proposed design framework with the modeled damage and ensure the applicability of the developed design framework. Figure 5.5 presents the final modeled damage states. For VS-1 case, this column failed with concrete core crushing and approximately 54% of longitudinal reinforcements buckled at the column base. For VS-2 case, this column sustained 6% of concrete spalled and 15% of longitudinal reinforcements buckled in the collision region, thus resulting in moderate damage. For VS-3 case, the column experienced minor damage with no concrete spalled and no reinforcement buckled. For VS-4 case, the 1200 mm diameter column exhibited significant concrete spalling and approximately 8% of longitudinal reinforcement buckled in the collision region. This column was observed to have had limited residual axial capacity with moderate damage. For VS-5 case, this column was shown to perform in operation with minor concrete spalling.

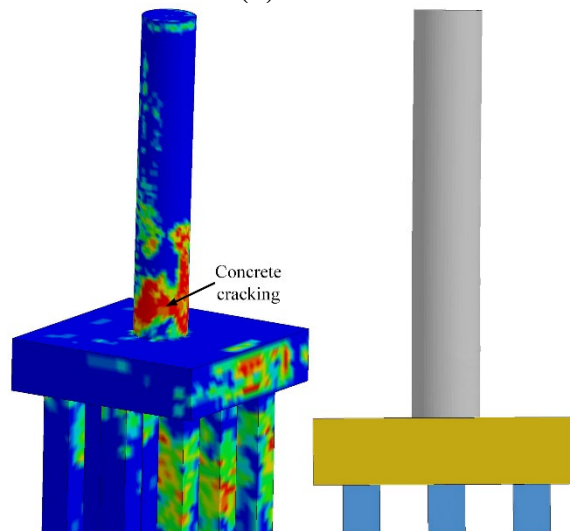
Overall, the column damage obtained from the numerical simulations were consistent with the predicted damaged based on the damage index and performance-based criteria. The validation cases demonstrated the ability of the damage index to estimate the damage intensity of the bridge column and evaluate column performance under the combined collision and blast. The performance-based design framework could reasonably achieve the desired column performance objectives. The round RC bridge column was involved in this study to develop the performance-based design framework. Further research studies should be conducted to consider the column configurations to extend the application of this framework for different types of bridge columns.



(a) VS-1



(b) VS-2



(c) VS-3

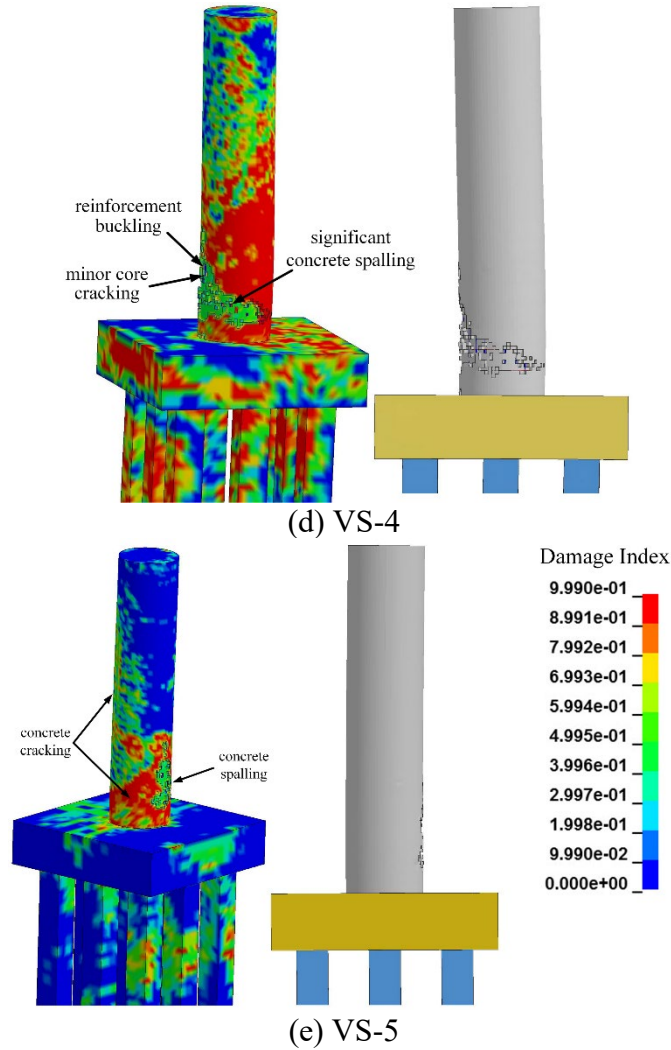


Figure 5.5 Observed column damage for validation cases

5.5 Conclusions

This chapter develops a performance-based design and analysis framework for RC highway bridge columns subjected to combined collision and blast. This performance-based design and analysis framework provided an efficient design approach considering column properties and demands from vehicle collisions and air blasts. Results from the studies indicated that:

- (1) Column performance level classifications included immediate use, life prevention, and near collapse and corresponded to minor, moderate, and severe states for the

combined collision and blast events. A damage index in terms of residual axial capacity and column nominal axial capacity was used to quantitatively estimate and evaluate damage states. Study results demonstrated that this damage index provided a useful measurement to assess column damage for a specified impact and blast combination.

- (2) A performance-based design and analysis framework was developed for RC highway bridge columns when subjected to combined vehicle collision and air blast, which gives a straightforward approach to achieve a balance of economic design and desired performance objectives. A validation study was conducted to identify the feasibility of the proposed performance-based criteria for the round RC bridge column under the combined collision and blast events.

Chapter 6 Investigation of In-Situ Retrofit Schemes

6.1 Introduction

This chapter investigates and compares the effectiveness of using fiber reinforced polymer (FRP) or polyurea coating schemes to improve performance of RC bridge columns subjected to collision and blast. The isolated LS-DYNA bridge column model used in previous chapters was implemented herein and strengthening using either FRP wrap or polyurea coating were examined. Strengthened and bare column response to various collision and blast demands was compared to assess effectiveness. Parametric studies were then conducted to identify optimal strengthening schemes.

6.2 Numerical modeling of strengthened bridge column

Column design and modeling schemes matched those described in previous chapters. Modeling details for the FRP wrap and polyurea coating are provided in the following sections.

6.2.1 FRP

The FRP was modeled using four-node, quadrilateral, shell elements utilizing the *Belytschko-Tsay* formulation. Shell element was selected to achieve a balance between minimal computation expenses and accurate numerical results. Element properties were simulated using LS-DYNA's *Part Composite* to reduce the modeling efforts and simulate layers in FRP composite [48, 49]. This command provides a simplified method of defining a composite material model that eliminates the need for user defined integration rules and properties for each composite layer. The *Mat Enhanced Composite Damage* (MAT_054) material model was utilized to simulate dynamic behavior based on previous research studies [50-52]. The nonlinear material model incorporates post-stress degradation and accounts for fiber and matrix failure in tension and compression. Failure between plies is represented using Chang-Chang failure

criteria. Carbon fibers were selected with properties taken from the literature [53-55] and are listed in Table 6.1, where: ρ_{FRP} is FRP mass density, E_a is longitudinal modulus, E_b is transverse modulus, G_{ab} is the in-plane shear modulus, G_{bc} is the out-of-plane shear modulus, ν_{ab} is the Poisson's ratio, X_T is the longitudinal tensile strength, X_C is the longitudinal compressive strength, Y_T is the transverse tensile strength, Y_C is the transverse compressive strength, S_{LT} is the in-plane shear strength, ε_t is the ultimate tensile strain, and ε_c is the ultimate compressive strain. Research studies [54, 56, 57] have indicated that strain rate has minimal effect on FRP performance compared to concrete and steel, therefore rate effects were not considered.

Table 6.1 Material properties of CFRP composite

FRP	Parameter	ρ_{FRP} (kg/m ³)	E_a (GPa)	E_b (GPa)	G_{ab} (GPa)	G_{bc} (GPa)
	Value	1512	118	5.5	4.8	4.8
	Parameter	ν_{ab}	X_T (MPa)	X_C (MPa)	Y_T (MPa)	Y_C (MPa)
	Value	0.0127	712.9	1095	26.4	84.4
	Parameter	S_{LT} (MPa)	ε_t	ε_c		
	Value	84.3	2.3%	1.4%		

Interaction between the FRP wrap and bridge column was modeled assuming epoxy would be used as the bonding agent. In the real application, the epoxy is commonly used to bond the FRP and structural component. As a result, adhesive contact was assumed and represented using the *Automatic Surface to Surface Tiebreak* command [51, 54, 57]. Adhesive failure occurred between the FRP and column if the failure criterion expressed in Equation 6.1 was exceeded:

$$\left(\frac{|\sigma_n|}{NFLS} \right)^2 + \left(\frac{|\sigma_s|}{SFLS} \right)^2 \geq 1 \quad (6.1)$$

where σ_n and σ_s are the interface normal and shear stresses; and $NFLS$ and $SFLS$ are failure tensile and shear stresses. Epoxy adhesive properties were adopted from previous studies with $NFLS_{FRP}$ taken as 32 MPa and $SFLS_{FRP}$ as 29.4 MPa [50, 51, 58].

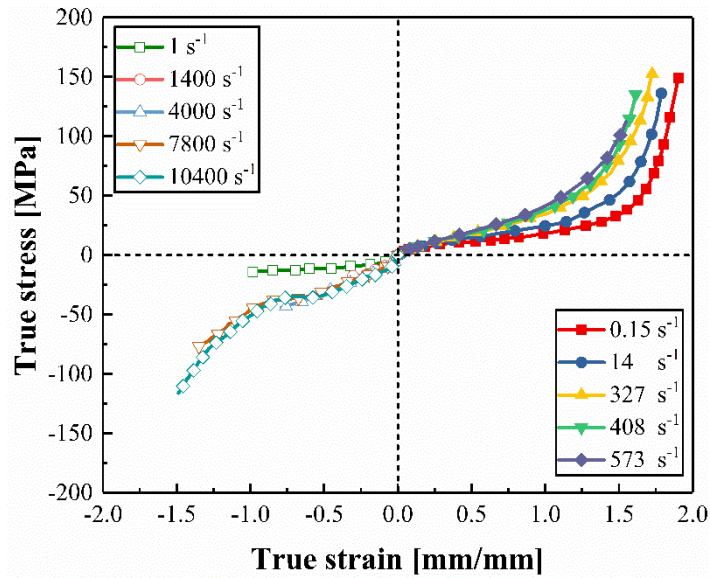
6.2.2 Polyurea

The polyurea was modeled using four-node, quadrilateral, shell element that also utilized the Belytschko-Tsay formulation. The LS-DYNA's *MAT Modified Piecewise Linear Plasticity* (MAT_123) material model was utilized to simulate polyurea behavior [59-62]. This nonlinear material model accounts for strain rate effects and the enhanced failure criteria with user-defined stress-strain curves. Failure criteria are based on effective plastic strain, plastic thinning, and major principles in plane strain for the shell elements. Polyurea properties were taken from a series of high strain rate tensile and compressive tests completed by Roland et al. [63] and are listed in Table 6.2. Figure 6.1 shows the stress-strain curves for the polyurea used to generate their stress-strain behaviors for different strain rates.

Contact between the polyurea and concrete was also modeled using the *Automatic Surface to Surface Tiebreak* command with failure assumed to occur when polyurea tensile and shear strength limits were exceeded. Tensile and shear limits were obtained from pull-out tests completed by Dinan et al. [64], with $NFLS_{POL}$ set to 1.04 MPa and $SFLS_{POL}$ equaling 6.90 MPa.

Table 6.2 Polyurea material properties

Material	Parameters	Values
Polyurea	Mass density	1442 kg/m ³
	Elasticity modulus	2520 MPa
	Poisson's ratio	0.465
	Yield stress	10 MPa

**Figure 6.1** Stress-strain curves for polyurea at different strain rates

6.2.3 Model development

Segment-based contact was used to simulate interactions between the SUT and the FRP wrap or polyurea coating and the exposed concrete. Contact was simulated using LS-DYNA's *Contact Automatic Surface to Surface* command, with similar friction coefficients to those selected for analyses discussed in previous chapters. A penalty-based coupling was employed to model the interactions between the blast wave and FRP/polyurea coating by setting CTYPE=4, which incorporates erosions for the Lagrange entities developed by the shell element using LS-DYNA's *Constrained Lagrange In Solid* command [11, 65]. Loads were applied in similar fashion to

analyses completed in previous chapters. Similar boundary conditions for the modeled air domain and soil volume were also selected.

6.2.4 Model validation

Experimental investigations examining response of FRP wrapped bridge columns under combined collision and blast loads were not located in the open literature. As a result, validation of selected modeling techniques involved comparing predictions against results from two separate experimental studies of FRP wrapped RC structural components subjected to impact and blast.

6.2.4.1 FRP wrapped column under impact load

A pendulum impact test of reduced-scale, FRP-strengthened RC bridge pier column was performed by Sha et al. [57]. An impact rig with a mass of 60 kg and a pendulum arm of 2850 mm impacted the column 570 mm above the ground as shown in Figure 6.2. The pendulum swing angle increased in 5° increments until the column failed. The column consisted of a circular section with a diameter of 78 mm and a height of 700 mm. It was reinforced with eight 2 mm diameter steel bars and 1 mm diameter hoops spaced at 12.5 mm. The concrete compressive strength was 28.3 MPa and the reinforcement yield strength was 550 MPa. FRP with a thickness of 0.13 mm was wrapped around the pier and bonded using epoxy. The tensile strength of the FRP composite was 3500 MPa and its modulus was 230 GPa. A block having a mass of 173.6 kg was placed on top of the column to simulate superstructure dead load. Additional details on the test can be found elsewhere [57].

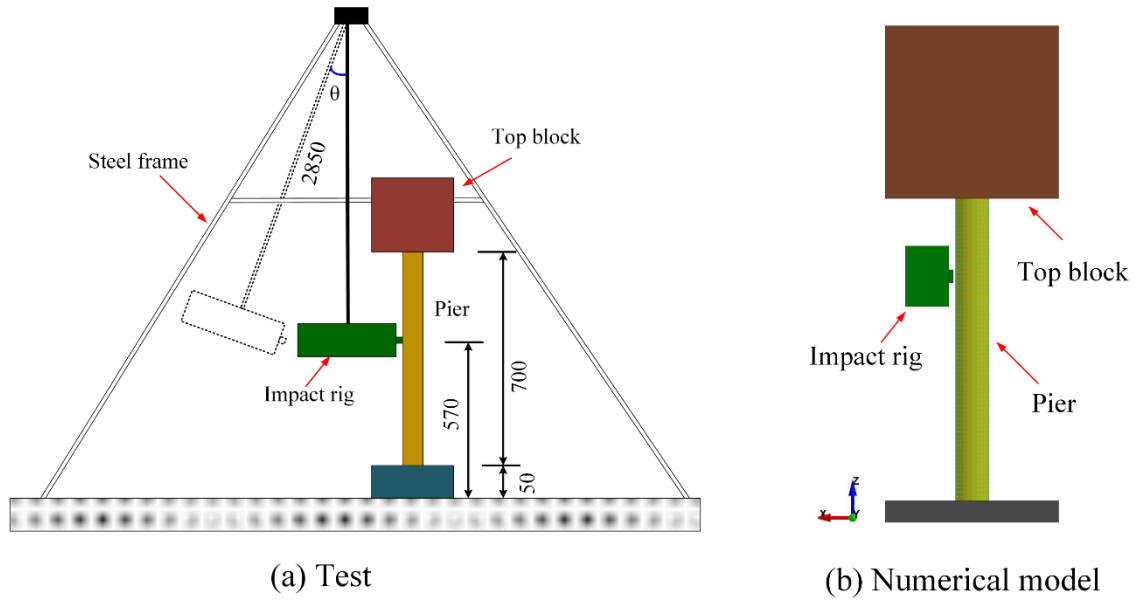


Figure 6.2 Pendulum impact test setup and numerical model (mm) [57]

A numerical model was developed following modeling procedures discussed in earlier chapters and in Section 6.2. The impactor was simulated as a rigid volume using LS-DYNA's *Mat Rigid* and contact between impactor and FRP strengthened column was defined using the *Contact Automatic Surface To Surface* command. The block at the top of the column was modeled as a rigid mass using the *MAT Rigid* command. Successive impacts were modeled in LS-DYNA using restart commands. Figure 6.3 compares experimental and simulated column damage at the completion of the tests when the column experienced direct shear failure at its top and base. The failure occurred at a swing angle of 20° . As shown in Figure 6.3, qualitatively modeled damage matched experimental results well.

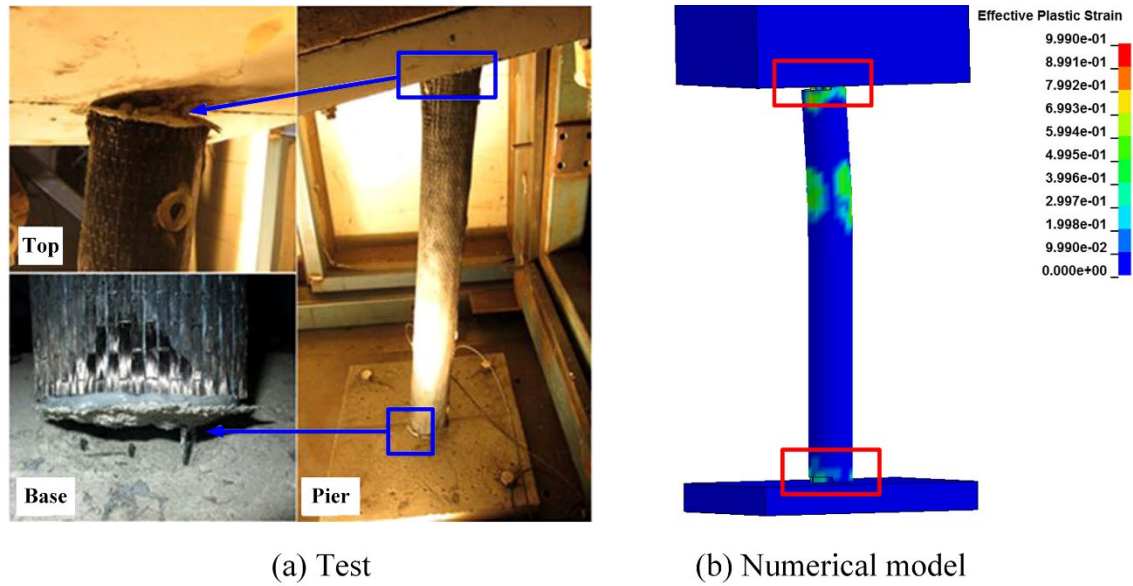
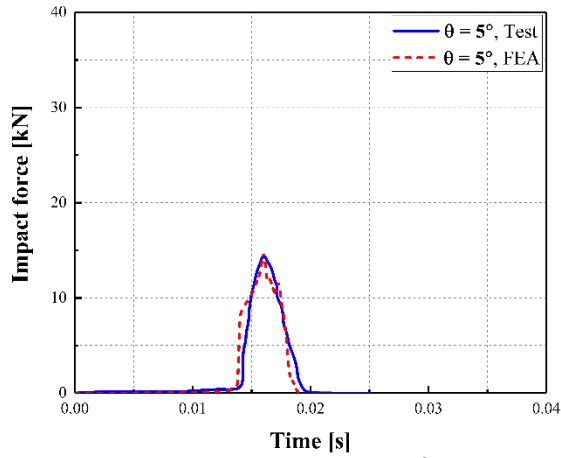
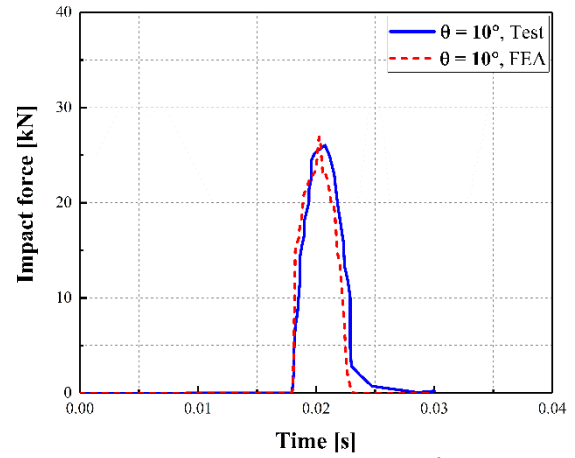


Figure 6.3 FRP-coated pier experimental [57] and modeled failure mode

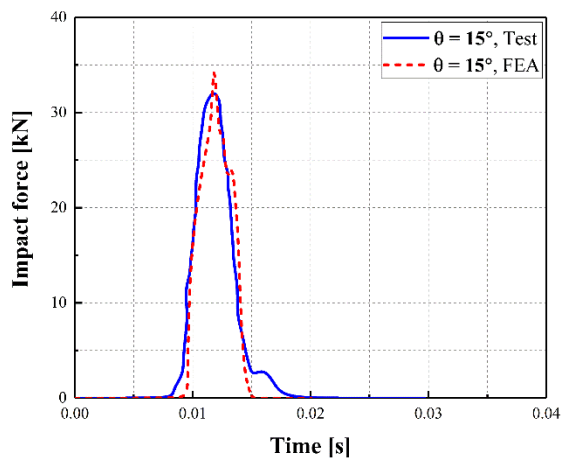
Comparisons between impact loads and steel reinforcement strains 75 mm from the base plate are shown in Figure 6.4 and Figure 6.5, respectively. Simulated loads and strains largely matched experimental results well, with simulated strains being, on average, 10 percent less than recorded values. Initial peak strains were in good agreement while post-impact strains were generally not in good agreement. Given that initial peak values are often of interest from a performance perspective, results were deemed acceptable for the current study.



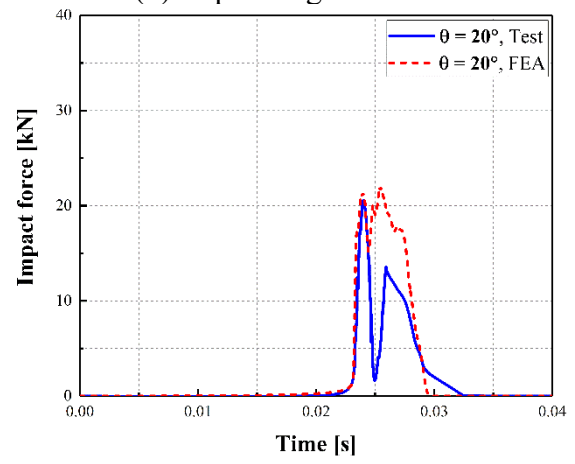
(a) Impact angle $\theta = 5^\circ$



(b) Impact angle $\theta = 10^\circ$



(c) Impact angle $\theta = 15^\circ$



(b) Impact angle $\theta = 20^\circ$

Figure 6.4 Numerical and experimental impact force time histories curves [57]

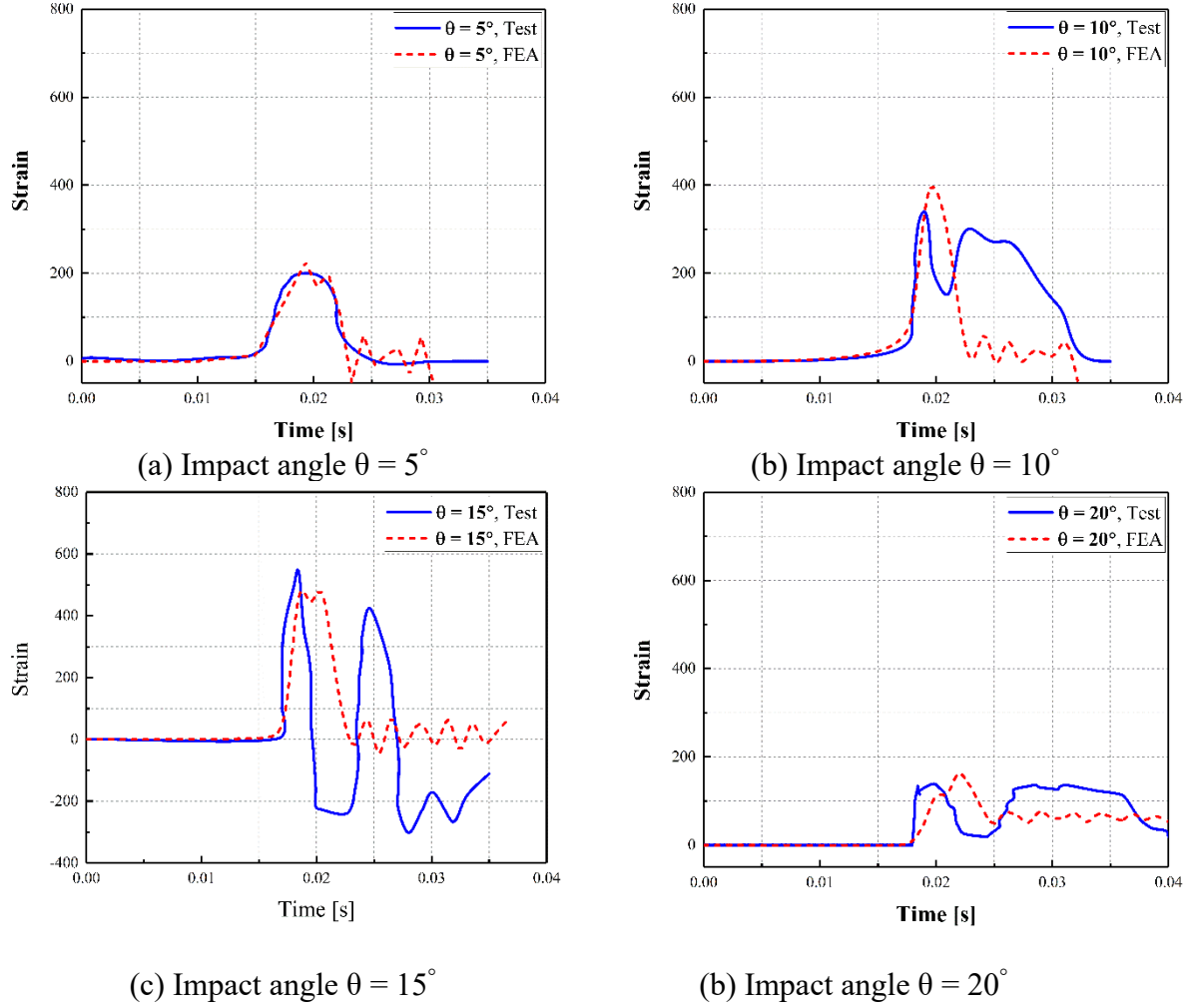


Figure 6.5 Numerical and experimental strain time histories curves [57]

6.2.4.2 FRP-wrapped slab under blast

Validation of models examining blast performance of concrete strengthened with FRP wrap used results from a test that investigated blast-resistance of an FRP-strengthened slab by Razaqpur et al. [66]. Slabs having dimensions of $1000 \text{ mm} \times 1000 \text{ mm} \times 70 \text{ mm}$, as shown in Figure 6.6, were subjected to blast load from 27.4 kg TNT at a 3000 mm standoff distance. The slab was reinforced with top and bottom steel meshes spaced 152 mm in each direction. The concrete compressive strength was 42 MPa and reinforcement yield strength was 480 MPa. Two laminates of glass fiber reinforced polymer (GFRP) were attached to both faces of the slab as

shown in Figure 6.6. Each GFRP laminate was 500 mm wide and 1.3 mm thick. The GFRP tensile strength was 580 MPa and its elastic modulus was 27.5 GPa. The tensile strength of epoxy used to bond the GFRP to the slab was 54 MPa. Additional details of the test are provided elsewhere [66].

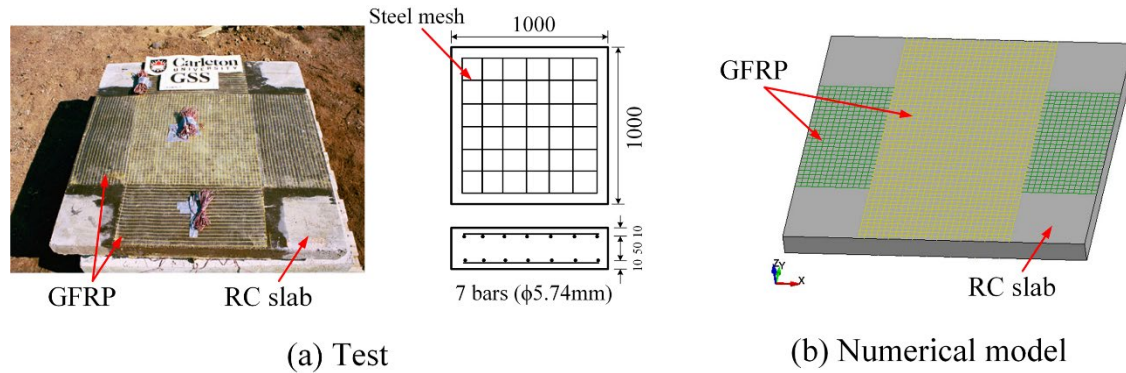


Figure 6.6 Blast test and numerical model (mm) [66]

The slab model was constructed following previously outlined procedures. The GFRP laminate was simulated using shell elements. GFRP was bonded to the concrete using the *Automatic Surface to Surface Tiebreak* with failure criteria determined using the experimental epoxy properties. The resulting numerical model is shown in Figure 6.6. To represent test restraints, translations and rotations were constrained along all four sides of the slab. Figure 6.7 compared tested and simulated pressure time histories, with good agreement being shown. Figure 6.8 compares displacement time-histories at the center of the slab, with predictions agreeing well with measured values. Peak central displacements were approximately 10 percent lower than experimental values and there was a minor phase shift. In similar fashion to the collision validation study, agreement was not as good after peak response occurred.

However, since first peak response is of higher interest, the model was determined to adequately predict an FRP strengthened blast and impact behavior.

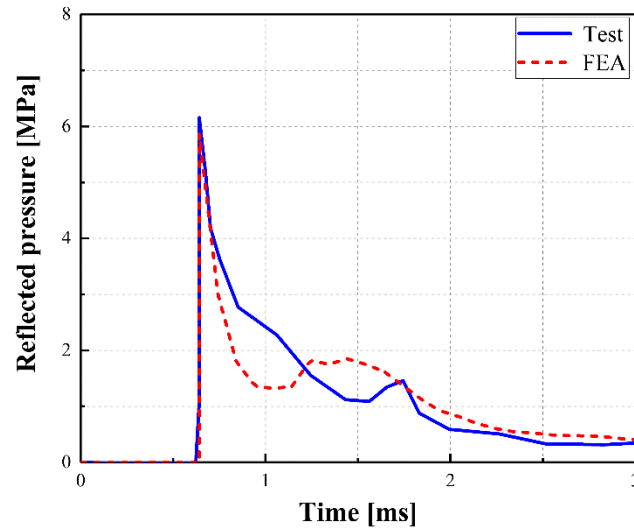


Figure 6.7 Pressure time histories [66]

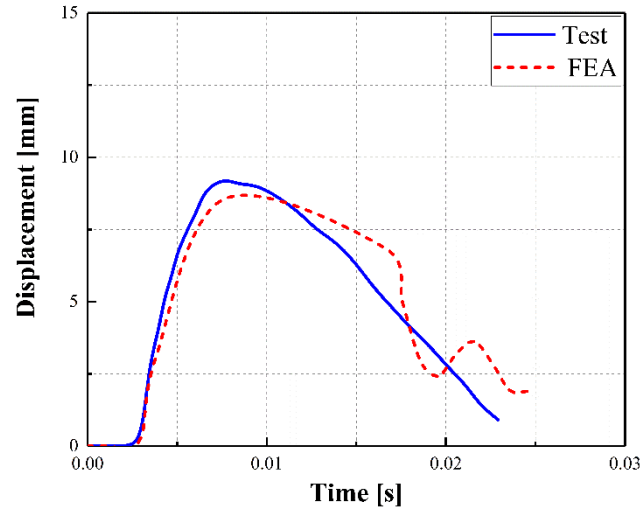


Figure 6.8 Displacement time histories [66]

6.3 Numerical studies

6.3.1 Studied column

The 750 mm diameter column examined in previous chapters was selected for the retrofit study. The studied column was longitudinally reinforced with no. 25 bars (a 1% longitudinal

reinforcement ratio) and no. 10 transverse bars at a space of 300 mm. The CFRP wrap and polyurea coating were placed along the entire height of the column. The CFRP thickness was 3 mm and the polyurea thickness was 9 mm. Thicknesses were selected from the literature and preliminary computational trials. Preliminary computational trials compared axial capacities of CFRP wrapped and polyurea coated columns to identify which polyurea thickness produced a similar axial capacity to using 3 mm of CFRP. A polyurea thickness of 9 mm was selected. Figure 6.9 provides details on the column and wrap or coating. Strengthened columns were subjected to similar SUT collision speeds and scaled distances as in previous chapters.

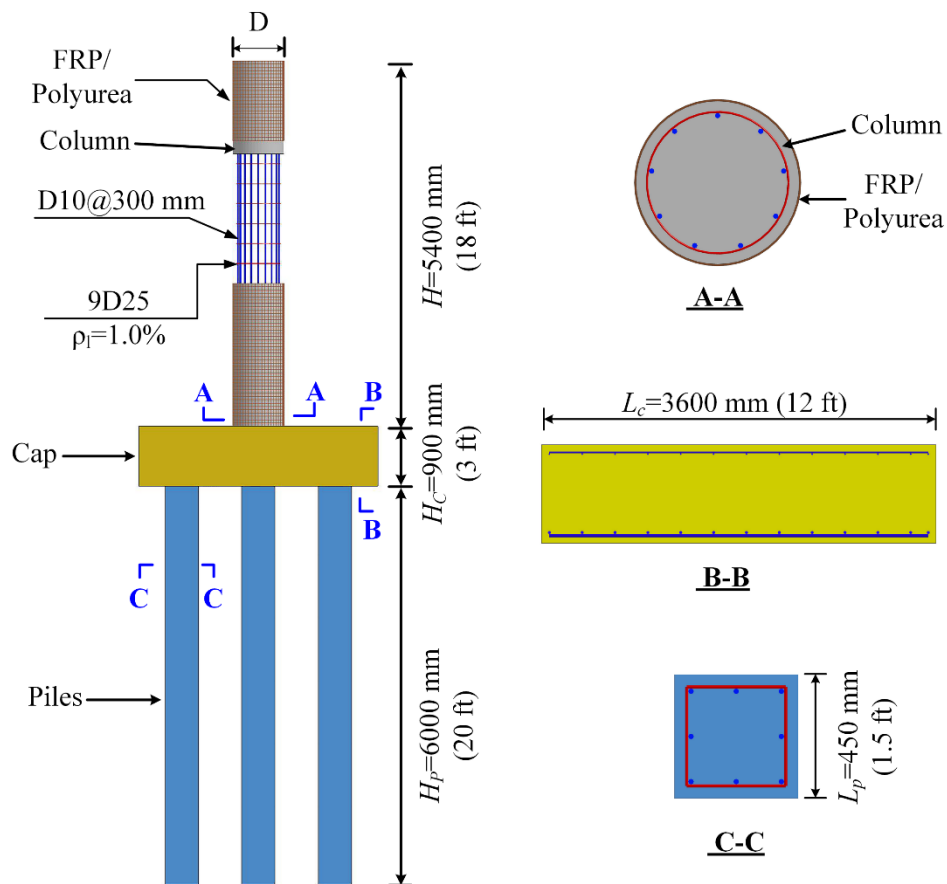


Figure 6.9 Geometries and reinforcement details in bridge column with a coating

6.3.2 Simulations of CFRP-wrapped bridge column

6.3.2.1 Collision velocity

Figure 6.10 compared column damage for bare and CFRP-wrapped bridge columns for varying collision velocities. As shown in Figure 6.10, the amount of eroded concrete and buckled longitudinal reinforcement in the cross-section reduced with the use of CFRP. The column performance was significantly improved. For the case with $v_0 = 65$ km/h, Figure 6.10 (a) indicates that M2 and M3 occurred at the base of bare column and the column could remain in operation with extensive repairs. Figure 6.10 (b) shows that the FRP-wrapped column sustained only M2 at its base, indicating less significant damage and the ability to sustain operations. For the case with $v_0 = 95$ km/h, M2, M4, and M5 were observed for the bare column, with shear failure occurring at the base. The CFRP-wrapped column sustained M2 with exposed reinforcement, indicating it could remain in operation. As shown in Figure 6.10, for the case with $v_0 = 95$ km/h, M2, M5, and M6 were observed and bare column failed due to loss of approximately 50% of concrete at the base. The CFRP-wrapped column sustained M2 and M3 at its base, indicating that it could continue in operation if repairs were completed.

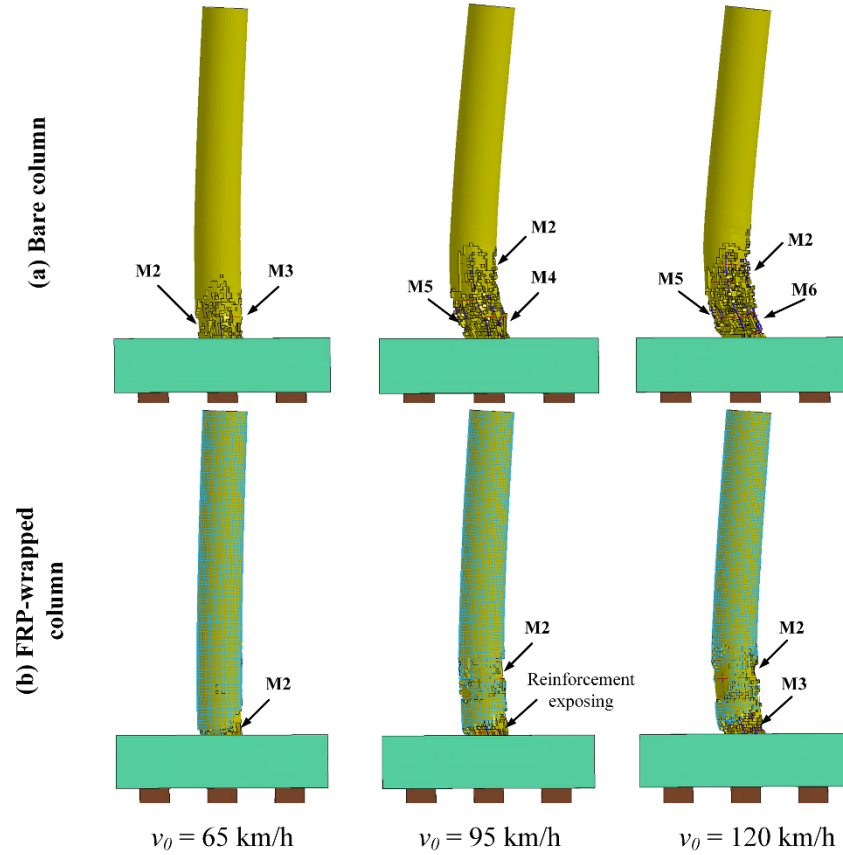
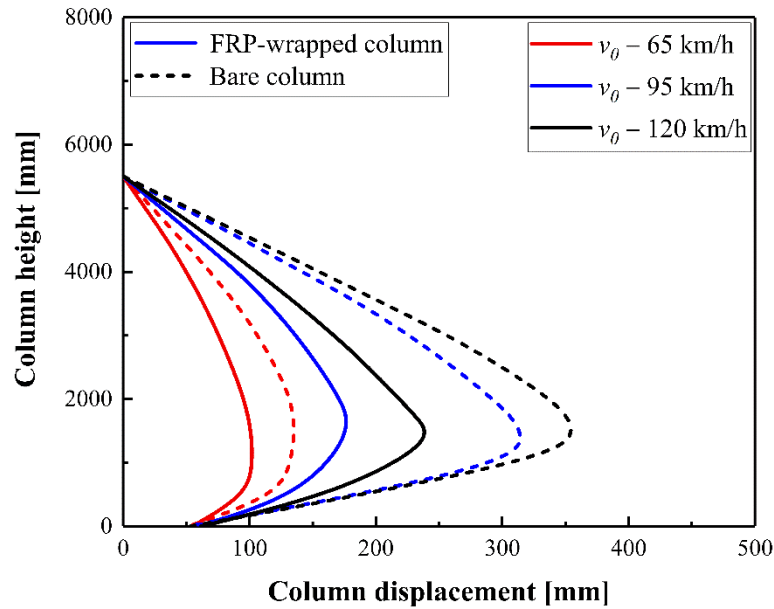


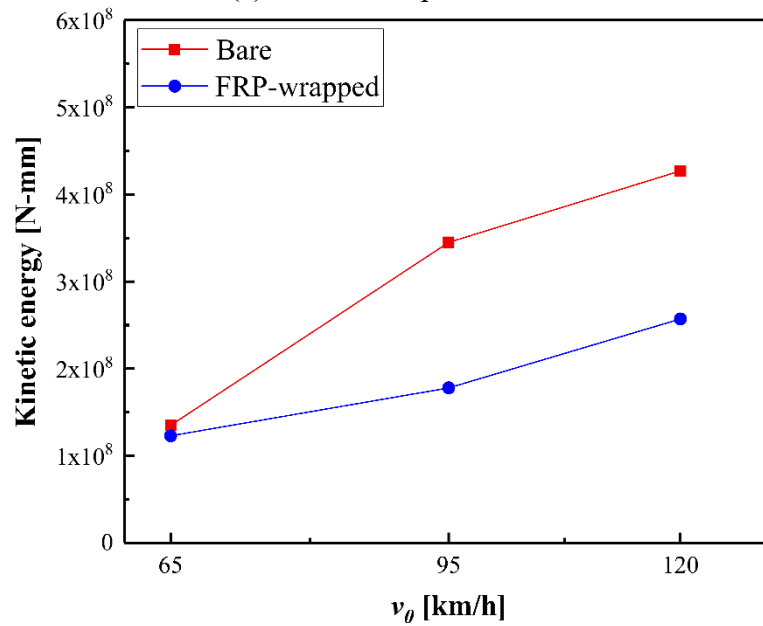
Figure 6.10 Comparison of final damage states, bare and CFRP-wrapped columns

Figure 6.11 compares final displacements along the column height and induced maximum kinetic energy. The column kinetic energy was obtained by using LS-DYNA DATABASE_MATSUM command and used to evaluate the effectiveness of the retrofit scheme to dissipate energy. These figures indicate that the CFRP-wrapped column displacements reduced approximately 55% less than the bare column, and the kinetic energy of the CFRP-wrapped column were approximately 30% lower than that experienced by the bar column. Figure 6.12 illustrates residual axial capacities and damage indices for bare and CFRP-wrapped bridge column for varying velocities. Residual axial capacity increased by about 70% due to the existence of the FRP coating and damage indices were reduced considerably. CFRP wrapped column performance improvements were more pronounced for $v_0 = 95$ km/h and 120 km/h

compared to $v_0 = 65$ km/h. At $v_0 = 95$ km/h and 120 km/h, CFRP wrap effectively mitigated collision effects and significantly reduced localized concrete erosion in the collision region prior to the occurrence of air blast which deteriorated the collision-related damage.



(a) Column displacement



(b) Column kinetic energy

Figure 6.11 Comparison of column displacement, bare and CFRP-wrapped columns

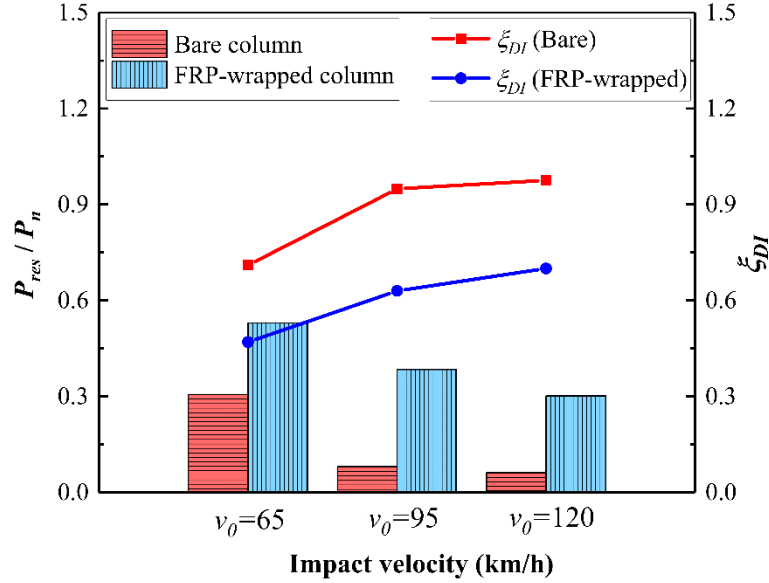


Figure 6.12 Comparison of residual axial capacity and damage indices, bare and CFRP-wrapped columns

6.3.2.2 Scaled distance

Numerical simulations were conducted that examined response to an SUT collision at 65 km/h and air blasts having $Z = 0.20 \text{ m/kg}^{1/3}$, $0.25 \text{ m/kg}^{1/3}$, and $0.30 \text{ m/kg}^{1/3}$. Figure 6.13 compares final damage states for bare and CFRP-wrapped columns at these scaled distances. In similar fashion to changes in collision velocity, the CFRP wrap significantly improved column performance when scaled distance changed. For the case with $Z = 0.30 \text{ m/kg}^{1/3}$, M2 was observed at the base of the bare column with exposed longitudinal reinforcement, and the column remained in operation if repairs occurred. The CFRP-wrapped column sustained minor spalling at its base, indicating less damage and the ability to perform in operation with no repairs. For the case $Z = 0.25 \text{ m/kg}^{1/3}$, the bare column sustained M2 and M3 at the base, could remain in operation, and required extensive repairs. The CFRP-wrapped column experienced M2 at its base and could remain operational. For the case with $Z = 0.20 \text{ m/kg}^{1/3}$, M2 and M3 were observed for

both the bare column and CFRP-wrapped column, with the CFRP-wrapped column having less volume of spalled concrete. These columns remained in operation and required extensive repair.

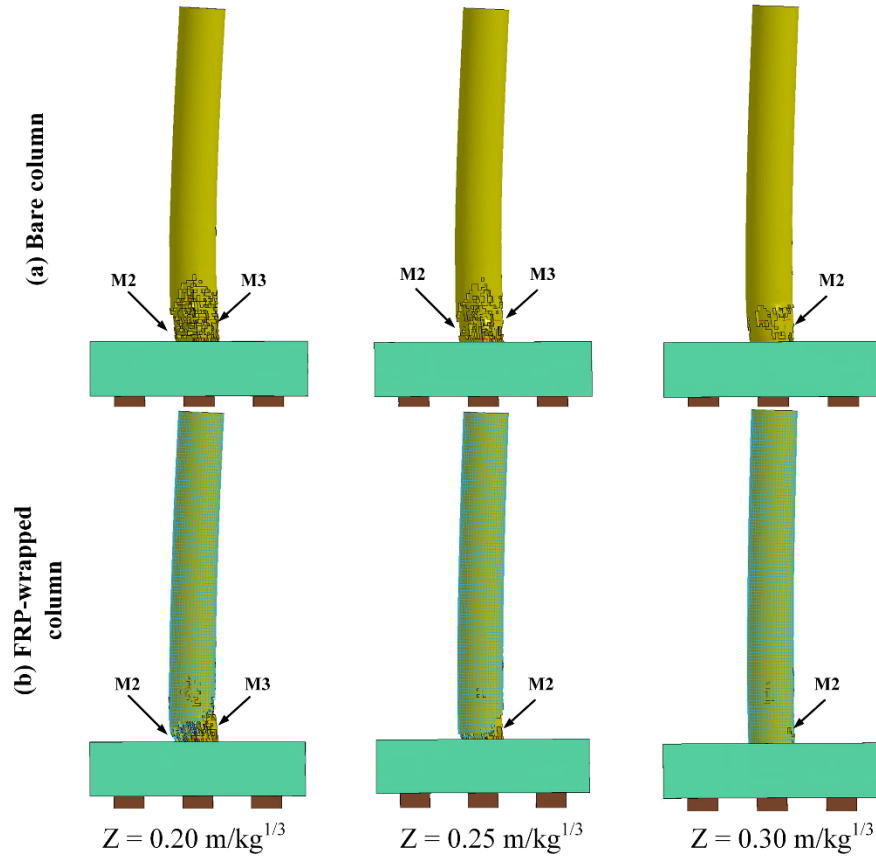
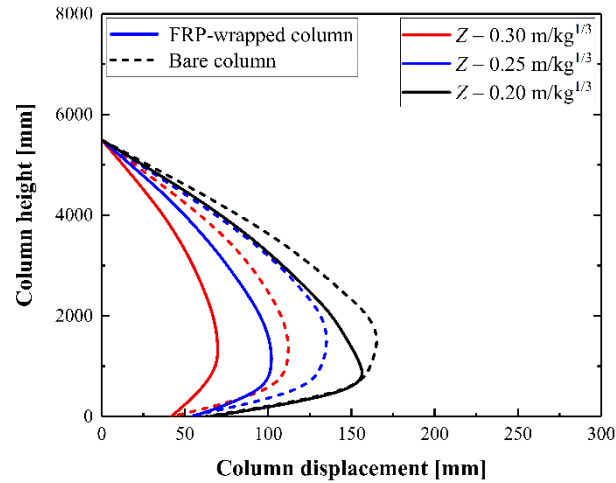


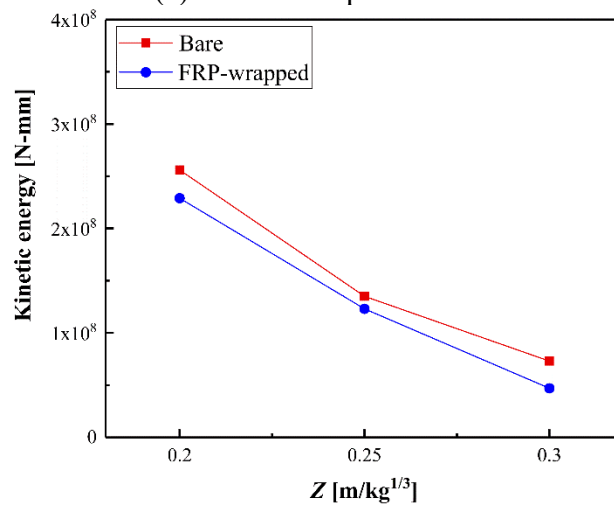
Figure 6.13 Comparison of final damage states, bare and CFRP-wrapped columns

Figure 6.14 compares final displacements along the column height and induced maximum kinetic energy. The figures indicate that the amount of CFRP-coated column deflections were reduced and were approximately 22% less than those for the bare column, and the CFRP-coated column possessed approximately 10% less kinetic energy than the bare column for varying scaled distances. It was noted that, for the case $v_0 = 65$ km/h and $Z = 0.20$ m/kg^{1/3}, both bare and CFRP-wrapped columns experienced similar maximum displacement in the collision region. The CFRP composite wrapped through the column resulted in the increased

column lateral stiffness, therefore increasing the shear force at the base and producing significant column deflection.



(a) Column displacement



(b) Column kinetic energy

Figure 6.14 Comparison of column deflection and kinetic energy, bare and CFRP-wrapped columns

Figure 6.15 illustrates residual axial capacities and damage indices for bare and CFRP-wrapped bridge columns for varying scaled distances. Residual axial capacity increased by about 65% with the use of the CFRP wrap. As a result, damage indices were reduced considerably and performance improved. It was noted that, in certain cases, the column retrofitted by the CFRP

composite would experience extensive damage at the base due to the increased base shear force as shown in Figure 6.14 and Figure 6.15. The CFRP coating should be extended to cover the footing top and provide additional shear resistance at the column base.

Studies of the effect of CFRP wrap on concrete bridge column performance indicated that:

- As expected, column performance generally improved to remain in operation;
- Performance improvements that were more pronounced for a high collision speed were examined;
- Performance improvements were attributed to the increased concrete compressive strength due to the CFRP confinement and the enhanced column shear capacity, which shifted column shear failure to flexural failure by the development of plastic hinge in the collision region.

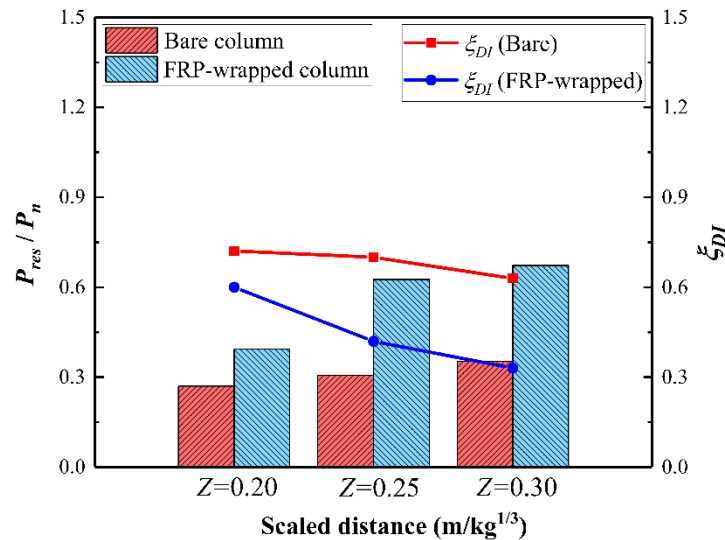


Figure 6.15 Comparison of residual axial capacity and damage index, bare and CFRP-wrapped columns

6.3.3 Simulations of polyurea-coated bridge column

6.3.3.1 Collision velocity

Figure 6.22 compared column damage between bare and polyurea-coated columns for varying collision velocities. As shown in Figure 6.22, the amount of eroded concrete and buckled longitudinal reinforcement in the cross-section decreased with the use of polyurea coating. The column performance improved. For the case with $v_0 = 65$ km/h, M2 and M3 occurred at the base of the bare column and this column could remain in operation while receiving extensive repairs. The polyurea-coated column sustained only M2 with exposed reinforcements at its base, indicating less significant damage and similar performance for the CFRP-wrapped column. For the case with $v_0 = 95$ km/h, M2, M4, and M5 were observed for the bare column with shear failure occurring at the base. The polyurea-coated column sustained M2 and M3 and could remain in operation with extensive repairment. The CFRP-wrapped column performed better at this collision velocity with considerably less damage. For the case with $v_0 = 120$ km/h, the bare column experiencing M2, M5, and M6 and failed. The polyurea-coated column experienced M2, M4, and M5 at the base with shear failure occurring, while for $v_0 = 120$ km/h the CFRP-wrapped column could continue in operation with extensive repairs. It was evident that performance changes between the polyurea and CFRP column were concentrated in the collision zone, with polyurea failing once the SUT engine collided with the column. Polyurea has lower shear strength and stiffness compared to the CFRP wrap, leading to its failure to resist a high-speed collision.

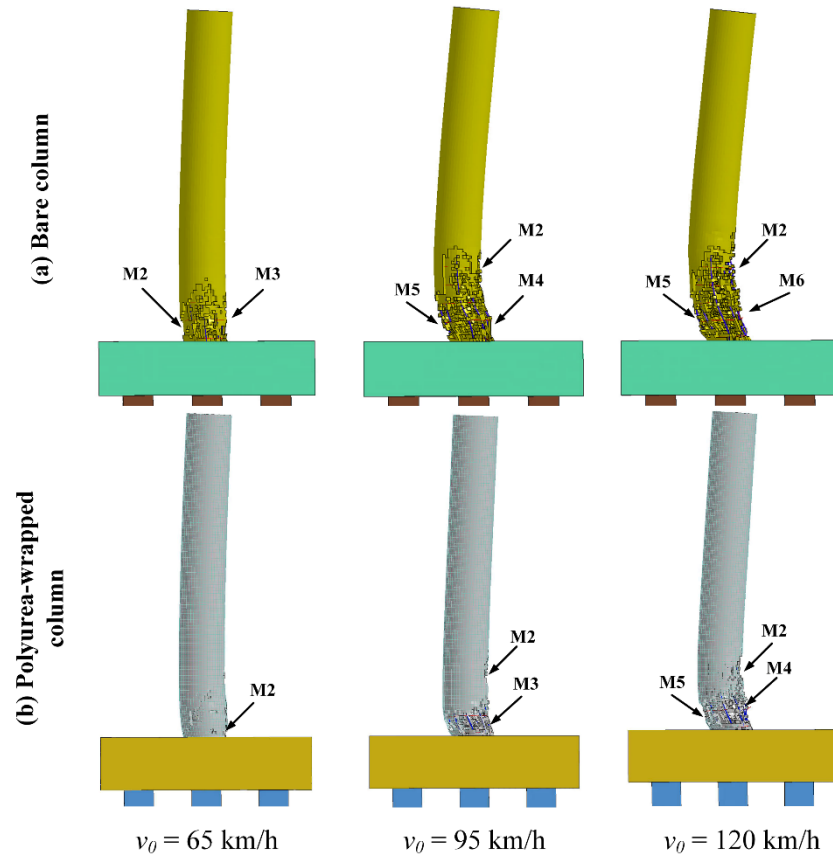
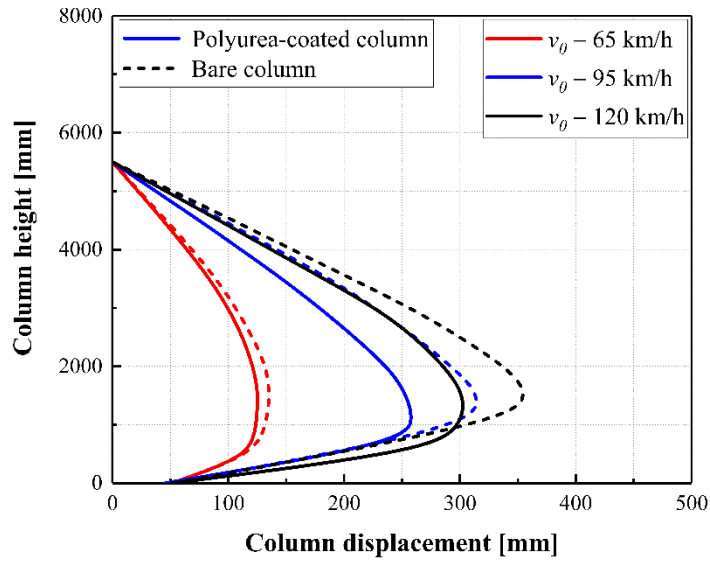
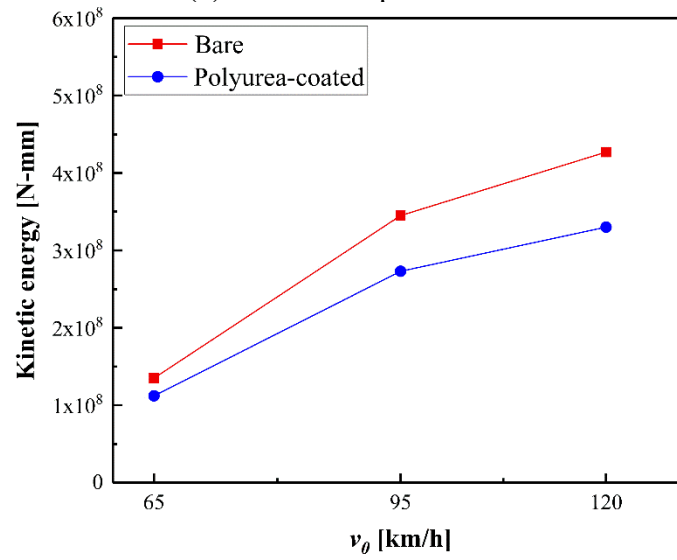


Figure 6.16 Comparison of final damage states, bare and polyurea-coated columns

Figure 6.17 compares final displacements along the column height and induced kinetic energy. Polyurea-coated column displacements decreased by approximately 20% when compared to the bare column, but were higher than CFRP-wrapped column displacements. Polyurea-coated column kinetic energy decreased by 18% when compared to the bare column, but were higher than the CFRP-wrapped column. Figure 6.18 illustrates residual axial capacities and damage indices. Residual axial capacity increased by about 40% with the use of the polyurea coating, and less than those for the CFRP-wrapped column. Thus, damage indices were reduced and column performance was improved due to the use of polyurea coating.



(a) Column displacement



(b) Column kinetic energy

Figure 6.17 Comparison of column deflection and kinetic energy, bare and polyurea-coated columns

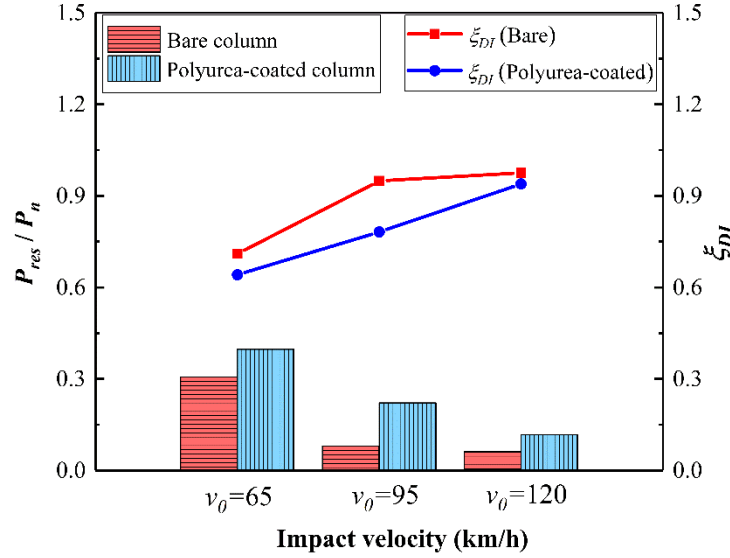


Figure 6.18 Comparison of residual axial capacity and damage index, bare and polyurea-coated columns

6.3.3.2 Scaled distance

Numerical simulations were conducted that examined response to an SUT collision at 65 km/h and air blasts having $Z = 0.20 \text{ m/kg}^{1/3}$, $0.25 \text{ m/kg}^{1/3}$, and $0.30 \text{ m/kg}^{1/3}$. Figure 6.19 compares final damage states for bare and polyurea-coated columns. Polyurea coating improved the column performance for the examined cases, and final damage states were similar to those for CFRP-wrapped columns. For the case with $Z = 0.30 \text{ m/kg}^{1/3}$, M2 was observed at the base of the bare column with exposed longitudinal reinforcement and the column remained in operation if repairs occurred. The polyurea-coated column sustained minor spalling at its base, indicating less damage and the ability to continue operation without repairs. For $Z = 0.25 \text{ m/kg}^{1/3}$, the bare column sustained M2 and M3 at the base and could remain in operation with extensive repairs. The polyurea-coated column experienced M2 at its base, indicating less significant damage and the ability to continue operation with simple repairs. For $Z = 0.20 \text{ m/kg}^{1/3}$, M2 and M3 were observed for both the bare column and polyurea-coated column, with less spalled concrete in the

polyurea-coated column. These columns could remain in operation after extensive repairs. Due to the better elasticity and tensile strength, the polyurea-coated column did not sustain shear-based damage at the base compared to the CFRP-wrapped column as shown in Figure 6.13 and Figure 6.19.

Figure 6.20 compares final displacements along the column height and induced maximum kinetic energy. Polyurea-coated column displacements decreased by approximately 15% compared to bare columns, while they were higher than those in CFRP-wrapped column. Column kinetic energy decreased by 10% due to the use of polyurea, but the CFRP-wrapped column possessed slightly less kinetic energy than the polyurea-coated column. Figure 6.21 illustrates residual axial capacities and damage indices for bare and polyurea-coated columns. Residual axial capacity increased by about 20% on average with the use of the polyurea coating, indicating the reduced column damage intensity.

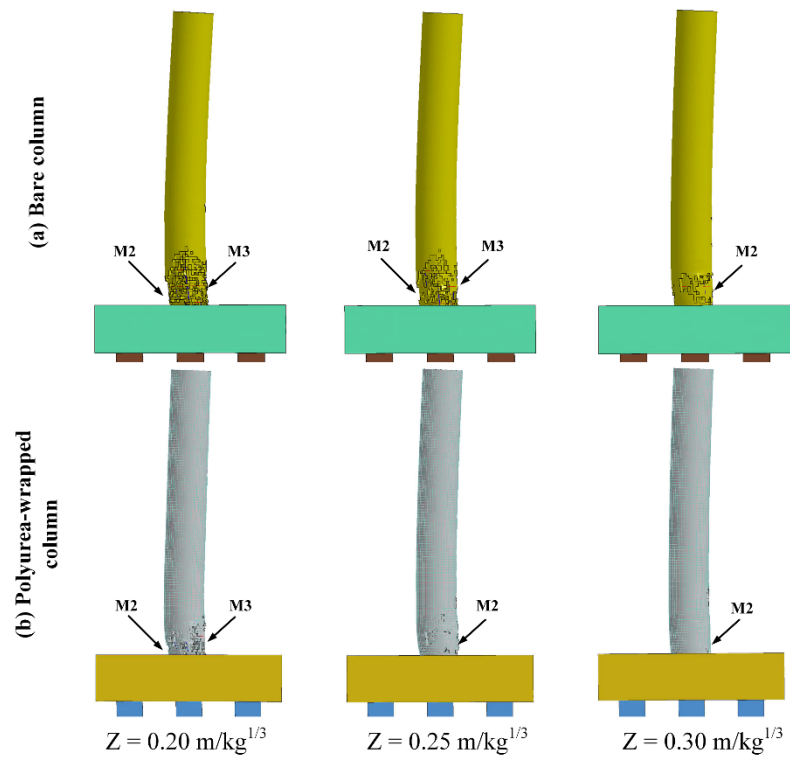
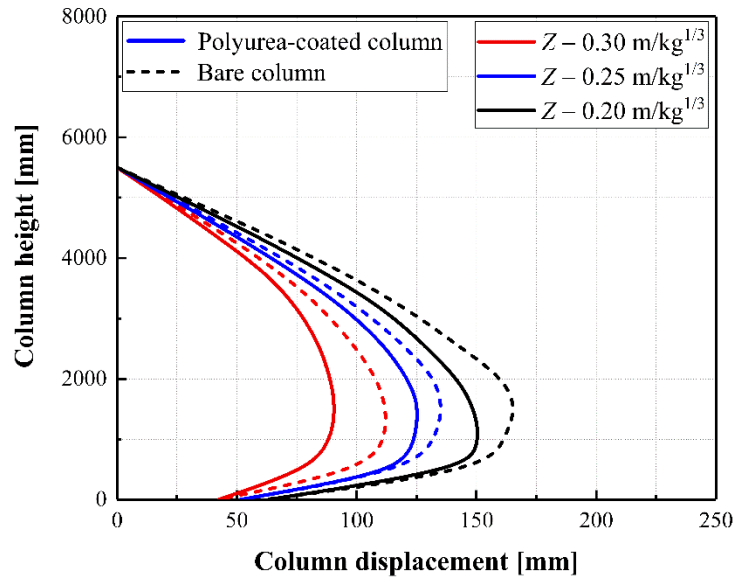
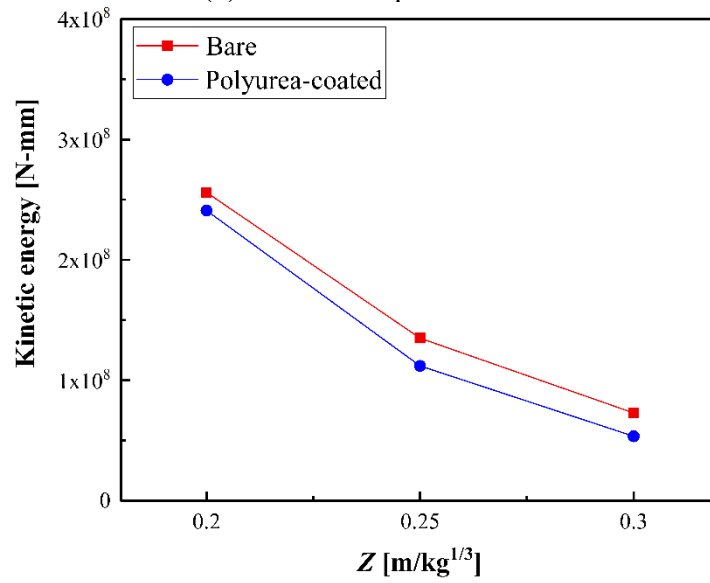


Figure 6.19 Comparison of damage mode, bare and polyurea-coated columns



(a) Column displacement



(b) Column kinetic energy

Figure 6.20 Comparison of column displacement and kinetic energy, bare and polyurea-coated columns

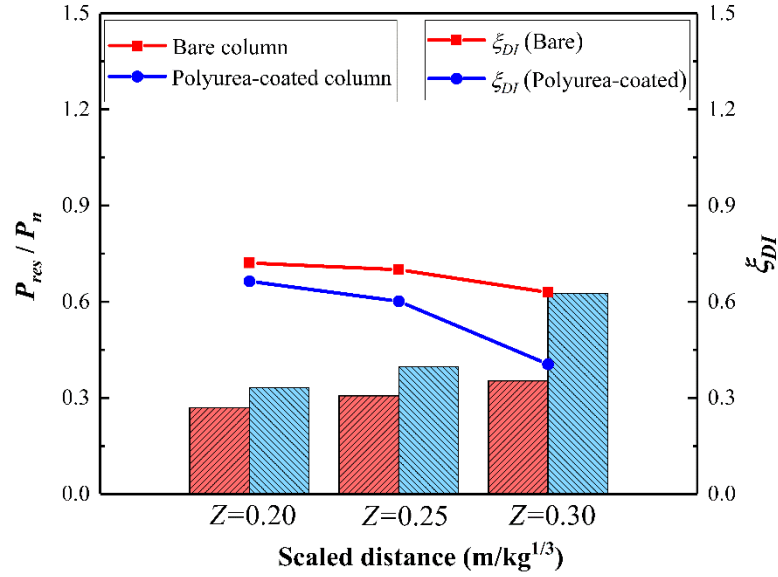


Figure 6.21 Comparison of residual axial capacity and damage index, bare and polyurea-coated columns

Studies of the effect of polyurea coating on concrete bridge column performance indicated that:

- Column performance generally improved with the polyurea coating;
- Improvements were more pronounced with the use of CFRP wrap compared to polyurea coating when changes in collision speed were examined. For the collision with $v_0 = 95$ km/h and 120 km/h examined in this study, the CFRP wrap is the preferred retrofit scheme to enhance column capacity and improve column performance.
- Effectiveness of the polyurea and CFRP wrap to mitigate column damage was similar when changes in scaled distance were examined. For a collision with $v_0 = 65$ km/h coupled with air blast, the polyurea coating could be a desired retrofit scheme to ensure serviceability of the bridge column.

6.4 Parametric studies

Parametric studies were used to identify controlling parameters for each strengthening scheme. They also helped identify a preferred retrofit scheme for certain situations and demands. Examined CFRP parameters included strength and thickness. Polyurea thickness was also examined. These parameters were selected because they significantly influence the CFRP or polyurea behavior under collision or blast loading and could change their effectiveness to mitigate the collision and blast effects. Performance was assessed in similar fashion to earlier parametric studies and also included assessing kinetic energy experienced by the FRP-wrapped or polyurea-coated column. Assessing kinetic energy would help better understand the ability of CFRP or polyurea to share the energy of the column and mitigate collision and blast effects. Parametric studies were completed for the 750 mm diameter column at a collision velocity of 120 km/h and a scaled distance of $0.25 \text{ m/kg}^{1/3}$.

6.4.1 CFRP strength

Three CFRP strengths were examined as outlined in Table 8.3 using data from tests completed by Han et al. (REF). These strengths were selected based on the availability and capability of the experimental data from previous studies. Figure 6.22 shows these columns sustained M2 and M3 in the collision region and indicates similar damage classifications for various CFRP strengths. These columns could remain in operation with extensive repairs.

Table 6.3 Effect of FRP strength on column response

D (mm)	t_{FRP} (mm)	FRP type	s_v (mm)	f_{FRP} (MPa)	d_{max} (mm)	ζ_{DI}	E_{in} (N-mm)	Performance level
750	3	CFRP	300	1095	190	0.70	2.57×10^8	Moderate damage
				1950	188	0.71	2.60×10^8	Moderate damage
				2280	186	0.69	2.59×10^8	Moderate damage

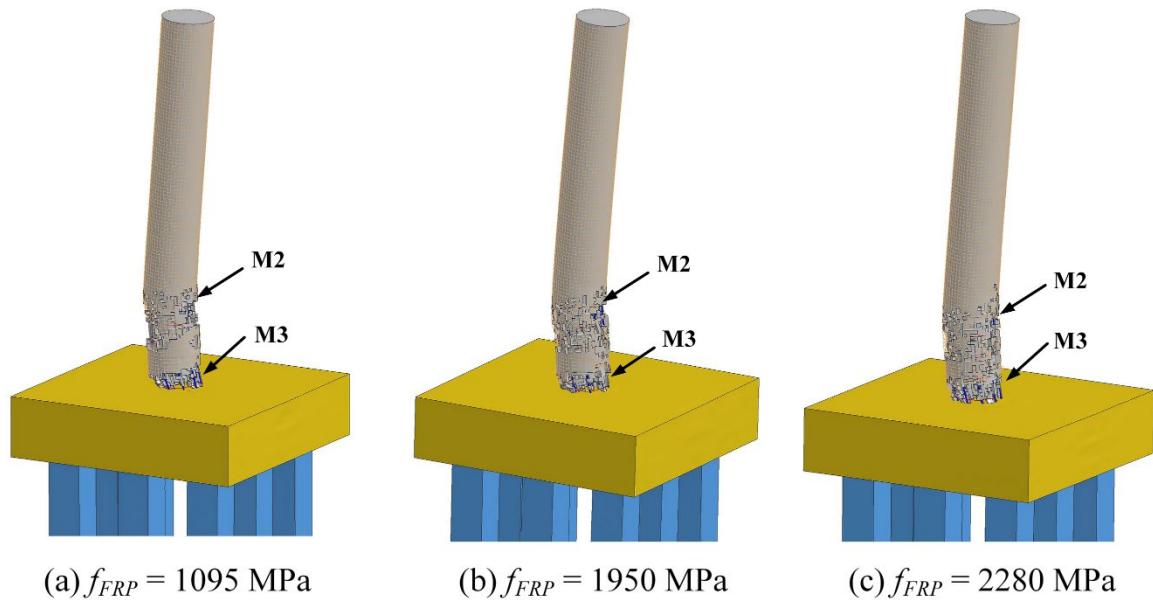


Figure 6.22 Effect of f_{FRP} on final damage states

Figure 6.23 plots final displacements and also indicates that CFRP strength had limited effect on response. Figure 6.24 shows that residual axial capacities were approximately 30% of nominal axial capacities and damage indices equaled 0.70 for all strengths.

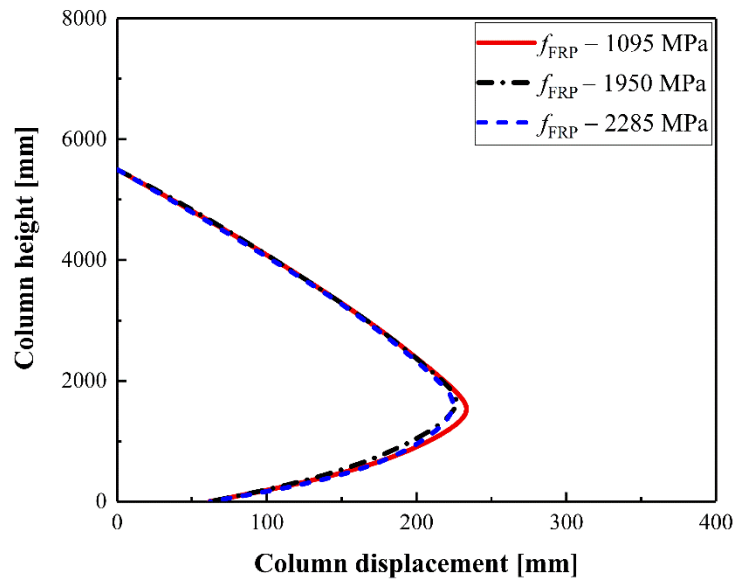


Figure 6.23 Effect of f_{FRP} on column displacement

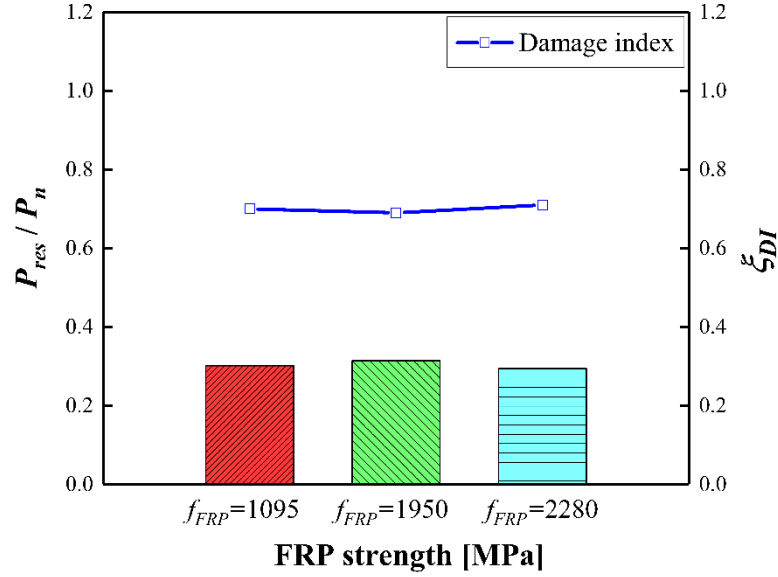


Figure 6.24 Effect of f_{FRP} on residual axial capacity and damage index

Figure 6.25 provides kinetic energy of the bare and CFRP-wrapped columns obtained by using LS-DYNA DATABASE_MATSUM command. The plot indicates that the amount of column kinetic energy was largely the same for varying the CFRP strength. No correlation between strength and rate of dissipation was evident.

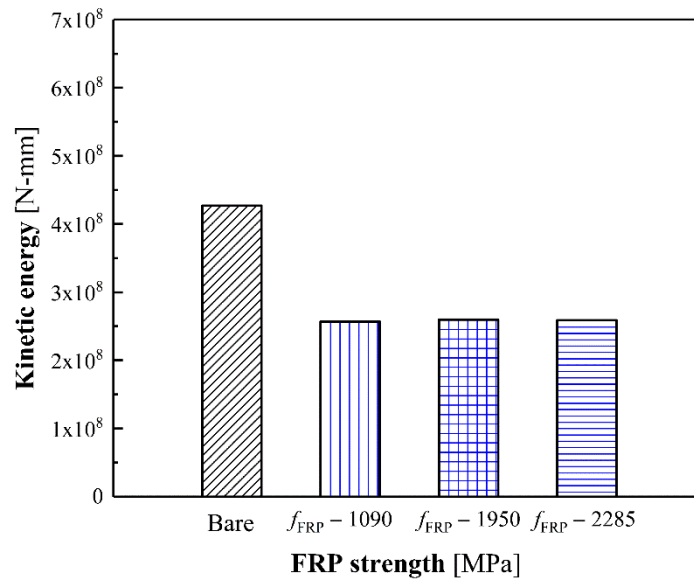


Figure 6.25 Effect of f_{FRP} on column kinetic energy

6.4.2 CFRP thickness

Four CFRP thicknesses were examined as outlined in Table 6.4. Figure 6.26 compared final damage. Thickness was selected based on previous research studies and resulting mitigation on the column damage. As expected, increased CFRP thickness significantly decreased damage. For the column with 2 mm thick CFRP wrap, M2, M4, and M5 were observed at the base and the column was deemed to have failed. An increase in thickness from 2 mm to 3 mm changed the column performance level from failing to remaining operational. When the CFRP thickness increased from 3 mm to 6 mm, the column sustained M2 and M3 in the collision region, and this column could remain in operation while receiving extensive repairs with the less spalled concrete at the thickness of 6 mm. As the CFRP thickness increased to 9 mm and 12 mm, M2 occurred at the column base, and the column could sustain operations with simple repairs being needed.

Table 6.4 Effect of CFRP thickness on column response

D (mm)	t_{FRP} (mm)	FRP type	s_v (mm)	f_{FRP} (MPa)	d_{max} (mm)	ζ_{DI}	E_{in} (N-mm)	Performance level
750	2	CFRP	300	1095	205	0.87	3.53×10^8	Severe damage
	3				190	0.70	2.57×10^8	Moderate damage
	6				148	0.55	2.43×10^8	Moderate damage
	9				95	0.31	2.01×10^8	Minor damage
	12				87.5	0.27	1.96×10^8	Minor damage

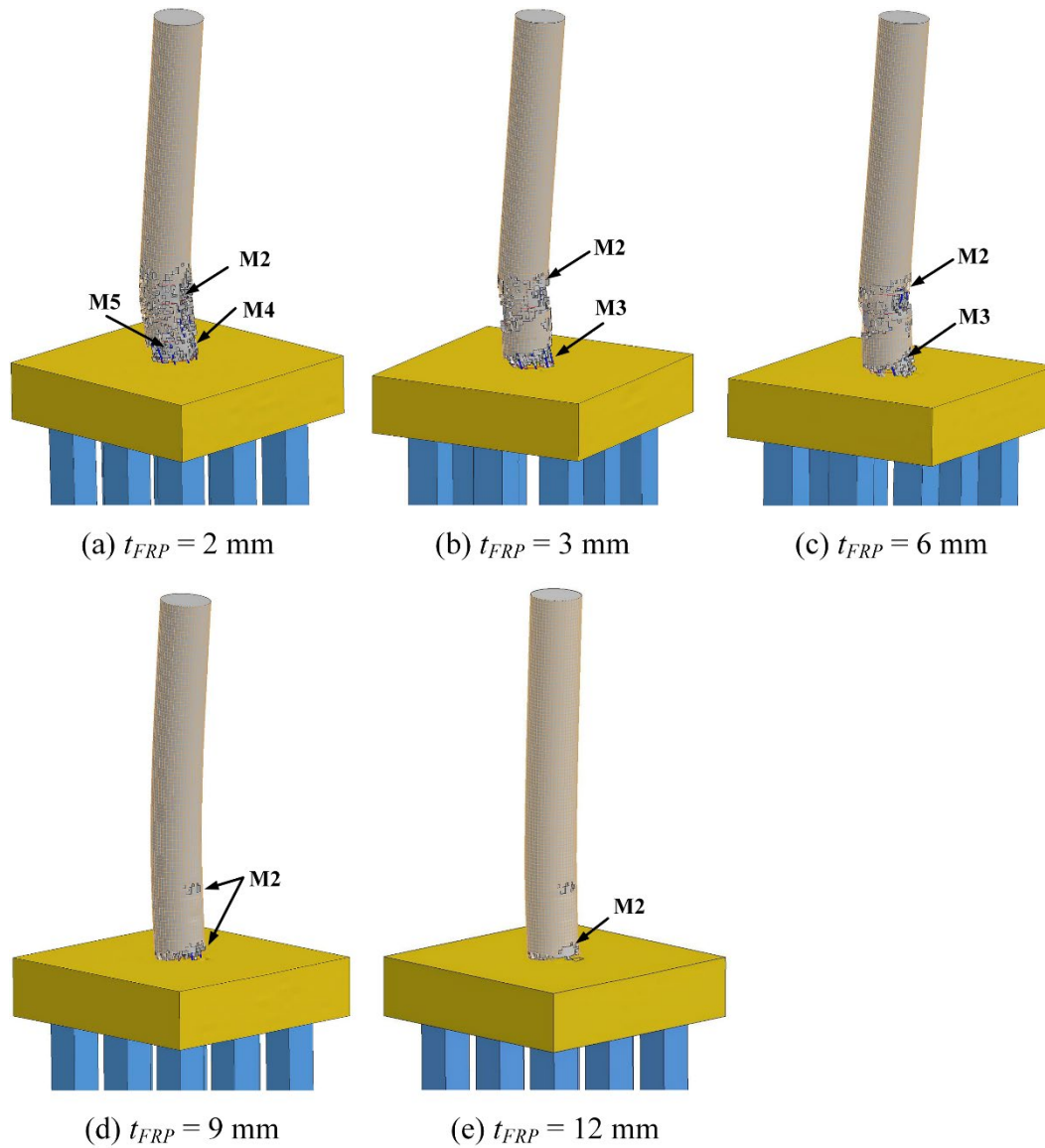


Figure 6.26 Effect of t_{FRP} on final damage state

Figure 6.27 plots final displacements and further indicates that the column displacement decreased with an increased CFRP thickness. When CFRP thickness increased to 12 mm, column displacement was 55% lower than that experienced by the column wrapped using 2 mm thick CFRP. Figure 6.28 shows that increased CFRP thickness increased residual axial capacity and decreased damage indices. Figure 6.29 provides column maximum kinetic energies for

various CFRP thicknesses. A reduction in the kinetic energy was more pronounced when the CFRP thickness increased from 2 mm to 3 mm, identifying significant improvement in effectiveness of CFRP to protect bridge columns. When the CFRP wrap increased from 9 mm to 12 mm, the effectiveness of increasing CFRP thickness was not as prominent as thinner cases with a small change in the column displacement and dissipated energy. This was due to the increased CFRP thickness being sufficient to mitigate collision and blast effects and prevent the column from failure. The 9 mm and 12 mm thick CFRP wraps had similar effectiveness to dissipate energy for the bridge column.

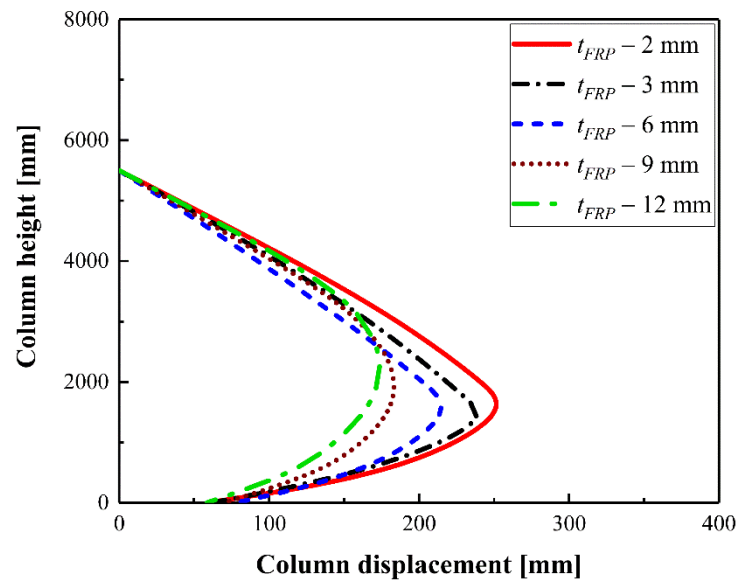


Figure 6.27 Effect of t_{FRP} on column displacement

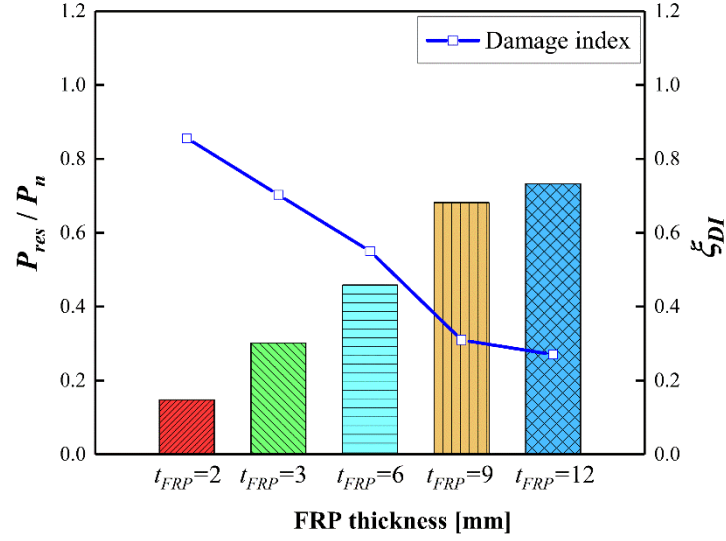


Figure 6.28 Effect of t_{FRP} on residual axial capacity and damage index

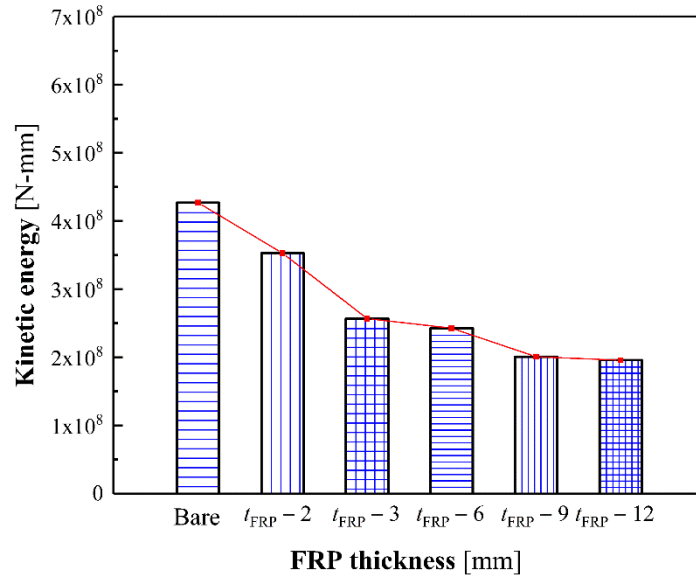


Figure 6.29 Effect of t_{FRP} on CFRP dissipated energies

6.4.3 Polyurea thickness

Three polyurea thicknesses of 6 mm, 9 mm, and 12 mm were examined as outlined in Table 6.4. As stated in the previous section, the 9 mm thickness was selected based on the equivalent axial capacity with the FRP-wrapped column. The remaining thickness was selected

based on the resulting mitigation on the column damage. Figure 6.30 compared final damage state for polyurea-coated bridge columns. The increased polyurea thickness reduced damage. As the polyurea thickness increased from 9 mm to 12 mm, the column performance changed from failing to remaining operational. When the polyurea thickness increased from 12 mm to 15 mm, the column sustained M2 and M3 at the base and this column could remain in operation while receiving extensive repairs with decreased concrete spalling at the 15 mm thickness.

Table 6.5 Effect of polyurea thickness on column response

D (mm)	t_{FRP} (mm)	s_v (mm)	d_{max} (mm)	ζ_{DI}	E_{in} (N-mm)	Damage level
750	6	300	272	0.93	3.68×10^8	Severe damage
	9		250	0.86	3.4×10^8	Severe damage
	12		205	0.70	2.93×10^8	Moderate damage
	15		181	0.64	2.77×10^8	Moderate damage

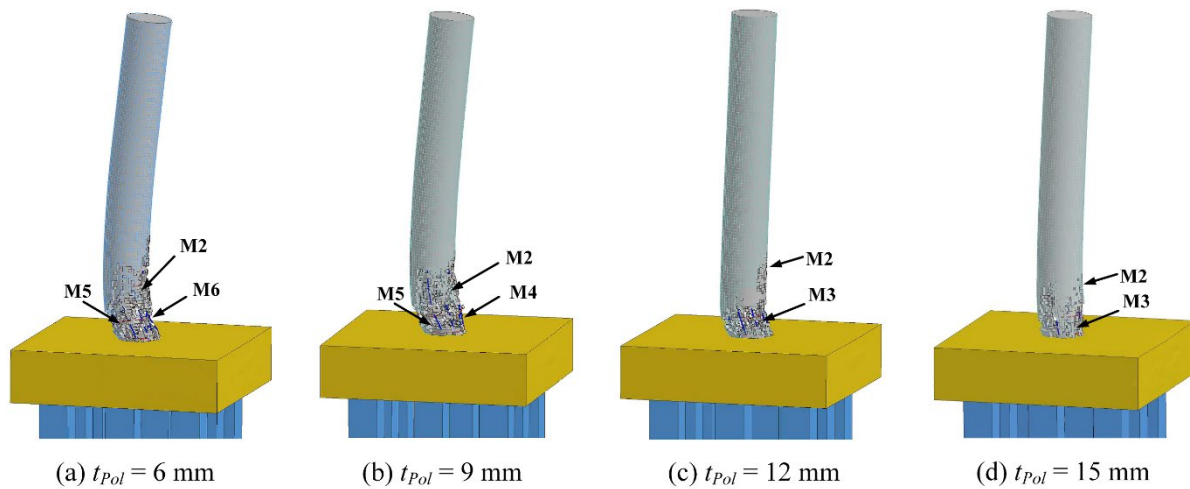


Figure 6.30 Effect of t_{Pol} on column damage

Figure 6.31 plots final displacements and further indicates that the column displacement decreased with the increased polyurea thickness. When polyurea thickness increased to 15 mm, the column displacement decreased by about 33% compared to the 6 mm thick polyurea. Figure 6.32 shows that increased polyurea thickness increased residual axial capacity and decreased damage indices. Figure 6.33 provides column maximum kinetic energy, with energy dissipated by the polyurea increasing as the polyurea thickness increased. A pronounced decrease in the column kinetic energy occurred with the increase in polyurea coating from 9 mm to 12 mm, indicating the prominent effectiveness of the increased polyurea thickness to promote energy dissipation and providing additional flexural and shear reinforcements for the column while the concrete spalling is contained by the polyurea coating.

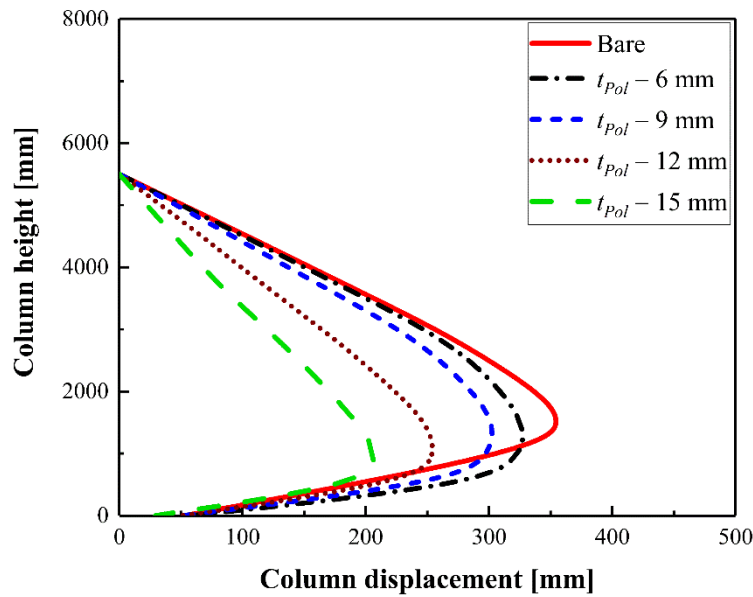


Figure 6.31 Effect of t_{Pol} on column deflection

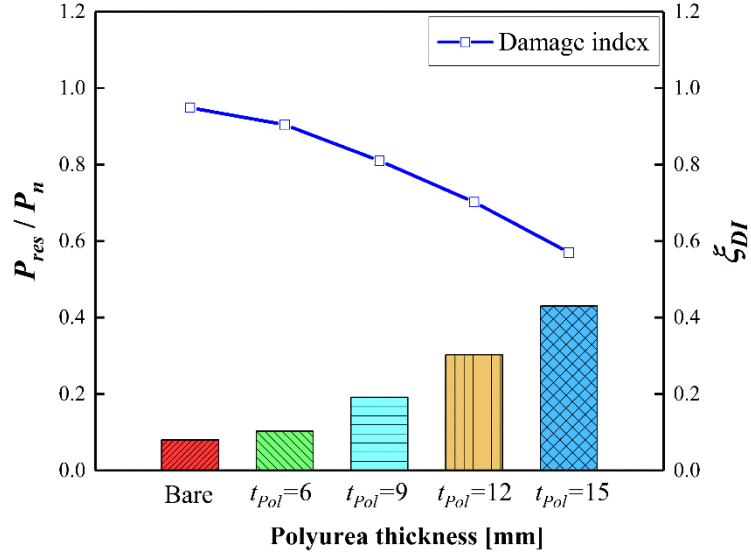


Figure 6.32 Effect of t_{Pol} on residual axial capacity and damage index

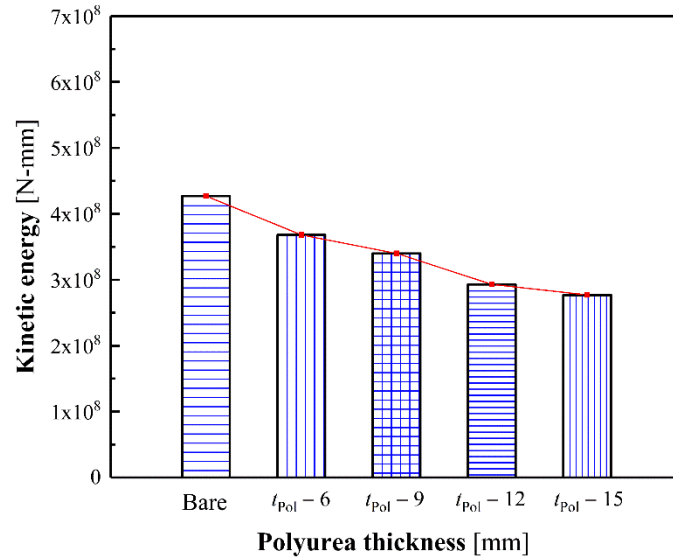


Figure 6.33 Effect of t_{Pol} on polyurea dissipated energies for polyurea-coated columns

6.5 Comparison of CFRP and polyurea retrofit effectiveness

To more directly compare the effectiveness of retrofitting columns using CFRP wrap and polyurea coating, three column diameters were investigated: 750 mm, 900 mm, and 1050 mm as outlined in Table 6.6. Each column was subjected to collision and blast loads when either wrapped with 3 mm thick CFRP or coated with 9 mm thick polyurea. All columns were

subjected to vehicle collision at a collision velocity of 120 km/h and air blast at scaled distance of $0.25 \text{ m/kg}^{1/3}$.

Figure 6.34 compares final damage states for bare, CFRP-wrapped and polyurea-coated columns. For the 750 mm diameter column, M2 and M3 were observed at the base when retrofitted using CFRP wrap, meaning this column could remain in operation while being repaired. The column retrofitting with polyurea coating sustained M2, M4, and M5 in the collision region, with shear failure occurring. The 900 mm diameter bare column experienced M2, M4, and M5 in the collision region, with shear failure being observed. The CFRP-wrapped column sustained M2 and exposed longitudinal reinforcements at the base and this column could remain in operation while being repaired. The polyurea-coated column experienced M2 and M3 in the collision region, indicating that it could continue in operation but extensive repairs would need to be completed. The bare 1050 mm diameter column experienced M2 and M3 in the collision region, and this column could remain in operation while being extensively repaired. The column retrofitted using either the CFRP wrap or polyurea coating sustained M2 in the collision region. This minor damage could be repaired during operation.

Table 6.6 Comparison of in-situ retrofit schemes

Coating type	D (mm)	s_v (mm)	t (mm)	d_{max} (mm)	ζ_{DI}	Damage level
CFRP wrap	750	300	3	148	0.70	Moderate damage
	900			36	0.47	Moderate damage
	1050			10	0.34	Minor damage
Polyurea coating	750	300	9	272	0.81	Severe damage
	900			88.5	0.65	Moderate damage
	1050			38.5	0.38	Minor damage

Figure 6.35 compares final displacements and column maximum kinetic energy. Displacements for the CFRP-wrapped columns were approximately 25% less than those experienced by the polyurea-coated columns. More energy was dissipated by the CFRP wrap than the polyurea coating. For 750 mm and 900 mm diameters, a decrease in the displacement and dissipated energy was more pronounced when the in-situ retrofit scheme changed from polyurea coating to CFRP wrap. For the 1050 mm diameter, effectiveness of the CFRP wrap and polyurea coating was not as prominent as the smaller column diameters.

Figure 6.36 compares residual axial capacities and damage indices for the CFRP-wrapped and polyurea-coated columns. Residual axial capacity for the CFRP-wrapped column was approximately 42% higher than that for a similar, polyurea-coated column. For the 750 mm and 900 mm diameter column, the CFRP wrap is the preferred retrofit scheme because of its higher stiffness that provides more efficient confinement of columns and larger shear strength that provides additional shear resistance of columns compared to the polyurea coating. For the 1050 mm diameter column, the CFRP wrap and polyurea coating have similar effectiveness because both retrofit schemes promote energy dissipation and provide additional flexural and shear reinforcements.

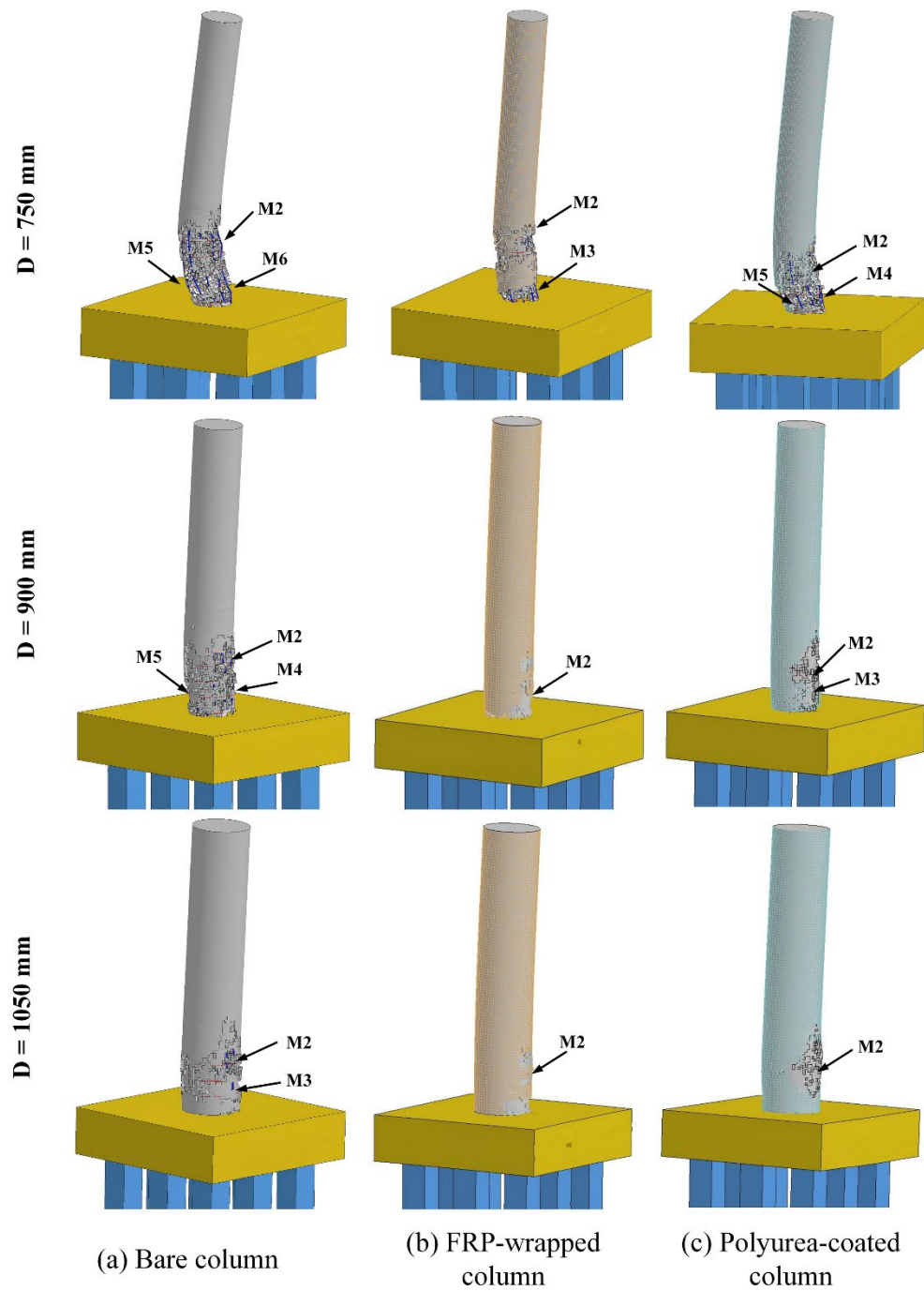
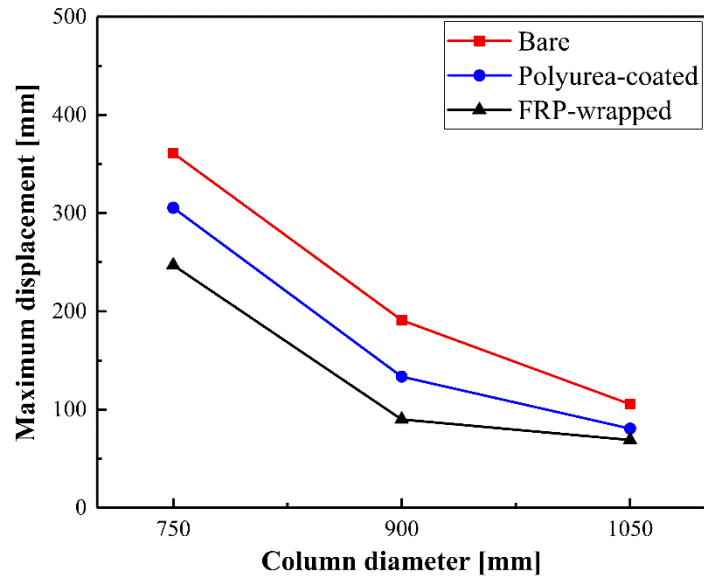
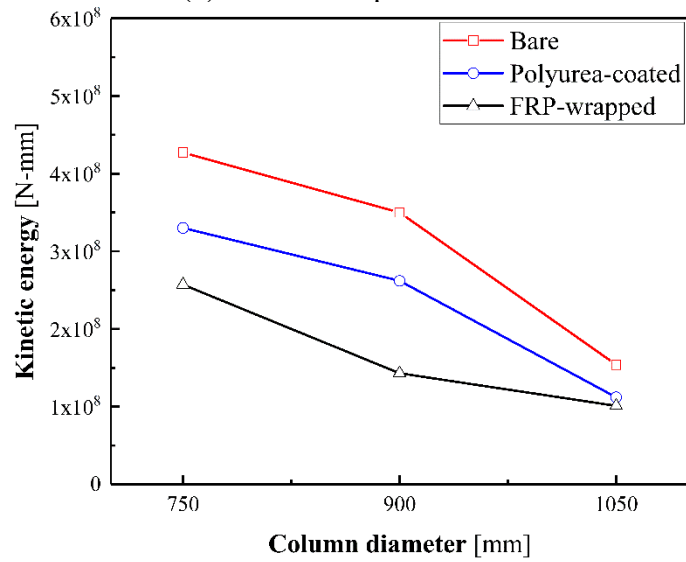


Figure 6.34 Final damage states for different in-situ retrofit schemes



(a) Column displacements



(b) Dissipated energies

Figure 6.35 Comparison of displacements and dissipated energies

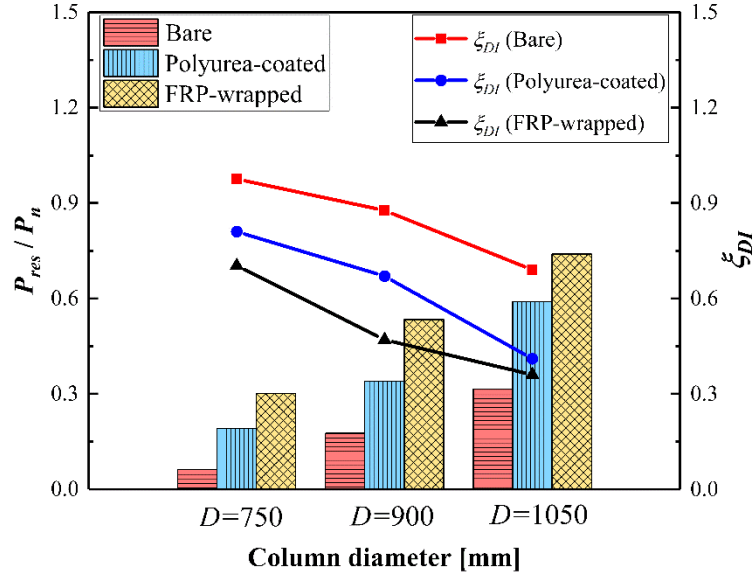


Figure 6.36 Comparison of residual axial capacity and damage index for different in-situ retrofit schemes

6.6 Conclusions

The effectiveness of in-situ retrofit schemes using either CFRP wrap or polyurea coating to improve isolated column performance was examined. Parametric studies for a critical single column were conducted to analyze effects of various design parameters on retrofitting effectiveness. The studies assumed that the entire column height would be wrapped or coated and examined for variations in FRP strength, FRP thickness, and polyurea thickness to investigate their effects on column performance. The studies indicated that:

- (1) Using CFRP wrap and polyurea coating on bridge columns can mitigate the effects of combined vehicle collision and air blast, with the effectiveness of each scheme differing as a function of studied geometric or material property as it pertains to column demand and performance.
- (2) For the variables and demands that were examined, thickness most significantly influenced the effectiveness of the CFRP wrap to improve column performance. The

- most dramatic effects from changes in CFRP thickness occurred between 2 and 3 mm because the column performance level changed from failing to remaining in operation while completing extensive repairs. Beneficial effects resulting from thicker FRP wrap had a limit, however, as using a 9 and 12 mm thick wrap this column sustained minor spalling at the base that could be repaired during the operation.
- (3) The influence of CFRP strength on retrofit effectiveness was largely insignificant for the variable and demands examined.
 - (4) It was noted that, in certain cases, the column retrofitted by the CFRP composite would experience extensive damage at the base due to the increased base shear force. The CFRP coating could be extended to cover the footing top and provide additional shear resistance at the base.
 - (5) For the variables and demands examined, increased polyurea thickness also affected column performance. The most dramatic effects from changes in polyurea thickness occurred between 9 and 12 mm because the column performance level changed from failing to remaining in operation while completing extensive repairs.
 - (6) As a result of these studies, an engineer selecting to retrofit a column should:
 - a. For the 750 mm and 900 mm diameter column, the CFRP wrap is the preferred retrofit scheme due to its high stiffness and strength to enhance column resistance.
 - b. For the 1050 mm diameter column, the CFRP wrap and polyurea coating have similar effectiveness so that the selection of the retrofit scheme depends on the criticality of the bridge and the available budget.

- c. Considering a vehicle collision at a speed higher than 95 km/h, the CFRP wrap is the preferred approach due to a large shear demand for the column and polyurea susceptibility of failure at the SUT engine collision.
- d. Given a vehicle collision at a speed around 65 km/h coupled with air blast, CFRP wrap and polyurea coating provide similar effectiveness to improve column performance and could be selected using the availability of installing equipment and retrofit budget.

Chapter 7 Multi-column Bridge Piers to Vehicle Collision and Air Blast

7.1 Introduction

Pier response was examined using numerical simulations of an SUT colliding with a multi-column bridge pier coupled with an air blast. Parametric studies were then conducted to investigate effects of design parameters on pier response to these demands. Studied parameters included vehicle impact angle, collision location, axial load ratio, longitudinal reinforcement ratio, and transverse reinforcement ratio. In addition, effectiveness of in-situ retrofit schemes using either FRP wrap or polyurea coating and considering effects of coating thickness and retrofitting location were studied.

7.2 Finite element modeling

Column design and modeling approaches matched those described in Section 2.2 through 2.6. Section 2.2 introduces determination of vehicle collision and blast modeling approaches. Section 2.3 and 2.4 describe numerical modeling means of material model, coupling, and boundary conditions. Section 2.6 presents selection of prototype pier and column.

7.2.1 Pier geometries and design details

The multi-column bridge pier obtained from the FHWA design example was again utilized as the prototype model in this section (see Figure 2.4). The pier has a height of 5400 mm (18 ft.) and length of 16500 mm (55 ft.). The pier contains four RC columns at a center-to-center spacing of 4300 mm (14.1 ft.). Columns have circular cross sections of 1050 mm (3.5 ft.) in diameter. They were reinforced with 18 No. 25 longitudinal bars for a 1% longitudinal reinforcement ratio and shear reinforcement consisting of No. 10 bars spaced 300 mm (12 in.) along the height. The pier is supported by a pile foundation system with a footing and eight piles. The footing is 3600 mm (12 ft.) wide, 3600 mm (12 ft.) long, and 900 mm (3 ft.) thick, and

reinforced with top and bottom steel meshes spaced 300 mm (12 in.) from the center in each direction. Piles are square with dimensions of 450 mm (1.5 ft.) \times 450 mm (1.5 ft.) and are 6000 mm (20 ft.) long. At their tops, the columns are connected to an RC cap with a rectangular cross section with dimensions of 1200 mm (4 ft.) wide, 16500 mm (55 ft.) long, and 1200 mm (4 ft.) thick. The cap is reinforced with 26 longitudinal bars and No. 16 (#5) hoops spaced at 300 mm (12 in.). A finite element model of the pier was developed using LS-DYNA as shown in Figure 7.1.

Three and two column pier designs were developed by the removal of supporting columns and the decrease in the cap length from the four-column pier. The other design variables remained the same for the three and two column piers. The resulting three-column is shown in Figure 7.2 (a) and has a total length of 12200 mm (40.7 ft.) and column center-to-center spacing of 4300 mm (14.1 ft.). The two-column pier is shown in Figure 7.2 (b) and has a total length of 12200 mm (40.7 ft.) with column spaced at 8600 mm (28.7 ft.) on center.

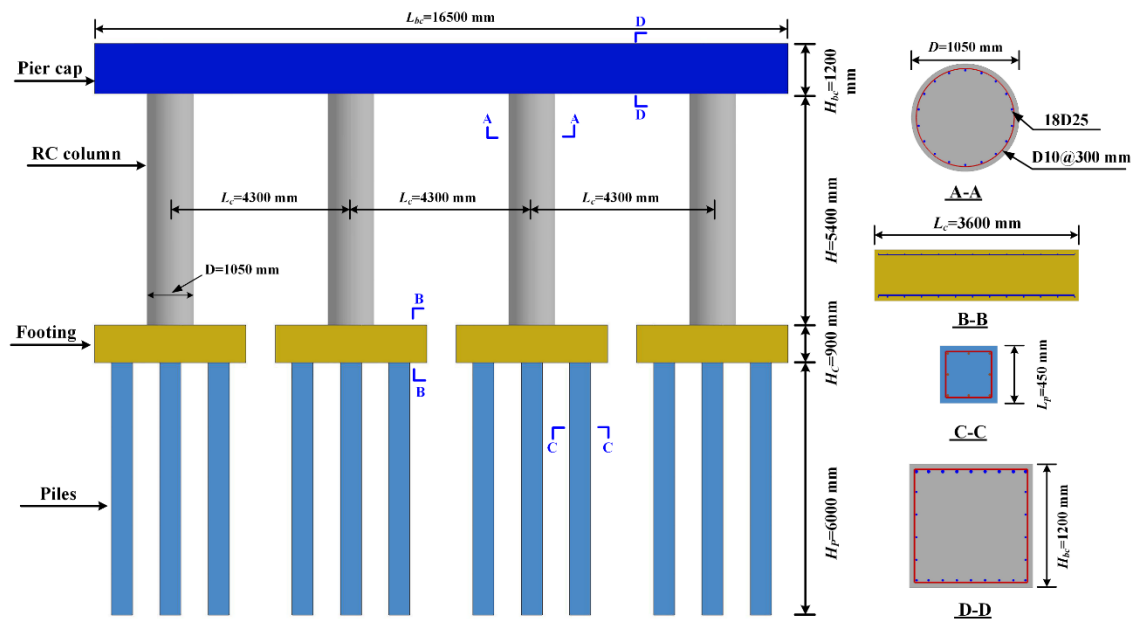
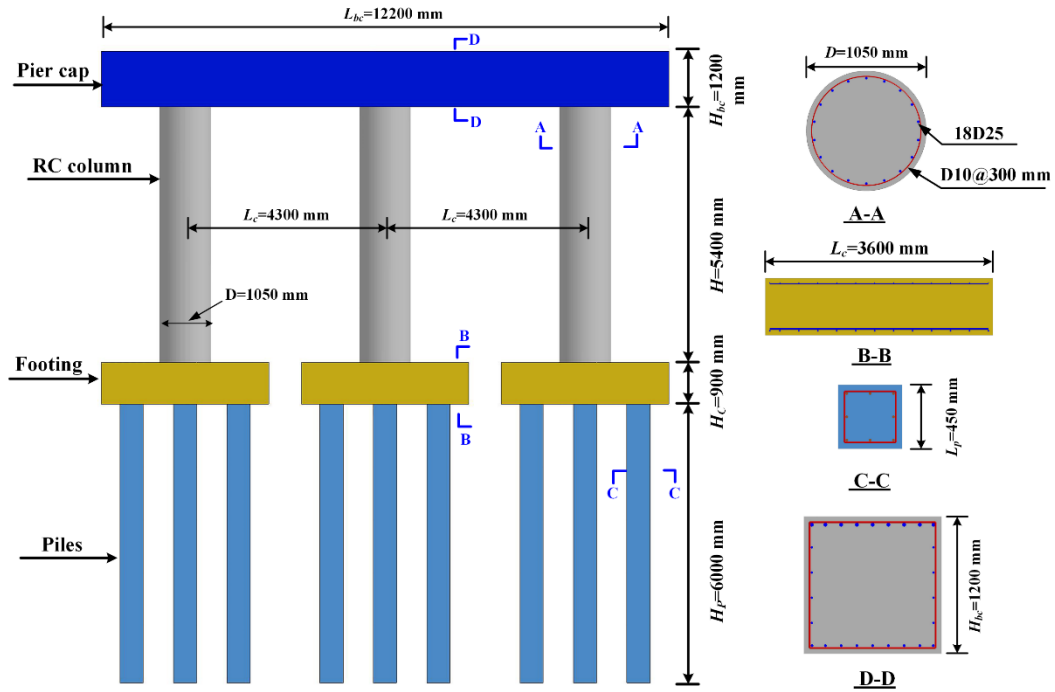
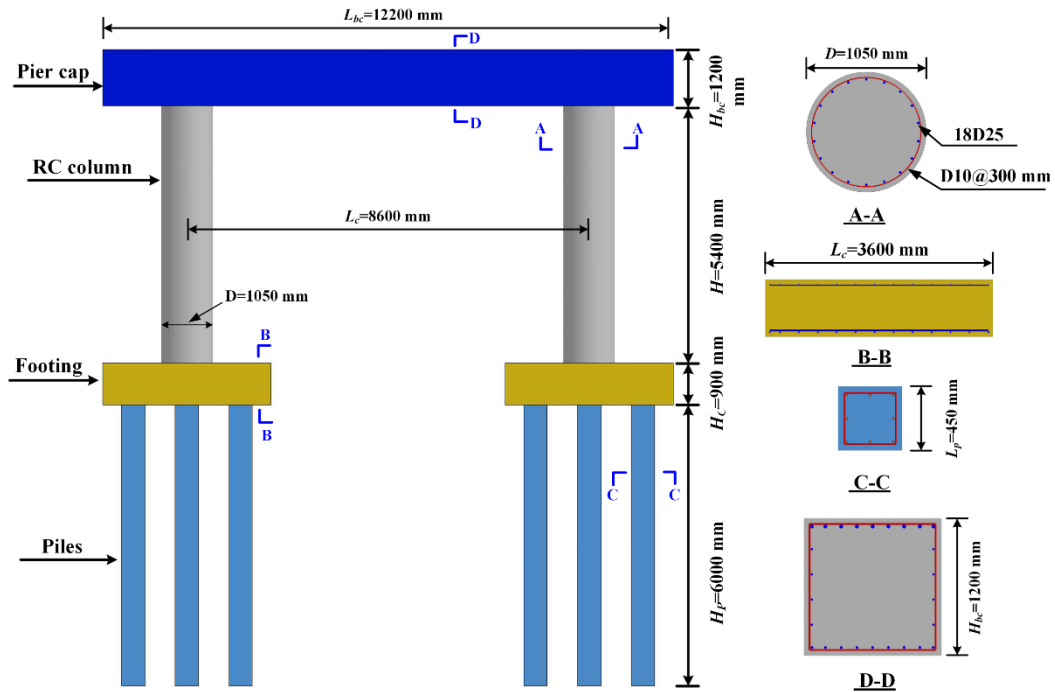


Figure 7.1 Finite element model of four-column pier [32]



(a) Three-column pier



(b) Two-column pier

Figure 7.2 Two and three column pier finite element models

7.2.2 Material models

Multi-column pier models were created using similar approaches to the isolated column model discussed in Chapter 2.

7.2.3 Boundary conditions

Non-reflecting boundary conditions (BNR) were defined along all sides to avoid dynamic wave reflections and superposition using LS-DYNA's *Boundary Non_Reflecting* algorithm. Superstructures dead loads were represented with an axial load at the top of the pier cap using *Load Node Set* algorithm. The axial load was set to 6% of the column's nominal axial capacity on each column, which was consistent with the preloading on the isolated column in Chapter 2. The axial load with the equal magnitude was placed at six locations along the pier length with an identical distance, as shown in Figure 7.3. Figure 7.3 shows the representative finite element models for the multi-column piers subjected to combined vehicle collision and air blast.

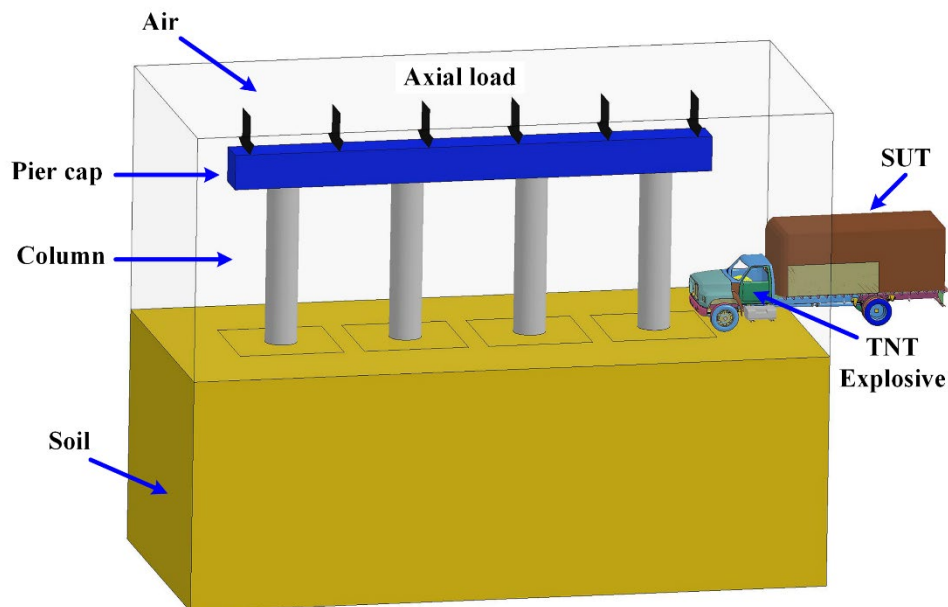


Figure 7.3 Numerical models representing multi-column pier

7.3 Response of Multi-Column Pier to Vehicle Collision and Air Blast

Simulations were completed to examine the effect of increased redundancy on combined collision-blast load response and to identify common damage states.

7.3.1 Combined collision-blast loading and pier response

Response to a vehicle collision at a speed of 95 km/h and blast at a scaled distance of $0.25 \text{ m/kg}^{1/3}$ was examined. The selected speed and scaled distance were anticipated to present the representative pier damage and its propagation at the time of interest. Representative results for the studied piers are provided below.

Figure 7.4 through Figure 7.6 illustrate loading increments and corresponding pier and reinforcement damage propagation for the two, three, and four column piers. It was observed from these figures that,

(a) *Initial collision at $t = 0.03 \text{ s}$.*

- (i) For all piers, cracking occurred on the front face of the impacted column.

(b) *Truck frame collision at $t = 0.05 \text{ s}$.*

- (i) For all piers, cracking propagated from the collision site through the height of the impacted column.
- (ii) For the two-column pier, cracking occurred at the mid-span of the pier cap. For the three column and four column piers, cracking occurred in the cap above the impacted column.

(c) *Engine collision at $t = 0.06 \text{ s}$.*

- (i) For all piers, maximum collision load occurred.
- (ii) For all piers, concrete began spalling at the collision point.

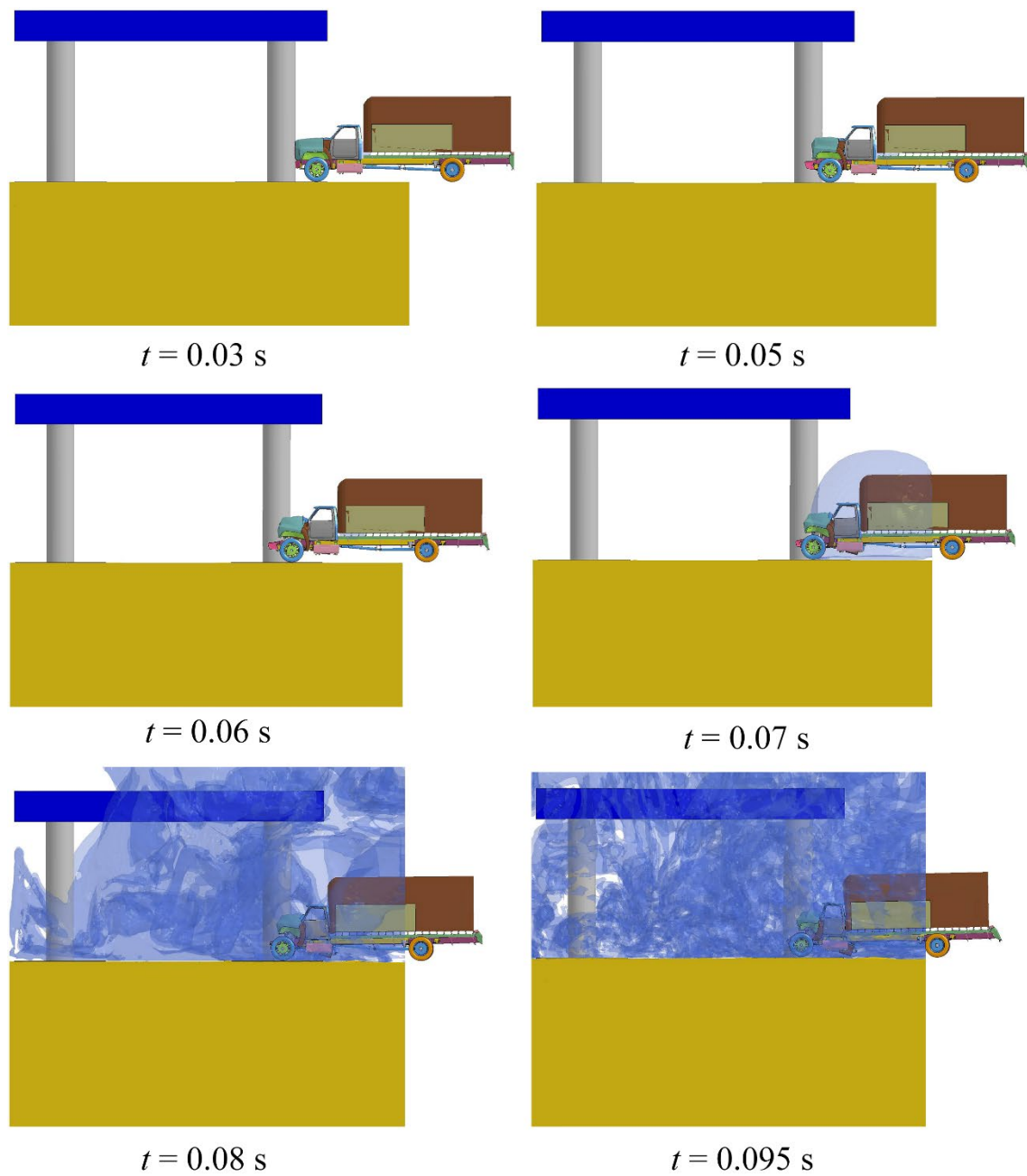
- (iii) For the three column and four column piers, cracking in the pier cap propagated to the top of the impacted column.
 - (iv) For all piers, reinforcements yielded in the collision region for the impacted column.
- (d) *Blast detonation at $t = 0.07$ s.*
- (i) For all piers, a 45° shear crack formed on the impacted column and radiated from the collision location to the non-collision face and at the base.
 - (ii) For all piers, additional concrete spalling was created at the collision location.
 - (iii) For the three-column pier, concrete spalling initiated in the pier cap above the impacted column.
 - (iv) For all piers, concrete cracking occurred on the collision side of the footing.
- (e) *Blast engulfment at $t = 0.08$ s.*
- (i) For the two-column pier, the impacted column had significant concrete spalling with exposed reinforcements at the collision location. Flexural cracking was also evident at the mid-height with cracks propagating to the pier cap.
 - (ii) For the three-column and four-column piers, a plastic hinge developed at the base of the impacted column. Flexural cracking was evident at the mid-height and shear cracking was observed at the column top and base.

- (iii) For the three-column pier, concrete spalling propagated in the pier cap and reinforcements were exposed above the impacted column.
- (iv) For all piers, concrete began cracking at the footing and in the support piles due to blast wave effects.
- (f) *Blast wave propagation at $t = 0.095$ s.*
 - (i) For the two-column pier, shear failure occurred at the mid-height of the impacted column. Flexural cracking was observed in the cap at the mid-span and shear cracking in the cap above both columns.
 - (ii) For the three column and four column piers, shear failure occurred at the base of the impacted column, and it was unable to resist additional load.
 - (iii) For the three-column pier, shear occurred in the pier cap.
 - (iv) For the four-column pier, concrete cracking occurred in the pier cap above the impacted column.
 - (v) For all piers, non-impact columns remained largely intact.
 - (vi) For all piers, concrete cracking was observed throughout the height of the support piles.

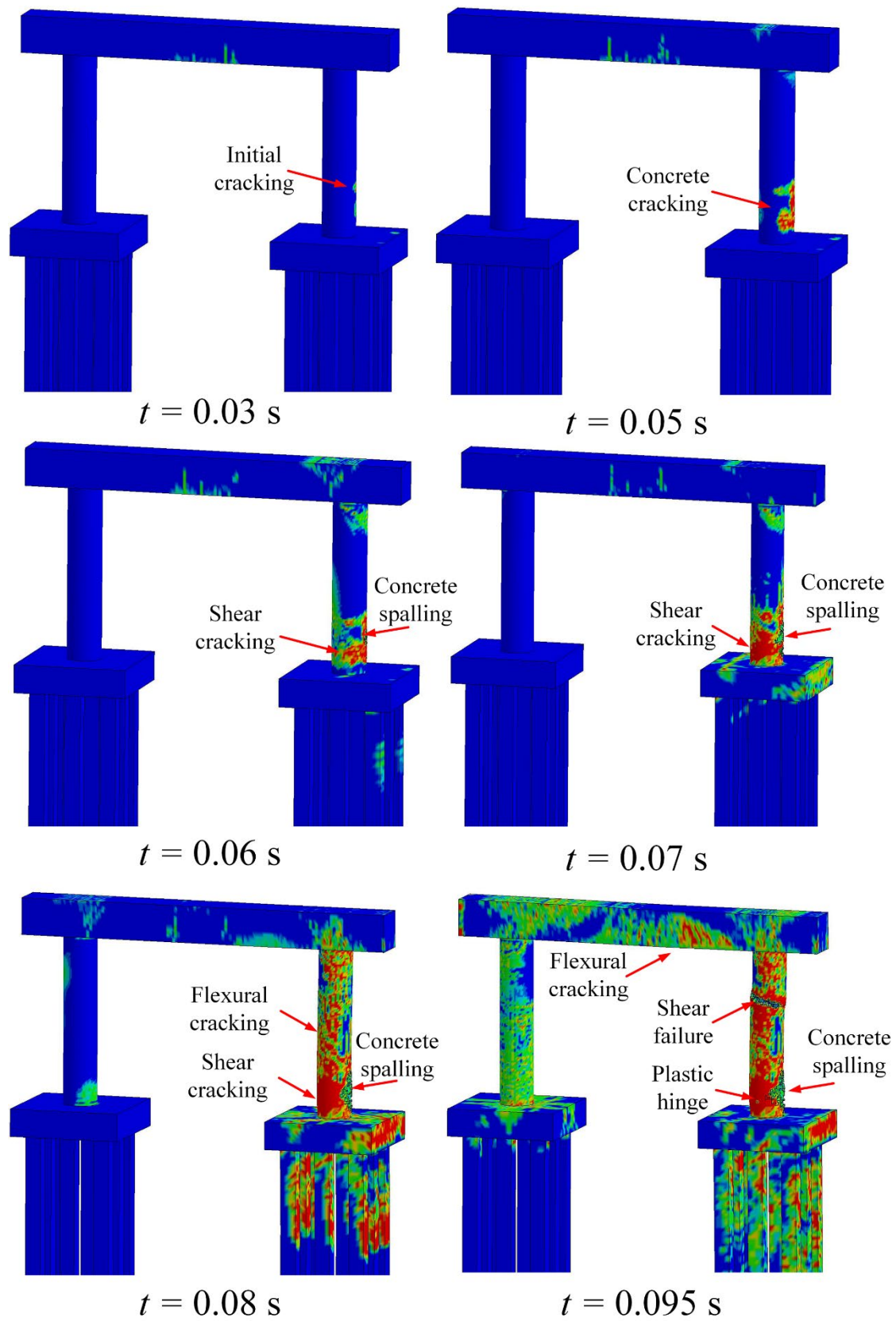
To summarize, numerical results indicated that:

- (a) For the two-column pier, the combined collision-blast load resulted in shear failure at the mid-height of the impacted column due to significant concrete spalling and longitudinal reinforcement buckling. A high risk of collapse existed, and the column should be replaced.
- (b) For the three-column and four-column piers, shear failure occurred at the base in the impacted column. Non-impact columns remained, and the damaged

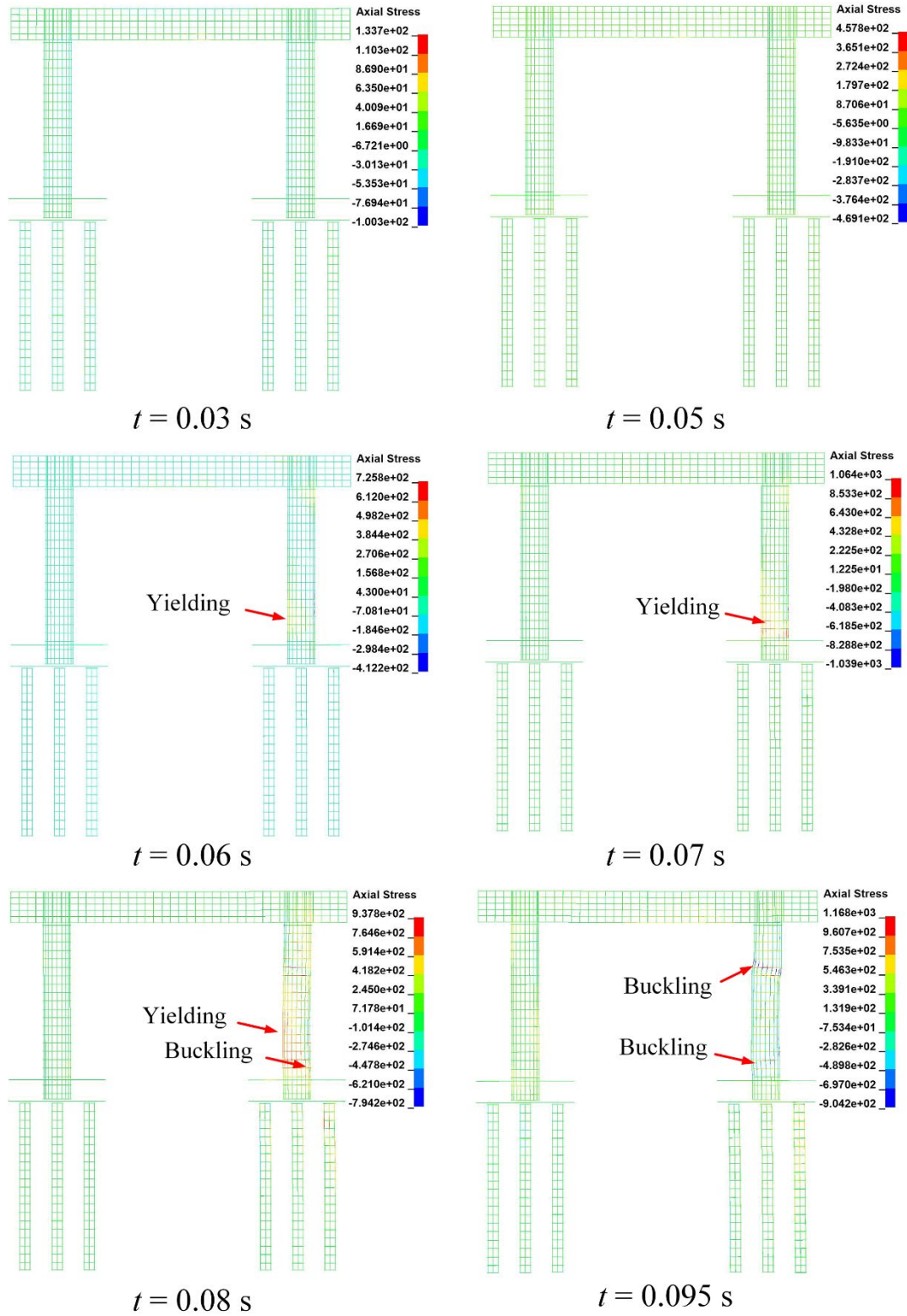
piers continued to adequately perform under operational conditions as a result of increased redundancy and load sharing via the pier cap. Necessary repairs can be completed under operational conditions.



(a) Times of interest

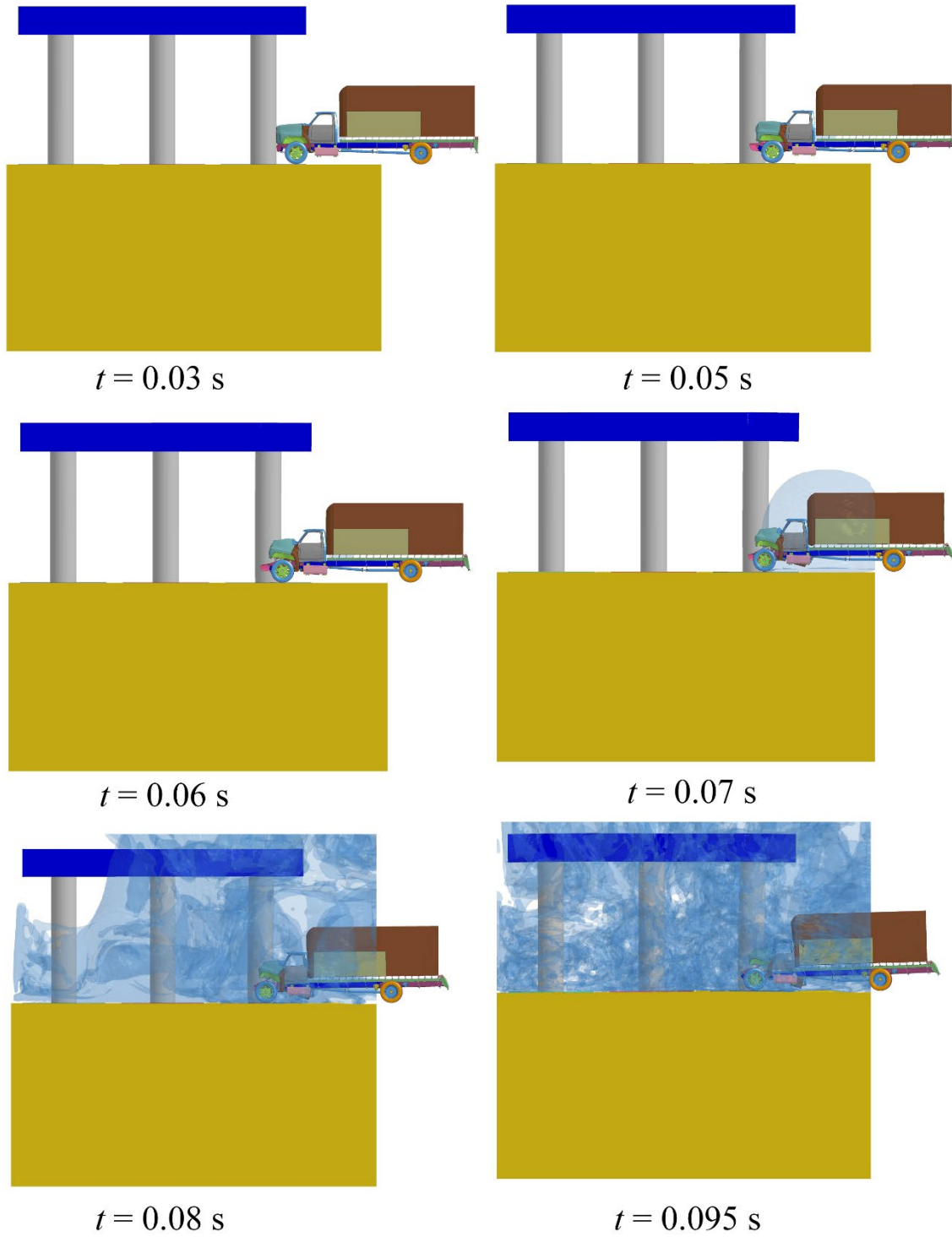


(b) Damage propagation

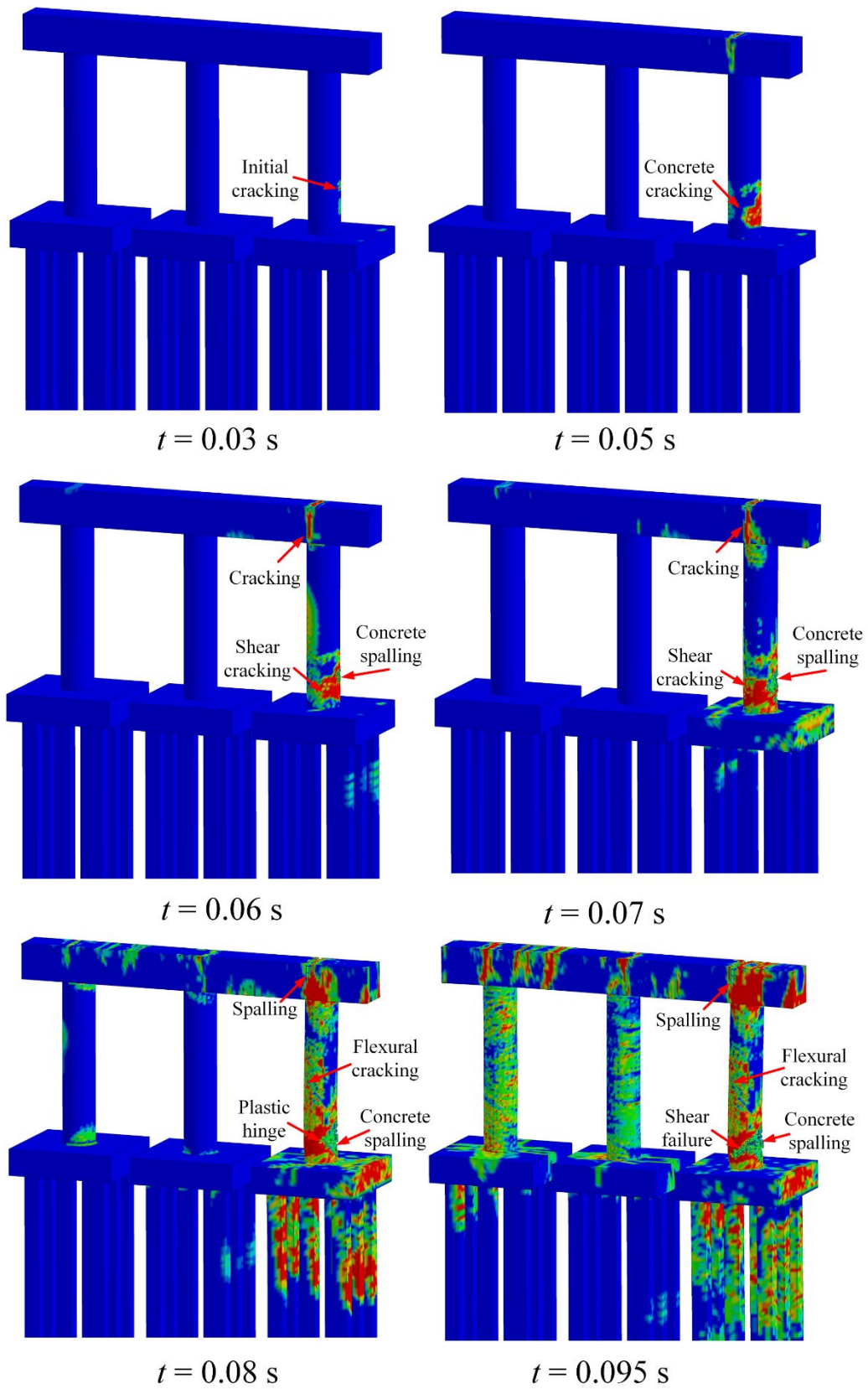


(c) Reinforcement behavior

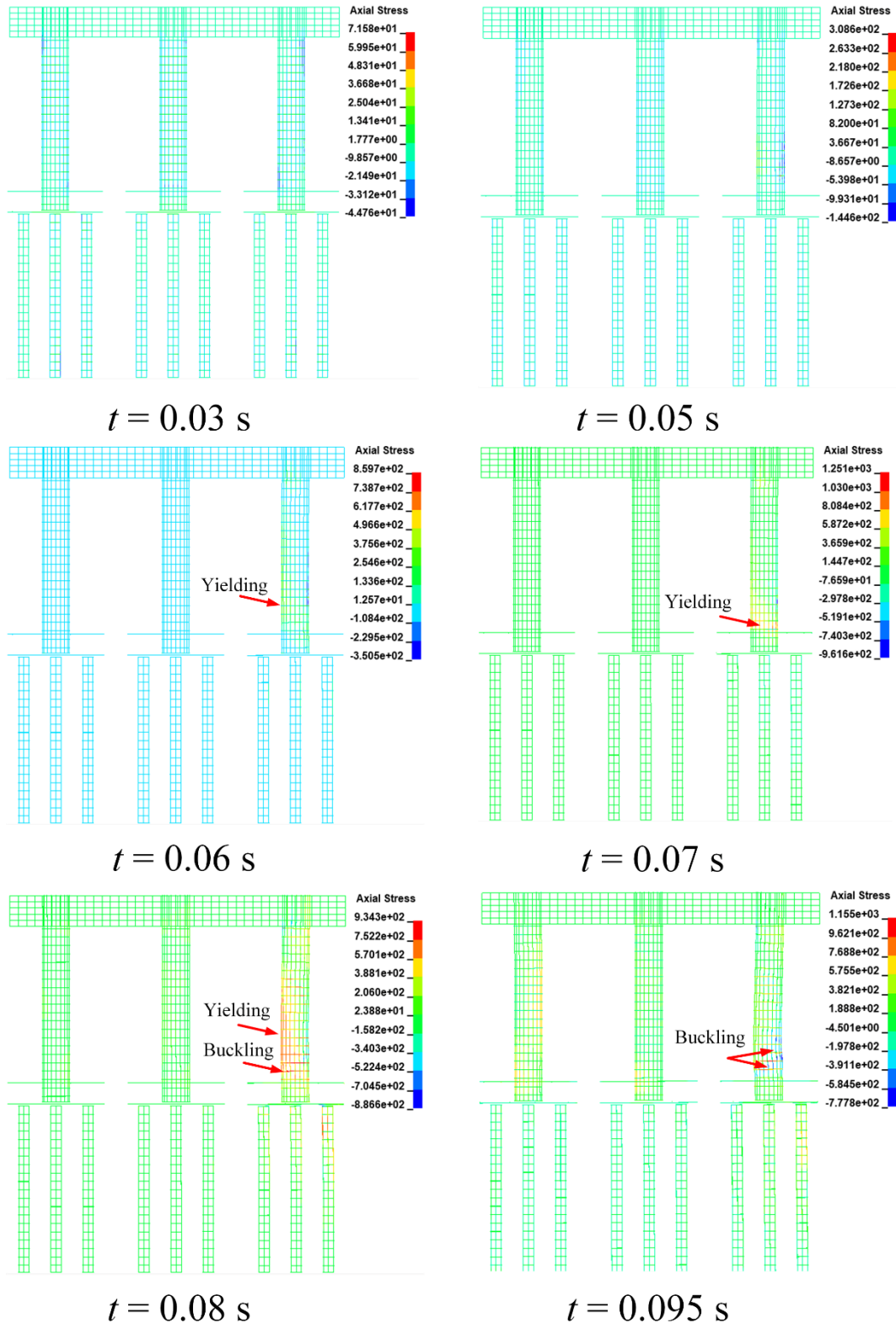
Figure 7.4 Two column pier: (a) times of interest; (b) damage propagation; (c) reinforcement behavior ($v_0 = 95$ km/h, $Z = 0.25$ m/kg^{1/3})



(a) Times of interest

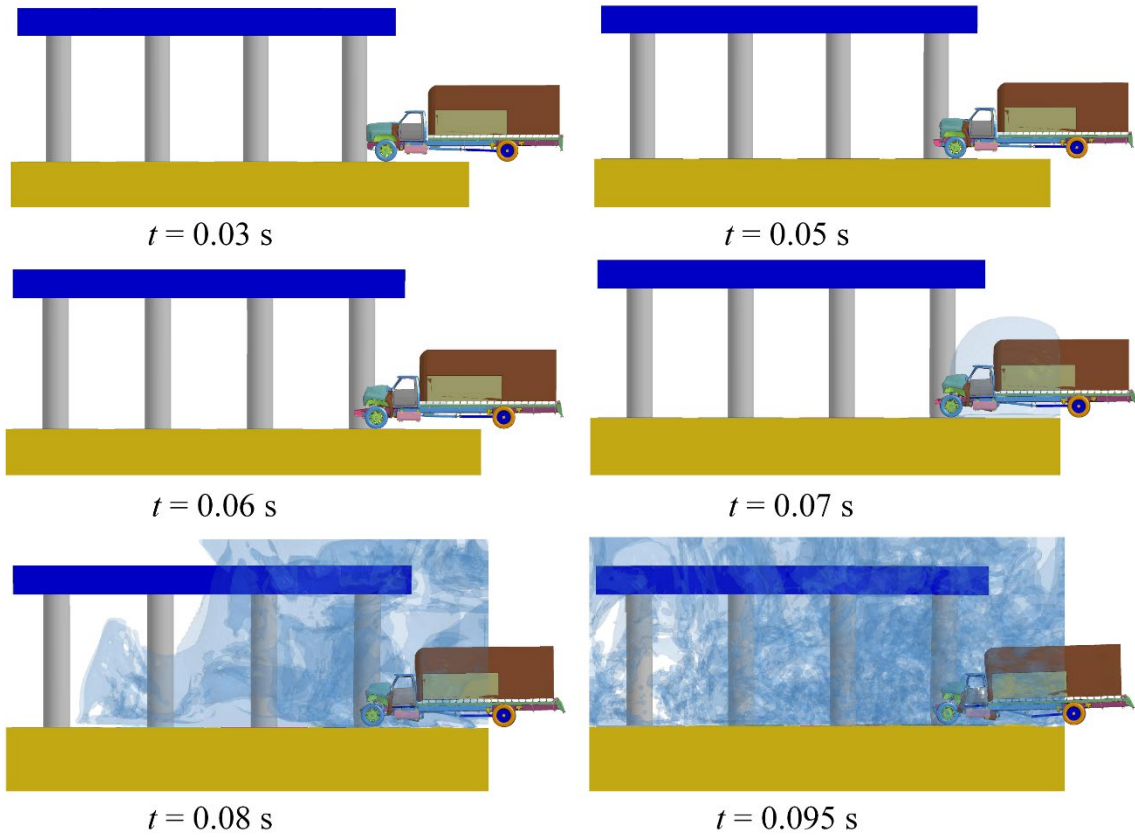


(b) Damage propagation

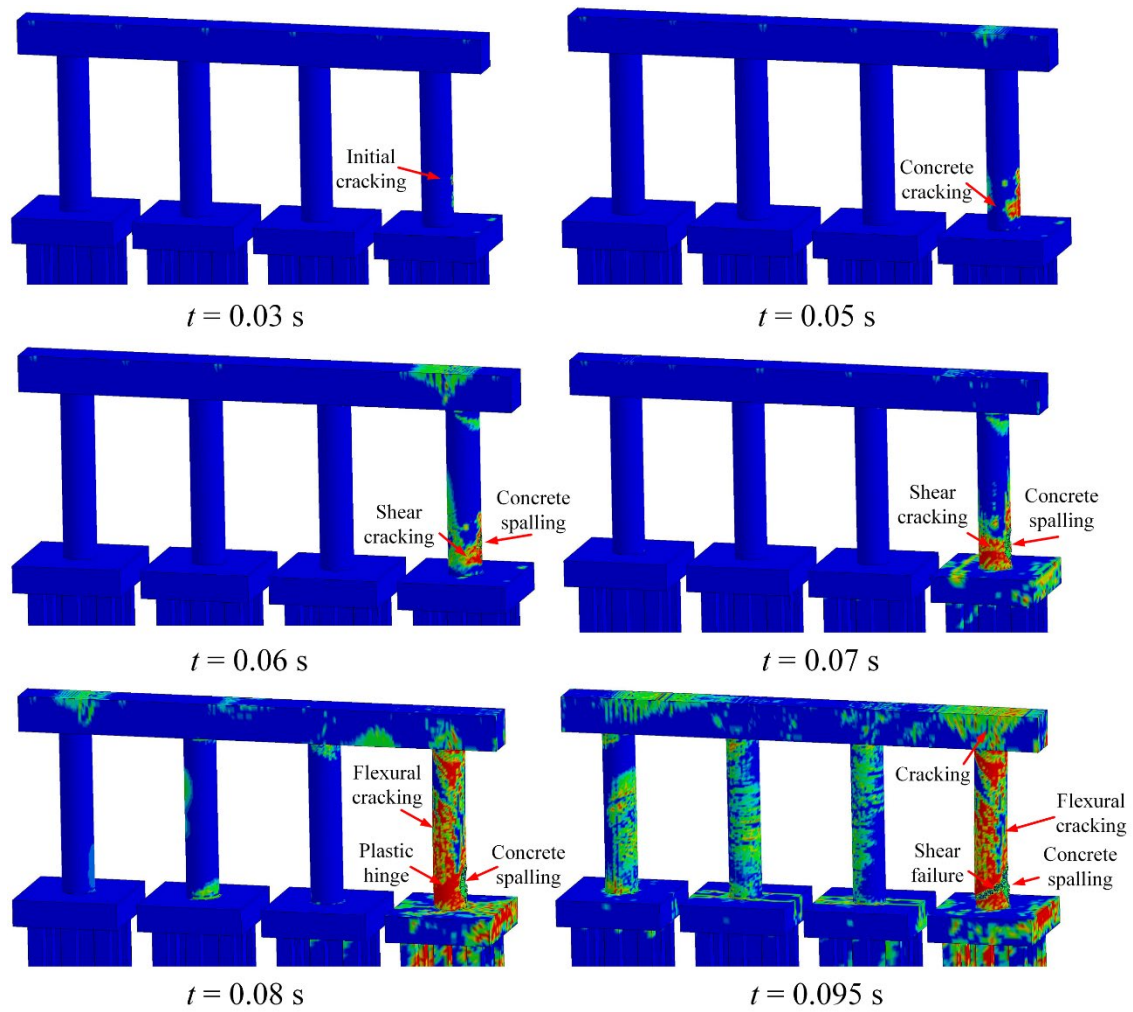


(c) Reinforcement behavior

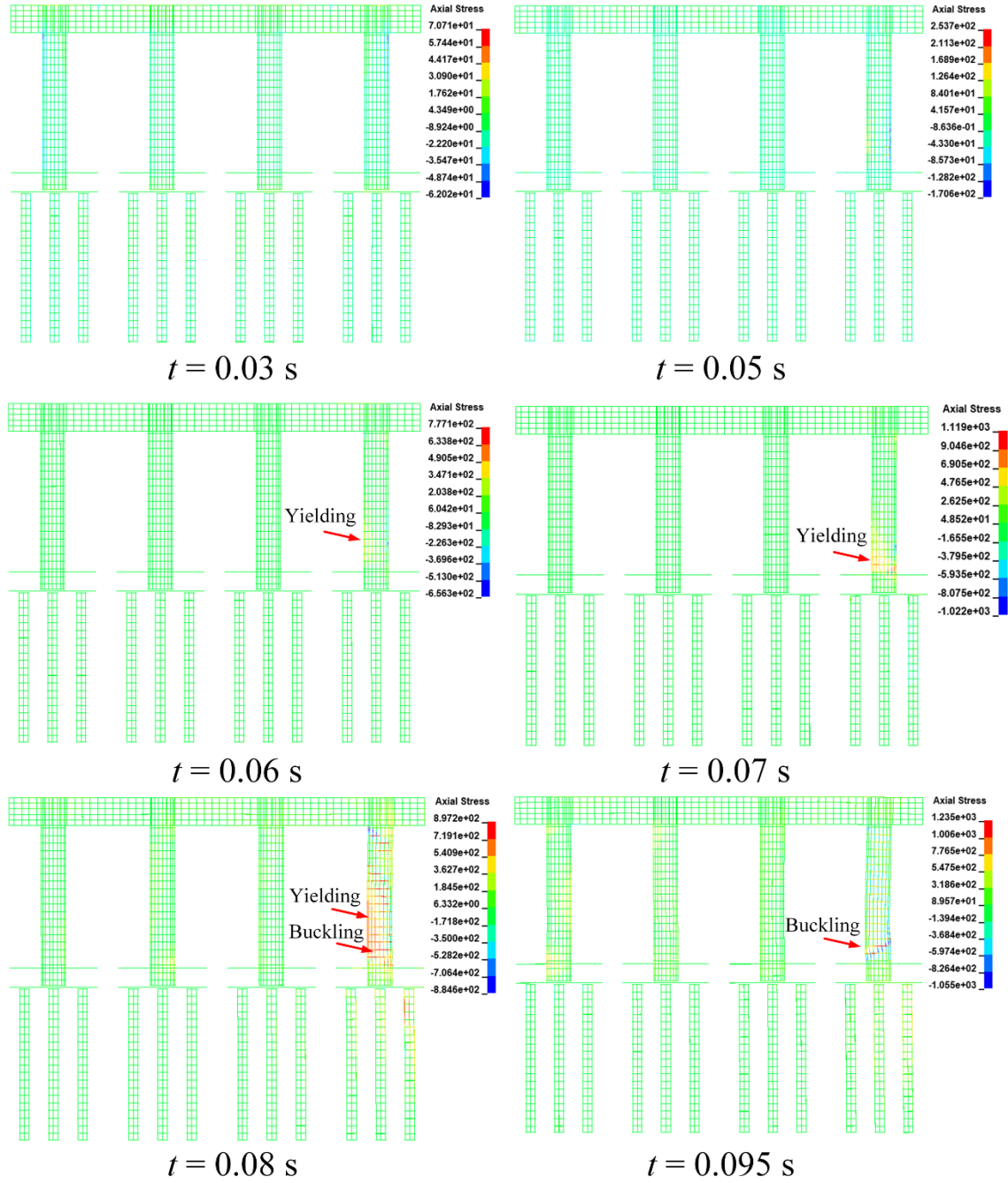
Figure 7.5 Three column pier: (a) times of interest; (b) damage propagation; (c) reinforcement behavior ($v_0 = 95$ km/h, $Z = 0.25$ m/kg^{1/3})



(a) Times of interest



(b) Damage propagation



(c) Reinforcement behavior

Figure 7.6 Four column pier: (a) times of interest; (b) damage propagation; (c) reinforcement behavior ($v_0 = 95$ km/h, $Z = 0.25$ m/kg^{1/3})

7.3.2 Pier damage

Damage categories identified for isolated columns in Chapter 3 were used to examine the multi-column pier damage as discussed in Section 3.4. The multi-column pier sustained various levels of damage with the variations of energy induced by vehicle collision and blast combination, and pier performance would be represented from the identified damage. Figure 7.7 through Figure 7.9 summarized final damage states for three modeled multi-column piers under various combinations of collision velocities and scaled distances. Results indicated that:

(i) For $v_0 = 65$ km/h, $Z = 0.30$ kg/m^{1/3} –

(a) For all piers, M1 was observed in the impacted column. The piers sustained minor damage with wide-spread cracking. These piers were deemed operational with repairable damage.

(ii) For $v_0 = 95$ km/h, $Z = 0.30$ kg/m^{1/3} –

(a) For all piers, M1, M2, and M3 were observed in the impact region of the impacted column, with remaining columns intact. These piers could remain in operation, but repair would be needed to ensure structural integrity.

(iii) For $v_0 = 120$ km/h, $Z = 0.25$ kg/m^{1/3} –

(a) For the two-column pier, the impacted column failed and sustained M1, M2, M4, and M5 at the mid-height of the impacted column. M1 was observed at the mid-span of the pier cap. The impacted column should be replaced to avoid pier collapse.

(b) For the three-column pier, shear failure occurred in the impacted column with M1, M2, M5, and M6 being observed in the collision region. M2 was observed in the pier cap above the impacted column. For the four-column pier,

M1, M2, M4, and M5 was observed at the base of the impacted column, with M1 in the pier cap. Remaining columns were intact. While the impacted column failed under the collision-blast event and would need to be replaced, the piers did not collapse.

Numerical results indicated that the two-column pier was vulnerable to the combined collision and blast, and the impacted column should be repaired to ensure the pier integrity and avoid pier collapse. For the three and four column piers, as demand increased, damage increased to the point where the impacted column failed in shear. While damage to the pier cap and adjacent column naturally increased as well, what was observed was never to the point where pier collapse was anticipated to occur. Extensive repair would be needed to restore the piers to the original level of performance.

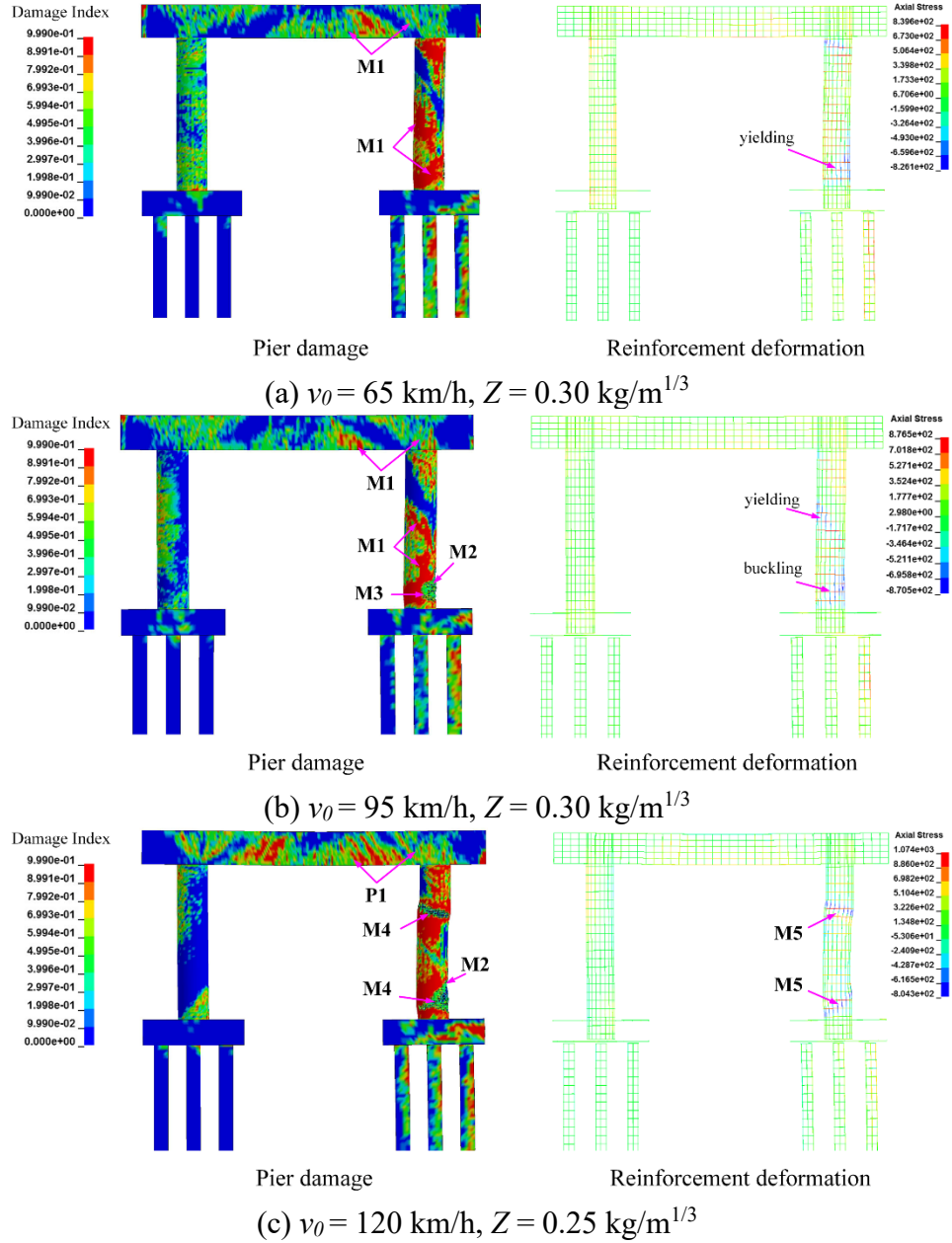


Figure 7.7 Damage and reinforcement deformation for two-column pier

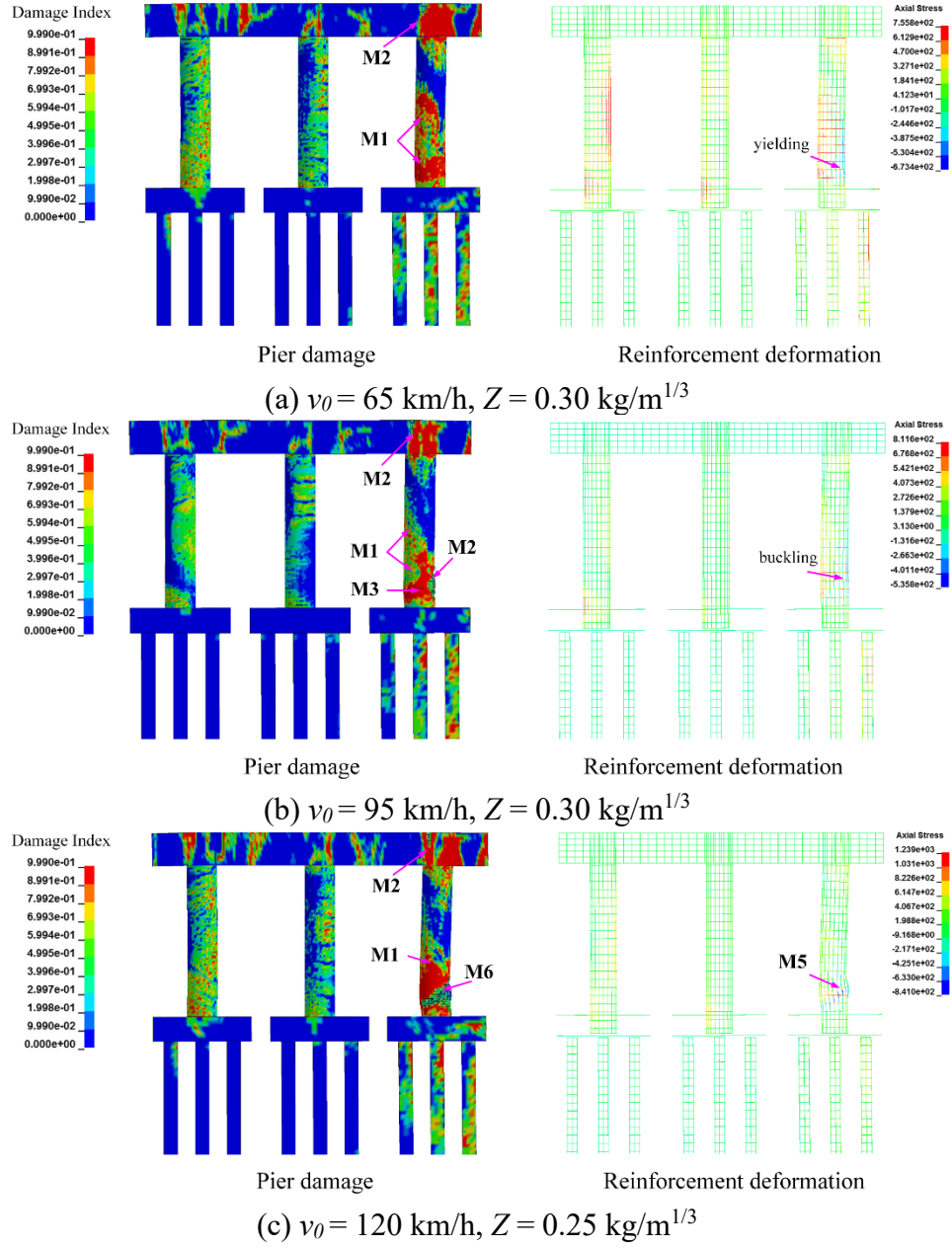


Figure 7.8 Damage and reinforcement deformation for three-column pier

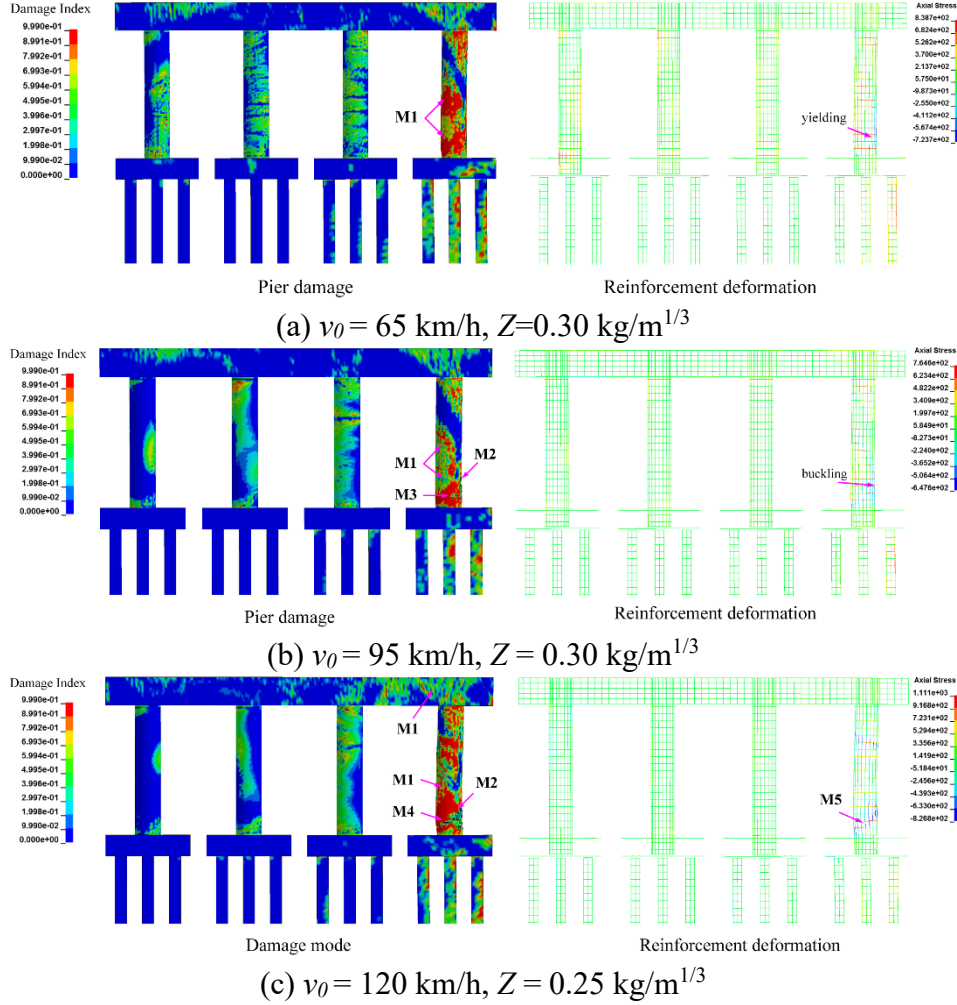


Figure 7.9 Damage and reinforcement deformation for four-column pier

7.4 Parametric studies and discussions

In a similar fashion to the parametric studies completed in Chapter 4, numerical simulations were conducted to evaluate the performance of the multi-column pier when critical parameters varied. These parameters were largely the same as those investigated in Chapter 4. In addition, the vehicle collision angle (θ_i) was also examined relative to the length of pier cap and collision location since they could more dramatically influence behavior in a multi-column pier as opposed to an isolated column.

7.4.1 Collision angle

For a highway bridge pier, most vehicle collisions are likely to occur at some angle to the pier's long axis. In this section, a collision at an angle of 0° was used as a control case. Angles of 30° , 60° , and 90° relative to the length of pier cap were also selected as shown in Figure 7.10. As presented in Section 7.3, the tow column pier was identified as being most vulnerable to combined vehicle collision and air blast and was subsequently utilized as the representative pier for the parametric studies. A collision speed of 95 km/h and an air blast at a scaled distance of $0.25 \text{ kg/m}^{1/3}$ were used as the demands as shown in Table 7.1.

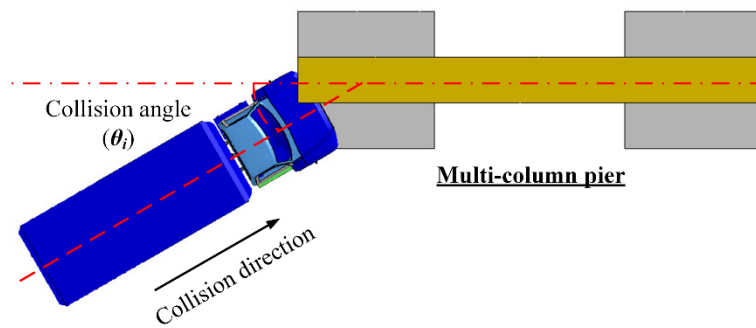


Figure 7.10 Vehicle-pier collision angle

Table 7.1 Effect of collision angle on pier response

Pier type	v_0 (km/h)	Z ($\text{kg/m}^{1/3}$)	θ_i	α_{ALE}	s_v (mm)	ρ_L	d_{max} (mm)	Damage categories
Two-column	95	0.25	0°	6%	300	1%	45	Severe damage
			30°				56	Severe damage
			60°				65.3	Severe damage
			90°				32.2	Moderate damage

Figure 7.11 depicts the final damage level for each collision angle. For the case with $\theta_i = 0^\circ$, M1, M2, M3, and M4 occurred in the impacted column and column failure occurred. For $\theta_i =$

30°, the pier remained in operation with M1, M2, and M3 observed in the impacted column and concrete spalling in the footing. For $\theta_i = 60^\circ$, M1, M2, and M3 were observed in the impacted column with shear failure of the corner at the footing. For $\theta_i = 90^\circ$, M1, M2, and M3 were produced in the impacted column and concrete cracking on the collision side of the cap. The pier remained in operation.

Figure 7.12 compares final displacements along the column height of the impacted column. Displacement in the column for the cases $\theta_i = 30^\circ$ and 60° were larger than those with $\theta_i = 0^\circ$ and 90° due to significant concrete spalling in the footing that resulted in pier instability. For the case with $\theta_i = 90^\circ$, both columns were engaged via pier cap axial stiffness, which enhanced load sharing ability and mitigated the displacement and damage. For the case with $\theta_i = 0^\circ$, the non-impacted column provided a restraint effect and generated a large shear force for the impacted column. It was noted that displacements were produced at the pier base due to interaction between the footing, piles, and surrounding soil volume.

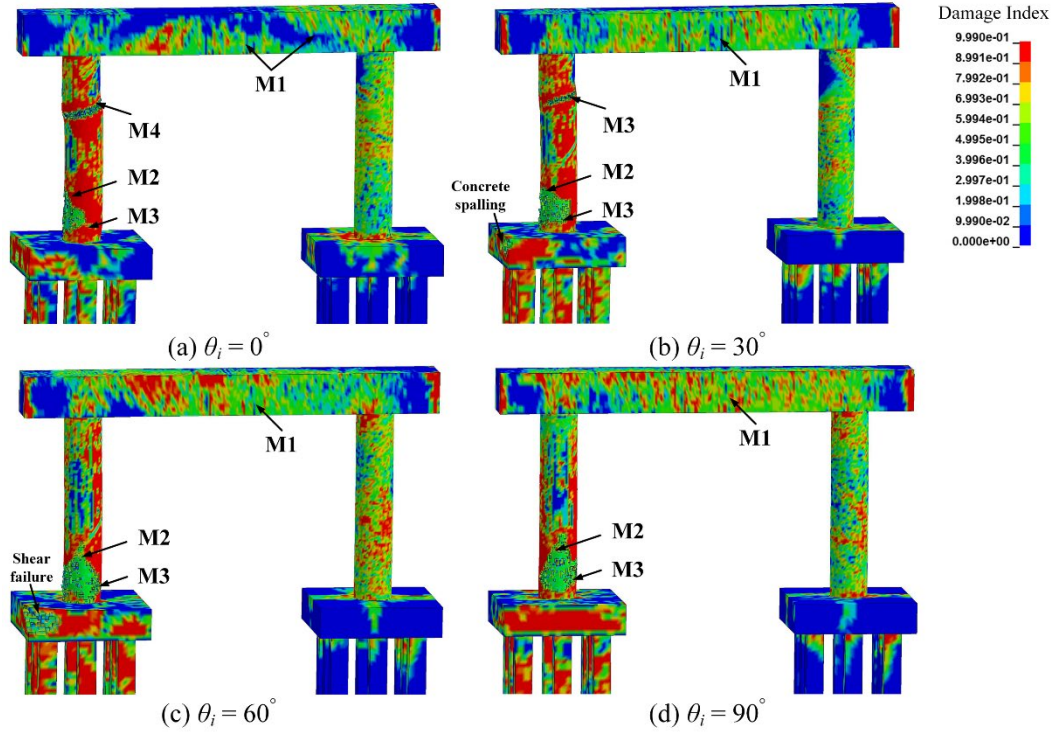


Figure 7.11 Effect of θ_i on pier damage

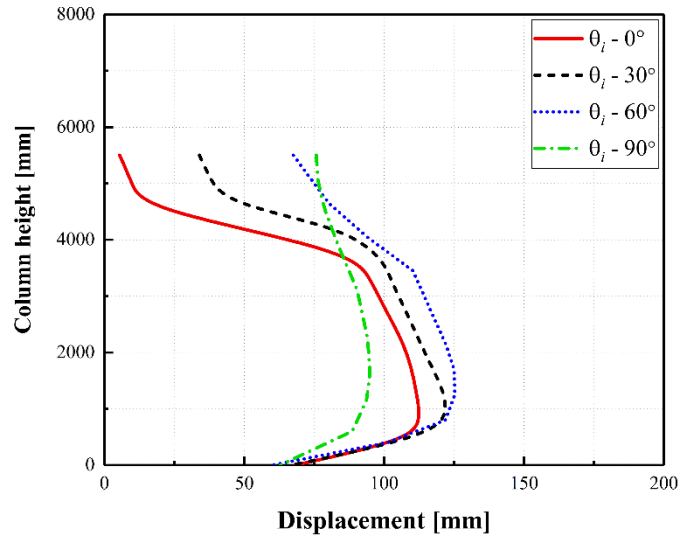


Figure 7.12 Effect of θ_i on maximum displacement of impacted column

7.4.2 Collision location

Examination of collision location encompassed evaluating performance of the three-column pier subjected to an SUT collision into the 1st, 2nd, and 3rd column in the west-east direction at an angle of 60° as shown in Figure 7.13 and outlined in Table 7.2. The three-column pier was selected because the vehicle collision with different columns presented different representative pier damage that could significantly affect pier integrity. The collision angle of 60° was identified as the worst threat case for the multi-column pier and subsequently selected in this section.

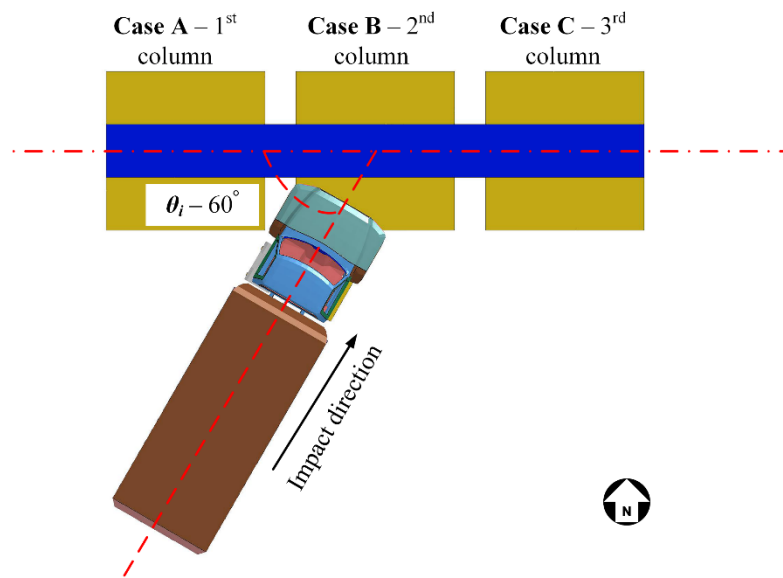


Figure 7.13 Vehicle-pier collision location

Table 7.2 Effect of collision location on pier response

Pier type	v_0 (km/h)	Z (kg/m ^{1/3})	θ_i	Impact location	s_v (mm)	ρ_L	d_{max} (mm)	Damage categories
Three-column	95	0.25	60°	1 st column	300	1%	65.4	Severe damage
				2 nd column			40.3	Severe damage
				3 rd column			63.5	Severe damage

Figure 7.14 depicts final damage levels for each collision case. For all three cases, M1, M2, and M3 occurred in the impacted column. For cases A and C, concrete spalling occurred in the pier cap above the columns and shear failure of the corner was observed in the footing. The piers performed at an unsafe condition and repairs would be needed to avoid collapse. For case B, shear failure occurred in the pier cap with significant spalling at mid-span. The collision with the 2nd column produced a significant tensile force at the mid-span to deteriorate concrete spalling in the pier cap. Repairs would be needed to ensure the pier integrity.

Figure 7.15 compares final displacements along the height of the impacted column. Displacements in the column were higher during case B since all three columns were engaged by the pier cap and it led to an enhanced pier ability to share the collision load. Furthermore, shear failure in the footing for cases A and B resulted in pier instability and increased column displacements.

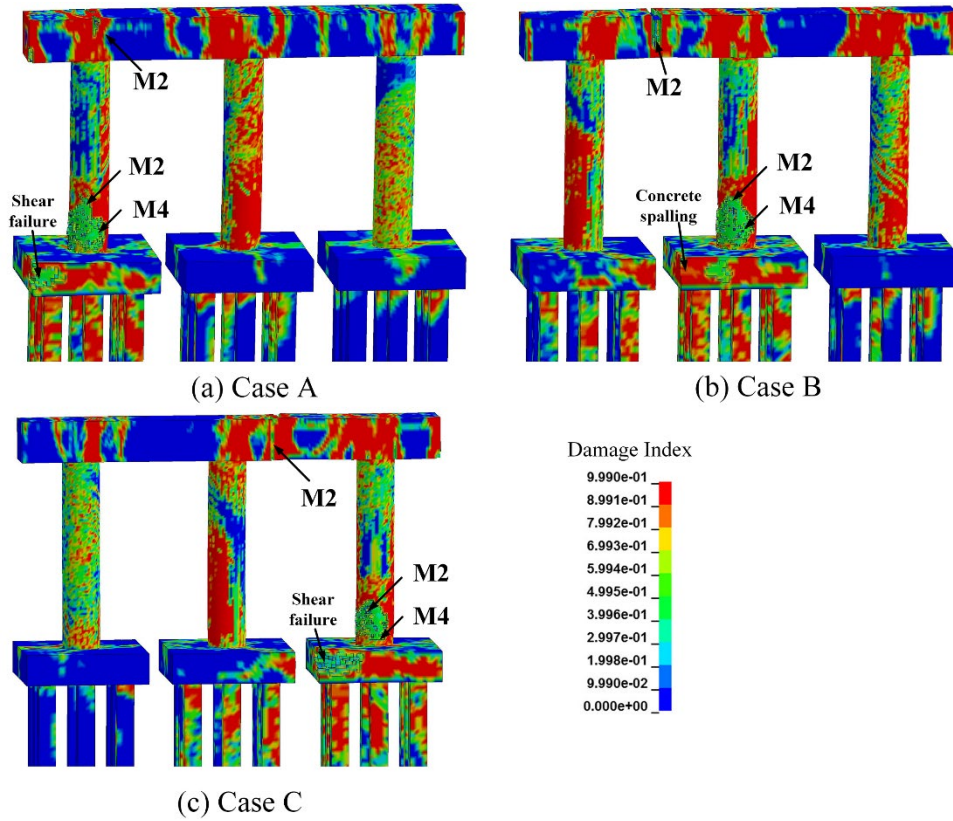


Figure 7.14 Pier damage for three collision locations

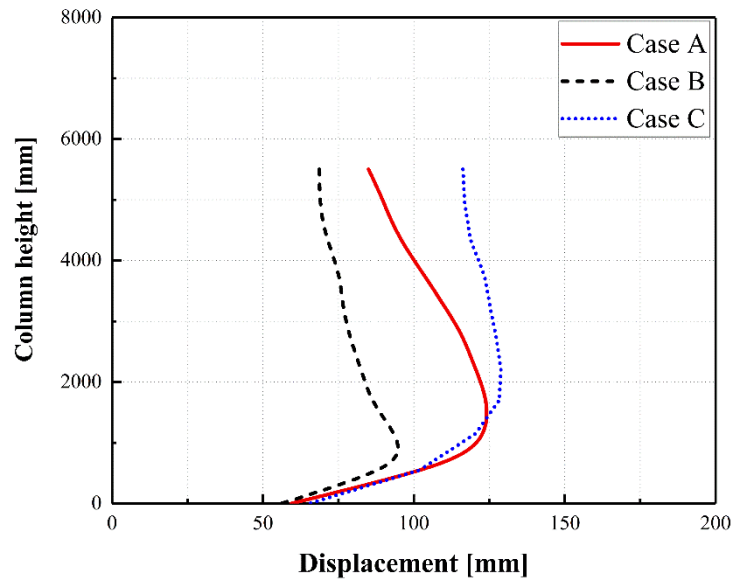


Figure 7.15 Maximum displacement of impacted column with three collision locations

7.4.3 Axial load ratio

Axial load ratios of 0%, 6%, and 12% were applied at the top of the cap as outlined in Table 7.3. These ratios matched those used in Section 4.3.

Table 7.3 Effect of axial load ratio on pier response

Pier type	v_0 (km/h)	Z (kg/m ^{1/3})	θ_i	α_{ALE}	s_v (mm)	ρ_L	d_{max} (mm)	Comments
Two column	95	0.25	0°	0%	300	1%	55	Severe damage
				6%			45	Severe damage
				12%			40	Severe damage

Figure 7.16 compares final damage states by varying axial load ratio. For the cases with $\alpha_{ALE} = 0\%$ and 6% , the pier performed at an unsafe condition as the impacted column sustained M1, M2, and M4 in the collision region. The damaged column should be repaired to avoid pier collapse. For the case with $\alpha_{ALE} = 12\%$, M1, M2 and M4 occurred at the base of the impacted column with M2 at the top. The impacted column should be repaired to avoid pier collapse. Compared to cases with $\alpha_{ALE} = 0\%$ and 6% in which shear failure occurred at the top of impacted column, when $\alpha_{ALE} = 12\%$, shear failure occurred at the column base. The increased axial load at the top resulted in the increased shear and bending capacity of the pier, but could amplify the column damage from plastic hinge to direct shear failure at the column base. Figure 7.17 compares final displacements along the impacted column height. The increased axial load produced a slight decrease in the displacement of the pier due to the increased column resistance from the pre-compression. At a 12% axial load ratio the impacted column failed due to shear in the collision region as the limit state shifted from the plastic hinge to a direct shear failure, negatively influencing the column performance.

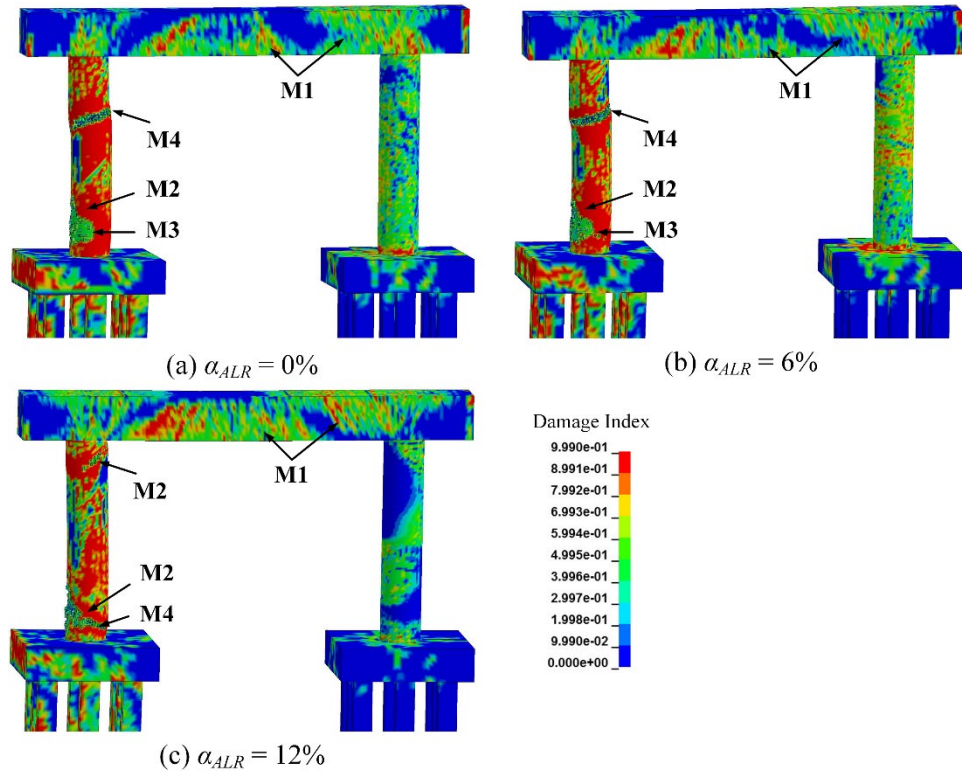


Figure 7.16 Effect of α_{ALE} on pier damage

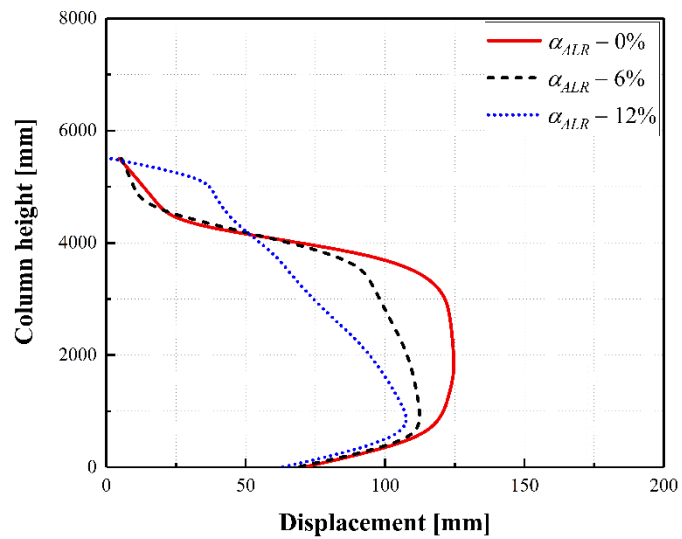


Figure 7.17 Effect of α_{ALE} on maximum displacement of impacted column

7.4.4 Shear reinforcement (hoop) spacing

Hoop spacings of 100 mm, 200 mm, and 300 mm were designed for all columns and examined as outlined in Table 7.4. Their spacings matched those studied for the isolated column in Section 4.3.

Table 7.4 Effect of hoop spacing on pier response

Pier type	v_0 (km/h)	Z (kg/m ^{1/3})	θ_i	α_{ALE}	s_v (mm)	ρ_L	d_{max} (mm)	Damage categories
Two column	95	0.25	0°	6%	100	1%	24.2	Minor damage
					200		31	Moderate damage
					300		45	Severe damage

Figure 7.18 shows final damage states for various hoop spacings. Smaller spacing decreased the amount of spalled concrete and buckled reinforcements. For the pier with $s_v = 300$ mm, M1, M2, and M4 were observed in the impacted column and column failure occurred. The pier performed at an unsafe condition and needed repairs for the impacted column. As s_v decreased to 200 mm, M1, M2, and M3 occurred in the impacted column. This pier could remain in operation but repair would be needed to ensure structural integrity. At $s_v = 100$ mm, impacted column sustained M1 and M2 and the pier was deemed operational. Figure 7.19 compares final displacements along the height of the impacted column. As expected, the decreased hoop spacing produced a decrease in the hoop displacement. A decrease in hoop spacing provides the increased constraint on the core concrete and the improved restraint against reinforcement buckling, resulting in the increased resistance and stiffness of the column. The enhanced column increased the pier integrity and improved the pier performance.

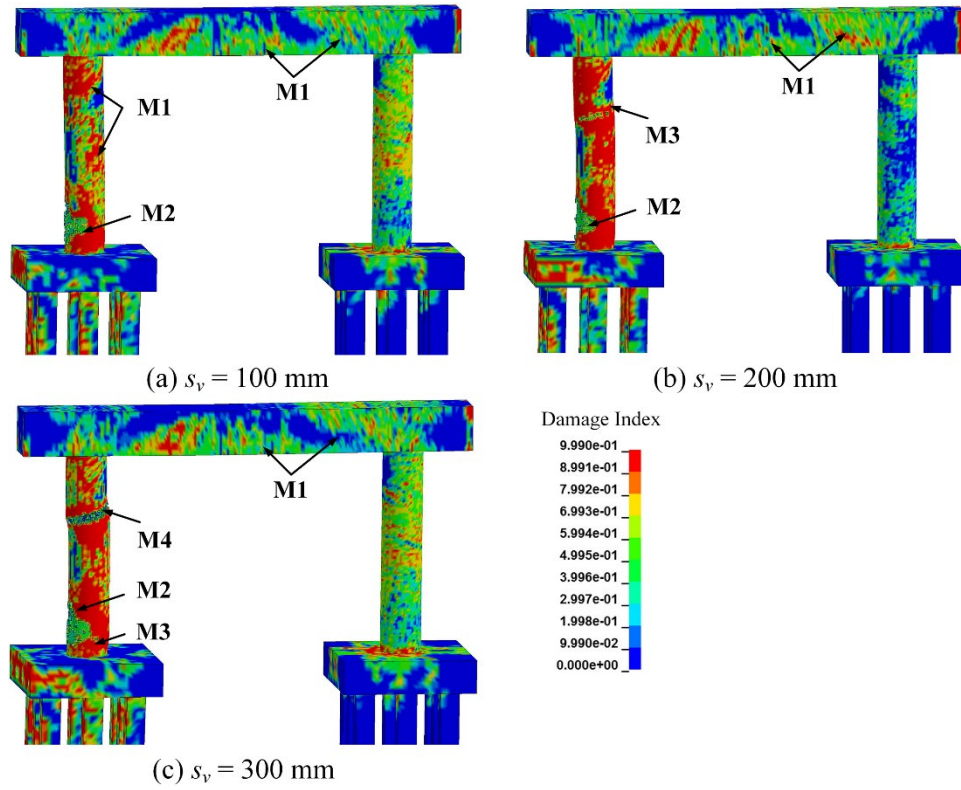


Figure 7.18 Effect of s_v on pier damage

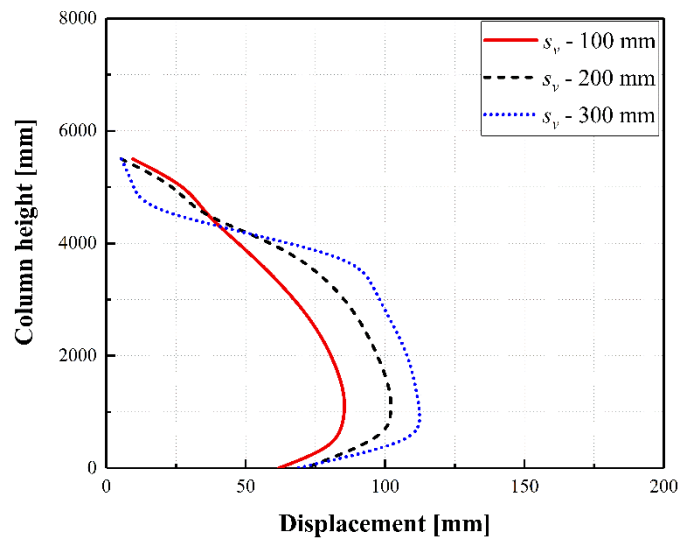


Figure 7.19 Effect of s_v on maximum displacement of impacted column

7.4.5 Longitudinal reinforcement ratio

In similar fashion to Section 4.3, longitudinal reinforcement ratios of 1%, 2%, and 3% for all columns were examined as outlined in Table 7.5

Table 7.5 Effect of longitudinal reinforcement ratio on pier response

Pier type	v_0 (km/h)	Z (kg/m ^{1/3})	θ_i	α_{ALE}	ρ_L	s_v (mm)	d_{max} (mm)	Comments
Two column	95	0.25	0°	6%	1%	300	45	Severe damage
					2%		32.3	Minor damage
					3%		19	Minor damage

Figure 7.20 depicts final damage levels by varying longitudinal reinforcement ratio. The increased longitudinal reinforcement ratio decreased the amount of spalled concrete and mitigated longitudinal reinforcement buckling. For the pier with $\rho_L = 1\%$, the impacted column sustained M1, M2, and M4 in the collision region and failed. The pier performed at an unsafe condition and needed repairs. For $\rho_L = 2\%$ and $\rho_L = 3\%$, M1 and M2 occurred in the impacted column, and these piers performed in operation. Figure 7.21 compares final displacements along the impacted column height by varying longitudinal reinforcement ratio. As expected, the increased longitudinal reinforcement ratio produced the decreased displacement, identifying the decreased damage in the pier. Increasing the longitudinal reinforcement ratio is advantageous to improve column stiffness, capacity, and pier integrity.

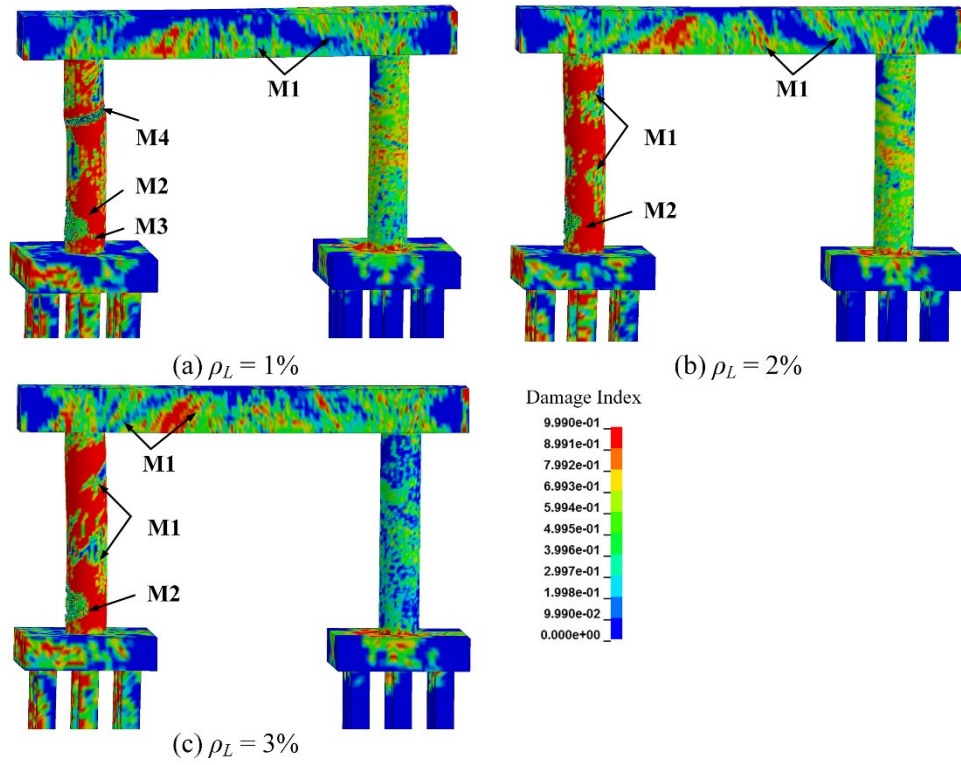


Figure 7.20 Effect of ρ_L on pier damage

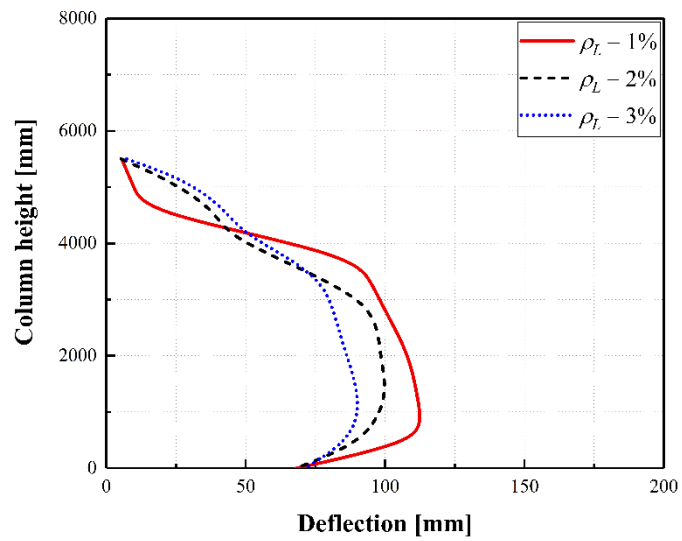


Figure 7.21 Effect of ρ_L on maximum displacement of impacted column

7.5 Multi-column pier retrofit

The effectiveness of using carbon fiber reinforced polymer (CFRP) or polyurea to mitigate damage to multi-column piers subjected to vehicle collision and blast was examined. Implemented modeling schemes for CFRP and polyurea matched those described in Chapter 6. To compare the effectiveness of retrofitting piers using CFRP wrap and polyurea coating, two, three, and four column piers were examined. Piers were subjected to an SUT collision at a speed of 95 km/h and an air blast at a scaled distance of $0.25 \text{ m/kg}^{1/3}$. Columns were wrapped along their height using 3 mm of CFRP or coated using 9 mm of polyurea, with thicknesses selected based on numerical results from Chapter 6 that examined axial capacity equivalencies.

Figure 7.22 compares final damage states for bare, CFRP-wrapped, and polyurea-coated piers. Damage reduced considerably using either CFRP wrap or polyurea coating. The bare columns in the three and four column piers sustained M4 at their bases. These piers could remain in operation, but the damaged column would need extensive repair or replacement. M2, M3, and M4 were observed in the impacted column of the two-column pier, which was considered unsafe. All piers retrofitted using either CFRP wrap or polyurea coating sustained M2 at the base of the impacted column and received damage that was repairable under operational conditions. For the multi-column piers examined in this study, the CFRP wrap and polyurea coating had similar retrofit effectiveness to reduce the pier damage and improve pier performance.

Figure 7.23 compares impacted column final displacement. CFRP-wrapped column displacement was approximately 35% less than the bare column and 18% less than the polyurea-coated column. Figure 7.24 compares column maximum kinetic energy. The kinetic energy for the CFRP-wrapped column was approximately 10% lower than that for the polyurea-coated column, identifying more energy dissipated by the CFRP wrap. As a result, using CFRP wrap is

more efficient for reducing pier displacement and absorbing energy than applying the polyurea coating. Compared to the polyurea coating, the CFRP wrap had a higher stiffness that provides efficient confinement on columns to improve column strength and shear strength to directly increase column shear resistance. However, all examined piers retrofitted with either CFRP wrap and polyurea coating sustained concrete spalling in the collision region, and these piers could remain in operation. Also, the decrease in the column displacement and kinetic energy was not prominent when the retrofit scheme changed from the CFRP wrap to the polyurea coating. Thus, the CFRP wrap effectiveness is close to the polyurea effectiveness for mitigating collision and blast effects for the piers examined in this study to ensure pier integrity.

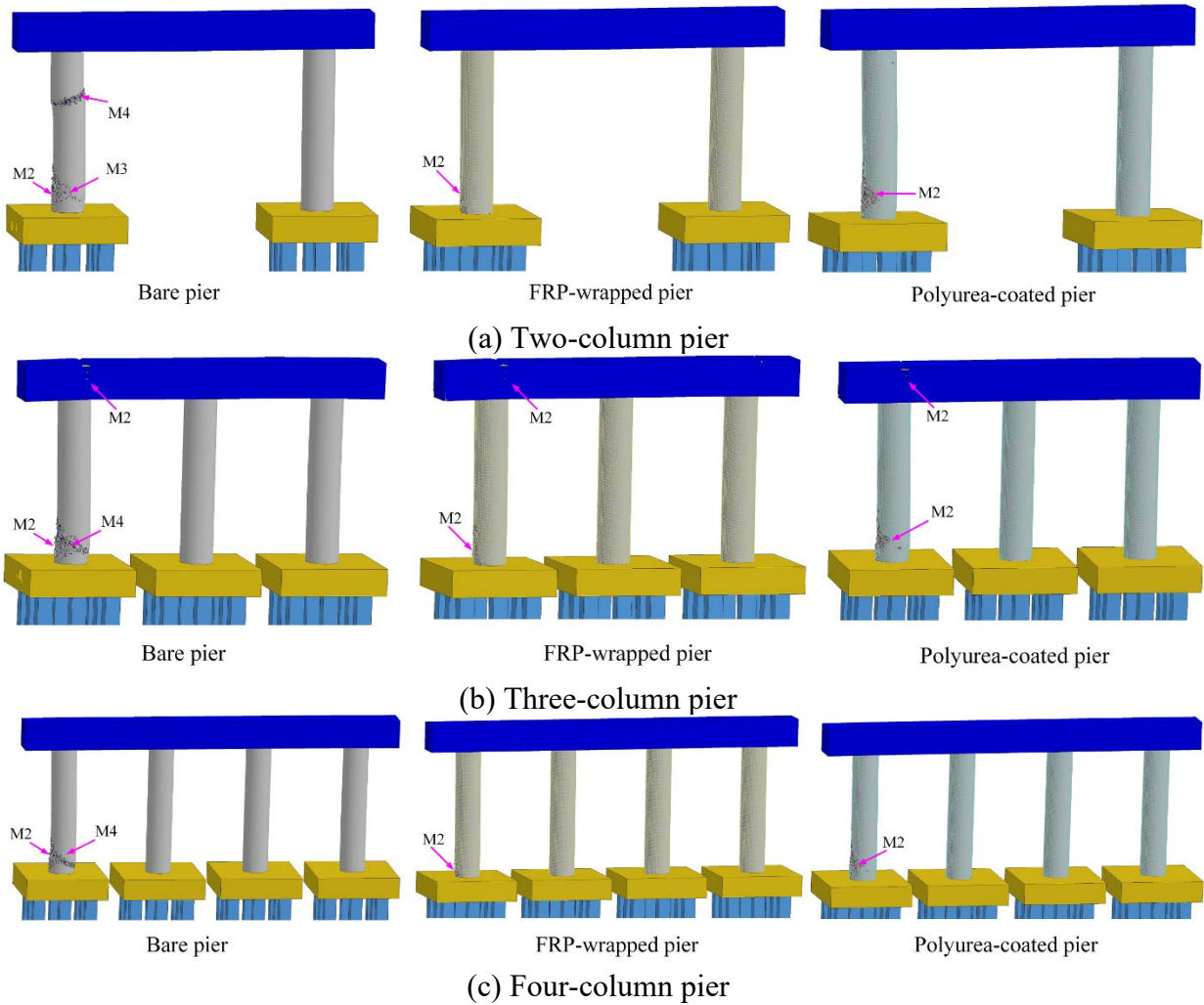


Figure 7.22 Comparison of pier damage for CFRP and polyurea retrofit schemes

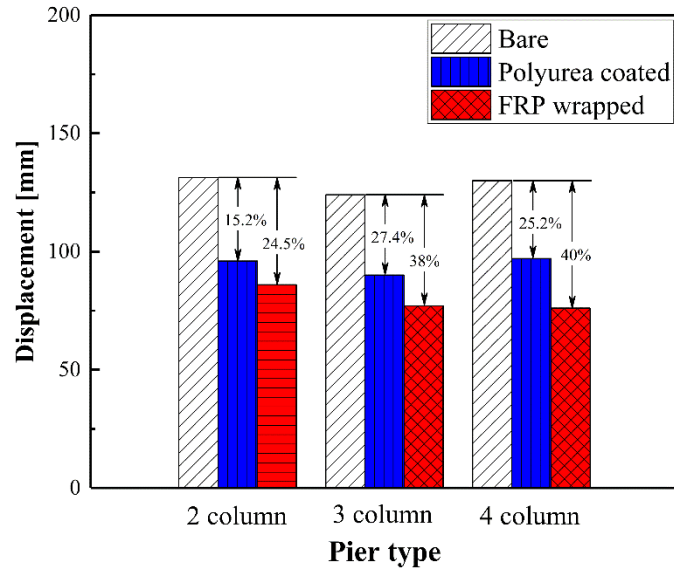


Figure 7.23 Comparison of displacement for CFRP and polyurea retrofit schemes

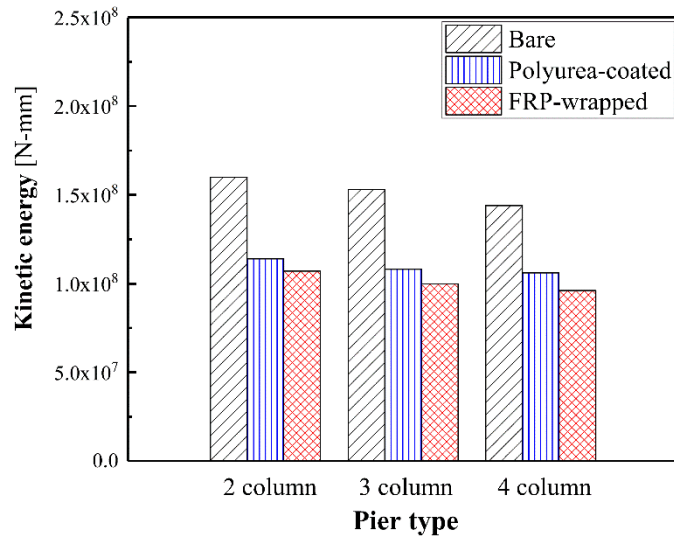


Figure 7.24 Comparison of column kinetic energy for CFRP and polyurea retrofit schemes

7.6 Conclusions

This chapter summarized numerical simulations of a multi-column pier subjected to combined vehicle collision and air blast. Simulations were used to examine the response of the multi-column piers and to conduct parametric studies that looked at the effects of collision angle, collision location, axial load ratio, and longitudinal and shear reinforcement ratios on the pier performance. The effectiveness of in-situ retrofit schemes using FRP wrap and polyurea coating were also explored, with multiple placement options being examined. Results from the studies indicated that:

- (1) Damage to the impacted column increased with higher impact velocity and blast loads. The two-column pier was vulnerable to combined collision and blast, while the three and four column piers were unlikely to collapse with the pier cap connecting all columns.
- (2) Increasing the longitudinal and shear reinforcement improved pier performance, columns had a larger axial load ratio due to higher dead loads, and the structure better resisted imposed collision and blast demands.
- (3) Vehicle collision angle into the column influenced pier performance, with pier damage shifting from impacted column failure to the development of a plastic hinge as collision angles changed from being parallel to the pier's longitudinal axis to being perpendicular to this axis. For the case $\theta_i = 0^\circ$, the pier integrity was compromised due to the failure of the impacted column. At $\theta_i = 30^\circ$ and 60° , pier integrity was compromised due to shear failure of the in footing corner. At $\theta_i = 90^\circ$, the pier remained in operation due to enhanced load sharing ability.

- (4) Wrapping or coating the entire height of all pier columns can effectively mitigate the effects of combined collision and blast.
- (5) CRFP thickness influenced behavior, with a thicker wrap reducing damage caused by the collision and blast. For the variables and demands examined, increased polyurea thickness also affected pier performance.
- (6) For the multi-column piers examined in this study, the effectiveness of CFRP wrap with 3 mm thickness was close to the polyurea effectiveness with a 9 mm thickness for mitigating collision and blast effects on the pier performance to ensure the pier integrity.

Chapter 8 Conclusions and On-going Research

8.1 Introduction

In summary, the research study focused on the round, RC, bridge piers subjected to combined vehicle collision and air blast. The objectives of this study were to improve resilience and robustness of bridge piers for collision and blast combination events and to develop numerical models to examine the performance of bridge columns and evaluate the effectiveness of different in-situ retrofit schemes on collision and blast mitigation. To achieve the research goal, numerical investigations were conducted that included the development of detailed bridge column and pier models, the validation of developed model, parametric studies that examined effects of specific design parameters on the performance of bridge column and pier, and the investigation of in-situ retrofit schemes for bridge pier resistance to the combined collision and blast.

8.2 Findings

For the research study, three-dimensional finite models of RC bridge columns and piers, their supporting footings, and piles were developed with the soil volume restraining the base and the air domain being used to create air blast. Reasonable material models for the concrete, reinforcement, soil, air, and TNT were selected. The numerical model was validated by comparing simulated results against the experimental data using two separate test programs reported in the open literature. The pier model was subjected to simulate Ford F800 SUT collision and air blast represented using LS-DYNA's MM-ALE approach. Pier response to vehicle collision and air blast was first examined, and parametric studies were conducted. Based on these results, a performance-based design and analysis framework was proposed and studied

for RC bridge columns under combined collision and blast events. Effectiveness of retrofit schemes using FRP or polyurea coating was investigated to improve pier performance.

8.2.1 Isolated column

8.2.1.1 Isolated column response:

- The selected modeling approaches were validated against experimental results, which identified their accuracy in predicting the response of RC members subjected to collision and blast.
- Vehicle collision followed by air blast was the critical sequence for demand ranges and combinations examined.
- During a collision-blast combination event, identified column damage states included: (a) plastic deformation with concrete cover spalling; (b) plastic hinge formation in the collision region; (c) the onset of column shear failure; and (d) shear failure with coupled concrete crushing, as listed in Table 8.1. For the six categories identified, concrete breach and direct shear failure were determined to be the top results in column failure.

Table 8.1 Identified damage state

Damage state	Plastic deformation	Plastic hinge formation	onset of shear failure	Shear failure
Column damage	M1, M2	M1, M2, M3	M1, M2, M4, M5	M1, M2, M5, M6

- For the column diameters examined, the 750 mm diameter column was vulnerable to the collision and blast combination. Except for the highest combination of collision and blast, the 1050 mm diameter columns were largely able to continue

to carry loads in their final, damaged states. The 1350 mm diameter column performed operationally to carry loads for all examined collision-blast combinations.

- Parametric studies showed that increase in the column diameter, longitudinal reinforcement ratio, and shear reinforcement improved column resistance to collision and blast loads, as listed in Table 8.2.
- The influence of column height on column performance was largely insignificant when the collision and blast combination was applied near the column base studied in this research.
- Increase in axial load imposed at the column top increased column bending capacity and shear strength and improved column resistance to collision and blast loads. A higher axial load would amplify column damage with the occurrence of plastic hinge in the collision region.

Table 8.2 Effects of specified design parameters

Desired effect	Diameter	Height	Longitudinal reinf. ratio	Shear reinf. Spacing	Axial load ratio
Decreased concrete erosion ratio	Increase	Slight effect	Inconclusive	Decrease	Inconclusive
Decreased buckled longitudinal reinf. ratio	Increase	Slight effect	Increase	Decrease	Inconclusive
Decreased column deflection	Increase	Slight effect	Increase	Decrease	Inconclusive
Increased residual axial capacity	Increase	Slight effect	Increase	Decrease	Slight increase
Recommendations for column	Increase	Slight effect	Increase (with sufficient shear reinforcement)	Decrease	Inconclusive

- An empirical equation was developed to estimate column residual axial capacity for the combined collision and blast events.

8.2.1.2 Isolated column performance:

- Column performance level classifications included immediate use, damage control, collapse prevention. The classifications corresponded to minor, moderate, and severe states for the combined collision and blast events, as listed in Table 8.3. A damage index in terms of residual axial capacity and column nominal axial capacity was used to quantitatively estimate and evaluate damage states.
- A performance-based design and analysis framework was developed for RC highway bridge columns when subjected to combined vehicle collision and air blast, which gives a straightforward approach to achieve a balance of economic design and desired performance objective.

Table 8.3 Performance-based design criteria for combined collision and blast

Performance level		Damage state	Damage description	ξ_{DI}
P1	Immediate use	Minor damage	Minor concrete cover spalling or cracking, minor yielding of longitudinal reinforcement	0~0.3
P2	Damage control	Moderate damage	Significant concrete spalling, minor concrete core cracking, reinforcement buckling	0.3~0.8
P3	Collapse prevention	Severe damage	Significant deterioration of core concrete, loss of axial load capacity	0.8~1.0

- Column performance improved using CFRP wrap or polyurea coating.
- For the variables and demands examined, thickness most significantly influenced the effectiveness of the CFRP wrap to improve column performance based on

Table 8.4. The influence of CFRP strength on retrofit effectiveness was largely insignificant for the variable and demands examined.

- For the variables and demands examined, increased polyurea thickness also affected column performance. The most dramatic effects were from changes in polyurea thickness that occurred between 9 and 12 mm.

Table 8.4 Effects of controlling parameters for retrofit schemes

Desired effect	CFRP strength	CFRP thickness	Polyurea thickness
Reduced column damage	No effect	2 mm→ 3 mm, severe → moderate; 6 mm→ 9 mm, moderate→ minor	9 mm→ 12 mm, severe → moderate;
Improved column performance	No effect	2 mm→3 mm, failure → remaining operational; 6 mm→9 mm, remaining operational → in operation	9 mm→ 12 mm, failure → remaining operational
Decreased column displacement	No effect	Increase	Increase
Increased residual axial capacity	No effect	Increase	Increase
Decreased column kinetic energy	No effect	increase	increase

- Comparison of CFRP wrap and polyurea coating in Table 8.5 indicated that, for the 750 mm and 900 mm diameter column, the CFRP wrap is the preferred retrofit scheme due to its high stiffness and strength to enhance column resistance. For the 1050 mm diameter column, the CFRP wrap and polyurea coating have similar effectiveness.

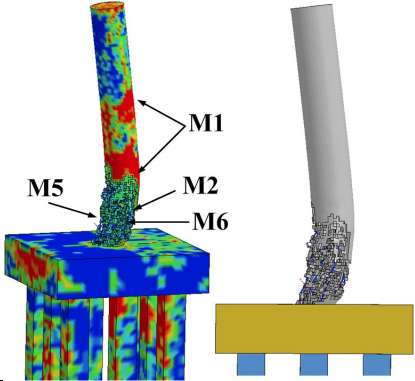
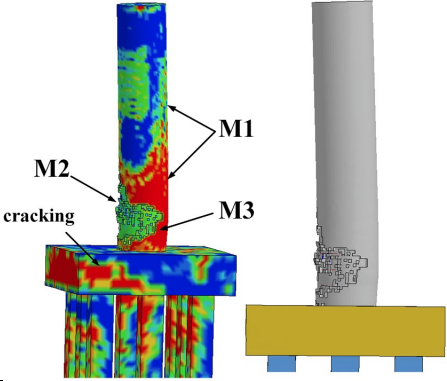
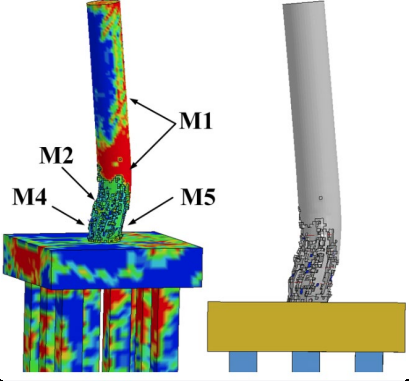
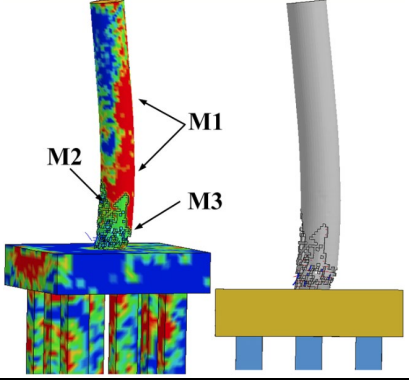
Table 8.5 Comparison of CFRP wrap and polyurea coating

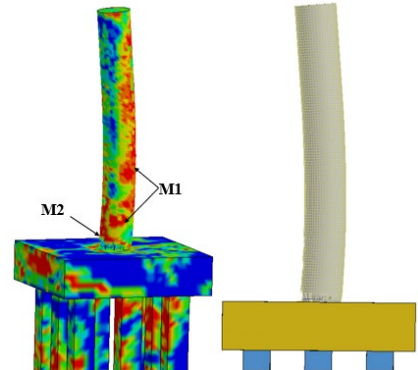
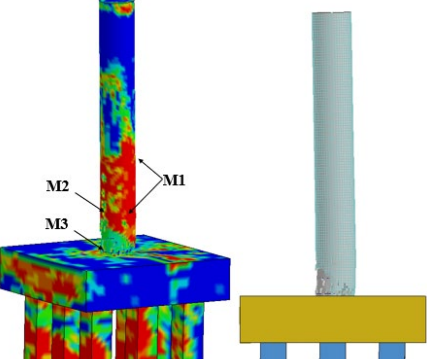
Column diameter	750 mm		900 mm		1050 mm	
	CFRP	Polyurea	CFRP	Polyurea	CFRP	Polyurea
Column damage	Moderate	severe	Moderate	Moderate	Minor	Minor
Column displacement*	Reduced 32%	Reduced 15%	Reduced 36%	Reduced 20%	Reduced 30%	Reduced 24%
Column kinetic energy*	Reduced 40%	Reduced 23%	Reduced 43%	Reduced 25%	Reduced 33%	Reduced 28%
Suggestion	CFRP wrap		CFRP wrap		Similar effectiveness	

Note: *Compared to bare column

- Investigation of column response and detailing under combined collision and blast provided useful information for both retrofitting existing and constructing new columns, as listed in Table 8.6. When designing or retrofitting the column, several alternatives could be selected to improve column performance when subjected to collision and blast. Increasing the column diameter and shear reinforcement ratio could achieve the same performance level for the column using CFRP wrap or polyurea coating.

Table 8.6 Comparison of controlling design parameter and retrofit schemes
 $(v_0 = 120 \text{ km/h; } Z = 0.25 \text{ m/kg}^{1/3})$

750 mm diameter	Damage	Performance level	Deflection
Bare column		P3 – collapse prevention	325 mm
Increased D ($D = 1050 \text{ mm}$)		P2 – damage control	43 mm
Increased ρ_L ($\rho_L = 3\%$)		P3 – collapse prevention	233 mm
Decreased s_v ($s_v = 100 \text{ mm}$)		P2 – damage control	120 mm

750 mm diameter	Damage	Performance level	Deflection
CFRP wrap ($t_{FRP} = 9$ mm)		P1 – immediate use	105 mm
Polyurea coating ($t_{Pol} = 15$ mm)		P2 – damage control	112 mm

8.2.2 Multi-column pier

8.2.2.1 Multi-column pier response:

- The twin-column pier was susceptible to the column failure, and the three-column and four-column piers appeared to be unlikely to collapse with the pier cap connecting all columns to increase the pier integrity.
- Vehicle collision angle into the column influenced pier performance, with pier damage shifting from impacted column failure to the development of a plastic hinge as collision angles changed from being parallel to the pier's longitudinal axis to being perpendicular to this axis.

- The response of the three-column pier examined in this study varied with SUT impact on a different column. For all three cases, M1, M2, and M3 occurred in the impacted column. When SUT impacted side columns, the pier integrity was compromised due to shear failure in footing. For the SUT collision with the middle column, the pier integrity was damaged with shear failure in the pier cap.

8.2.2.2 Multi-column pier performance:

- Increasing the longitudinal and shear reinforcement improved pier performance and columns had a larger axial load ratio due to higher dead loads being better at resisting imposed collision and blast demands.
- Using FRP wrap and polyurea coating on bridge columns can effectively increase pier resistance and promote energy dissipation compared to a bare pier, thus mitigating effects of combined collision and blast.
- The full wrapping scheme through entire columns was more effective to improve pier performance compared to the polyurea coating scheme.
- CRFP thickness influenced behavior, with a thicker wrap reducing damage caused by the collision and blast. For the variables and demands examined, increased polyurea thickness also affected pier performance.
- For the multi-column piers examined in this study, the effectiveness of CFRP wrap with 3 mm thickness was close to the polyurea effectiveness with a 9 mm thickness for mitigating collision and blast effects on the pier performance to ensure the pier integrity.

8.3 On-going Research

While findings and tools developed during Phases 1 and 2 were certainly of benefit to science and bridge design practice, the focus of Phase 3 work in relation to the MATC research portfolio will be methods to reduce and potentially eliminate negative effects from crashes into a bridge pier that are accompanied by air blast and fire. Further research is needed to ensure that a reasonable, not excessive, level of conservatism exists with recommended analysis methods and designs and/or retrofits when subjected to aforementioned multiple hazards. Tasks proposed for Phase 3 will address these items and add considerable information to bridge engineering and infrastructure material bodies-of-knowledge, especially as they relate to: material behavior under high strain rates and excessive temperatures; rate-based effects on bridge system sub- and superstructure response under high strain rates and fire; and how system robustness influences response to multiple hazards. The on-going research studies will expand on work completed during phases 1 and 2 by:

- Expanding Phases 1 and 2 literature searches to include:
 - a. Studies completed in the public domain that focus on bridge system response to multiple hazards and methods to enhance system resiliency.
 - b. Studies completed in the public domain that investigate the performance of reinforced concrete structural elements subjected to blast and impact after or before being exposed to fire.
 - c. Studies completed in the public domain that inspect material behavior under high strain rates and extreme temperature.

- d. Studies completed in the public domain that further examine development and implementation of techniques used to enhance bridge resistance to blast, impact, and temperature demands.
- Expanding computational studies that advance work completed for Phases 1 and 2 to include those that:
 - a. Analytically investigate the performance of uncoated and FRP/polyurea-coated single and multiple bridge pier columns and the entire bridge system subjected to combined blast, impact, and fire loads with pressure, temperature, and material response time-histories being investigated.
 - b. Use validated bridge system and surrounding soil finite element models, and complete parametric studies that examine representative bridge system response to multiple hazards that include impact, blast, extreme temperature, and their combinations.
 - c. Use models parametrically to improve upon findings from Phases 1 and 2 so that reasonable, not excessive, levels of conservatism exist with recommended analysis methods and designs and/or retrofits.
- Expanding and refining Phases 1 and 2 design aids and language based on findings from studies discussed above for potential adoption in relevant codes and specifications.
- Developing, submitting, and revising the report detailing previous tasks and findings.

References

1. Tennessean News. *Tennessean News Archive*. 2014 [cited 2012 August 15th]; Available from: <https://www.tennessean.com/story/news/local/williamson/2014/08/15/franklin-tanker-explosion-65/14097717/>.
2. AASHTO, "AASHTO LRFD bridge design specifications, eighth edition." 2017: Washington, DC.
3. Abdelkarim, O.I. and M.A. ElGawady. 2017. "Performance of bridge piers under vehicle collision." *Engineering Structures*. 140: pp. 337-352.
4. AuYeung, S. and A. Alipour. 2016. "Evaluation of AASHTO Suggested Design Values for Reinforced Concrete Bridge Piers Under Vehicle Collisions." *Transportation Research Record: Journal of the Transportation Research Board*.(2592): pp. 1-8.
5. Buth, E.C., M.S. Brackin, W.F. Williams, and G.T. Fry, "Collision loads on bridge piers: phase 2, report of guidelines for designing bridge piers and abutments for vehicle collisions." 2011, Texas Transportation Institute.
6. Buth, E.C., W.F. Williams, M.S. Brackin, D. Lord, S.R. Geedipally, and A.Y. Abu-Odeh. 2010. "Analysis of large truck collisions with bridge piers: phase 1. Report of guidelines for designing bridge piers and abutments for vehicle collisions." Texas: Texas Transportation Institute.
7. Linzell, D.G., C. Fang, Y.R. Kim, and G.M. Nsengiyumva, "Protecting Critical Civil Infrastructure Against Impact from Commercial Vehicles, Phase I." 2019, Mid-American Transportation Center: Lincoln, Nebraska.
8. Mohan, P., D. Marzougui, and C.D.S. Kan. 2007. "Validation of a single unit truck model for roadside hardware impact." *International Journal of Vehicle Systems Modelling and Testing*. 2(1): pp. 1-15.
9. Carrigan, C.E. and M.H. Ray, "Assessment of the MASH Heavy Vehicle Weights for Field Relevancy." 2017.
10. Miele, C., C. Plaxico, J. Kennedy, S. Simunovic, and N. Zisi. 2005. "Heavy vehicle infrastructure asset interaction and collision." National Transportation Research Center, Knoxville, TN.
11. Hallquist, J., "LS-DYNA keyword user's manual, version 971." in *Livermore Software Technology Corporation*. 2007: Livermore, CA.
12. Crowl, W. 1969. "Structures to resist the effects of accidental explosions, technical manual TM 5-1300." US Army, Navy and Air Force, US Government Printing Office, Washington DC.

13. Williamson, E.B. 2010. "*Blast-resistant highway bridges: design and detailing guidelines*. Vol. 645. Transportation Research Board.
14. Brown, M. and A. Lowe. 2003. "*Reference Manual to Mitigate Potential Terrorist attacks against Buildings, Federal Emergency Management Agency (FEMA)*." Risk Management Series. 426.
15. Murray, Y.D., "*Users manual for LS-DYNA concrete material model 159*." 2007, U.S. Department of Transportation: McLean, VA.
16. Coughlin, A., E. Musselman, A. Schokker, and D. Linzell. 2010. "*Behavior of portable fiber reinforced concrete vehicle barriers subject to blasts from contact charges*." International Journal of Impact Engineering. 37(5): pp. 521-529.
17. Murray, Y.D., A.Y. Abu-Odeh, and R.P. Bligh, "*Evaluation of LS-DYNA concrete material model 159*." 2007, U.S. Department of Transportation: McLean, VA.
18. Sharma, H., S. Hurlebaus, and P. Gardoni. 2012. "*Performance-based response evaluation of reinforced concrete columns subject to vehicle impact*." International Journal of Impact Engineering. 43: pp. 52-62.
19. O'Hare, E.V. 2011. "*Computational Assessment of Steel-Jacketed Bridge Pier Column Performance Under Blast Loads*."
20. Malvar, J.L. and J.E. Crawford. 1998 "Dynamic increase factors for steel reinforcing bars." in *28th DDESB Seminar. Orlando, USA*.
21. Lewis, B.A., "*Manual for LS-DYNA soil material model 147*." 2004.
22. Jayasinghe, L.B., D.P. Thambiratnam, N. Perera, and J. Jayasooriya. 2013. "*Computer simulation of underground blast response of pile in saturated soil*." Computers & Structures. 120: pp. 86-95.
23. Koneshwaran, S., D.P. Thambiratnam, and C. Gallage. 2015 "Blast response of segmented bored tunnel using coupled SPH-FE method." in *Structures*. Elsevier.
24. Reid, J., B. Coon, B. Lewis, S. Sutherland, and Y. Murray, "*Evaluation of LS-DYNA soil material model 147*." 2004.
25. Agrawal, A.K., S. El-Tawil, R. Cao, X. Xu, X. Chen, and W. Wong, "*A Performance-Based Approach for Loading Definition of Heavy Vehicle Impact Events*." 2018, United States. Federal Highway Administration. Office of Research
26. Agrawal, A.K., G.Y. Liu, and S. Alampalli. 2013 "Effects of truck impacts on bridge piers." in *Advanced Materials Research*. Trans Tech Publ.

27. Reese, L., T. Qiu, D. Linzell, E. O'hare, and Z. Rado. 2014. "*Field tests and numerical modeling of vehicle impacts on a boulder embedded in compacted fill.*" International Journal of Protective Structures. 5(4): pp. 435-451.
28. Williamson, E.B., O. Bayrak, C. Davis, and G. Daniel Williams. 2011. "*Performance of bridge columns subjected to blast loads. II: Results and recommendations.*" Journal of Bridge Engineering. 16(6): pp. 703-710.
29. Williamson, E.B., O. Bayrak, C. Davis, and G.D. Williams. 2011. "*Performance of bridge columns subjected to blast loads. I: Experimental program.*" Journal of Bridge Engineering. 16(6): pp. 693-702.
30. Fujikake, K., B. Li, and S. Soeun. 2009. "*Impact response of reinforced concrete beam and its analytical evaluation.*" Journal of structural engineering. 135(8): pp. 938-950.
31. Baylot, J.T. and T.L. Bevins. 2007. "*Effect of responding and failing structural components on the airblast pressures and loads on and inside of the structure.*" Computers & structures. 85(11-14): pp. 891-910.
32. Wassef, W., C. Smith, C. Clancy, and M. Smith. 2003. "*Comprehensive design example for prestressed concrete (PSC) girder superstructure bridge with commentary.*" Federal Highway Administration report no. FHWA NHI-04-043, grant no. DTFH61-02-D-63006. Washington, DC: US Government Printing Office.
33. Do, T.V., T.M. Pham, and H. Hao. 2018. "*Dynamic responses and failure modes of bridge columns under vehicle collision.*" Engineering structures. 156: pp. 243-259.
34. Liu, G., "*Behavior of bridge piers during vehicular impacts.*" in *Department of Civil Engineering*. 2012, The City College of New York: New York.
35. Williams, G.D., "*Analysis and response mechanisms of blast-loaded reinforced concrete columns.*" 2009.
36. Yi, Z., A. Agrawal, M. Ettouney, and S. Alampalli. 2013. "*Blast load effects on highway bridges. I: Modeling and blast load effects.*" Journal of Bridge Engineering. 19(4): pp. 04013023.
37. Yi, Z., A. Agrawal, M. Ettouney, and S. Alampalli. 2013. "*Blast load effects on highway bridges. II: Failure modes and multihazard correlations.*" Journal of Bridge Engineering. 19(4): pp. 04013024.
38. Oswald, C. 2005 "*Prediction of injuries to building occupants from column failure and progressive collapse with the BICADS computer program.*" in *Structures Congress 2005: Metropolis and Beyond*.
39. Bao, X. and B. Li. 2010. "*Residual strength of blast damaged reinforced concrete columns.*" International journal of impact engineering. 37(3): pp. 295-308.

40. Wu, K.-C., B. Li, and K.-C. Tsai. 2011. "*Residual axial compression capacity of localized blast-damaged RC columns.*" International journal of impact engineering. 38(1): pp. 29-40.
41. Cooper, P.W. 2018. "*Explosives engineering.* John Wiley & Sons.
42. Lomax, R.G. and D.L. Hahs-Vaughn. 2013. "*An introduction to statistical concepts.* Routledge.
43. FEMA, B., "*Prestandard and commentary for the seismic rehabilitation of buildings.*" 2000, Washington, DC.
44. Sharma, H., P. Gardoni, and S. Hurlebaus. 2015. "*Performance - based probabilistic capacity models and fragility estimates for RC columns subject to vehicle collision.*" Computer - Aided Civil and Infrastructure Engineering. 30(7): pp. 555-569.
45. Cao, R., A.K. Agrawal, S. El-Tawil, X. Xu, and W. Wong. 2019. "*Performance-based design framework for bridge piers subjected to truck collision.*" Journal of Bridge Engineering. 24(7): pp. 04019064.
46. Auyeung, S., A. Alipour, and D. Saini. 2019. "*Performance-based design of bridge piers under vehicle collision.*" Engineering Structures. 191: pp. 752-765.
47. Shi, Y. and M.G. Stewart. 2015. "*Spatial reliability analysis of explosive blast load damage to reinforced concrete columns.*" Structural Safety. 53: pp. 13-25.
48. Liu, L., H. Feng, H. Tang, and Z. Guan. 2018. "*Impact resistance of Nomex honeycomb sandwich structures with thin fibre reinforced polymer facesheets.*" Journal of Sandwich Structures & Materials. 20(5): pp. 531-552.
49. Wade, B. and P. Feraboli, "*Crushing Behavior of Laminated Composite Structural Elements: Experiment and LS-DYNA Simulation.*" 2016, DOT/FAA/TC-15/25, Federal Aviation Administration.
50. Mutalib, A.A. and H. Hao. 2010. "*Numerical analysis of FRP-composite-strengthened RC panels with anchorages against blast loads.*" Journal of Performance of Constructed Facilities. 25(5): pp. 360-372.
51. Nam, J.-W., H.-J. Kim, S.-B. Kim, N.-H. Yi, and J.-H.J. Kim. 2010. "*Numerical evaluation of the retrofit effectiveness for GFRP retrofitted concrete slab subjected to blast pressure.*" Composite Structures. 92(5): pp. 1212-1222.
52. Wang, W., C. Wu, and J. Li. 2018. "*Numerical simulation of hybrid FRP-concrete-steel double-skin tubular columns under close-range blast loading.*" Journal of Composites for Construction. 22(5): pp. 04018036.

53. Han, H., F. Taheri, N. Pegg, and Y. Lu. 2007. "*A numerical study on the axial crushing response of hybrid pultruded and $\pm 45^\circ$ braided tubes.*" *Composite Structures*. 80(2): pp. 253-264.
54. Mutalib, A.A. and H. Hao. 2011. "*Development of PI diagrams for FRP strengthened RC columns.*" *International journal of impact engineering*. 38(5): pp. 290-304.
55. Zhang, Z., "*Investigation on dynamic pulse buckling and damage behavior of composite laminated beams subject to axial impulse.*" in *Department of Civil Engineering*. 2004, Dalhousie University: Nova Scotia, Canada.
56. Kimura, H., M. Itabashi, and K. Kawata. 2001. "*Mechanical characterization of unidirectional CFRP thin strip and CFRP cables under quasi-static and dynamic tension.*" *Advanced Composite Materials*. 10(2-3): pp. 177-187.
57. Sha, Y. and H. Hao. 2015. "*Laboratory tests and numerical simulations of CFRP strengthened RC pier subjected to barge impact load.*" *International Journal of Structural Stability and Dynamics*. 15(02): pp. 1450037.
58. Sayed-Ahmed, E.Y. 2006 "Numerical investigation into strengthening steel I-section beams using CFRP strips." in *Structures Congress 2006: Structural Engineering and Public Safety*.
59. Chen, C.C. and D.G. Linzell. 2014. "*Numerical Simulations of Dynamic Behavior of Polyurea Toughened Steel Plates under Impact Loading.*" *Journal of Computational Engineering*. 2014.
60. Davidson, J.S., S. Sudame, and R.J. Dinan, "*Development of computational models and input sensitivity study of polymer reinforced concrete masonry walls subjected to blast.*" 2004, ALABAMA UNIV IN BIRMINGHAM SCHOOL OF ENGINEERING.
61. Gauch, E., J. LeBlanc, and A. Shukla. 2018. "*Near field underwater explosion response of polyurea coated composite cylinders.*" *Composite Structures*. 202: pp. 836-852.
62. LeBlanc, J., C. Shillings, E. Gauch, F. Livolsi, and A. Shukla. 2016. "*Near field underwater explosion response of polyurea coated composite plates.*" *Experimental Mechanics*. 56(4): pp. 569-581.
63. Roland, C., J. Twigg, Y. Vu, and P. Mott. 2007. "*High strain rate mechanical behavior of polyurea.*" *Polymer*. 48(2): pp. 574-578.
64. Dinan, R., J. Fisher, M.I. Hammons, and J.R. Porter, "*Failure mechanisms in unreinforced concrete masonry walls retrofitted with polymer coatings.*" 2003, AIR FORCE RESEARCH LAB TYNDALL AFB FL.
65. LS-DYNA Aerospace Working Group, "*Modeling Guidelines Document Version 13-1.*" 2013.

66. Razaqpur, A.G., A. Tolba, and E. Contestabile. 2007. "*Blast loading response of reinforced concrete panels reinforced with externally bonded GFRP laminates.*" *Composites Part B: Engineering*. 38(5-6): pp. 535-546.